Bergische Universität Wuppertal
Fakultät für Mathematik und Naturwissenschaften
Makromolekulare Chemie

PhD – Thesis

Title:

Carbon-Based Materials for Energy Conversion and Storage

By **Kai Yuan**

Born in Jiangxi, China

Wuppertal, January 2017

Die Dissertation kann wie folgt zitiert werden:

urn:nbn:de:hbz:468-20170127-084544-0
[http://nbn-resolving.de/urn/resolver.pl?urn=urn%3Anbn%3Ade%3Ahbz%3A468-20170127-084544-0]

I would like to dedicate this dissertation to my parents and wife Ting Hu for their continuous understanding and support.

This work was carried out during the period from March 2014 to January 2017 in the Department of Chemistry, Macromolecular Chemistry group, Bergische Universität Wuppertal, under the supervision of Prof. Dr. Ullrich Scherf.

1. Supervisor: Prof. Dr. Ullrich Scherf, Bergische Universität Wuppertal.

2. Reviewer: Prof. Dr. Xinliang Feng, Technische Universität Dresden.

3. Reviewer: Prof. Dr. Yiwang Chen, Nanchang University.

Abstract

Graphene, a two-dimensional monolayer of sp^2-carbon atoms arranged in a honeycomb network, is considered as one of the most promising candidates for use as electrode material of electrochemical capacitors due to its high maximum specific-surface area (~2600 m^2 g^{-1}) and superior electrical conductivity, combined with excellent mechanical properties and outstanding chemical stability. In this thesis, microporous, pillared graphene-based frameworks (PGF) are generated in a simple functionalization/coupling procedure starting from reduced graphene oxide and have been used for the fabrication of high performance supercapacitor devices.

Light-emitting, nanofibrous films were fabricated by electrospinning conjugated microporous polymer (CMP)/poly(lactic acid) (PLA) mixtures. The resulting nanofibrous films show a high flexibility combined with high porosity and surface-area-to-volume ratios. The CMP-based nanofibrous films have been used as sensitive sensors in the detection of nitroaromatic and benzoquinone vapors as well as oxidizing metal ions.

Thereby, conjugated microporous polymer-graphene (G-CMP) sandwiches have been synthesized using 4-iodophenyl-substituted graphene as structure-directing template. Hierarchically, porous nanosheets with high specific surface area are readily obtained by direct pyrolysis of the G-CMP sandwiches. The novel carbon hybrid materials display a very promising capacitive performance in supercapacitor devices.

Two-dimensional (2D) transition-metal dichalcogenides (TMDs) have drawn much attention due to their unique physical and chemical properties. A series of sandwich-like MoS_2-templated conjugated microporous polymer nanosheets with high specific surface area was also successfully fabricated by utilizing 4-iodophenyl-functionalized MoS_2 as template. By direct pyrolysis, 2D

MoS_2/nitrogen-doped porous carbon (M-CMPs-*T*) hybrids were obtained with large specific surface areas and aspect ratios as well as a hierarchically porous structure. The M-CMPs-*T* hybrids have been used for electrochemical catalyzed oxygen reduction reaction (ORR) with high activity and selectivity as well as in excellently performing supercapacitor devices due to the maximized interfacial interaction between nitrogen-doped porous carbon and MoS_2 layers.

Table of Contents

Chapter 1

Introduction

1.1 Background

The climate change and exhaustion of fossils fuels are among the most urgent and critical issues faced by our modern society. In oder to satisfy the growing energy consumption requirement, there is an urgent need to design low-cost, efficient and sustainable devices for energy generation and storage. Being confronted with the really existing energy crisis and global warming, the exploration of renewable, clean and sustainable energy materials as well as the corresponding devices is highly desirable. Utilizing renewable energy from wind or sunlight sources is a first consideration for sustainable energy production. However, they are diffuse and intermittent, owing to the unreliability of nature. For example, energy is mainly captured in the early morning hours for wind power when winds are at their peak or during daylight for solar power. Conversely, geothermal energy, wave energy and tidal power are more predictable and abundant, but can only be produced at selected sites; the collection of the generated energy and its transmission is unfortunately a big obstacle towards these technologies. These pending hurdles have stimulated the research on efficient energy conversion and storage devices. Energy storage devices such as batteries and supercapacitors (electrochemical capacitors), featuring high power/energy densities and excellent cycle performance, are expected to play essential roles in our daily life.[1-3] Currently, there is an increasing demand for low-cost, efficient, flexible, lightweight, and environmentally benign energy storage devices, which can be used to power portable electronic devices, electric vehicles and smart grids. Novel electrode materials, with high energy and power density are urgently needed for realizing high-performance energy storage devices. The recent development in the field of carbon-based materials has shown promise for a wide range of applications.[4-10] In particular, graphene and other 2D materials, due to their

remarkable physical, chemical and electrochemical properties, have shown great potential in energy-related applications.[11-18]

1.2 Supercapacitors and Charge Storage Mechanisms

Supercapacitors, also named as utracapacitors or electrochemical capacitors, have attracted tremendous attention during the past decades, primarily due to their high power density, excellent reversibility, rapid charging/discharging, and outstanding cycle stability (>100000 cycles).[18,19] Undoubtedly, supercapacitors provide a promising approach to resolve the growing energy needs by allowing fast storage of intermittent renewable energy. Defined by the underlying charge storage mechanism, supercapacitors can be divided into two types: (i) devices with electrostatical storing of charges at the interface of the capacitor electrode(s) (electrical double-layer capacitors), and (ii) devices with faradaical storing of charges at the electrode surface(s) (pseudocapacitors).[18,19]

1.2.1 Electrical Double Layer Capacitors (EDLCs)

Electricity storage and delivery via electrical double layers was first proposed by Becker in 1957, and the resulting supercapacitors are called electrical double layer capacitors (EDLCs). In EDLCs, the capacitance arises from the two charged layers formed by adsorption of both positive and negative ions in a double layer at the electrode/electrolyte interfaces. The capacitance is highly dependent on the accessible, electroactive specific surface area to electrolyte ions of the electrode materials. In the charging process, positive ions move to the negative electrode, while negative ions are transfered towards the positive electrode (Figure 1.1). During the discharging process, the directions of the ions movements are reversed. Normally, the electrode materials used in EDLCs are composed of high-surface-area porous carbon-based materials, such as activated carbon, carbon nanofibers, carbon nanosheets, carbon nanotubes, graphene, mesoporous carbon, and carbide-derived carbons.[8,20,21]

1.2.2 Pseudocapacitors

In contrast to EDLCs, the charges are faradaically stored in pseudocapacitors.

The energy is stored through fast and reversible faradaic redox reactions between the electrolyte and electro-active species with charge transfer occurring at/near the electrode surfaces. The most commonly known redox-active electrode materials are ruthenium oxide (RuO_2), manganese oxide (MnO_2), electrically conducting polymers such as polypyrrole or polyaniline, and nitrogen- or oxygen-containing functional surface groups.[8,20] During the charging process, the redox-active electrode materials in the surface region are reduced to lower oxidation states coupled with adsorption/insertion of cations from the electrolyte at/near the electrode surfaces. Upon discharging, the process can be almost fully reversed. Pseudocapacitors can achieve much higher (10 to 100 times) energy densities than EDLCs, since they can adopt multiple oxidation states for efficient redox charge transfer processes between electrodes and adsorbed/inserted electrolyte ions. While the capacitance of pseudocapacitors can be higher as that of EDLCs, it suffers from the main shortcomings of a lowered power density due to the poor electrical conductivity, and the lack of cycle stability.

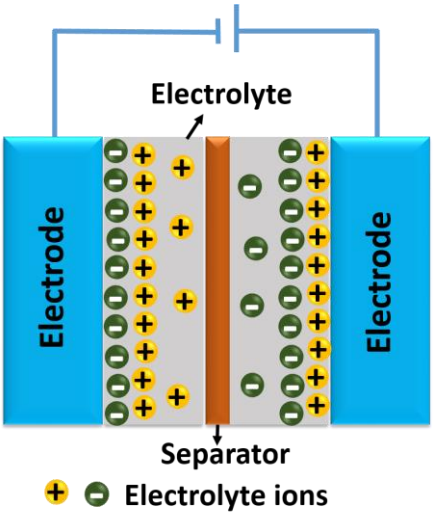

Figure 1.1 Schematic illustration of an electrical double-layer capacitor (EDLC) in its charged state.

1.3 Performance Evaluation for Supercapacitors

The performance of supercapacitor is often evaluated by the following essential parameters, (i) capacitance, (ii) energy/power density, (iii) cycle lifetime, (iv)

operating voltage, and (v) equivalent series resistance.[18-20] An overview of the complex interrelationship between the different performance metrics, the major factors affecting them, and the corresponding test methods is presented in Figure 1.2. Several factors significantly affect the performance of a supercapacitor, such as the porous structure of the electrode materials (specific surface area and pore size distribution), electrical conductivity and morphology/microstructure of electroactive materials, intrinsic properties of the electrolyte, and the interface between electrolyte and electrodes.[4,8,20,22] In addition to the above mentioned factors, some other influencing parameters, such as the choice of electrode configuration, operating voltage, mass loading, reasonable electronic match of negative/positive electrodes, and the (a)symmetric design play an important role for the final performance of supercapacitors. Recently, more and more research efforts on supercapacitors are focussed on developing/discovering novel nanostructured electrode materials with enhanced electrochemical energy storage capability and a long cycle life, meanwhile reducing the manufacturing cost in order to allow their widespread use in our daily life.

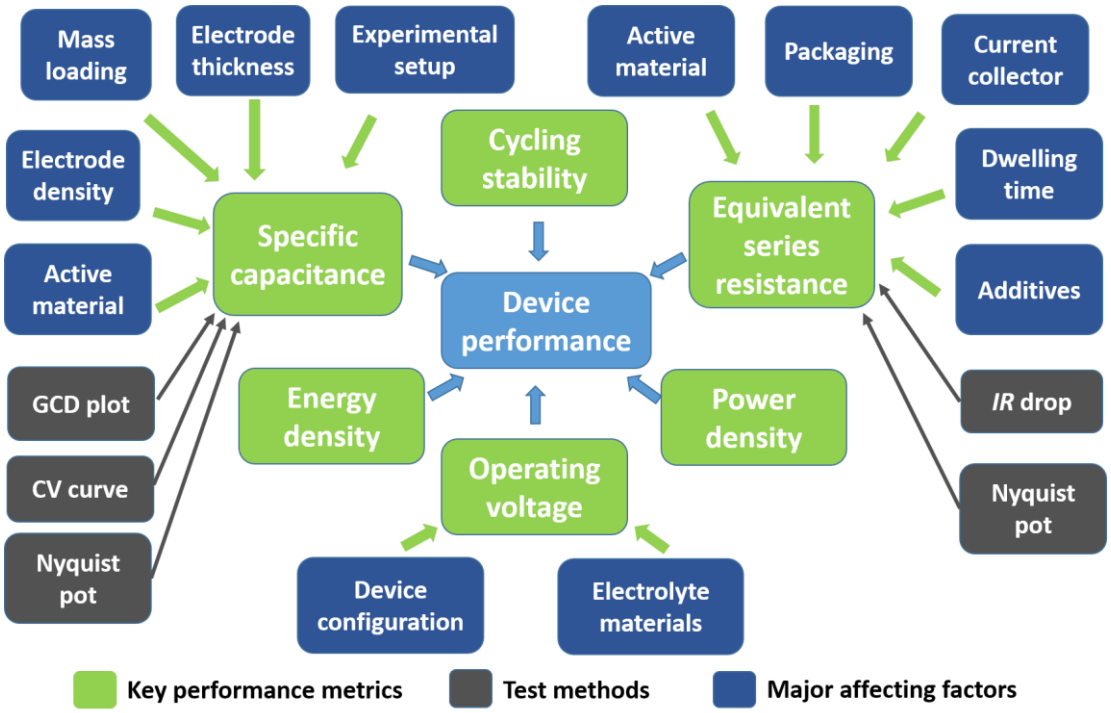

Figure 1.2 An illustration of key performance metrics, test methods, major affecting factors for the evaluation of supercapacitors.

A varity of instruments and test methodes have been developed and used to evaluate the electrochemical performance of supercapacitors. Cyclic voltammetry (CV), galvanostatic charge/discharge (GCD), and electrochemical impedance spectroscopy (EIS) tests are most commonly used. These instruments can be used to measure the fundamental parameters such as voltage, current density and charge/discharge time. Subsequently, capacitance, operating voltage, equivalent series resistance, as well as energy and power density of supercapacitors can be derived from them. The specific capacitance of supercapacitors can be calculated by the following equation:

$$C = I \Delta t / m \Delta V$$

where C (F/g) is the specific capacitance, I (mA) the discharge current, and Δt (s), m (mg), and ΔV (V) the total discharge time, the mass of active material, and the potential drop (by excluding the voltage (IR) drop) during discharge, respectively. The energy density (E) can be calculated from the discharge profiles of the GCD curves by using the following equation:

$$E = 0.5 C \Delta V^2 / 3.6$$

where E (Wh kg^{-1}) is the energy density, C (F g^{-1}) the specific capacitance and ΔV (V) the discharge voltage range. With a factor 3.6, the energy density is converted from J g^{-1} to Wh kg^{-1}. The power density (P) can be calculated as follows:

$$P = E \times 3600 / \Delta t$$

where P (kW kg^{-1}) is the power density, and E (Wh kg^{-1}) and Δt (s) energy density and discharge time, respectively.

1.4 Carbon Materials for Supercapacitores

Commonly, different forms of porous carbon materials such as activated carbons,[23,24] mesoporous carbons,[25,26] carbon xerogels,[27,28] carbide-derived carbons,[29,30] templated carbons,[31-33] carbon nanotubes (CNTs),[34,35] graphene,[15,16,36,37] porous carbon spheres,[38,39] carbon nanosheets,[40-43] and carbon onions,[44] have been investigated extensively as the electrode materials of supercapacitors. It has been,

both theoretically and experimentally, demonstrated that several factors significantly affect the electrochemical performances of carbon materials including specific surface area, pore size and distribution, electrical conductivity, and pore volume.

1.4.1 Activated Carbon

Activated carbons are the most used electrode materials for EDLCs attribute to their high specific surface area, moderate cost, relatively high electrical conductivity as well as excellent thermal and chemical stability. Activated carbons are generally produced from various types of carbon-rich precursors (such as wood, nutshells, coal, polymers, etc.) by carbonization in inert atmosphere with subsequent physical and/or chemical activation to increase the specific surface area and pore volume. Depending on the used carbon precursors and the activation process, a variety of activated carbons with different physicochemical properties and high specific surface area of up to 3000 m^2 g^{-1} have been prepared and used as electrode materials for supercapacitors.

Due to the electrical double-layer storage mechanism of carbon materials, it is usually anticipated that there it a direct relation between specific surface area and supercapacitor performance. With increasing specific surface area more electrolyte ions can be accumulated at the electrode/electrolyte interfaces. Therefore, various approaches have been developed to increase the specific surface area of carbon materials, including alkaline treatment, heat treatment, surface plasma treatment, and physical or chemical activation. Although the specific surface area is a significant factor for the performance of EDLCs, some other important parameters of the carbon materials including pore size distribution, electrical conductivity, pore shape and structure as well as the surface functionality can also affect the electrochemical performance.

Generally, a narrowing of the pore size distribution leads to an increase in capacitance, which means that monodispersed pores and optimized pore size distributions would be ideal for improving the energy storage process and the stored

energy density of supercapacitors. Efforts have been made to search for a relationship between capacitive performance and nanoporous structure of actived carbons in different electrolytes. Recent studies by Largeot et al. have demonstrated the relationship between pore size and electrolyte ion size for an EDLC and concluded that the maximum electrical double layer capacitance is obtained when the pore size matches the electrolyte ion size.[45] Such a pore size-dependent capacitive behavior is shown in Figure 1.3. Kondrat and coworkers both theoretically and experimentally demonstrated that an optimal pore size results in the maximal energy density.[46] This optimum pore size increases with increasing operating voltage.

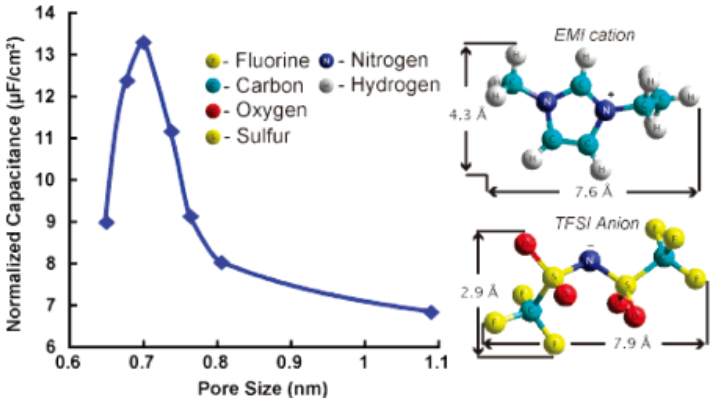

Figure 1.3 Normalized capacitance change as a function of the pore size of carbide-derived carbon samples. Samples were prepared at different temperatures in an ethyl-methylimidazolium/trifluoromethanesulfonylimide (EMI, TFSI) ionic liquid at 60 °C. Inset shows structure and size of the EMI and TFSI ions. The maximum capacitance is obtained when the pore size is in the same range as the maximum ion dimension. Reproduced with permission.[45] Copyright 2008, American Chemical Society.

In short, activated carbons have been commercially used as electrode materials for supercapacitors. However, their practical applications are still restricted due to the limited energy storage capability. Although activated carbons provide a high specific surface area, the control of pore structure and pore size distribution is still a great challenge. Therefore, it is of great significance to design and produce activated carbons with tailored pore size distribution, interconnected pore structure, short pore length, minimized pore tortuosity, and controlled surface chemistry, thus facilitating the ion transport and enhancing energy storage without sacrificing their power capability and cycle life.

1.4.2 Templated Carbons

Most porous carbon materials feature a very wide pore size distribution with disordered pores randomly connected, resulting in poor electronic conductivity and ionic transport ability, and very limited rate capability for supercapacitor applications. In addition, it is extremely difficult to precisely control the porous structure of conventional carbon materials at the nanometer level. Therefore, the templating method is considered to be an another effective way to produce nanostructured carbon materials with well controlled narrow pore size distributions, large specific surface areas, ordered pore structures, and an interconnected pore network. There has been remarkable progress in the synthesis of ordered nanostructured carbons through templating techniques (soft- and hard-template methods). Generally, the preparation procedure of templated carbons includes (a) impregnation of a carbon precursor (such as propylene, pitch, or polymer solution. etc.) into the pores of the nanostructured template, followed by (b) a carbonization treatment and finally (c) the removal of the template to liberate the resulting porous carbon.

Various carbon materials with well controlled micropores, mesopores and/or macropores synthesized by using different kinds of carbon precursors and templates have been studied for supercapacitor applications. Templated carbons with their uniform pore sizes, high specific surface area, large pore volumes, ordered structure and desirable physical and chemical properties are promising candidates for an use as electrode materials of supercapacitor with high energy and power densities. However, disadvantages of templated carbons such as relatively high production costs, low reproducibility, and safety considerations seriously limit their potential for commercial applications. Additionally, many template materials are not available by ton or even kilogram range, makig them unsuitable for a large-scale production. Therefore, it will be necessary to develop simpler, economical, and environmentally benign template approches towards mass applications. Despite the costs, templated carbons are promising materials for scientific studies. They can provide valuable information about the effect of channel structure, pore shape, pore size, and other

parameters on the ion diffusion and charge storage in nanostructured systems.

1.4.3 Carbide-Derived Carbons

Carbide-derived carbons are generally produced by selective extraction of non-carbon atoms from carbides (such as TiC, ZrC, B_4C, Ti_3SiC_2 and Ti_2AlC) at high-temperature (800-1200 °C). Thereby, high-temperature chlorination is the most widely used approache for carbide-derived carbon synthesis:

$$MC + nCl_2 \rightarrow MCl_{2n} + C$$

The as-synthesized carbide-derived carbons possess a narrow and tunable pore size distribution in sub-angstrom accuracy, an average pore size of 0.6-2 nm, and specific surfaces area of up to 3100 $m^2\ g^{-1}$. Therefore, they can exhibit outstanding electrochemical performance in aqueous, organic, and ionic liguid electrolytes.[20,21] Carbide-derived carbon technology allows for the control of carbon growth on the atomic level, monolayer by monolayer. Mean pore size, pore size distribution, pore volume, and specific surface area of the carbide-derived carbons can be controlled and tailored by selecting the precursors, by optimizing the process parameters and the chlorination conditions, such as environment, temperature and time. However, carbide-derived carbons still have very limited commercial potential owing to serious safety and environmental concerns associated with production to high costs, and to the requirement of high process temperatures.[20]

1.4.4 Carbon Nanotubes

The discovery of carbon nanotubes has significantly advanced the science and engineering of carbon materials. Carbon nanotubes have attracted a big portion of attention for supercapacitor applications due to their unique pore structure, excellent electrical conductivity, and outstanding mechanical, chemical and thermal stability.[47] Carbon nanotubes can be categorized into single-walled carbon nanotubes and multi-walled carbon nanotubes, both of which have been widely applied as energy storage electrode materials. Carbon nanotubes are usually regarded as an electrode material of choice for high-power devices due to their readily accessible surface area and excellent electrical conductivity. Moreover, carbon nanotubes can be used as

good support for preparing composite electrodes by decorating or coating the carbon nanotube surface with a thin film of electroactive materials due to their high mechanical resilience and due to the formation of open tubular networks.

However, carbon nanotubes usually show a high tendency to aggregate into bundles because of strong van der Waals forces. This process consequently distinctly reduces the effective ion-accessible surface area. Additionally, electrodes based on carbon nanotubes usually do not possess the appropriate pore structure for a facile access by electrolyte ions. The energy density of supercapacitors based on carbon nanotubes is still low due to the limitations in the accessible surface area (generally < 600 m^2 g^{-1}). Due to this issue, it is highly desirable to find a large-scale fabrication approaches that can accuratly control morphology, alignment and spatial arrangement of carbon nanotube arrays for an effective utilization of the surface area that carbon nanotubes can theoretically provide with the final goal of a significant improvement of the supercapacitor performance. In addition, the present high costs of carbon nanotube production and difficulties in their purification still restrict their practical application potential.

1.4.5 Graphene

Graphene is a one-atom-thick and two-dimensional (2D) sp^2-hybridized carbon allotrope with a hexagonal lattice. The extended honeycomb network of graphene is the basic building priciple of other important carbon allotropes (that is, graphite, fullerenes and carbon nanotubes). Depending on its unique structure, graphene possesses a very high theoretical specific surface area (2630 m^2 g^{-1}) and excellent electronic, optical, thermal, and mechanical properties.[15,16,36] Thus, graphene-derived materials hold great promise for potential applications in enrgy storage and conversion devices. Interest in graphene has grown continuously in the scientific community in recent years, and tremendous achievements have been obtained, e.g. for applications of supercapacitors.

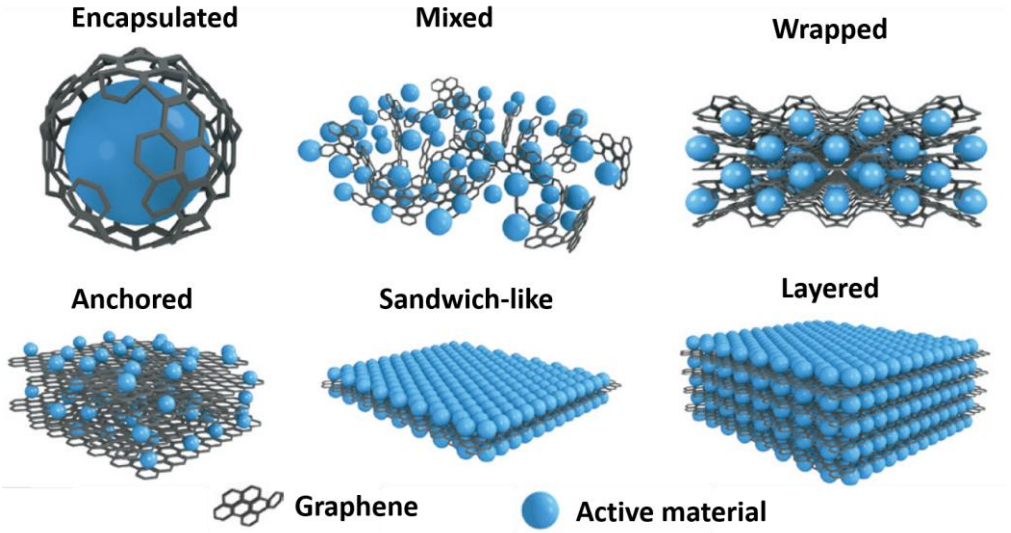

Figure 1.4 Schematic of the different structures of graphene-based composite materials for electrodes. Reproduced with permission.[15] Copyright 2015, Nature Publishing Group.

However, the research in the field is still in the infancy and there are several obstacles significantly preventing practical and commercial applications. (1) First, the large scale fabrication of high-quality graphene with controllable layer thickness on a large scale in an environmentally benign and cost-effective approache is the major technical hindrance inhibiting the further application of graphene as an alternate electrode materials of supercapacitors. Towards this goal, effective, scalable, low-cost, and environmentally friendly approaches to control thickness, number of layers, surface functionalities and the defect content must be developed. (2) Second, graphene materials have a natural tendency for re-aggregation/re-stacking during synthesis or electrode preparation due to their high surface area as well as strong π–π interactions and van der Waals forces between adjacent graphene sheets. Re-aggregation and re-stacking significantly decrease the electrochemically active surface area and limit the access of electrolyte ions to the surface of the sheets. This can result in a deteriorated supercapacitor performance. Hence, it is of great significance to develop effective procedures to inhibit the irreversible re-stacking and to preserve the high specific surface area. High electrical conductivity and chemical stability in addition to the high surface area defines 2D graphene sheets as excellent substrates/templates for the design of functional hybrid nanomaterials, in combination

with other carbon allotropes, inorganic nanostructures, and conducting polyelectrolytes. This strategy may effectively prevent the aggregation of the hybrid sheets and result in graphene-based composite materials with high surface area (Figure 1.4). (3) Last but not least, a better understanding of the interrelationship between supercapacitor performance and molecular structure as well as interactions within the hybrids will be essential.

1.4.6 Heteroatom-Doped Carbon Materials

The electrical conductivity of most porous carbon materials usually suffers from a deterioration with increasing porosity and specific surface area caused by a destruction of conductive pathways. This behaviour consequently limits the power capability of supercapacitors. In order to improve the energy density, the incorporation of doping of the carbon materials with heteroatoms (such as B, N, O, S, and P) for introducing pseudocapacitances has attracted increasing attention during the last years.

Among various heteroatoms, nitrogen has become the most widely investigated heteroatomicdopant in the optimization of carbonaceous electrode materials. N-doping shows effects on the resulting capacitance for both aqueous and organic electrolytes. Commonly, there are four different states of doped N-atoms found: pyridinic N, pyrrolic N, quaternary N, and N-oxide.[6] Among these, pyridinic N and pyrrolic N are assumed to be the main states contributing to the creation of pseudocapacitances. The presence of quaternary N atoms can improve the electrical conductivity, which can be beneficial for enhancing the supercapacitor performance. In addition, N-doping can change the electron distribution of the carbon material and can enhance the wettability between electrolyte and electrode material, resulting in a significant increase of active, accessible surface area.

The integration of oxygen-containing surface groups is also a promising strategy to enhance the supercapacitor performance based on the presence of reversibly oxidizible/reducible hydroquinone/quinone groups. Moreover, the hydrophilic nature

of oxygen functional groups can also improve the wettability. However, irreversible reactions between oxygen and electrolyte ions can cause decomposition of the electrolyte, an increase of the internal resistance of the electrode, and, finally, inferior rate capability and cycle life.[20]

Additionally, other heteroatoms, such as B, P or S can be salso advantageous in improving the supercapacitor performance. However, the mechanisms of how these introduced heteroatoms (including location and electronic configuration in the carbonaceous skeletons) affect the performance of supercapacitors is still not fully understood. Therefore, more research into the doping mechanism are required towards the future applications as energy storage matrials.

1.4.7 Conjugated Microporous Polymers (CMPs)

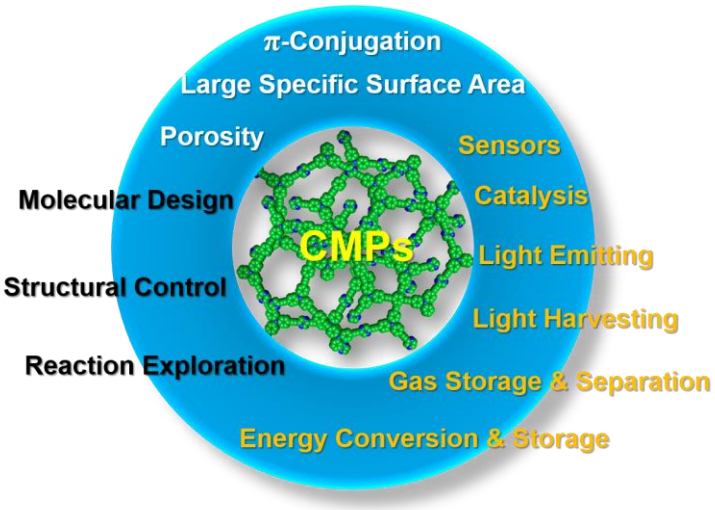

Figure 1.5 Schematic illustration of properties and potential applications of congjugated microporous polymers (CMPs).

Conjugated microporous polymers (CMPs) as a subclass of porous polymers have attracted tremendous attention due to their attractive properties (Figure 1.5), such as porosity, π-conjugated skeleton, large specific surface area, high physical and chemical stability.[48,49] The porous structure can be controlled by molecular design via changes of the building blocks (tectons). Different types of C-C coupling reactions can be applied to synthesize microporous conjugated polymers, such as the

Suzuki-type aryl-aryl-coupling, the Sonogashira-Hagihara coupling, the Yamamoto coupling, and the ethynyl trimerization.[49] CMPs show a large application potential in gas storage/separation, superabsorption, sensing and light harvesting as well as in light emitting devices, heterogeneous catalysis, and electric energy conversion/storage.[6,50-53]

Moreover, carbon-rich CMPs can be used as precusors for pyrolysis into hierarchically porous carbons materials. Such porous carbon materials are discussed as potential electrode materials for supercapacitors.[54-56] Using CMP-derived carbons as electrode materials, several advantages towards high-performance supercapacitors can be mentioned: (1) Materials with well-defined pore size distribution can be formed by adjusting the size of the building blocks. This approach significantly contributes to a systematic understanding of the relation between pore size effect and supercapacitor performances; (2) Materials with different dimensions can be constructed by tailoring the configurations of building blocks, templates. (3) Various heteroatom-doped materials can be synthesized by using diverse heteroatom-containing building blocks. Thereby, the heteroatom-related pseudocapacitance can be controlled; (4) Metal atoms can also be introduced into the carbonaceous skeletons by employing metal atom-containing precursors. Thereby, metal-related pseudocapacitance contributions can be expected.

The excellent intrinsic properties of carbonaceous CMP networks make them attractive components of electrode materials for supercapacitors. More importantly, the bottom-up synthetic protocols toward CMPs provide an ideal platform for the design of carbon-based material for supercapacitor materials in a more controlled manner. Therefore, it can be expected that CMP-based hybrid materials will play an important role in the development of next generation carbon-based supercapacitors.

1.5 Overview of the Dissertation

This dissertation describes design, fabrication, and characterization of

carbon-based materials for use in enery storage and conversion. The major objectives include:

(1) Generation of pillared, microporous graphene frameworks for use in supercapacitors
(2) Fabrication of nanofibrous and graphene-templated conjugated microporous polymer materials for flexible chemosensors and supercapacitors
(3) Generation of 2D porous carbon nanosheets for high performance supercapacitors
(4) Fabrication of nitrogen-doped porous carbon/graphene nanosheets with promising capacitive performance
(5) Synthesis of two-dimensional core-shelled porous hybrids as highly efficient catalysts for oxygen reduction reaction

In Chapter 2, microporous, pillared graphene-based frameworks are generated in a simple functionalization/coupling procedure starting from reduced graphene oxide. They have been used for the fabrication of high performance supercapacitor devices. In Chapter 3, conjugated microporous polymer (CMP)-based nanofibrous chemosensors were simply fabricated by electrospinning. Moreover, 4-iodophenyl-substituted graphene was used as structure-directing template towards hierarchically porous carbon nanosheets with promising supercapacitor performance. In Chapter 4 and Chapter 5, a series of hierarchically, nanostructured, nitrogen-doped porous carbon/graphene nanosheets with very promising supercapacitive performance are prepared in a straightforward procedure. In Chapter 6, hierarchically 2D MoS_2/nitrogen-doped porous carbon hybrids are fabricated. They show a promising performance in the oxygen reduction reaction (ORR) and in supercapacitor devices. In the final Chapter of this dissertation conclusion and outlook are presented.

1.6 References

(1) Miller, J. R.; Simon, P. *Science* **2008**, *321*, 651-652.
(2) Gogotsi, Y.; Simon, P. *Science* **2011**, *334*, 917-918.

(3) Simon, P.; Gogotsi, Y.; Dunn, B. *Science* **2014**, *343*, 1210-1211.

(4) Simon, P.; Gogotsi, Y. *Nat. Mater.* **2008**, *7*, 845-854.

(5) Pandolfo, A. G.; Hollenkamp, A. F. *J. Power Sources* **2006**, *157*, 11-27.

(6) Hao, L.; Li, X.; Zhi, L. *Adv. Mater.* **2013**, *25*, 3899-3904.

(7) Zhai, Y.; Dou, Y.; Zhao, D.; Fulvio, P. F.; Mayes, R. T.; Dai, S. *Adv. Mater.* **2011**, *23*, 4828-4850.

(8) Zhang, L. L.; Zhao, X. S. *Chem. Soc. Rev.* **2009**, *38*, 2520-2531.

(9) Wang, Q.; Yan, J.; Fan, Z. *Energy Environ. Sci.* **2016**, *9*, 729-762.

(10) Yang, Z.; Ren, J.; Zhang, Z.; Chen, X.; Guan, G.; Qiu, L.; Zhang, Y.; Peng, H. *Chem. Rev.* **2015**, *115*, 5159-5223.

(11) Xu, Y.; Shi, G.; Duan, X. *Acc. Chem. Res.* **2015**, *48*, 1666-1675.

(12) Ma, Y.; Chang, H.; Zhang, M.; Chen, Y. *Adv. Mater.* **2015**, *27*, 5296-5308.

(13) Mendoza-Sanchez, B.; Gogotsi, Y. *Adv. Mater.* **2016**, *28*, 6104-6135.

(14) Shao, Y.; El-Kady, M. F.; Wang, L. J.; Zhang, Q.; Li, Y.; Wang, H.; Mousavi, M. F.; Kaner, R. B. *Chem. Soc. Rev.* **2015**, *44*, 3639-3665.

(15) Raccichini, R.; Varzi, A.; Passerini, S.; Scrosati, B. *Nat. Mater.* **2015**, *14*, 271-279.

(16) Bonaccorso, F.; Colombo, L.; Yu, G.; Stoller, M.; Tozzini, V.; Ferrari, A. C.; Ruoff, R. S.; Pellegrini, V. *Science* **2015**, *347*, 1246501.

(17) Yang, Y.; Han, C.; Jiang, B.; Iocozzia, J.; He, C.; Shi, D.; Jiang, T.; Lin, Z. *Mat. Sci. Eng. R.* **2016**, *102*, 1-72.

(18) Zhang, X.; Hou, L.; Ciesielski, A.; Samorì, P. *Adv. Energy Mater.* **2016**, 1600671.

(19) Zhang, S.; Pan, N. *Adv. Energy Mater.* **2015**, *5*, 1401401.

(20) Yan, J.; Wang, Q.; Wei, T.; Fan, Z. J. *Adv. Energy Mater.* **2014**, *4*, 1300816.

(21) Simon, P.; Gogotsi, Y. *Acc. Chem. Res.* **2013**, *46*, 1094-1103.

(22) Salanne, M.; Rotenberg, B.; Naoi, K.; Kaneko, K.; Taberna, P. L.; Grey, C. P.; Dunn, B.; Simon, P. *Nat. Energy* **2016**, *1*, 16070.

(23) Bao, L.; Li, X. *Adv. Mater.* **2012**, *24*, 3246-3252.

(24) Wei, L.; Sevilla, M.; Fuertes, A. B.; Mokaya, R.; Yushin, G. *Adv. Funct. Mater.*

2012, *22*, 827-834.

(25) He, X.; Li, R.; Qiu, J.; Xie, K.; Ling, P.; Yu, M.; Zhang, X.; Zheng, M. *Carbon* **2012**, *50*, 4911-4921.

(26) Lin, T.; Chen, I.-W.; Liu, F.; Yang, C.; Bi, H.; Xu, F.; Huang, F. *Science* **2015**, *350*, 1508-1513.

(27) Moreno-Castilla, C.; Dawidziuk, M. B.; Carrasco-Marín, F.; Zapata-Benabithe, Z. *Carbon* **2011**, *49*, 3808-3819.

(28) Chien, H.-C.; Cheng, W.-Y.; Wang, Y.-H.; Lu, S.-Y. *Adv. Funct. Mater.* **2012**, *22*, 5038-5043.

(29) Xie, K.; Qin, X.; Wang, X.; Wang, Y.; Tao, H.; Wu, Q.; Yang, L.; Hu, Z. *Adv. Mater.* **2012**, *24*, 347-352.

(30) Liu, H.-J.; Wang, J.; Wang, C.-X.; Xia, Y.-Y. *Adv. Energy Mater.* **2011**, *1*, 1101-1108.

(31) Itoi, H.; Nishihara, H.; Kogure, T.; Kyotani, T. *J. Am. Chem. Soc.* **2011**, *133*, 1165-1167.

(32) Yan, J.; Wang, Q.; Wei, T.; Jiang, L.; Zhang, M.; Jing, X.; Fan, Z. *ACS Nano* **2014**, *8*, 4720-4729.

(33) Xue, Y.; Ding, Y.; Niu, J.; Xia, Z.; Roy, A.; Chen, H.; Qu, J.; Wang, Z. L.; Dai, L. *Sci. Adv.* **2015**, *1*, e1400198.

(34) Izadi-Najafabadi, A.; Yasuda, S.; Kobashi, K.; Yamada, T.; Futaba, D. N.; Hatori, H.; Yumura, M.; Iijima, S.; Hata, K. *Adv. Mater.* **2010**, *22*, E235-E241.

(35) Izadi-Najafabadi, A.; Futaba, D. N.; Iijima, S.; Hata, K. *J. Am. Chem. Soc.* **2010**, *132*, 18017-18019.

(36) El-Kady, M. F.; Shao, Y.; Kaner, R. B. *Nat. Rev. Mater.* **2016**, *1*, 16033.

(37) El-Kady, M. F.; Strong, V.; Dubin, S.; Kaner, R. B. *Science* **2012**, *335*, 1326-1330.

(38) Xu, F.; Tang, Z.; Huang, S.; Chen, L.; Liang, Y.; Mai, W.; Zhong, H.; Fu, R.; Wu, D. *Nat. Commun.* **2015**, *6*, 7221.

(39) Liu, J.; Wickramaratne, N. P.; Qiao, S. Z.; Jaroniec, M. *Nat. Mater.* **2015**, *14*, 763-774.

(40) Zheng, X.; Luo, J.; Lv, W.; Wang, D. W.; Yang, Q. H. *Adv. Mater.* **2015**, *27*, 5388-5395.

(41) Ling, Z.; Wang, Z.; Zhang, M.; Yu, C.; Wang, G.; Dong, Y.; Liu, S.; Wang, Y.; Qiu, J. *Adv. Funct. Mater.* **2016**, *26*, 111-119.

(42) Hou, J.; Cao, C.; Idrees, F.; Ma, X. *ACS Nano* **2015**, *9*, 2556-2564.

(43) Fan, X. M.; Yu, C.; Yang, J.; Ling, Z.; Hu, C.; Zhang, M. D.; Qiu, J. S. *Adv. Energy Mater.* **2015**, *5*, 1401761.

(44) Pech, D.; Brunet, M.; Durou, H.; Huang, P.; Mochalin, V.; Gogotsi, Y.; Taberna, P.-L.; Simon, P. *Nat. Nanotechnol.* **2010**, *5*, 651-654.

(45) Largeot, C.; Portet, C.; Chmiola, J.; Taberna, P.-L.; Gogotsi, Y.; Simon, P. *J. Am. Chem. Soc.* **2008**, *130*, 2730-2731.

(46) Kondrat, S.; Perez, C. R.; Presser, V.; Gogotsi, Y.; Kornyshev, A. A. *Energy Environ. Sci.* **2012**, *5*, 6474-6479.

(47) Zhang, G. H.; Song, Y.; Zhang, H.; Xu, J.; Duan, H. G.; Liu, J. Y. *Adv. Funct. Mater.* **2016**, *26*, 3012-3020.

(48) Cooper, A. I. *Adv. Mater.* **2009**, *21*, 1291-1295.

(49) Xu, Y.; Jin, S.; Xu, H.; Nagai, A.; Jiang, D. *Chem. Soc. Rev.* **2013**, *42*, 8012-8031.

(50) Vilela, F.; Zhang, K.; Antonietti, M. *Energy Environ. Sci.* **2012**, *5*, 7819-7832.

(51) Xiang, Z.; Dai, Q.; Chen, J. F.; Dai, L. *Adv. Mater.* **2016**, *28*, 6253-6261.

(52) Talapaneni, S. N.; Hwang, T. H.; Je, S. H.; Buyukcakir, O.; Choi, J. W.; Coskun, A. *Angew. Chem., Int. Ed.* **2016**, *55*, 3106-3111.

(53) Hao, L.; Ning, J.; Luo, B.; Wang, B.; Zhang, Y.; Tang, Z.; Yang, J.; Thomas, A.; Zhi, L. *J. Am. Chem. Soc.* **2014**, *137*, 219-225.

(54) Zhuang, X.; Zhang, F.; Wu, D.; Forler, N.; Liang, H.; Wagner, M.; Gehrig, D.; Hansen, M. R.; Laquai, F.; Feng, X. *Angew. Chem., Int. Ed.* **2013**, *52*, 9668-9672.

(55) Zhuang, X.; Zhang, F.; Wu, D.; Feng, X. *Adv. Mater.* **2014**, *26*, 3081-3086.

(56) Xiang, Z.; Cao, D.; Huang, L.; Shui, J.; Wang, M.; Dai, L. *Adv. Mater.* **2014**, *26*, 3315-3320.

Chapter 2

Straightforward Generation of Pillared, Microporous Graphene Frameworks for Use in Supercapacitors[1]

2.1 Introduction

Driven by the limited supply of fossil fuels and environmental problems, the development of clean and renewable energy sources and novel energy storage and transformation devices are urgently needed.[2-6] During the past decades, extensive research on the exploration of novel concepts for energy storage, transport and rectification have been conducted, and various electrical energy storage devices have been developed. Among other energy storage technologies, rechargeable batteries and electrochemical capacitors are typically regarded as promising candidates for energy storage by transforming chemical energy into electrical energy.[7,8] Electrochemical capacitors, also called ultracapacitors or supercapacitors, which use either reversible ion adsorption (electric double-layer capacitors) or fast surface redox reactions (pseudocapacitors) to store energy, have attracted considerable attention, and are supposed to be a suitable choice for alternate electrical energy storage devices. This is attributed to potential advantages, as high power density, rapid charging/discharging rate, exceptional cycling stability, high reliability and low maintenance costs.[9-11]

Currently, one major challenge in the field of electrochemical capacitors is to improve their energy density while maintaining their high power density and long cycling life time with the future goal to reach or surpass the performance of fuel cells or Li-ion batteries, most favourably at low manufacture costs. It is well accepted that the supercapacitive performance of an electrochemical capacitor is not only significantly related to the accessible specific surface area of the electrode material but also to the transport kinetics of ions and electrons. Generally, an ideal electrode material of an electrochemical capacitor should satisfy the following features: (i) a

porous structure with high specific surface as well as a hierarchical, well-balanced pore size distribution for efficient charge storage and high specific capacitance, (ii) high electrical conductivity for high power density and rate capability, and (iii) a superior compatibility with the electrolyte to facilitate ion diffusion and to maximize the ion-accessible surface area.[6,11,12]

Graphene, a two-dimensional monolayer of sp^2-carbon atoms arranged in a honey comb network, is considered as one of the most promising candidates for the electrode materials of electrochemical capacitors due to its high maximum specific-surface area (~2600 m^2 g^{-1}) and superior electrical conductivity, combined with excellent mechanical properties and outstanding chemical stability.[10,13,14] Therefore, electrochemical capacitors based on graphene-type materials could, in principle, achieve a maximum theoretical electric double-layer capacitance value as high as ~550 F/g if their full surface area is used.[15,16] However, graphene nanosheets show a high tendency for re-aggregation and stack together in the course of utilization as electrode materials due to their high surface area as well as strong π-π interactions and van der Waals forces between adjacent graphene sheets.[15,16] This inevitable re-aggregation and stacking significantly decreases the electrochemically active surface area and limits the access of electrolyte ions to the surface of the sheets through a interpenetrating pore system, thus resulting in a deteriorated supercapacitor performance.[17] Various strategies have been developed to overcome this bottleneck, as the introduction of a second component between adjacent graphene layers for blocking the restacking of graphene sheets, or the development of well-defined graphene-based nanomaterials with 3D morphology.[18-20] Graphene-based materials, e.g., graphene/polymer (such as polypyrrole and polyaniline) and graphene/transition metal oxides (MnO_2, NiO and RuO_2) composites have been employed in this direction and displayed improved specific capacitances than graphene itself.[21-26] However, the high costs of Ru-based oxides limits their application, and the poor rate performance and/or cycling stability induced by both polymers or Mn-based oxides is still a critical problem.

In this chapter, we present a novel strategy for the design and generation of nanoarchitectures based on porous graphene frameworks (PGF) via *in situ* covalent functionalization of reduced graphene oxide (RGO) with 4-iodophenyl substitutes followed by an aryl-aryl-coupling reaction. Compared to RGO, our 3D PGF displays high specific surface areas thank to the introduction of the biphenyl pillars. Considering the inherent and permanent porous structure of PGF combined with the presence of their extended π-conjugated system and high electric conductivity, the application of PGF in supercapacitors was investigated in detail. Due to its unique structure, the 3D PGF as electrode materials exhibit a promising electrochemical performance if compared to RGO, including high specific capacitances combined with a very high cycling stability in both three-electrode systems and two-electrode symmetric supercapacitor devices. These results confirm that such nanostructured PGF electrodes held great promise for future applications in energy storage.

2.2 Results and Discussion

2.2.1 Sythesis of Porous Graphene Frameworks (PGF)

The strategy for the synthesis of PGF is presented in Scheme 2.1. First, graphene oxide (GO) was prepared according to a modified Hummers protocol and reduced with $NaBH_4$ according to a reported literature procedure. Then RGO is functionalized with 4-iodophenyl groups by reaction with 4-iodobenzene diazonium salt under aqueous conditions (detailed procedures see Experimental section).[27-30] The size of the GO sheets used in the modification process ranges from hundreds of nanometers to several micrometers with an uniform thickness of ~1 nm (Figure 2.1). The obtained 4-iodophenyl-functionalized graphene (RGO-IBz) can be well-dispersed in different organic solvents, for instance, N, N-dimethylformamide (DMF), toluene and chlorobenzene. Next, bis(cyclooctadiene)nickel, 2,2'-bipyridyl and 1,5-cyclooctandiene were mixed with the degassed dispersion of RGO-IBz in DMF, and the reaction mixture was stirred under Yamamoto aryl-aryl-coupling conditions. After cooling to room temperature, concentrated HCl was added to the mixture, a black solid was collected by filteration and purified by Soxhlet extraction with H_2O

and THF for 1 day, respectively. Finally, PGF as product was obtained after vacuum drying.

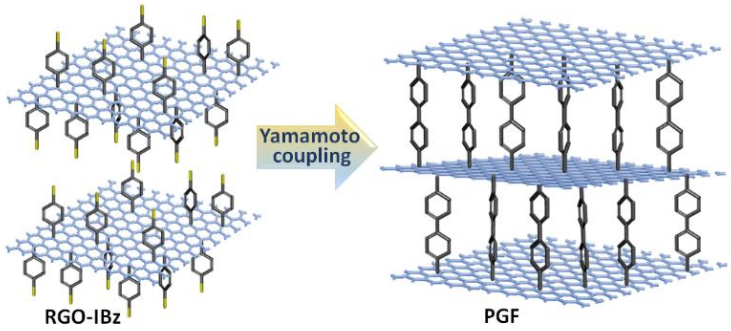

Scheme 2.1 Synthesis strategy for the generation of PGF.

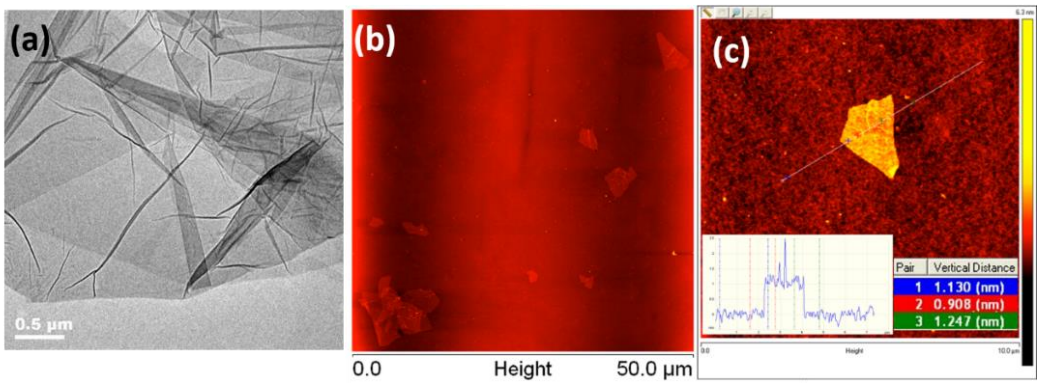

Figure 2.1 (a) TEM and (b) AFM images of GO sheets, (c) the corresponding height profile of one GO sheet, with a thickness of ca. 1 nm.

Solid state ^{13}C magic angle spinning (MAS) NMR spectroscopy has been employed as the primary method to characterize GO, RGO, RGO-IBz and PGF at the molecular level, as shown in Figure 2.2a. The three major resonances in the ^{13}C NMR spectrum of GO correspond to epoxy carbons (59.5 ppm), hydroxylated carbons (69.6 ppm) and non-oxidized sp^2 carbons (131.9 ppm).[31-33] Weak resonances at 167 and 193 ppm are assigned to carboxy and carbonyl carbons.[31,32] After reduction, the peaks at 59.5 and 69.6 ppm disappeared, and the resonance at 131.9 ppm is shifted to 121.3 ppm due to the variations of the chemical environment of the sp^2 carbons.[32] As shown in the NMR spectrum of RGO-IBz, after functionalization with 4-iodophenyl substitutes this peak of sp^2 carbons is again low field-shifted to 128.4 ppm, and a shoulder arising at 136 ppm is attributed to the 4-iodophenyl moiety that is covalently

attached to the sp^2 carbons of the graphene layers, thus demonstrating that covalent modification of RGO occurred. Intensity changes in the aromatic carbon region and a newly emerging resonance peaking at 139 ppm of PGF indicate the successful conversion of RGO-IBz into PGF.

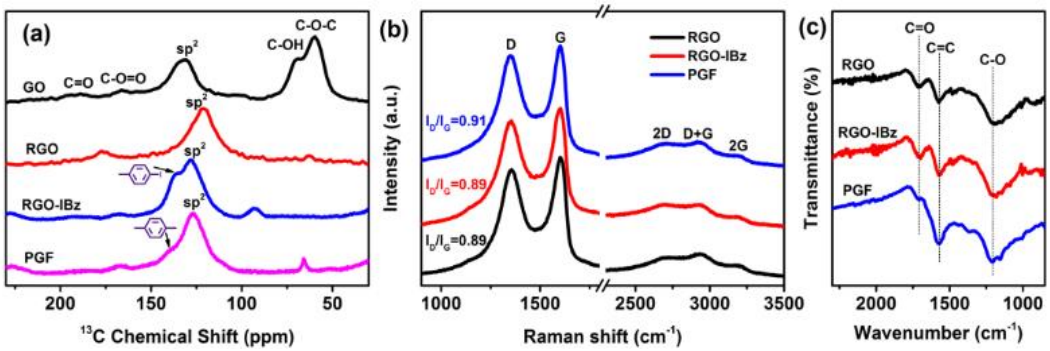

Figure 2.2 (a) Solid-state ^{13}C MAS NMR spectra of GO, RGO, RGO-IBz and PGF. (b) Raman and (c) FTIR spectra of RGO, RGO-IBz and PGF.

The UV−vis absorption spectra of GO, RGO, RGO-IBz and PGF in aqueous dispersion are presented in Figure 2.3. The π-π* absorption band of RGO shows a red-shift to 253 nm in contrast with that of GO at 232 nm in agreement with a partial recovery of the 2D conjugated system. This absorption band is further shifted to 262 nm for PGF due to an extension of the π-conjugated framework. The powder X-ray diffraction (XRD) pattern of GO is presented in Figure 2.3c. A characteristic peak at 10.6° was observed for our GO, correspond to a *d*-spacing of ~0.834 nm. Compared to GO, this peak was significantly shifted for RGO, the broad peak was centered at 25.4° (*d*-spacing ~0.35 nm). The reduction of the spacing distance originates from the removal of surface-located functional groups. Figure 2.3d displays the thermogravimetric analyses (TGA) as plots of weight loss as a function of temperature (at a heating rate of 10 °C/min) for RGO, RGO-IBz and PGF under a nitrogen atmosphere. The RGO-IBz sample shows an increased weight loss if compared to RGO at slightly higher temperature (>350 °C), which should result from an elimination of the 4-iodophenyl groups of the graphene layers. Finally, PGF exhibited a higher thermal stability than RGO and RGO-IBz due to the occurrence of a covalently bond 3D network.

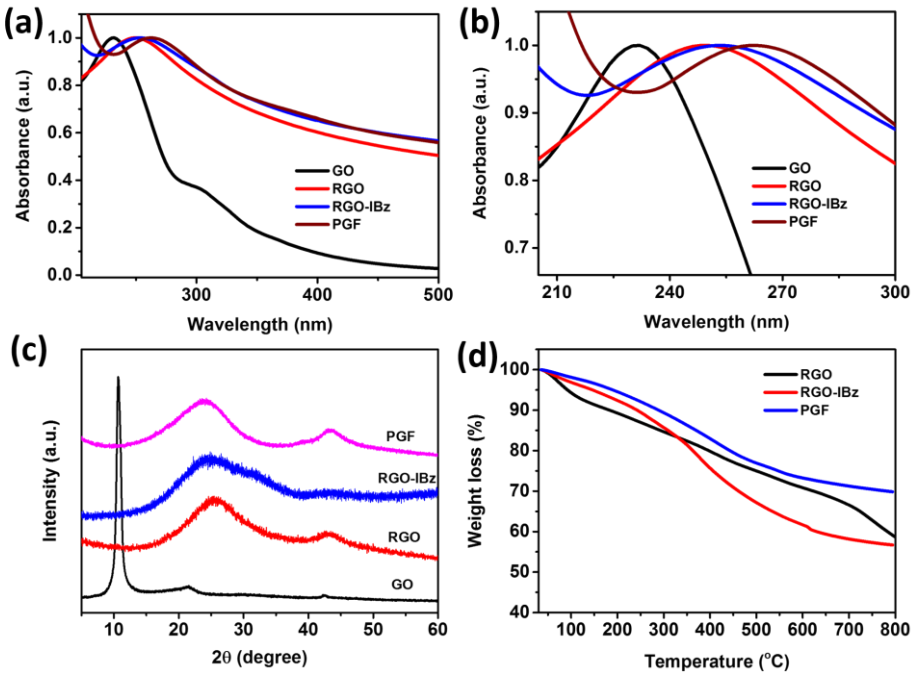

Figure 2.3 (a) Normalized UV-vis absorption spectra of GO, RGO, RGO-IBz, and PGF. (b) Depicts extended UV-vis absorption spectra in the spectral region of 200-300 nm. (c) XRD patterns of GO, RGO, RGO-IBz and PGF. (d) TGA thermograms for RGO, RGO-IBz and PGF.

High resolution Raman spectroscopy provides a non-destructive and fast method for characterizing graphene and graphene derivatives.[34] Graphene-based materials typically show three main Raman features, a G-band, a D-band and several two-dimensional modes, each having different physical origins. Figure 2.2b shows the Raman spectra of bulk RGO, RGO-IBz and PGF using 514 nm laser excitation which display two typical main peaks (attributed to the D and G bands, respectively) as well as three weaker peaks (assigned to the 2D, D+G and 2G bands, respectively). The intensity ratios of the D band at ~1350 cm^{-1} to the G band at ~1595 cm^{-1} (I_D/I_G) of RGO, RGO-IBz and PGF were 0.89, 0.89 and 0.91, respectively. The similar Raman spectral profiles of RGO, RGO-IBz and PGF confirm that the integrity of the graphene layers was not strongly altered during functionalization with the 4-iodobenzene diazonium salt and the subsequent coupling into PGF, thus verifying that RGO-IBz and PGF maintain their sp^2-type graphitic domains.[35,36]

Fourier transform infrared (FTIR) spectroscopy was carried out in order to follow the surface functionalization of RGO, RGO-IBz and PGF. As shown in Figure 2.2c, three peaks at 1721 cm^{-1}, 1573 cm^{-1} and 1186 cm^{-1} were found for RGO, RGO-IBz and PGF samples. The peak at 1721 cm^{-1} is assigned to the C=O stretching vibration of carboxyl and carbonyl groups.[37] The characteristic peak at 1573 cm^{-1} corresponds to a skeletal vibration of the graphene sheets (aromatic C=C stretching).[21] The peak at 1193 cm^{-1} is ascribed to a C-O stretching vibration.[32,37] These assignments are consistent with the solid ^{13}C NMR data.

2.2.2 XPS of GO, RGO, RGO-IBz and PGF

Surface, chemical structure and composition of GO, RGO, RGO-IBz and PGF samples were further studied by X-ray photoelectron spectroscopy (XPS) measurements. The XPS spectra are summarized in Figure 2.4a. Similar to GO, C 1s and O 1s peaks were observed for RGO and PGF, but the peak intensity of the oxygen signal is much weaker if compared to those in GO. I 3d, I 3p, I 4d, C 1s and O 1s peaks were obtained for RGO-IBz. The typical I3d core level line is visible as a twin peak that is located at ~620.4 eV (I 3d5/2) and ~631.8 eV (I 3d3/2). The I 3p peak was found at ~876 eV, the C 1s peak at ~284.5 eV, and the O 1s peak at ~533 eV. The detailed I 3d spectrum of the RGO-IBz is shown in Figure 2.4b. The I 3d5/2 peak displays a binding energy at 620.4 eV (C-I bond).[38,39] The I 3d, I 3p and I 4d signals in the XPS spectra further confirm the presence of the 4-iodophenyl substitutes in RGO-IBz. High resolution C 1s XPS spectra of GO, RGO, RGO-IBz and PGF are presented in Figure 2.4c-f, respectively. The different peaks are centered at 284.4, 285.6, 286.3, 286.7, 287.8, and 289.1 eV, corresponding to sp^2 C, sp^3 C, C-I, C-O, C=O, and O=C-O groups, respectively.[40-42] It is noteworthy that we found very similar amounts of oxygen-containing functional groups in RGO and PGF. It has been reported that oxygen-containing functional groups on the graphene sheets can enhance the wettability of the electrodes of supercapacitors. This behavior has been attributed to an increased hydrophilicity, thus improving the supercapacitor performance.[36,43,44]

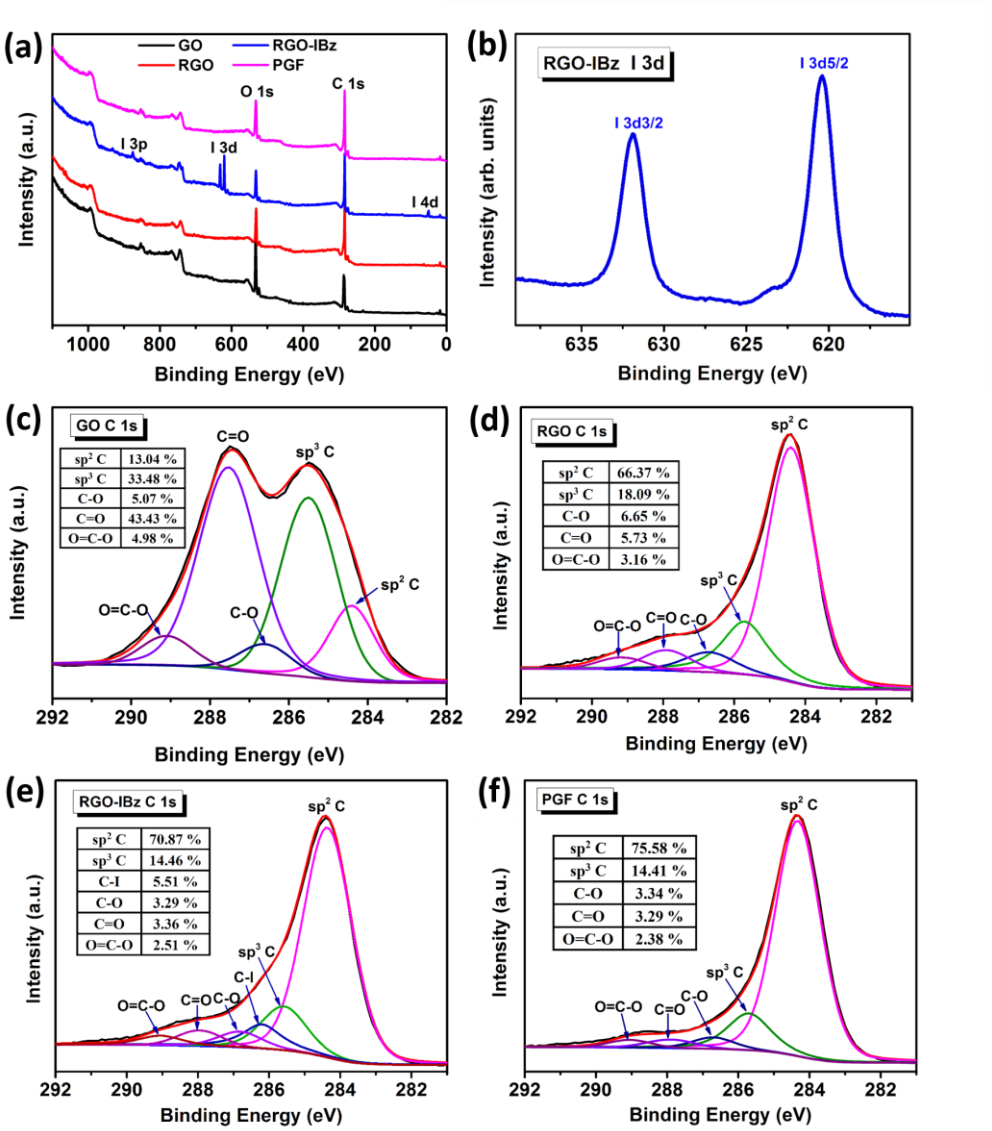

Figure 2.4 (a) XPS survey spectra of GO, RGO, RGO-IBz and PGF. (b) I 3d high-resolution XPS spectra of RGO-IBz. High-resolution C 1s XPS profiles for (c) GO, (d) RGO, (e) RGO-IBz and (f) PGF. The relative ratios of the different surface functionalities are shown in their respective insets.

2.2.3 Morphology and microstructure of GO, RGO, RGO-IBz and PGF

Morphology and microstructure of our GO, RGO, RGO-IBz and PGF materials were investigated by scanning electron microscopy (SEM) and transmission electron microscopy (TEM). The SEM images of Figure 2.5a-c all show a folded and wrinkled surface for GO, RGO and RGO-IBz sheets. SEM images of PGF at different magnification also exhibit a 3D morphology of folded, flake-like graphene sheets that form a loosely packed structure (Figure 2.6a-c). This arrangement should enable a

high ion and energy storage capability when used in the electrode material during the charge/discharge process. As presented in Figure 2.6d, RGO-IBz forms ultrathin, two-dimensional sheets with some amount of folding, indicating that the RGO-IBz sheets can be efficiently exfoliated and dispersed. Figure 2.6e shows a typical TEM image of PGF.

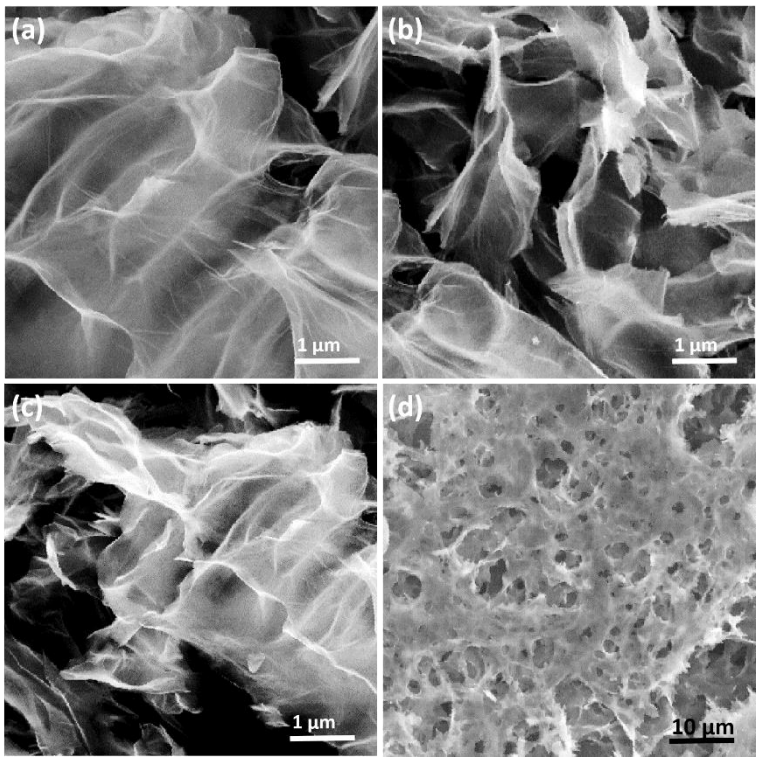

Figure 2.5 SEM images of (a) GO, (b) RGO and (c) RGO-IBz. (d) SEM image of the surface of a PGF film made by the filtration procedure (see Figure 2.6).

The stacked arrangement of individual RGO-IBz sheets into packages should be caused by the biphenyl pillars acting as sheet-to-sheet connectors. This packing of a few individual graphene sheets into thicker aggregates contrasts to the morphology of RGO-IBz, in agreement with an increased average sheet thickness of ca. 20 nm due to atomic force microscopy (AFM) data (Figure 2.7). This proposed structure for PGF is further illustrated by high resolution TEM (HRTEM) images (Figure 2.6f), showing the occurrence of multilayer stacks in PGF. The identified domains with graphene stacks may enhance the charge transport ability and stabilize the PGF-based electrodes during repeated charge/discharge cycles. This arrangement should also

limit the volume expansion, thus leading to a better cycling performance. When processing PGF, homogeneous thin films can be prepared by vacuum filtration of PGF dispersions on a membrane filter, as shown in Figure 2.6g. The SEM image of such a PGF film is depicted in Figure 2.5d, showing an interconnected framework of the PGF aggregates with a porous framework. Therefore, our simple procedure produces good quality films that are suitable for the fabrication of electrochemical energy storage and conversion devices.

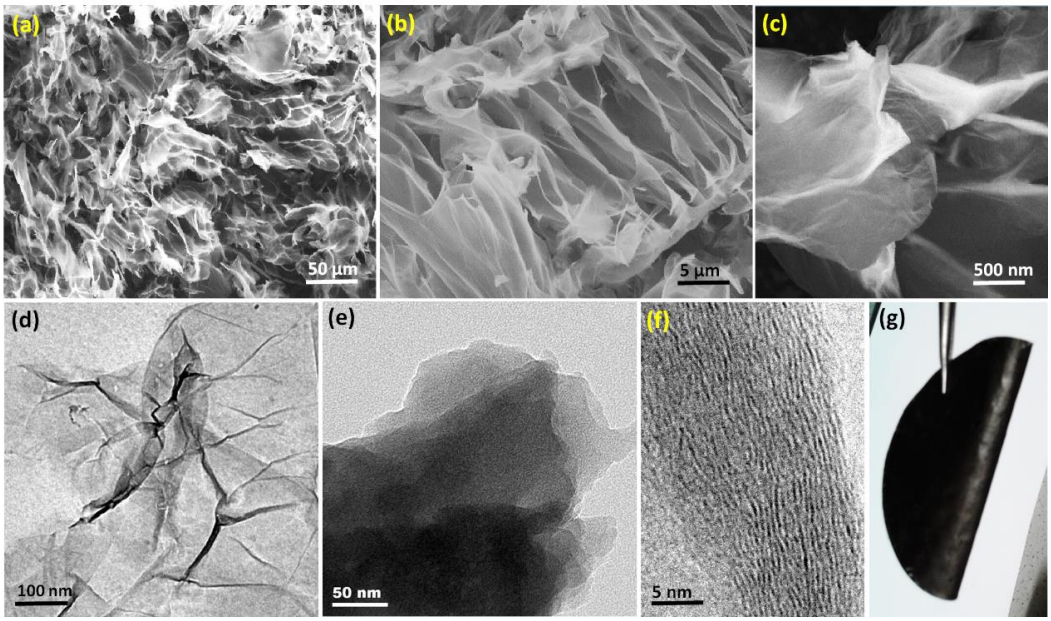

Figure 2.6 (a) (b) and (c) SEM images of PGF at different magnifications. TEM of (d) RGO-IBz and (e) PGF. (f) HRTEM image of PGF. (g) Flexible PGF thin film made on a membrane filter.

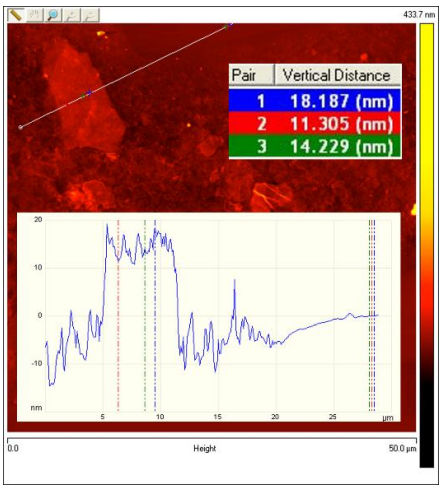

Figure 2.7 AFM image of a PGF sheet, including thickness analyses.

2.2.4 Porous Strcture of PGF

The microporous nature of PGF is demonstrated by nitrogen adsorption-desorption measurements. The measurements were carried out at 77 K after heating the samples at 140 ^{o}C over night to remove remaining moisture and solvent molecules that retain in the pores. PGF delivers a type I isotherm (Figure 2.8a), the Brunauer-Emmett-Teller (BET) surface area of PGF was calculated to 242 m^2 g^{-1} (RGO-IBz for comparison, 127 m^2 g^{-1}) based on the nitrogen adsorption-desorption curves with a total pore volume of 0.13 cm^3 g^{-1}. In contrast and due to the π-π stacking RGO exhibits a type III adsorption/desorption isotherm corresponding to a low BET surface area of only 11 m^2 g^{-1} with a total pore volume of 0.015 cm^3 g^{-1}. A non-local density functional theory (NLDFT) model fitted to the nitrogen adsorption isotherms allows for a simulation of the pore size distribution. The obtained multimodal pore size distributions for RGO and RGO-IBz samples are presented in Figure 2.8b,c and 2.9 showing the occurrence of both micro- and mesopores. PGF is characterized by a narrow, unimodal pore size distribution peaking at ca. 1 nm (Figure 2.8d), thus confirming the microporosity of PGF.

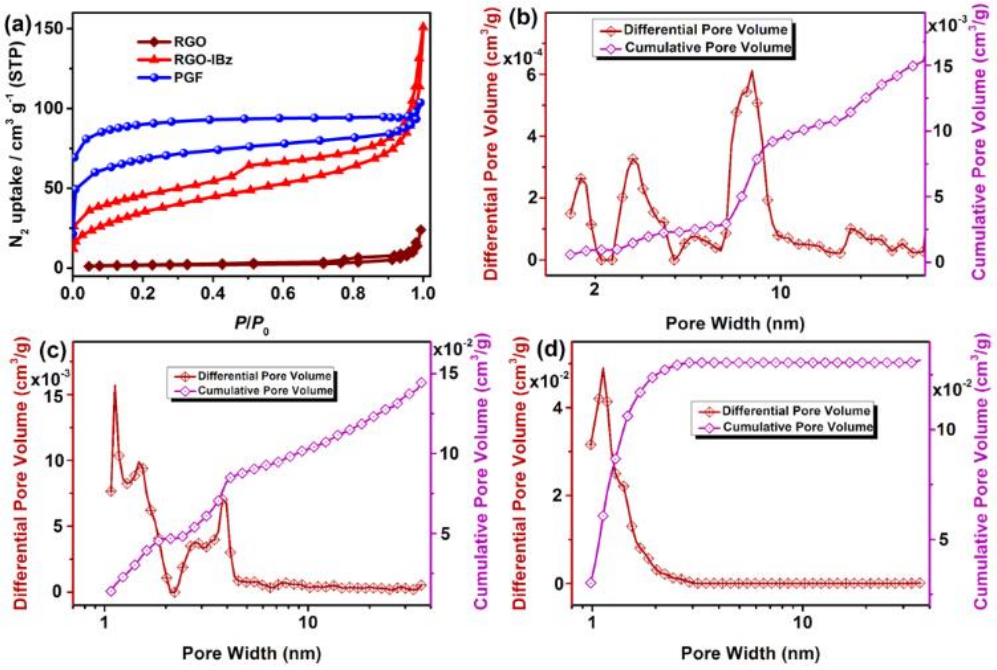

Figure 2.8 (a) N_2 adsorption/desorption isotherms for RGO, RGO-IBz and PGF. Incremental and cumulative pore size distribution plots for (b) RGO, (c) RGO-IBz and (d) PGF.

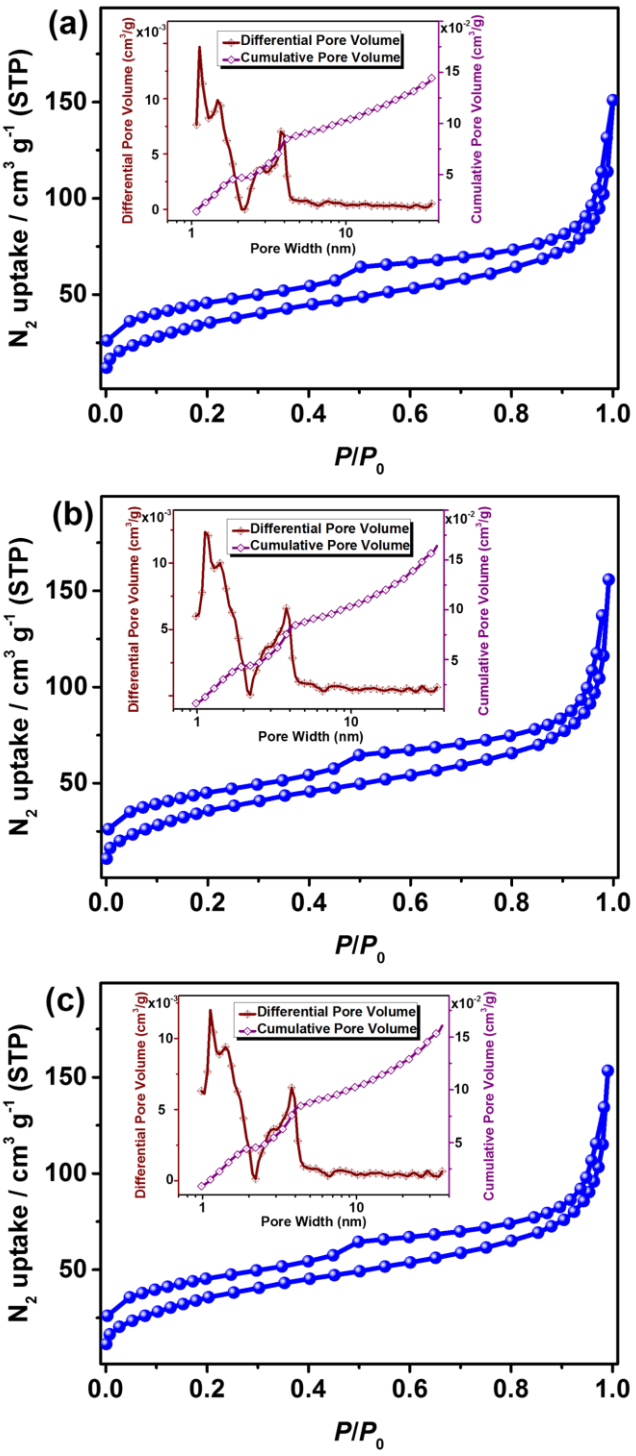

Figure 2.9 N_2 adsorption/desorption isotherms for RGO-IBz at different storage periods: (a) after 1 month, (b) after2 months, and (c) after 3 months. Insets: incremental and cumulative pore size distributions. No obvious changes of BET surface areas and pore size distributions were found even after storage for 3 months.

2.2.5 Electrochemical Capabilities of RGO and PGF

Considering the inherent and permanent microporosity of our PGF networks and assuming a sufficient electrical conductivity PGF seems very promising for use as electrode materials of electrochemical energy storage devices. We have explored PGF as electrode material of supercapacitors. Recently, graphene-based materials have been employed in supercapacitors as an alternative to conventional carbon electrodes and have shown superior performance.[43,45,46] The electrochemical capabilities of PGF and RGO as control material were examined first in a three-electrode cell where a 6 M aqueous KOH solution was used as electrolyte. Figure 2.10a,b shown the cyclic voltammetry (CV) curves of RGO and PGF in the potential range of -1 to 0 V at scan rates between 10 and 200 mV s^{-1} *vs* Ag/AgCl. Faradaic peaks corresponding to redox reactions which provide pseudocapacitances were observed in the CV curves of both RGO and PGF, obviously implying the coexistence of electric double layer capacitance and pseudocapacitance. The results are similar to those of recent reports on related cells based on functionalized graphene electrodes and reflect the presence of oxygen-containing functionalities in RGO and PGF as verified by FTIR and XPS measurements.[36,44]

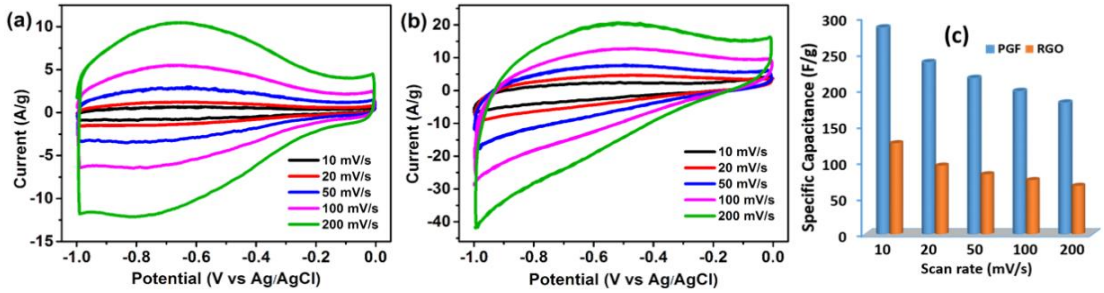

Figure 2.10 Cyclic voltammograms of (a) RGO and (b) PGF at different scan rates. (c) Specific capacitance for different scan rates of RGO and PGF.

Figure 2.11 shows a comparison of CV curves of supercapacitors devices with RGO and PGF electrodes at a scanning rate of 100 mV s^{-1}. Current density and enclosed CV area of PGF are significantly higher for PGF if compared to RGO electrodes, revealing the increased energy storage capability of PGF. The gravimetric

capacitances of RGO and PGF were calculated as 75 and 198 F g^{-1}, respectively. The reason for the increased capacitance of PGF electrodes is most probably due to an increased ion-accessible surface area and to a more appropriate pore size distribution of PGF. The specific capacitance values of RGO were calculated as 126, 95, 83, 75 and 67 F g^{-1} for scan rates of 10, 20, 50, 100 and 200 mV s^{-1}, respectively (Figure 2.10a). The corresponding specific capacitances of PGF were 286, 238, 216, 198 and 182 F g^{-1} for scan rates of 10, 20, 50, 100 and 200 mV s^{-1}, respectively (Figure 2.10b). The effect of the scan rate on the specific capacitance for RGO or PGF is depicted in Figure 2.10c. PGF maintains 64% of its capacitance when the scan rate is increased from 10 to 200 mV s^{-1} (for RGO: 53%). The higher rate capability of PGF can be also attributed to an increased ion-accessible surface area leading to an improved ion diffusion and faster ion extraction/insertion.[47,48]

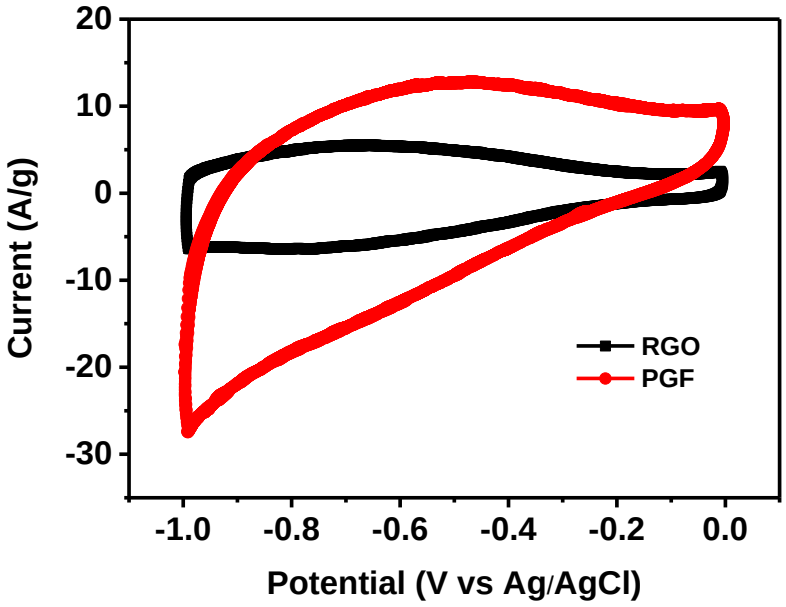

Figure 2.11 Cyclic voltammograms of RGO and PGF for a scan rate of 100 mV/s in a three-electrode cell where a 6 M aqueous KOH solution was used as electrolyte.

Galvanostatic charge-discharge (GCD) measurements are suitable for evaluating the performance of electrode materials for energy storage devices.[49,50] Obvious differences were observed between PGF and RGO as electrode materials from their

GCD profiles (Figure 2.12). More symmetrical triangles of the GCD curves and increased charge/discharge times indicate higher specific capacitance values for PGF. RGO exhibited gravimetric specific capacitances of 103, 85, 77, 68, and 61 F g^{-1} at current densities of 0.2, 0.5, 1, 2 and 5 A g^{-1}, respectively. The corresponding capacitance values of PGF are 237, 201, 186, 177, and 165 F g^{-1} at current densities of 0.2, 0.5, 1, 2 and 5 A g^{-1}, respectively. These capacitance values are comparable to those of 3D porous carbon and B/N doped graphene materials (Table 2.1). According to these GCD profiles, the capacitance of PGF is increased by a factor of ca. 2.3 if compared to RGO. The significant capacitance enhancement for PGF that is documented both in the CV and GCD measurements is attributed to the pillared, microporous structure of PGF. In preserving the polar functional groups of RGO, sufficient wetting between electrode surface and aqueous electrolyte is guaranteed thus supporting ion transport through the graphene surface. Moreover, the introduction of the biphenyl pillars between the graphene sheets during PGF formation suppresses the agglomeration of individual graphene layers and preserves the microporosity. The hierarchically porous PGF structure should be favorable in lowering the internal resistance, in accelerating ion diffusion/transport, and in improving ion storage, leading to a higher storage capacity of PGF in relation to RGO.

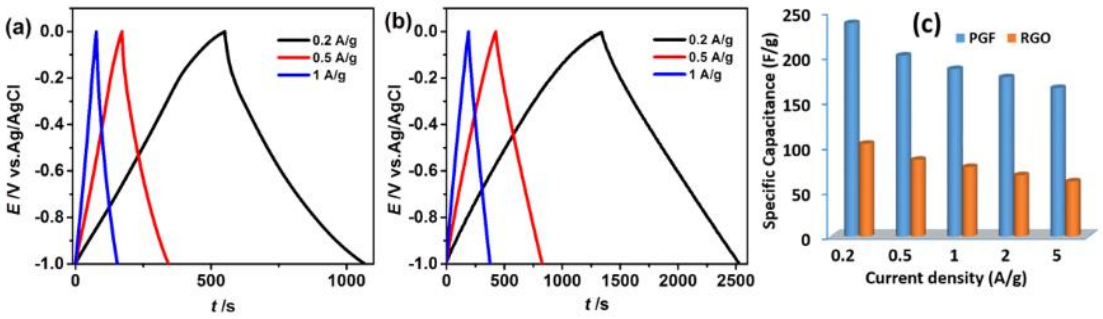

Figure 2.12 Galvanostatic charge-discharge curves of (a) RGO and (b) PGF at different current densities. (c) Specific capacitances *vs*. different current densities of RGO and PGF.

Table 2.1 Comparison of gravimetric capacitances of carbon-based materials as electrodes of supercapacitors.

Materials	Gravimetric capacitance (F/g)	Electrolyte	References
High density porous graphene macroform	238 (0.1 A/g)	6 M KOH	51
S-porous carbon/graphene	109 (0.05 A/g)	6 M KOH	52
Reduced graphite oxide with high density	182 (1 A/g)	6 M KOH	53
Porous graphene nanosheets	241 (2 mV s^{-1})	6 M KOH	54
Activated microwave exfoliated graphite oxide	137 (1 A/g)	BMIM BF_4/AN	55
	154 (1 A/g)	EMIM TFSI/AN	
KOH activated graphene	166 (0.7 A/g)	BMIM BF_4/AN	56
Compressed KOH activated graphene	147 (1.24 A/g)	BMIM BF_4/AN	57
Hydrazine reduced graphene oxide	123 (10 mV s^{-1})	6 M KOH	58
Activated graphene-derived carbon	174 (4.2 A/g)	Ionic liquid	59
Holey graphene framework	298 (1 A/g)	BMIM BF_4/AN	60
Nitrogen-enriched nonporous carbon	115 (0.05 A/g)	1 M H_2SO_4	61
Seaweeds derived carbon	198 (2 mV s^{-1})	1 M H_2SO_4	62
Activated carbon aerogel	220 (0.125 A/g)	1 M H_2SO_4	63
Copper nanocrystal modified activated carbon	79 (0.2 A/g)	TEATFB	64
N-doped reduced graphene oxide	255 (0.5 A/g)	6 M KOH	65
3D nitrogen and boron co-doped graphene	239 (1 A/g)	1 M H_2SO_4	66
Crumpled N-doped graphene nanosheets	245.9 (1 A/g)	BMIM BF_4/AN	67
3D Nitrogen-doped graphene-CNT	180 (0.5 A/g)	6 M KOH	68
Boron-doped graphene nanoplatelets	160 (1 A/g)	6 M KOH	69
Graphene sponge	204.66 (5 mV s^{-1})	1 M NaCl	70
3D porous carbon	176 (10 mV s^{-1})	1 M H_2SO_4	71
Reduced graphene oxide	41.5 (0.1 A/g)	6 M KOH	17
FGF	**286 (10 mV s^{-1})**	**6 M KOH**	**This work**
	237 (0.2 A/g)	**6 M KOH**	

2.2.6 Supercapacitors Based on PGF

In order to further investigate the supercapacitor performance of PGF electrodes for electrochemical energy storage, conventional two-electrode symmetric supercapacitor devices with PGF as active electrode material were assembled with 6M aqueous KOH as electrolyte. Figure 2.13a depicts CV curves of PGF-based symmetric supercapacitors for different scan rates in a potential window between -1

and 0 V. In contrast to three-electrode supercapacitors, no apparent Faradaic peaks were observed in the two-electrode system. The CV profiles exhibit a rectangle-like shape even when the scan rate increases to 100 mV s^{-1}. GCD measurements were performed at current densities from 0.2 to 10 A/g. All GCD curves show a very regular, triangular shape (Figure 2.13b) for all current densities thus indicating that fast charge and ion propagation occurs. The specific capacitances of the symmetric supercapacitors at different current densities are shown in the inset of Figure 2.13c. The specific capacitance, was measured to ca. 46 F g^{-1} at a current density of 0.2 A g^{-1}, corresponding to a capacitance of 184 F g^{-1} of a single electrode,[21] a slightly lower specific capacitance value as that extracted from the three-electrode tests of Figure 2.12. This is attributed to the higher loading density and internal resistance for the two electrode configuration if compared to three-electrode arrangement, resulting in an increased diffusion resistance of electrolyte ions within the electrode materials.[22 72] The specific capacitance value is still ca. 30 F g^{-1} for a high current density of 10 A g^{-1}, thus confirming a good rate capability. We compared the performance of our PGF material with those of a broad range of alternate materials for supercapacitor electrodes (Table 2.2). As a result, PGF shows a comparable rate capability in relation to these recently reported carbon-based supercapacitor materials, such as B/N-doped graphene or porous carbons. Moreover, due to Figure 2.13d, our PGF-based supercapacitor devices exhibit rather promising cycle stability and rate capability, ~98% capacitance retention after 2000 cycles at 2 A g^{-1}, and ~97% capacitance retention after 5000 cycles at a high current density of 10 A g^{-1} (Figure 2.1). These values are superior in relation to those of e.g. N-doped graphene, graphene/polymer or graphene/metal oxide hybrid materials (Table 2.3). Ragone plots are connecting the power and energy density as a very useful indicator for the performance of supercapacitor devices. For our devices, a maximum energy density of 6.4 W h kg^{-1} was achieved for a current density of 0.2 A g^{-1}, and a maximum power density of 4560 W kg^{-1} for a slightly reduced energy density of 3.8 W h kg^{-1}. As concrete illustration of the energy storage performance of our supercapacior devices, a PGF-based device was used as power supply for commercial, small electronic devices,

in our example for a red-emitting light-emitting diode (LED) that is powered by three charged supercapacior devices connected in series (Figure 2.13e).

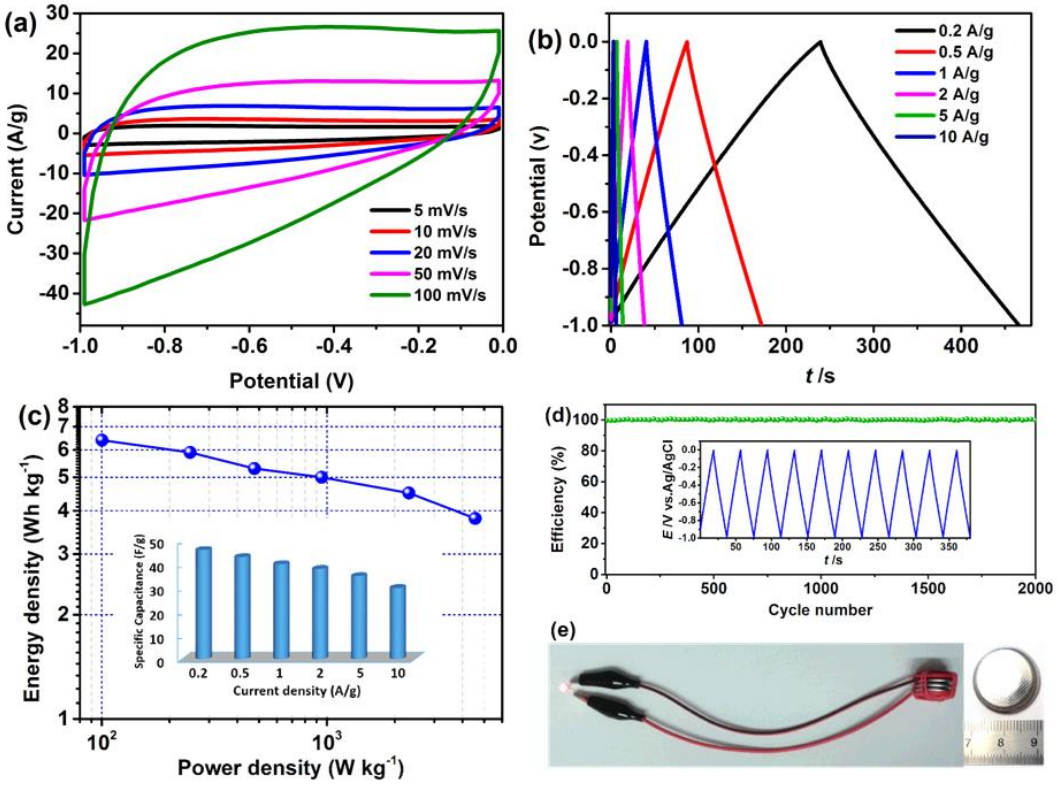

Figure 2.13 Electrochemical characterization of PGF-based two-electrode supercapacitor devices. (a) Cyclic voltammograms at different scan rates. (b) Galvanostatic charge-discharge curves at different current densities. (c) Ragone plot for the devices with different specific capacitances shown in the insert. (d) Cycling stability for a current density of 2 A g^{-1}. (e) Photographs of a red light-emitting-diode (LED) powered by three supercapacitor devices connected in series (left) and of an individual coin-sized PGF-based supercapacitor device.

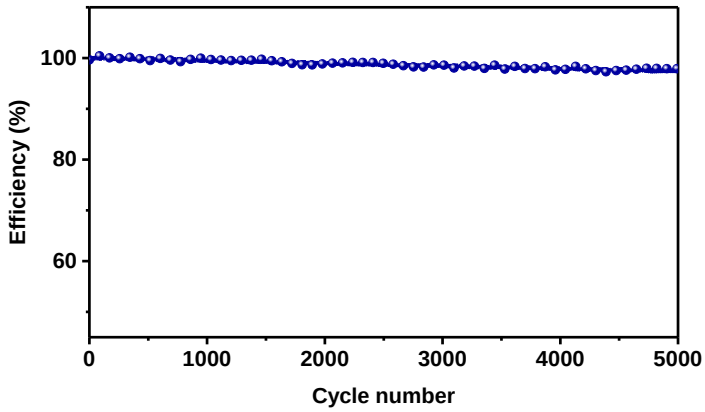

Figure 2.14 Cycling stability of PGF-based two-electrode supercapacitor devices for a current density of 10 A g^{-1}.

Table 2.2 Comparison of the rate capability of carbon-based materials as electrodes of two-electrode symmetric cell supercapacitors.

Materials	Current density	Retention ratio (%)	References
Porous N-doped hollow carbon spheres	0.5-10A/g	55.6	73
N-doped ordered nanoporous carbon	0.1-10A/g	50	74
3D N-doped graphene-CNT	0.5-5 A/g	52.8	68
Microporous carbon nanosphere	0.02-2 A/g	57.9	75
Active nitrogen-rich carbon	0.2-2 A/g	68	76
Boron-doped graphene	0.2-10 A/g	51	77
PAF-Carbon	0.2-10 A/g	41	78
N-PAF-Carbon	0.2-10 A/g	43	78
$CoMoO_4$-3D graphene	1.43-9.28 A/g	68	79
CNT supported graphene-based aerogel	0.1-10 A/g	36.9	80
N-doped graphene	0.2-3 A/g	66	81
Mesoporous graphene	0.5-8 A/g	59	15
3D N-containing porous frameworks	0.2-10 A/g	62	82
Porous active carbon	0.25-10 A/g	49	83
3D Porous Graphene/Carbon composites	0.1-0.5 A/g	59	84
Layered polyaniline/graphene film	0.5-10 A/g	50	85
Graphene-based fiber	0.49-6.13	59	86
PGF	**0.2-10 A/g**	**65**	**This work**
	0.5-10 A/g	**70**	
	0.5-5 A/g	**81**	

Table 2.3 Comparison of the cycling performance of carbon-based materials as electrodes of supercapacitors.

Materials	Electrolyte	Current density /scan rate	Retention ratio	References
Polyoxometalate/RGO	0.5 M H_2SO_4	10 A/g	77% (2000 cycles)	87
Graphene/polyaniline nanofiber	1 M H_2SO_4	3 A/g	79% (800 cycles)	48
Microporous carbon nanofibers	6 M KOH	1 A/g	92% (1000 cycles)	88
P/N doped mesoporous carbon	6 M KOH	5 mV s^{-1}	86% (5000 cycles)	89
rGO-MoS_2 hybrid fiber	PVA-H_2SO_4	-	~80% (1000 cycles)	90
Mesoporous carbon/RGO	6 M KOH	0.5 A/g	~94% (1000 cycles)	17
RGO–RuO_2	2 M H_2SO_4	-	70% (2500 cycles)	21
Porous carbon nanosheets	6 M KOH	10 A/g	95% (5000 cycles)	91
Graphite flakes/Polypyrrole	1 M H_2SO_4	-	91% (5000 cycles)	92
Fe_3O_4 @graphene	Saturated KCl	5 mA/g	91.5% (1000 cycles)	93
Carbon decorated graphene	6 M KOH	0.5 A/g	95.4% (1000 cycles)	94
Porous active carbon	6 M KOH	4 A/g	89.4% (2000 cycles)	83
Hydrazine reduced GO paper	30 wt% KOH	0.5 A/g	~90% (1200 cycles)	43
N-doped graphene	0.5 M H_2SO_4	1 A/g	90.3% (5000 cycles)	81
COF-RGO	1.0 M Na_2SO_4	0.2 A/g	79% (1000 cycles)	95
Graphene paper	1 M H_2SO_4	2 A/g	86.9% (1000 cycles)	66
Thermal-reduced GO	6 M KOH	200 mV s^{-1}	<90% (2000 cycles)	96
Aniline tetramer-graphene oxide	1 M H_2SO_4	100 mV s^{-1}	89.1% (1000 cycles)	22
PGF	**6 M KOH**	**2 A/g**	**98% (2000 cycles)**	**This work**
	6 M KOH	**10 A/g**	**97% (5000 cycles)**	

2.3 Conclusions

In summary, microporous graphene frameworks were successfully synthesized by covalent functionalization of RGO with 4-iodophenyl diazonium salts followed by a Yamamoto aryl-aryl-coupling reaction. The novel, pillared graphene-based PGF electrode materials display improved electrochemical performances in energy storage decives if compared to RGO, including high specific capacitance in combination with high cycling stability in both three-electrode and symmetric two-electrode supercapacitor devices. The promising electrochemical performance of our materials is attributed to their inherent and stable microporous structure thus providing a high ion-accessible surface area and facilitating ion extraction/insertion. This guarantees an improved specific capacitance as well as high cycling stability and rate capability. Our results outline a promising strategy towards improved graphene-based electrode materials for high performance energy storage devices.

2.4 Experimental

All reagents, unless otherwise stated, were obtained from commercial sources (Sigma Aldrich, Alfa Aesar and Acros) and were used without further purification.

2.4.1 Synthesis of Graphene Oxide (GO)

Graphene oxide was synthesized using a modified Hummers method.[27] In an ice bath 150 mL of conc. H_2SO_4 were mixed with 3.0 g graphite powder and 3.0 g $NaNO_3$ and stirred for 30 min. In to this mixture 20 g of $KMnO_4$ were slowly added under rapid stirring. Next, the mixture was heated up to 40 ^oC and stirred for another 1 h. Into this mixture 150 mL of deionized water were slowly added followed by stirring for 15 min at 70 ^oC. A uniform brown suspension is formed. The temperature was then raised to 80 ^oC and 30 mL of concentrated aqueous H_2O_2 (37 wt%) in 300 mL warm water (70 ^oC) was added. The color of the suspension changed from brown to yellow. The reaction product was isolated by centrifugation and repeatedly washed with deionized water. Finally, the graphene oxide was re-dispersed in water and dialyzed against water until the dialysate became neutral. The solid product was

isolated by centrifugation. 4.1g GO powder were obtained after drying under vacuum at room temperature.

2.4.2 Preparation of Reduced Graphene Oxide (RGO)

The reduction of GO was accomplished with $NaBH_4$ as reducing agent according to a procedure reported in the literature, as show in Scheme 2.2.[28] In the reduction step, 400 mg GO in 320 mL of deionized water were sonicated for 1 h for complete dispersion of the GO sheets. Following, 50 mL (0.047 mol) of a 5% aqueous sodium carbonate solution were added for adjusting a pH value of 10. The solution was stirred in a round-bottom flask at a temperature 90±5 ^oC for 9 h. This was followed by the addition of 3.2 g sodium borohydride (0.085 mol) in 80 mL of water to the GO dispersion at pH=10. The mixture was stirred at 80 ^oC for 3 h under rapid stirring. During reduction, the color of the dispersion turned from dark brown to black accompanied by outgassing. The resulting product was finally filtered through membrane filter (polyamide, pore size 0.2 μm) and washed with deionized water. Finally, the product (RGO) was dried in vacuum at room temperature (yield: 256 mg RGO).

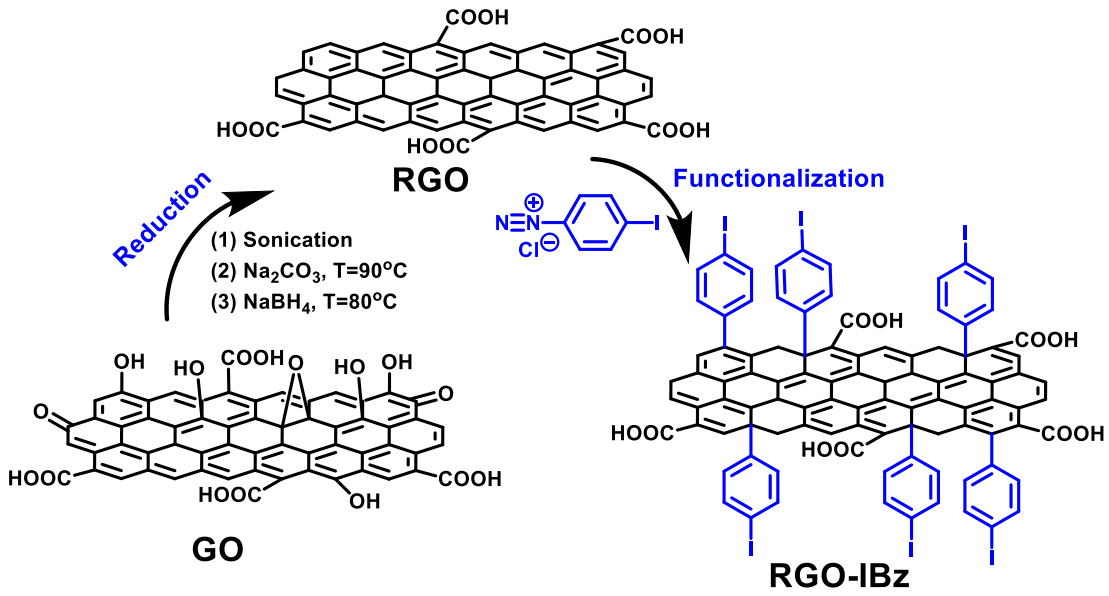

Scheme 2.2 Idealized formula scheme depicting the reduction of GO and functionalization with 4-iodophenyl substituents under formation of the further RGO-IBz.

2.4.3 Synthesis of the 4-Iodophenyl Diazonium Salt

The 4-iodophenyl diazonium salt that is used for the functionalization of RGO was prepared starting from 4-iodoaniline. 1.535 g (7 mmol) 4-iodoaniline were dissolved in 80 mL of deionized water by dropwise addition of the minimum amount of conc. aqueous HCl necessary for dissolution. The resulting solution of the hydrochloride was then transferred to a round bottom flask kept at 0 ^{o}C in an ice bath. Next, 526 mg $NaNO_2$ (7.6 mmol) in 10 mL of water were dropwise added during 45 min under rapid stirring. Thereby, the color of the solution changes from colorless to yellow under the formation of the corresponding diazonium salt.

2.4.4 Preparation of 4-Iodophenyl-Substituted Graphene (RGO-IBz)

The functionalization of RGO was carried out according to a published procedure.[28-30] RGO obtained after sodium borohydride reduction is strongly agglomerated and forms a poor dispersion with water. RGO (125 mg) was dispersed in 125 mL of a 1 wt% sodium dodecylbenzene sulfonate (SDBS) solution. The solution of the diazonium salt was next added dropwise with rapid stirring of the RGO dispersion. The reaction mixture was maintained at 0 ^{o}C for additional 2 hours. After stirring at room temperature for next 6 hours, the mixture was poured into acetone. Purification of the RGO-IBz reaction product was done by filtration and washing with deionized water, acetone, and DMF. The solid product (RGO-IBz) was dried in vacuum at room temperature (yield: 213 mg RGO-IBz). The obtained RGO-IBz can be well-dispersed in different organic solvents, for instance, DMF (Figure 2.15), toluene and chlorobenzene.

Figure 2.15 Photographs of RGO-IBz dispersions in DMF after storage for different time. No obvious precipitation was found even after storage for 4 weeks.

2.4.5 Synthesis of PGF

To a dried and degassed reaction flask, 100 mg bis(cyclooctadiene)nickel was added, followed by a mixture of 2,2'-bipyridyl (70 mg) and 1,5-cyclooctandiene (50 µL) in 20 mL of dried and degassed DMF. The reaction mixture was heated up to 60 °C for 30 minutes. The degassed dispersion of RGO-IBz (60 mg) in DMF (80 mL) was added to the reaction flask. The reaction mixture was heated up to 80 °C for 3 days. The reaction flask was cooled to room temperature and treated with concentrated, aqueous HCl. After stirring overnight, the formed precipitate was collected by filteration and washed with H_2O and THF, ensuring that the distinct smell of cyclooctadiene was not present anymore. The resulting material was Soxhlet extracted with H_2O and THF for 1 day, respectively, to remove all remaining, soluable impurities. The resulting solid was dried in vacuum at room temperature (yield: 47 mg PGF).

2.4.6 Characterization

Fourier transform infrared (FTIR) spectroscopy studies were conducted on a JASCO FT/IR-4200 Fourier-transform-spectrometer. Raman spectra were recorded on a LabRAM HR Raman Microscope with an excitation length of 514 nm. UV-Vis absorption spectra were recorded on a Shimadzu UV-2401 PC spectrophotometer at room temperature. The nanomorphology of GO, RGO-IBz and PGF were characterized by transmission electron microscopy (TEM, JEOL, JEM-2100F). The TEM samples were prepared by transferring GO, RGO-IBz and PGF onto copper grids. The AFM images were obtained with an atomic force microscope Bruker diInnova operated in the tapping mode. The SEM studies were carried out at a Philips XL30S FEG microscope with a field emission cathode. Thermogravimetric analysis was performed on a Mettler Toledo TGA Stare System under argon flow.

XPS measurements. The X-ray photoelectron spectroscopy (XPS) measurements were carried out by a multi-chamber UHV system from Omicron Nano Technology, which is equipped with an X-ray source type DAR 400 and a

hemispherical analyzer type EA 125. Base pressure in the analyzer chamber is 5×10^{-10} mbar. For excitation, Mg Ka radiation with an energy of 1253.6 eV has been used. All spectra have been referenced to the Au 4f7/2 peak at an energy of 84.0 eV.

Nitrogen adsorption-desorption measurements. The nitrogen adsorption-desorption measurements were performed on a BELSORB Max (BEL Japan Inc.). The surface areas were calculated using the BET model in the pressure range p/p_0 from 0.05-0.3. The total pore volume was determined at a relative pressure of 0.99. The pore size distribution was analyzed from the nitrogen adsorption data using a NLDFT method with a slit pore model.

Solid-state NMR measurements. Solid-state ^{13}C MAS NMR spectra were recorded at 75.48 MHz using a Bruker Avance III 300 spectrometer with a contact time of 2.5 ms coadding 4096 up to 16392 transients, depending on the required relaxation delay of 2 s up to 60 s. All experiments were carried out at room temperature using a standard Bruker 4 mm double resonance MAS probe spinning at 12 kHz, typical π/2-pulse lengths of 4 μs and SPINAL64 proton decoupling. The spectra were referenced with respect to tetramethyl silane (TMS) using solid adamantane as secondary standard (29.46 ppm for ^{13}C).

2.4.7 Supercapacitor Fabrication

Coin-cell-type symmetric supercapacitors were fabricated to evaluate the supercapacitive performance. Briefly, 80 wt% PGF, 10 wt% active carbon, and 10 wt% polyvinylidene fluoride (PVDF, as a binder) were homogeneously mixed into a paste. Then, the mixture was rolled onto a nickel foil as current collector. After drying at 120 ^{o}C overnight, the electrodes/collectors were assembled in CR2032 stainless steel coin cell with 6 M aqueous KOH solution and a porous cellulose membrane as electrolyte and separator, respectively.

2.4.8 Electrochemical Measurements and Calculations

The electrochemical experiments were first carried out using a conventional, aqueous three-electrode system employing 6 M aqueous KOH as electrolyte at room temperature. The three-electrode cell was incorporated Ag/AgCl as reference electrode, Pt as the counter electrode and the RGO or PGF sample as working electrode. The working electrode was prepared by loading RGO or PGF onto a glassy carbon electrode. Thereby, PGF was first dispersed in water by sonication under formation of a homogeneous dispersion (1 mg/mL). Next, 6 μL of the dispersion were loaded onto a glassy carbon electrode with a diameter of 5 mm. The modified electrode was slowly dried in air until a uniform PGF layer was formed at the electrode surface. The following cyclic voltammetry (CV) and galvanostatic charge/discharge (GCD) measurements in both three-electrode and two-electrode arrangements were performed using a PAR VersaSTAT 4 electrochemical workstation within the voltage range from -1 to 0 V.

The specific capacitance was calculated by the following equation:

$$C = I \Delta t / m \Delta V$$

where C (F/g) is the specific capacitance, I (mA) the discharge current, and Δt (s), m (mg), and ΔV (V) the total discharge time, the mass of active material, and the potential drop (by excluding the voltage (IR) drop) during discharge, respectively.

The energy density (E) was calculated from the discharge profiles of the two-electrode system by using the following equation:

$$E = 0.5 C \Delta V^2 / 3.6$$

where E (Wh kg^{-1}) is the energy density, C (F g^{-1}) the specific capacitance of the active material and ΔV (V) the discharge voltage range. With a factor 3.6, the energy density is converted from J g^{-1} to Wh kg^{-1}.

The power density (P) was calculated as follows:

$$P=E\times 3600/\Delta t$$

where P (kW kg^{-1}) is the power density, and E (Wh kg^{-1}) and Δt (s) energy density and discharge time, respectively.

2.5 References

(1) Yuan, K.; Xu, Y.; Uihlein, J.; Brunklaus, G.; Shi, L.; Heiderhoff, R.; Que, M.; Forster, M.; Chasse, T.; Pichler, T.; Riedl, T.; Chen, Y.; Scherf, U. *Adv. Mater.* **2015**, *27*, 6714-6721.

(2) Zhang, Q.; Uchaker, E.; Candelaria, S. L.; Cao, G. *Chem. Soc. Rev.* **2013**, *42*, 3127-3171.

(3) Yang, Z.; Zhang, J.; Kintner-Meyer, M. C. W.; Lu, X.; Choi, D.; Lemmon, J. P.; Liu, J. *Chem. Rev.* **2011**, *111*, 3577-3613.

(4) Mai, L.; Tian, X.; Xu, X.; Chang, L.; Xu, L. *Chem. Rev.* **2014**, *114*, 11828-11862.

(5) Sun, Y.; Wu, Q.; Shi, G. *Energy Environ. Sci.* **2011**, *4*, 1113-1132.

(6) Simon, P.; Gogotsi, Y. *Nat. Mater.* **2008**, *7*, 845-854.

(7) Miller, J. R.; Simon, P. *Science* **2008**, *321*, 651-652.

(8) Zhai, Y.; Dou, Y.; Zhao, D.; Fulvio, P. F.; Mayes, R. T.; Dai, S. *Adv. Mater.* **2011**, *23*, 4828-4850.

(9) Zhang, L. L.; Zhao, X. S. *Chem. Soc. Rev.* **2009**, *38*, 2520-2531.

(10) Shao, Y.; El-Kady, M. F.; Wang, L. J.; Zhang, Q.; Li, Y.; Wang, H.; Mousavi, M. F.; Kaner, R. B. *Chem. Soc. Rev.* **2015**, *44*, 3639-3665.

(11) Yan, J.; Wang, Q.; Wei, T.; Fan, Z. J. *Adv. Energy Mater.* **2014**, *4*, 1300816.

(12) Zhao, J.; Lai, H.; Lyu, Z.; Jiang, Y.; Xie, K.; Wang, X.; Wu, Q.; Yang, L.; Jin, Z.; Ma, Y.; Liu, J.; Hu, Z. *Adv. Mater.* **2015**, *27*, 3541-3545.

(13) Raccichini, R.; Varzi, A.; Passerini, S.; Scrosati, B. *Nat. Mater.* **2015**, *14*, 271-279.

(14) Bonaccorso, F.; Colombo, L.; Yu, G.; Stoller, M.; Tozzini, V.; Ferrari, A. C.; Ruoff, R. S.; Pellegrini, V. *Science* **2015**, *347*, 1246501.

(15) Liu, C.; Yu, Z.; Neff, D.; Zhamu, A.; Jang, B. Z. *Nano Lett.* **2010**, *10*,

4863-4868.

(16) El-Kady, M. F.; Strong, V.; Dubin, S.; Kaner, R. B. *Science* **2012**, *335*, 1326-1330.

(17) Lei, Z.; Christov, N.; Zhao, X. S. *Energy Environ. Sci.* **2011**, *4*, 1866-1873.

(18) Choi, B. G.; Yang, M.; Hong, W. H.; Choi, J. W.; Huh, Y. S. *ACS Nano* **2012**, *6*, 4020-4028.

(19) Wang, C.; Li, Y.; Chui, Y.-S.; Wu, Q.-H.; Chen, X.; Zhang, W. *Nanoscale* **2013**, *5*, 10599-10604.

(20) Wang, C.; Chui, Y.-S.; Ma, R.; Wong, T.; Ren, J.-G.; Wu, Q.-H.; Chen, X.; Zhang, W. *J. Mater. Chem. A* **2013**, *1*, 10092-10098.

(21) Zhang, J.; Jiang, J.; Li, H.; Zhao, X. S. *Energy Environ. Sci.* **2011**, *4*, 4009-4015.

(22) Yan, J.; Yang, L. P.; Cui, M. Q.; Wang, X.; Chee, K. J. J. Z.; Nguyen, V. C.; Kumar, V.; Sumboja, A.; Wang, M.; Lee, P. S. *Adv. Energy Mater.* **2014**, *4*, 1400781.

(23) Wu, Z.-S.; Ren, W.; Wang, D.-W.; Li, F.; Liu, B.; Cheng, H.-M. *ACS Nano* **2010**, *4*, 5835-5842.

(24) Wang, C.; Xu, J.; Yuen, M.-F.; Zhang, J.; Li, Y.; Chen, X.; Zhang, W. *Adv. Funct. Mater.* **2014**, *24*, 6372-6380.

(25) Wang, D.-W.; Li, F.; Zhao, J.; Ren, W.; Chen, Z.-G.; Tan, J.; Wu, Z.-S.; Gentle, I.; Lu, G. Q.; Cheng, H.-M. *ACS Nano* **2009**, *3*, 1745-1752.

(26) Mini, P. A.; Balakrishnan, A.; Nair, S. V.; Subramanian, K. R. V. *Chem. Commun.* **2011**, *47*, 5753-5755.

(27) Hummers, W. S.; Offeman, R. E. *J. Am. Chem. Soc.* **1958**, *80*, 1339-1339.

(28) Jahan, M.; Bao, Q.; Yang, J.-X.; Loh, K. P. *J. Am. Chem. Soc.* **2010**, *132*, 14487-14495.

(29) Zhuang, X.; Zhang, F.; Wu, D.; Forler, N.; Liang, H.; Wagner, M.; Gehrig, D.; Hansen, M. R.; Laquai, F.; Feng, X. *Angew. Chem., Int. Ed.* **2013**, *52*, 9668-9672.

(30) Kumar, R.; Suresh, V. M.; Maji, T. K.; Rao, C. N. R. *Chem. Commun.* **2014**, *50*, 2015-2017.

(31) Cai, W.; Piner, R. D.; Stadermann, F. J.; Park, S.; Shaibat, M. A.; Ishii, Y.; Yang, D.; Velamakanni, A.; An, S. J.; Stoller, M.; An, J.; Chen, D.; Ruoff, R. S. *Science* **2008**, *321*, 1815-1817.

(32) Si, Y.; Samulski, E. T. *Nano Lett.* **2008**, *8*, 1679-1682.

(33) He, H.; Riedl, T.; Lerf, A.; Klinowski, J. *J. Phys. Chem.* **1996**, *100*, 19954-19958.

(34) Ferrari, A. C.; Basko, D. M. *Nat. Nanotechnol.* **2013**, *8*, 235-246.

(35) Ferrari, A. C.; Meyer, J. C.; Scardaci, V.; Casiraghi, C.; Lazzeri, M.; Mauri, F.; Piscanec, S.; Jiang, D.; Novoselov, K. S.; Roth, S.; Geim, A. K. *Phys. Rev. Lett.* **2006**, *97*, 187401.

(36) Fang, Y.; Luo, B.; Jia, Y.; Li, X.; Wang, B.; Song, Q.; Kang, F.; Zhi, L. *Adv. Mater.* **2012**, *24*, 6348-6355.

(37) Feng, H.; Cheng, R.; Zhao, X.; Duan, X.; Li, J. *Nat. Commun.* **2013**, *4*, 1539.

(38) Cabibil, H.; Ihm, H.; White, J. M. *Surf. Sci.* **2000**, *447*, 91-104.

(39) Yao, Z.; Nie, H.; Yang, Z.; Zhou, X.; Liu, Z.; Huang, S. *Chem. Commun.* **2012**, *48*, 1027-1029.

(40) Simek, P.; Klimova, K.; Sedmidubsky, D.; Jankovsky, O.; Pumera, M.; Sofer, Z. *Nanoscale* **2015**, *7*, 261-270.

(41) Park, S.; An, J.; Piner, R. D.; Jung, I.; Yang, D.; Velamakanni, A.; Nguyen, S. T.; Ruoff, R. S. *Chem. Mater.* **2008**, *20*, 6592-6594.

(42) Fan, Z.-J.; Kai, W.; Yan, J.; Wei, T.; Zhi, L.-J.; Feng, J.; Ren, Y.-m.; Song, L.-P.; Wei, F. *ACS Nano* **2011**, *5*, 191-198.

(43) Wang, Y.; Shi, Z.; Huang, Y.; Ma, Y.; Wang, C.; Chen, M.; Chen, Y. *J. Phys. Chem. C* **2009**, *113*, 13103-13107.

(44) Lin, Z.; Liu, Y.; Yao, Y.; Hildreth, O. J.; Li, Z.; Moon, K.; Wong, C.-p. *J. Phys. Chem. C* **2011**, *115*, 7120-7125.

(45) Han, S.; Wu, D.; Li, S.; Zhang, F.; Feng, X. *Adv. Mater.* **2014**, *26*, 849-864.

(46) Stoller, M. D.; Park, S.; Zhu, Y.; An, J.; Ruoff, R. S. *Nano Lett.* **2008**, *8*, 3498-3502.

(47) Hou, Y.; Cheng, Y.; Hobson, T.; Liu, J. *Nano Lett.* **2010**, *10*, 2727-2733.

(48) Wu, Q.; Xu, Y.; Yao, Z.; Liu, A.; Shi, G. *ACS Nano* **2010**, *4*, 1963-1970.

(49) Stoller, M. D.; Ruoff, R. S. *Energy Environ. Sci.* **2010**, *3*, 1294-1301.

(50) Zhang, S.; Pan, N. *Adv. Energy Mater.* **2015**, *5*, 1401401.

(51) Tao, Y.; Xie, X.; Lv, W.; Tang, D. M.; Kong, D.; Huang, Z.; Nishihara, H.; Ishii, T.; Li, B.; Golberg, D.; Kang, F.; Kyotani, T.; Yang, Q. H. *Sci. Rep.* **2013**, *3*, 2975.

(52) Seredych, M.; Bandosz, T. J. *J. Mater. Chem. A* **2013**, *1*, 11717-11727.

(53) Li, Y.; Zhao, D. *Chem. Commun.* **2015**, *51*, 5598-5601.

(54) Fan, Z.; Zhao, Q.; Li, T.; Yan, J.; Ren, Y.; Feng, J.; Wei, T. *Carbon* **2012**, *50*, 1699-1703.

(55) Ghaffari, M.; Zhou, Y.; Xu, H.; Lin, M.; Kim, T. Y.; Ruoff, R. S.; Zhang, Q. M. *Adv. Mater.* **2013**, *25*, 4879-4885.

(56) Zhu, Y.; Murali, S.; Stoller, M. D.; Ganesh, K. J.; Cai, W.; Ferreira, P. J.; Pirkle, A.; Wallace, R. M.; Cychosz, K. A.; Thommes, M.; Su, D.; Stach, E. A.; Ruoff, R. S. *Science* **2011**, *332*, 1537-1541.

(57) Murali, S.; Quarles, N.; Zhang, L. L.; Potts, J. R.; Tan, Z.; Lu, Y.; Zhu, Y.; Ruoff, R. S. *Nano Energy* **2013**, *2*, 764-768.

(58) Yan, J.; Wei, T.; Shao, B.; Ma, F.; Fan, Z.; Zhang, M.; Zheng, C.; Shang, Y.; Qian, W.; Wei, F. *Carbon* **2010**, *48*, 1731-1737.

(59) Kim, T.; Jung, G.; Yoo, S.; Suh, K. S.; Ruoff, R. S. *ACS Nano* **2013**, *7*, 6899-6905.

(60) Xu, Y.; Lin, Z.; Zhong, X.; Huang, X.; Weiss, N. O.; Huang, Y.; Duan, X. *Nat. Commun.* **2014**, *5*, 4554.

(61) Hulicova-Jurcakova, D.; Kodama, M.; Shiraishi, S.; Hatori, H.; Zhu, Z. H.; Lu, G. Q. *Adv. Funct. Mater.* **2009**, *19*, 1800-1809.

(62) Raymundo-Piñero, E.; Leroux, F.; Béguin, F. *Adv. Mater.* **2006**, *18*, 1877-1882.

(63) Zapata-Benabithe, Z.; Carrasco-Marín, F.; Moreno-Castilla, C. *J. Power Sources* **2012**, *219*, 80-88.

(64) Zhang, L.; Candelaria, S. L.; Tian, J.; Li, Y.; Huang, Y.-x.; Cao, G. *J. Power Sources* **2013**, *236*, 215-223.

(65) Lei, Z.; Lu, L.; Zhao, X. S. *Energy Environ. Sci.* **2012**, *5*, 6391-6399.

(66) Wu, Z.-S.; Winter, A.; Chen, L.; Sun, Y.; Turchanin, A.; Feng, X.; Müllen, K. *Adv. Mater.* **2012**, *24*, 5130-5135.

(67) Wen, Z.; Wang, X.; Mao, S.; Bo, Z.; Kim, H.; Cui, S.; Lu, G.; Feng, X.; Chen, J. *Adv. Mater.* **2012**, *24*, 5610-5616.

(68) You, B.; Wang, L.; Yao, L.; Yang, J. *Chem. Commun.* **2013**, *49*, 5016-5018.

(69) Han, J.; Zhang, L. L.; Lee, S.; Oh, J.; Lee, K.-S.; Potts, J. R.; Ji, J.; Zhao, X.; Ruoff, R. S.; Park, S. *ACS Nano* **2013**, *7*, 19-26.

(70) Xu, X.; Sun, Z.; Chua, D. H.; Pan, L. *Sci. Rep.* **2015**, *5*, 11225.

(71) Wu, Z.-S.; Sun, Y.; Tan, Y.-Z.; Yang, S.; Feng, X.; Müllen, K. *J. Am. Chem. Soc.* **2012**, *134*, 19532-19535.

(72) Yan, J.; Khoo, E.; Sumboja, A.; Lee, P. S. *ACS Nano* **2010**, *4*, 4247-4255.

(73) Han, J.; Xu, G.; Ding, B.; Pan, J.; Dou, H.; MacFarlane, D. R. *J. Mater. Chem. A* **2014**, *2*, 5352-5357.

(74) Liang, Y.; Liu, H.; Li, Z.; Fu, R.; Wu, D. *J. Mater. Chem. A* **2013**, *1*, 15207-15211.

(75) Li, Z.; Wu, D.; Liang, Y.; Fu, R.; Matyjaszewski, K. *J. Am. Chem. Soc.* **2014**, *136*, 4805-4808.

(76) Gao, F.; Shao, G.; Qu, J.; Lv, S.; Li, Y.; Wu, M. *Electrochim. Acta* **2015**, *155*, 201-208.

(77) Peng, Z.; Ye, R.; Mann, J. A.; Zakhidov, D.; Li, Y.; Smalley, P. R.; Lin, J.; Tour, J. M. *ACS Nano* **2015**, *9*, 5868-5875.

(78) Xiang, Z.; Wang, D.; Xue, Y.; Dai, L.; Chen, J. F.; Cao, D. *Sci. Rep.* **2015**, *5*, 8307.

(79) Yu, X.; Lu, B.; Xu, Z. *Adv. Mater.* **2014**, *26*, 1044-1051.

(80) Ma, Z.; Zhao, X.; Gong, C.; Zhang, J.; Zhang, J.; Gu, X.; Tong, L.; Zhou, J.; Zhang, Z. *J. Mater. Chem. A* **2015**, *3*, 13445-13452.

(81) Haque, E.; Islam, M. M.; Pourazadi, E.; Hassan, M.; Faisal, S. N.; Roy, A. K.; Konstantinov, K.; Harris, A. T.; Minett, A. I.; Gomes, V. G. *RSC Adv.* **2015**, *5*, 30679-30686.

(82) Hao, L.; Ning, J.; Luo, B.; Wang, B.; Zhang, Y.; Tang, Z.; Yang, J.; Thomas, A.; Zhi, L. *J. Am. Chem. Soc.* **2014**, *137*, 219-225.

(83) Zhao, Z.; Hao, S.; Hao, P.; Sang, Y.; Manivannan, A.; Wu, N.; Liu, H. *J. Mater. Chem. A* **2015**, *3*, 15049-15056.

(84) Li, X. J.; Xing, W.; Zhou, J.; Wang, G. Q.; Zhuo, S. P.; Yan, Z. F.; Xue, Q. Z.; Qiao, S. Z. *Chem. Eur. J.* **2014**, *20*, 13314-13320.

(85) Tong, Z.; Yang, Y.; Wang, J.; Zhao, J.; Su, B.-L.; Li, Y. *J. Mater. Chem. A* **2014**, *2*, 4642-4651.

(86) Zhao, X.; Zheng, B.; Huang, T.; Gao, C. *Nanoscale* **2015**, *7*, 9399-9404.

(87) Yang, M.; Choi, B. G.; Jung, S. C.; Han, Y.-K.; Huh, Y. S.; Lee, S. B. *Adv. Funct. Mater.* **2014**, *24*, 7301-7309.

(88) Le, T.; Yang, Y.; Huang, Z.; Kang, F. *J. Power Sources* **2015**, *278*, 683-692.

(89) Nasini, U. B.; Bairi, V. G.; Ramasahayam, S. K.; Bourdo, S. E.; Viswanathan, T.; Shaikh, A. U. *J. Power Sources* **2014**, *250*, 257-265.

(90) Sun, G.; Liu, J.; Zhang, X.; Wang, X.; Li, H.; Yu, Y.; Huang, W.; Zhang, H.; Chen, P. *Angew. Chem., Int. Ed.* **2014**, *53*, 12576-12580.

(91) Fan, X. M.; Yu, C.; Yang, J.; Ling, Z.; Hu, C.; Zhang, M. D.; Qiu, J. S. *Adv. Energy Mater.* **2015**, *5*, 1401761.

(92) Raj, C. J.; Kim, B. C.; Cho, W.-J.; Lee, W.-g.; Jung, S.-D.; Kim, Y. H.; Park, S. Y.; Yu, K. H. *ACS Appl. Mater. Interfaces* **2015**, *7*, 13405-13414.

(93) Li, B.; Cao, H.; Shao, J.; Qu, M.; Warner, J. H. *J. Mater. Chem.* **2011**, *21*, 5069-5075.

(94) Li, M.; Ding, J.; Xue, J. *J. Mater. Chem. A* **2013**, *1*, 7469-7476.

(95) Wang, P.; Wu, Q.; Han, L.; Wang, S.; Fang, S.; Zhang, Z.; Sun, S. *RSC Adv.* **2015**, *5*, 27290-27294.

(96) Jiang, L. L.; Sheng, L. Z.; Long, C. L.; Wei, T.; Fan, Z. J. *Adv. Energy Mater.* **2015**, *5*, 1500771.

Chapter 3

Nanofibrous and Graphene-Templated Conjugated Microporous Polymer Materials for Flexible Chemosensors and Supercapacitors[1]

3.1 Introduction

Conjugated microporous polymers (CMPs) as a subclass of porous polymers have attracted tremendous attention due to their attractive properties and the combination of a delocalized π-conjugated skeleton with permanent nanoporosity, large specific surface area, low density as well as high physical and chemical stability.[2-4] In addition, CMPs are characterized by a high flexibility of their molecular design. Various CMPs have been obtained in template-free chemical or electrochemical processes via selection of proper building blocks (tectons) and crosslinking strategies.[3,5-7] Therefore, CMPs emerged as a new class of porous materials with a big application potential in environmental and energy-related fields, e.g., in gas storage and separation,[8-10] superabsorption,[11] sensors,[12,13] light harvesting[14] and light emitting devices,[15,16] heterogeneous catalysis,[17-19] and electric energy conversion and storage.[20,21]

However, CMPs are mostly formed under kinetic control, and thus usually amorphous or semicrystalline powders are obtained. Their insolubility and non-processability are highlighted as serious bottlenecks that hamper many CMPs applications.[4,13] Most of previous work about CMPs was concentrated on developing new tectons and polymerization strategies for varying specific surface area and pore size distribution of the resulting networks by tuning the size of the tectons without a rigorous morphology control.[3] Only a few approaches have been reported for CMPs preparation under nanostructure control, for instance, towards microspheres (quasi-zero-dimensional, 0D),[22] nanotubes and nanofibers (one-dimensional, 1D),[23]

thin films (quasi-two-dimensional, 2D), and compact monoliths (three-dimensional, 3D).[13,24-29] The synthesis of really two-dimensional (2D) CMP nanosheets remained largely unexplored.[18,26,30]

Graphene, with its single-atom-thick layer of carbon atoms arranged in a honeycomb lattice is characterized by a high specific surface area, a large aspect ratio, and many exceptional chemical and physical properties and represents an excellent template for constructing graphene-based, porous nanohybrid materials.[18,30] Electrospinning is a well-established and versatile technique for fabricating nanofibers with diameters ranging from dozens of nanometers to several micrometers.[31,32] This method has proved to be a unique, simple, cost-effective and scalable approach to generate nonwoven nanofibrous materials containing a dense network of fully interconnected meso- and macro-pores throughout the material. These materials are often characterized by a high flexibility and surface-area-to-volume ratio, which favors the fabrication of chemical sensor devices with fast response and high sensitivity.[31,32]

In this chapter, thin films of fluorescent, nanofibrous networks based on our light-emitting CMPs were fabricated by electrospinning CMPs/poly(lactic acid) (PLA) mixtures. The CMP-based nanofibrous films can be used as efficient fluorescence sensors for detecting nitroaromatic and benzoquinone vapors as well as oxidzing metal ions with high sensitivity. Moreover, our synthetic approach was used to tailor the morphology by using graphene templates. Sandwich-like, graphene-based CMP (G-CMP) nanosheets with high specific surface areas and large aspect ratios were synthesized in which each graphene sheet is fully covered by two porous polymer shells. The carbon-rich G-CMPs were used as precursors for pyrolytic conversion into hierarchically porous carbon nanosheets. These carbon materials have been exploited as electrode materials for use in suppercapacitors with promising performance, e.g., a 48% increased capacitance, if compared to porous carbon without the graphene additive.

3.2 Results and Discussion

3.2.1 Synthesis of Conjugated Microporous Polymers (CMPs) and Graphene-Templated CMPs (G-CMPs)

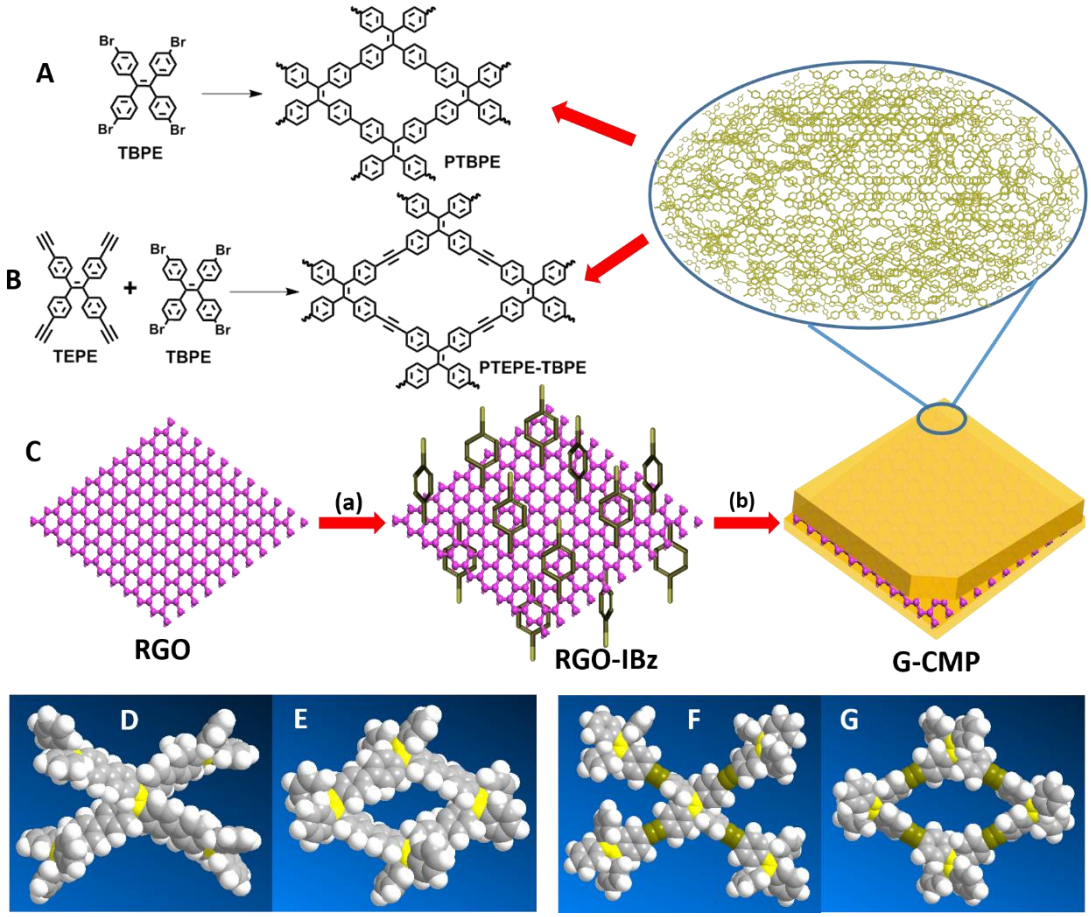

Figure 3.1 Preparation of CMPs: (A) PTBPE and (B) PTEPE-TBPE; (C) Process of generating graphene-templated CMPs, (a) 4-iodobenzene diazonium salt, 0°C to RT, 4 h; (b) Yamamoto-type coupling: TBPE, 1,5-cyclooctadiene, $Ni(cod)_2$, 2,2′-bipyridyl, DMF/THF, RT, 3 days; Sonogashira-Hagihara-type coupling: TEPE, TBPE, $Pd(PPh_3)_4$, CuI, Et_3N, DMF, 140°C, 3 days. (D) and (F) Open framework and (E) and (G) closed macrocyclic units as segments of PTBPE and the PTEPE-TBPE, respectively, simulated by DFT calculations at the B3LYP 6-31G* level (phenyl: gray, H: white, C=C: yellow; C≡C: green).

The synthetic strategy towards conjugated microporous polymers (CMPs) and the graphene-templated CMP hybrids (G-CMPs) is presented in Figure 3.1. Tetraphenylethene (TPE)-cored monomers were selected due to their high solid state photoluminescent quantum yields (PLQY) caused by the aggregate induced emission (AIE)-effect.[33] Tetrakis(4-bromophenyl)ethene (TBPE) was used as monomer for the

Yamamoto-type homocoupling into TPE-based polymer networks (PTBPE), in which the TPE units are covalently incorporated into CMP network, thus restricting the rotation of individual phenylene rotors and guaranteeing a high PLQY thanks to the AIE-effect.[15,33] In contrast, allowing the rotation of the phenyl groups of TPE derivatives (including the linear conjugated analogue) results in a significant reduction of the PLQY.[15,34-37] PTEPE-TBPE was prepared from tetrakis(4-ethynylphenyl)ethene (TEPE) and TBPE as monomers in a Sonogashira-Hagihara-type cross-coupling. The graphene-templated CMP hybrids (G-CMPs) G-PTBPE and G-PTEPE-TBPE were synthesized by reacting TBPE or a TEPE/TBPE mixture with 4-iodophenyl-substituted graphene (RGO-IBz) as templates in Yamamoto-type or Sonogashira-Hagihara-type coupling reactions, respectively (detailed experimental procedures are given in the Supporting Information). The RGO-IBz template is highly dispersible in various organic solvents, for example, toluene or dimethylformamide (DMF), without occurrence of aggregation.[38] In such dispersions, RGO-IBz acts as a versatile 2D template for the CMPs efficient graft onto the graphene surface.[18,26]

The conversion of the functional groups was monitored by Fourier transform infrared (FTIR) and Solid-state ^{13}C MAS NMR spectroscopy (Figure 3.2). The FTIR spectrum of TBPE exhibits the diagnostic C-Br stretch vibration at 1072 cm^{-1}.[15] This characteristic bond is absent in PTBPE and G-PTBPE (Figure 3.2A), thus documenting the formation of biphenyl bridges under aryl-aryl coupling. By comparing the FTIR spectra of TBPE, TEPE, PTEPE-TBPE and G-PTEPE-TBPE, a weak peak at 2110 cm^{-1} is assigned to alkyne -C≡C- stretch.[18,26] The intense stretch vibration of ethynyl C-H near 3280 cm^{-1} almost disappeared in the FTIR spectra of PTEPE-TBPE and G-PTEPE-TBPE if compared to TEPE spectrum (Figure 3.2B). The G-CMPs show similar structural features in comparison with those of the CMPs, suggesting a high conversion of functional groups also for G-CMPs synthesis. Therefore, we conclude that the polymerization reaction is not significantly affected by the presence and incorporation of the RGO-IBz templates.[26]

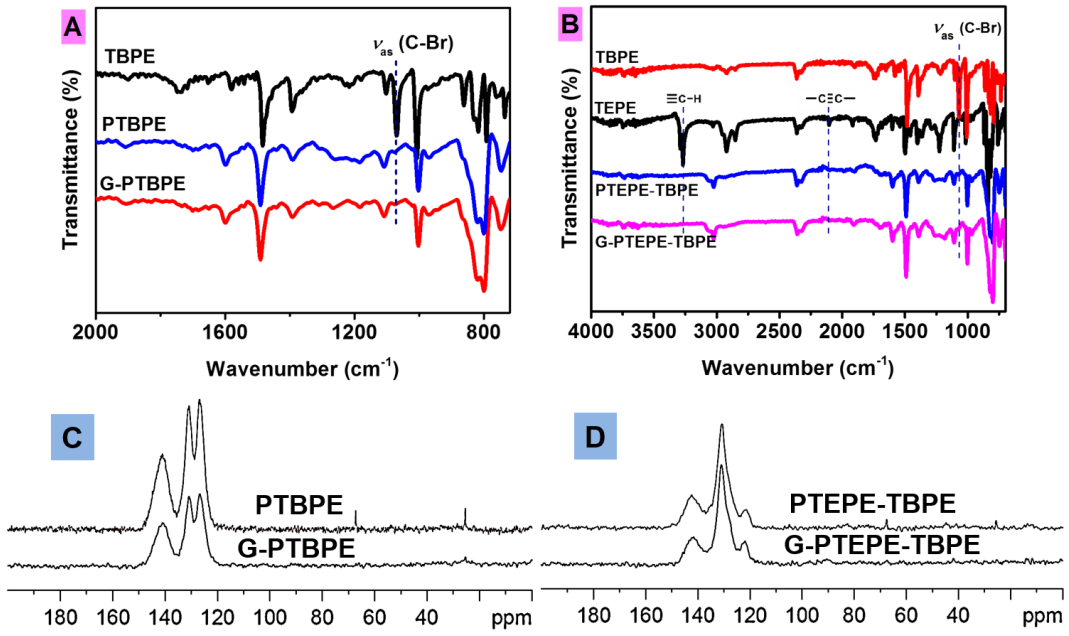

Figure 3.2 FTIR spectra of (A) TBPE, PTBPE and G-PTBPE, and (B) TBPE, TEPE, PTEPE-TBPE and G-PTEPE-TBPE. Solid-state ^{13}C MAS NMR spectra of (C) TBPE, PTBPE and G-PTBPE, and (D) TBPE, TEPE, PTEPE-TBPE and G-PTEPE-TBPE.

3.2.2 Micromorphology and Porosity of CMPs and G-CMPs

Micromorphology and nanostructure of CMPs and G-CMPs were investigated by transmission electron microscopy (TEM) and high resolution TEM (HRTEM), as shown in Figure 3.3A-D and Figure 3.4. TEM images of the CMPs without RGO-IBz templates display a nanoparticular morphology with an average diameter of the nanoparticles of ca. 80 nm. In contrast, the G-CMPs exhibited a flake-like structure with dimensions similar to those of the used graphene sheets. No free CMPs particles or “naked” RGO-IBz templates are observed, thus indicating that the majority of the monomers is bond to the surface of the graphene sheet. The microporous structure of CMPs and G-CMPs can be directly visualized by HRTEM. One obvious feature of both microporous structures is that the micropores are characterized by similar dimensions and that they are homogenously distributed both in CMPs and G-CMPs.

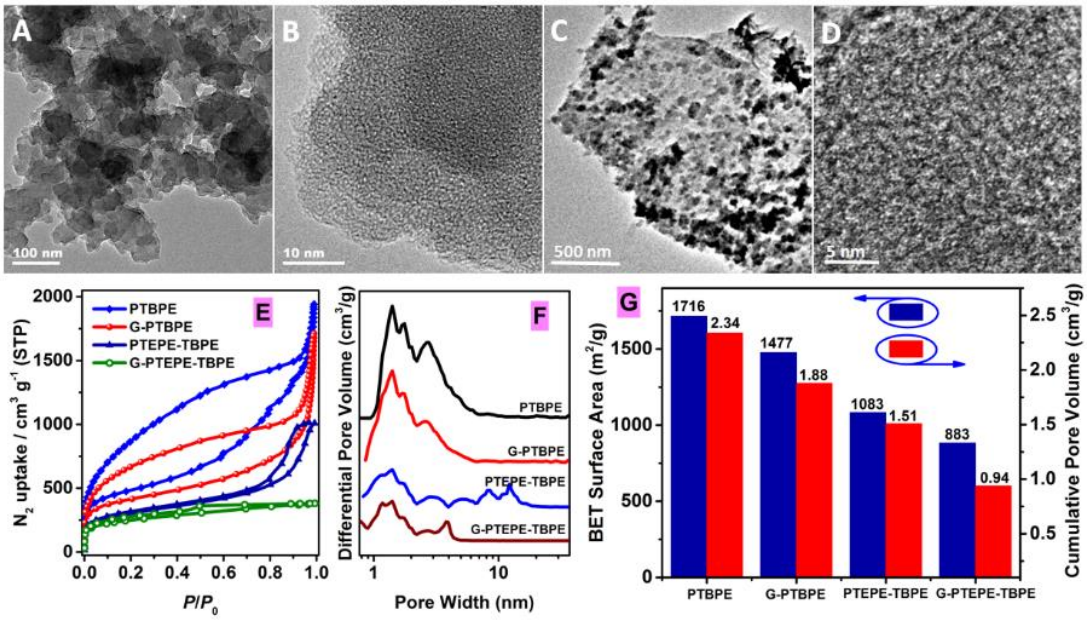

Figure 3.3 TEM images of (A) PTBPE and (C) G-PTBPE. HRTEM images of (B) PTBPE and (D) G-PTBPE. (E) Nitrogen adsorption/desorption isotherms, (F) Pore size distribution profiles, and (G) comparative diagram with BET surface areas and corresponding cumulative pore volumes of PTBPE, G-PTBPE, PTEPE-TBPE and G-PTEPE-TBPE.

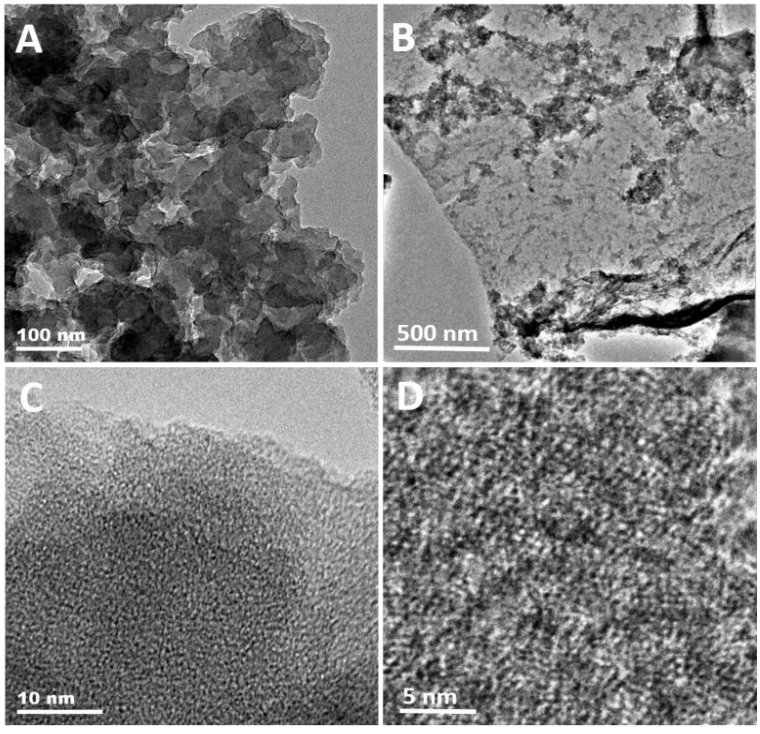

Figure 3.4 TEM images of (A) PTEPE-TBPE and (B) PTEPE-TBPE. HRTEM images of (C) PTEPE-TBPE and (D) G-PTEPE-TBPE.

The porosity of CMPs and G-CMPs was characterized by nitrogen physisorption measurements performed at 77 K. All CMPs and G-CMPs samples gave reversible isotherms characteristic of microporous materials (Figure 3.3E). The extracted Brunauer-Emmett-Teller (BET) surface areas for PTBPE, G-PTBPE, PTEPE-TBPE and G-PTEPE-TBPE are 1716, 1477, 1083 and 883 m^2/g, and the corresponding cumulative pore volumes were 2.34, 1.88, 1.51 and 0.94 cm^3/g, respectively (Figure 3.3G), with slightly reduced values for the graphene-templated hybrid materials. The pore size distribution profiles for the CMPs and G-CMPs were calculated by using a nonlocal density functional theory (NLDFT) approach. The pore size distributions imply the co-existence of micro- and mesopores in both CMPs and G-CMPs (Figure 3.3F and Figure 3.5). To get a deeper insight into the generation of the CMPs networks, DFT calculations were performed at the B3LYP/6-31G level. Two possible features of the frameworks (open framework and closed macrocyclic skeleton, Figure 3.1D-G) were considered for PTBPE and PTEPE-TBPE. In the open framework structure, significant twisting and distortion of peripheral TPE units supports the growth of the CMP skeleton into a microporous 3D morphology.

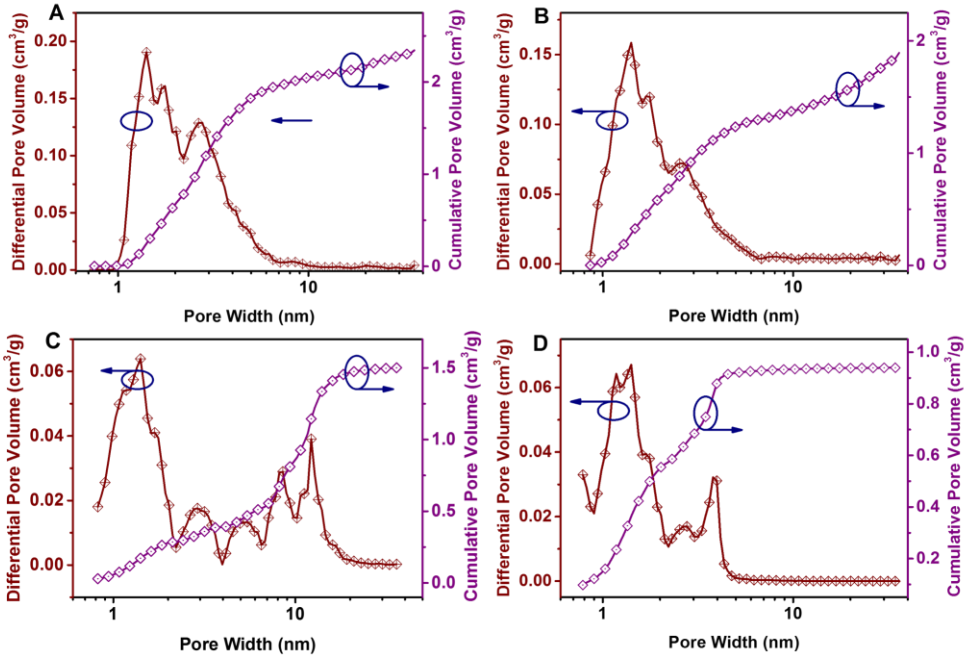

Figure 3.5 Pore size distribution profiles and corresponding cumulative pore volumes of (A) PTBPE, (B) G-PTBPE, (C) PTEPE-TBPE and (D) G-PTEPE-TBPE.

3.2.3 Photophysical Properties

The electronic structure of CMPs and G-CMPs was studied by absorption spectroscopy. A solution of the monomer TBPE in THF shows an absorption band peaking at 322 nm. For the PTBPE dispersion a red-shift of 72 nm is observed (λ_{max}: 394 nm), indicating an extension of electronic conjugation in PTBPE. Upon excitation at 322 nm, the TBPE monomer emits weakly in THF solution ($\lambda_{max,em}$: 482 nm). In contrast, the PTBPE sample is strongly emissive with the photoluminescence (PL) band peaking at 575 nm upon excitation at 394 nm (Figure 3.6). PTBPE showed a high PL quantum yield of 31.9%. The absorption band of a G-PTBPE dispersion peaks at 380 nm, slightly blue-shifted if compared to PTBPE. Upon excitation at 380 nm, the G-PTBPE sample emits yellow light, (band peaking at 575 nm) but much weaker as PTBPE (inset of Figure 3.7B). This UV/Vis and PL properties of PTEPE-TBPE and G-PTEPE-TBPE are quite similar (Figure 3.7C, D). Generally, the reduced photoluminescence of the templated hybrids is attributed to the electron-accepting properties of graphene.[18,26] The porous PTBPE and PTEPE-TBPE coatings at both sides of the graphene templates act as electron donors (D), the graphene sheets as electron-acceptors (A), thus reducing the amount of radiative deactivation of excited states.

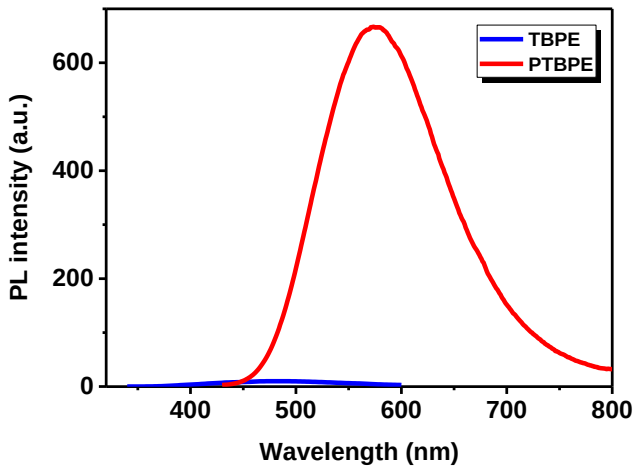

Figure 3.6 Photoluminescence spectra of TBPE and PTBPE in THF. Upon excitation at 322 nm, the TBPE monomer emits weakly in THF solution ($\lambda_{max,em}$: 482 nm). In contrast, the sample of the PTBPE dispersion is strongly emissive with the photoluminescence (PL) band peaking at 575 nm (excitation at 394 nm).

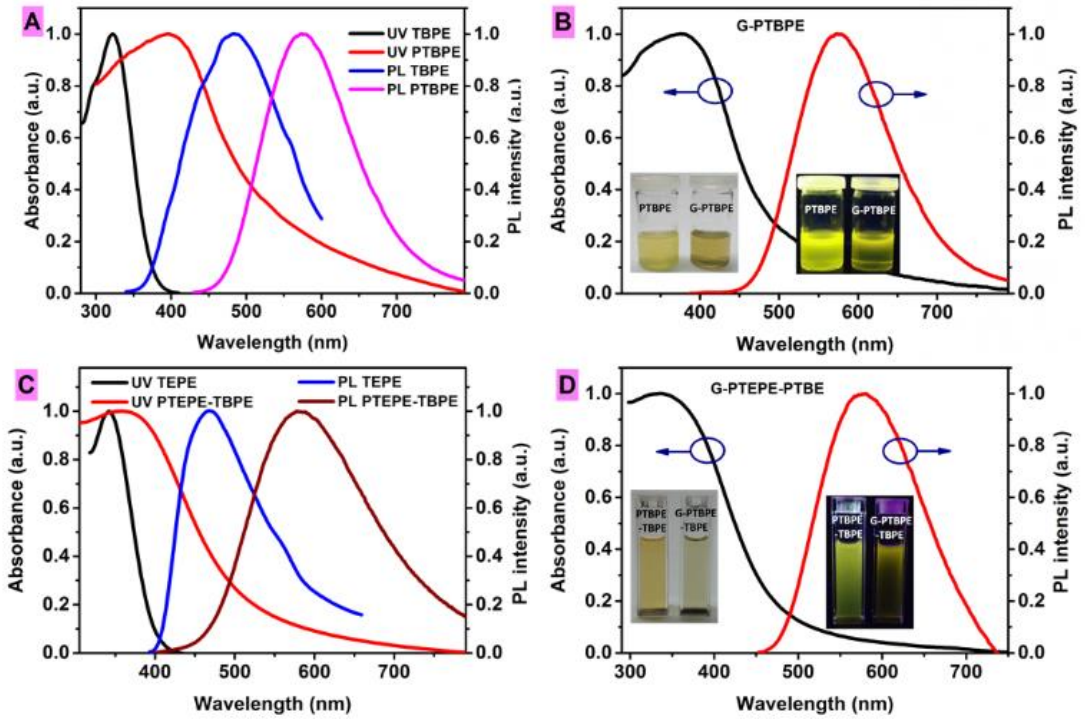

Figure 3.7 Normalized electronic absorption and fluorescence spectra of (A) TBPE and PTBPE, (B) G-PTBPE, (C) TEPE and PTEPE-TBPE and (D) G-PTEPE-TBPE. Insets: Photographs of PTBPE, G-PTBPE, PTEPE-TBPE and G-PTEPE-TBPE dispersions in THF excited by sun-light (left) and a UV lamp (365 nm, right).

PTBPE dispersions are strongly luminescent in various solvents (such as THF, DMF, acetone and $CHCl_3$) as well as PTBPE in the solid state (Figure 3.8) making this material suitable for sensing experiments via fluorescence qenching. Unfortunately, since the PTBPE powder is insoluble, it is difficult to generate thin films directly. We fabricated PTBPE-based nanofibrous films by electrospinning PTBPE/poly(lactic acid) (PLA) mixtures under formation of nanofibrous films. These flexible, electrospun PTBPE/PLA films are highly emissive if excited by UV light (Figure 3.8 and Figure 3.9A). The PTBPE/PLA nanofibers show a smooth and featureless surface as confirmed by scanning electron microscopy (SEM) and TEM as shown in Figure 3.9 B, C. A HRTEM image (Figure 3.9D) implies that the PTBPE component is homogenously distributed within the PLA matrix.

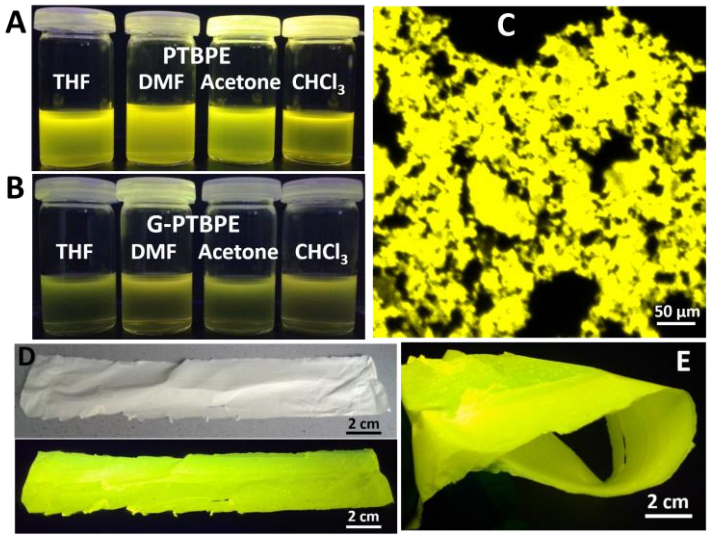

Figure 3.8 Photographs of (A) PTBPE and (B) G-PTBPE dispersions in THF, DMF, acetone and $CHCl_3$ under UV excitatioin. (C) Fluorescence microscopic image of PTBPE. (D) Photographs of electrospun, nanofibrous PTBPE/PLA films excited by sun-light (top) and a UV lamp (365 nm, bottom). (E) Photograph of a flexible, nanofibrous PTBPE/PLA film bended by 180 degree under UV light (365 nm).

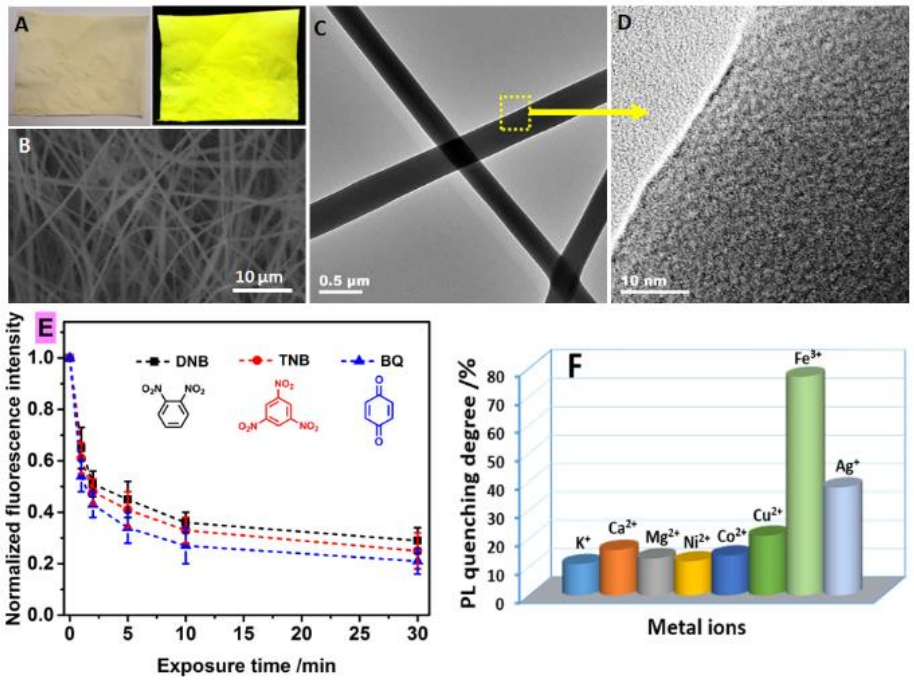

Figure 3.9 (A) Photographs of electrospun PTBPE/PLA nanofibrous films excited by sun-light (left) and a UV lamp (365 nm, right). (B) SEM, (C) TEM and (D) HRTEM image of the nanofibers. (E) Normalized fluorescence intensity of the electrospun PTBPE/PLA nanofibrous films upon exposure to vapors of 1,2-dinitrobenzene (DNB), 1,3,5-trinitrobenzene (TNB) and 1,4-benzoquinone (BQ) for different time periods. (F) Degree of fluorescence quenching of the electrospun PTBPE/PLA nanofibrous films upon 1 min immersion with aqueous solutions of different metal ions (10^{-4} mol L^{-1}).

3.2.4 Chemosensing Properties of the Nanofibrous PTBPE/PLA Films

Polymers containing TPE units, linear, hyperbranched as well as crosslinked ones, have been used for detection of nitroaromatic explosives.[28,39,40] Therefore, chemosensing measurements were conducted by exposing electrospun PTBPE/PLA nanofibrous films to nitroaromatic and benzoquinone vapors for a designated period at room temperature under PL monitoring. Several individual electrospun PTBPE/PLA nanofibrous films were used for each chemosensing experiment. The electrospun PTBPE/PLA nanofibrous films sensitively respond towards the investigated analytes, as shown in Figure 3.9E and Figure 3.10. For example, the PL of an electrospun PTBPE/PLA nanofibrous film is significantly quenched upon exposure to 1,2-dinitrobenzene (DNB) vapor, to 51% of the initial intensity after 2 min exposure and to 29% for a prolonged exposure of 30 min. Similar numbers are observed for other electron-deficient analytes, e.g., for 1,3,5-trinitrobenzene (TNB) and 1,4-benzoquinone (BQ). 2 min exposure resulted in 52% and 57% PL quenching, a prolonged exposure of 30 min in 75% and 79% PL quenching for TNB and BQ, respectively. The significant quenching response should originate from a photoinduced electron transfer between the PTBPE and the electron-deficient analytes due to the offset of their lowest unoccupied molecular orbital energies.[12,13,41] Thereby, the PL quenching process is characterized by good reproducibility (Figure 3.11).

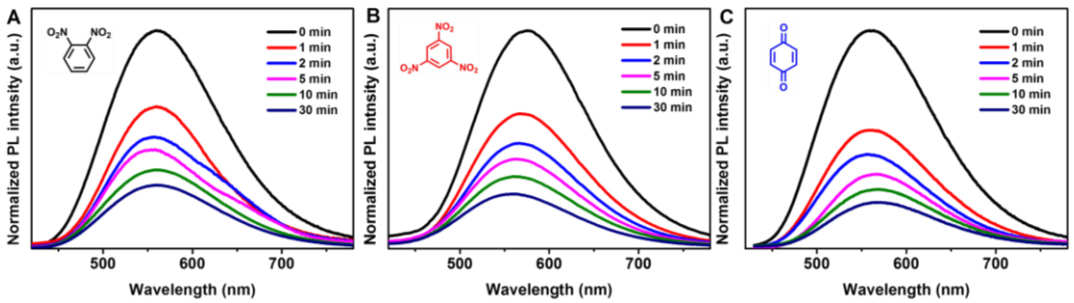

Figure 3.10 Normalized fluorescence intensity of nanofibrous PTBPE/PLA films upon exposure to vapors of (A) 1,2-dinitrobenzene (DNB), (B) 1,3,5-trinitrobenzene (TNB) and (C) 1,4-benzoquinone (BQ) for different times.

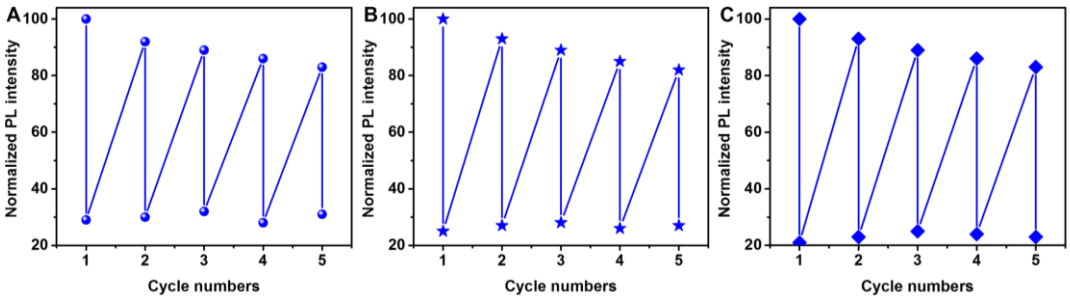

Figure 3.11 Cycling test with the nanofibrous PTBPE/PLA films upon exposure to vapors of (A) 1,2-dinitrobenzene (DNB), (B) 1,3,5-trinitrobenzene (TNB), and (C) 1,4-benzoquinone (BQ). The PL quenching ability id characterized by good reproducibility.

We further investigated the PL response to different metal ions in aqueous solution (10^{-4} mol L^{-1}), including K^+, Ca^{2+}, Mg^{2+}, Fe^{3+}, Co^{2+}, Ni^{2+}, Cu^{2+} and Ag^+. Slight fluorescence quenching (10-20%) was observed if the electrospun PTBPE/PLA nanofibrous films are contacted with aqueous solutions of most of the metal ions for 1 min (Figure 3.9F and Figure 3.12). However, significant increased fluorescence quenching was found for Ag^+ (38%) and Fe^{3+} (77%) as oxidizing metal ions. Fe^{3+} with its high electron affinity (0.77 V, $E_{Fe(III)/Fe(II)}$)[13] may cause photooxidation of PTBPE, thus resulting in PL quenching. These data distinctly confirm that the electrospun PTBPE/PLA nanofibrous films selectively respond to electron-deficient oxidizing metal ions, such as Ag^+ or Fe^{3+}.

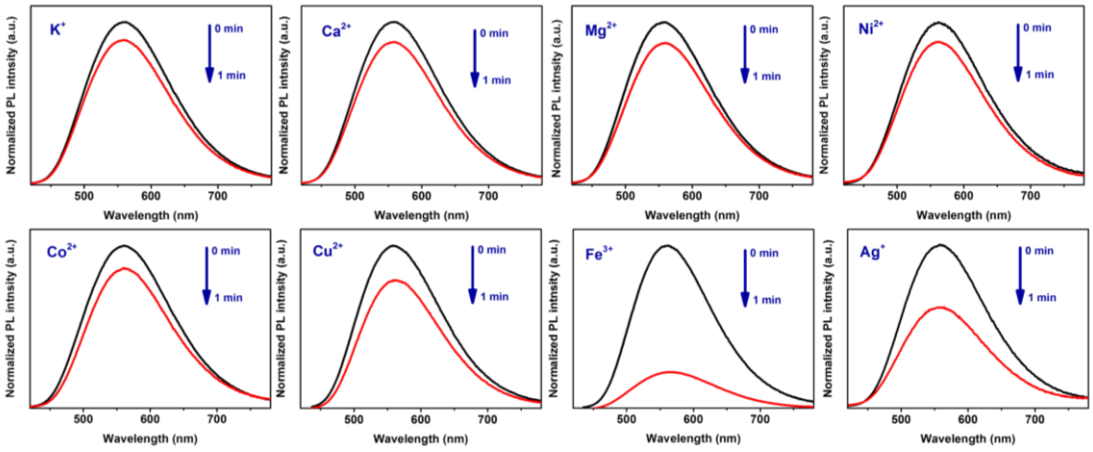

Figure 3.12 Fluorescence quenching of nanofibrous PTBPE/PLA films upon 1 min immersion in aqueous solutions of different metal ions (10^{-4} mol L^{-1}).

3.2.5 Pyrolytic Generation and Characterization of CMP- and G-CMP-Derived Carbons and Carbon Nanosheets

The carbon-rich CMPs and G-CMPs can be used for pyrolysis into hierarchically porous carbons and carbon nanosheets. Such porous carbon materials are discussed as potential electrode materials for various applications, such as lithium ion batteries,[42] metal-free catalysts,[18,43] supercapacitors[18,30,44,45] and sensing.[46] The thermogravimetric analysis (TGA) under inert atmosphere implied that CMPs and G-CMPs can be converted into carbons with a high yield at a temperature of 800 °C. Thereby, the higher carbon yield for G-CMPs is attributed to the presence of the inherently stable graphene templates that do not undergo much conversion.[45] Porous carbon materials denoted PTBPE-C, PTEPE-TBPE-C, G-PTBPE-C and G-PTEPE-TBPE-C were generated by direct, inert gas pyrolysis of PTBPE, PTEPE-TBPE, G-PTBPE and G-PTEPE-TBPE, respectively, at 800 °C for 2 h (under argon atmosphere). Concerning the morphology of the resulting materials, the results for PTEPE-TBPE-C and G-PTEPE-TBPE-C are discussed here as example.

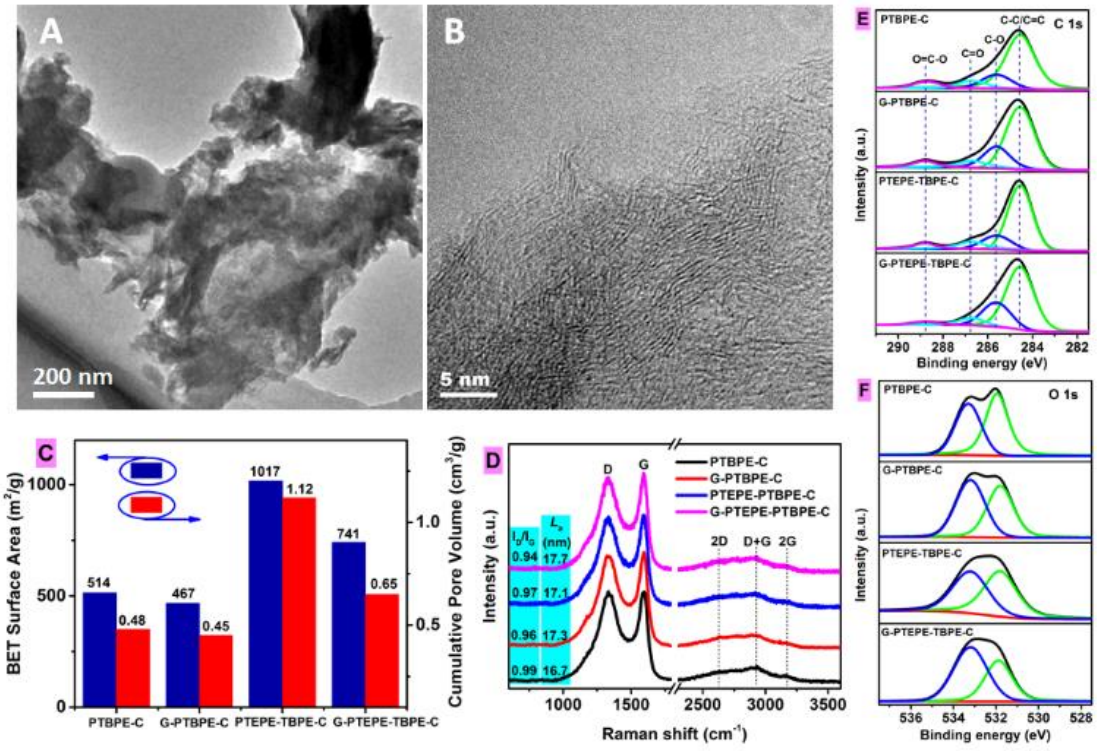

Figure 3.13 (A) TEM and (B) HRTEM images of G-PTEPE-TBPE-C. (C) Comparative diagram with BET surface areas and corresponding cumulative pore volumes of PTBPE-C, G-PTBPE-C, PTEPE-TBPE-C and G-PTEPE-TBPE-C. (D) Raman spectra, (E) C 1s and (F) O 1s core-level XPS spectra of PTBPE-C, G-PTBPE-C, PTEPE-TBPE-C and G-PTEPE-TBPE-C.

Due to the TEM image of Figure 3.13A, G-PTEPE-TBPE-C maintained the nanosheet morphology of the G-PTEPE-TBPE precursor with its high aspect ratio. The individual nanosheets are, thereby, ridged and wrinkled states, as supported by the HRTEM image of Figure 3.13B. In contrast, PTEPE-TBPE-C displayed a nanoparticular structure (Figure 3.14A). PTBPE-C, PTEPE-TBPE-C, G-PTBPE-C and G-PTEPE-TBPE-C display BET surface areas of 514, 1017, 467 and 741 m^2 g^{-1}, respectively (Figure 3.13C, Figure 3.14B and Figure 3.15). The reduced BET surface area for the porous carbons and carbon nanosheets relative to the corresponding CMP and G-CMP precursors is attributed to the restructuring during pyrolysis of the polymeric precursors with a recombination of fragments during carbonization.[18]

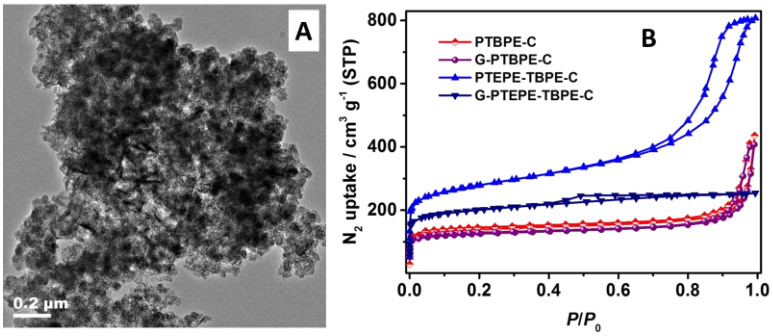

Figure S3.14 (A) TEM image of PTEPE-TBPE-C. (B) Nitrogen adsorption/desorption isotherms of PTBPE-C, G-PTBPE-C, PTEPE-TBPE-C and G-PTEPE-TBPE-C.

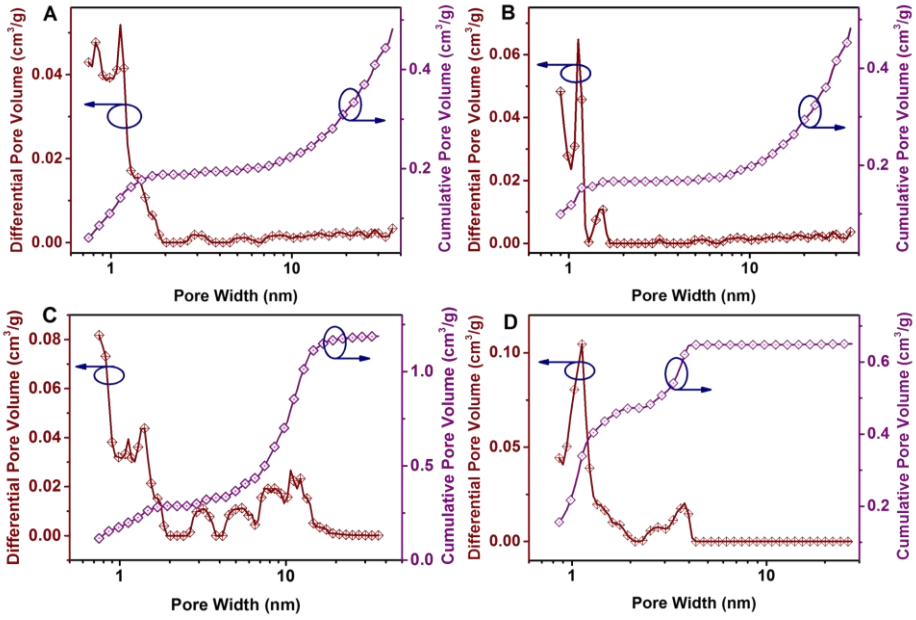

Figure 3.15 Pore size distribution profiles and corresponding cumulative pore volumes of (A) PTBPE-C, (B) G-PTBPE-C, (C) PTEPE-TBPE-C and (D) G-PTEPE-TBPE-C.

Raman spectroscopy provides a fast, high resolution and non-destructive characterization tool in the structural characterization of graphene-based and carbon materials. Raman spectra are also employed to determine thickness and size of graphene domains of sp^2 carbon materials.[47-49] The porous carbon and carbon nanosheet samples all show two broad peaks (Figure 3.13D), i.e. a D-band at ca. 1335 cm^{-1} and a G-band at ca. 1590 cm^{-1}. The D-band is generally relate to vibrations of carbon atoms of disordered, structural defects (such as amorphous domains), while the G-band is assigned to the E_{2g} mode of sp^2 carbon atoms in ordered, crystallite domains, such as graphene.[50,51] The size of sp^2 graphene domains (L_a, nm) can be calculated from the equation: L_a (nm) = $(560/E^4)(I_D/I_G)^{-1}$, where E is laser energy (514 nm, 2.41 eV), and I_D/I_G is intensity ratio of D and G bands.[49] The approximate size of the sp^2 carbon domains of our porous carbons and carbon nanosheets was found to be 16-18 nm.

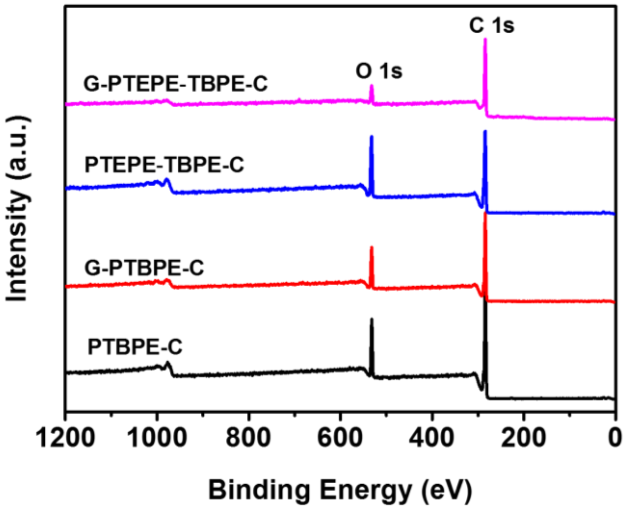

Figure 3.16 XPS spectra of PTBPE-C, G-PTBPE-C, PTEPE-TBPE-C and G-PTEPE-TBPE-C.

The chemical nature of our porous carbons and carbon nanosheets was further investigated by X-ray photoelectron spectroscopy (XPS, Figure 3.13E, F and Figure 3.16). According to the deconvoluted high-resolution XPS spectra for C 1s, four individual peaks were found, which were assigned to graphitic/graphenic carbons (284.5 eV), -C-OH (285.6 eV), -C=O (286.7 eV), and -COOH (288.8 eV), as shown in Figure 3.13E. The results show that the obtained porous carbons and carbon

nanosheets are mainly composed of sp^2 carbons, only a small amount of carbon atoms exists as either carbonyl or carboxyl groups.[52] The XPS analysis also indicates that most oxygen atoms were located near the carbon surface, they should mainly originate from oxygen traces that are introduced during carbonization or from absorbed oxygen or water molecules. High-resolution XPS spectra for O 1s of the porous carbons and carbon nanosheets are shown in Figure 3.13F. The signals at 531.9 and 533.3 eV represent C=O, C-OH and/or C-O-C ether groups, absorbed oxygen or water.[53,54]

3.2.6 Electrochemical Properties of Carbon Materials

Our porous carbons and carbon nanosheets with their hierarchically porous structure hold promise for an application in electrochemical capacitors. As example, the electrochemical performance of PTEPE-TBPE-C and G-PTEPE-TBPE-C were examined under alkaline conditions using 6 M KOH aqueous solution as electrolyte in a conventional three-electrode configuration. As shown in Figure 3.17A, typical symmetric and rectangular shaped, cyclic voltammetry (CV) curves were observed for both PTEPE-TBPE-C and G-PTEPE-TBPE-C for a scan rate of 100 mV s^{-1}, suggesting ideal capacitive behavior. Moreover, a distinctly higher current density was observed for G-PTEPE-TBPE-C if compared to PTEPE-TBPE-C, which indicates that the incorporated graphene layers of G-PTEPE-TBPE-C contribute to the capacitance improvement. KOH-activation of carbon-based materials has been reported to improve porosity and supercapacitor performance.[55-57] Therefore, KOH-activation at 800 ^{o}C was also tested for G-PTEPE-TBPE-C with the mass ratio of KOH to G-PTEPE-TBPE-C of 2:1 resulting in a sample named aG-PTEPE-TBPE-C. As expected, current density and enclosed CV area of aG-PTEPE-TBPE-C are increased if compared to G-PTEPE-TBPE-C electrodes (Figure 3.17A and Figure 3.18), thus indicating higher electrochemical reactivity leading to an improved energy storage capacity. The enhanced electrochemical performance should mainly originate from an increased BET surface area of aG-PTEPE-TBPE-C after activation (1234 m^2/g, Figure 3.18), if compared to the S_{BET} value of the precursor (741 m^2/g).

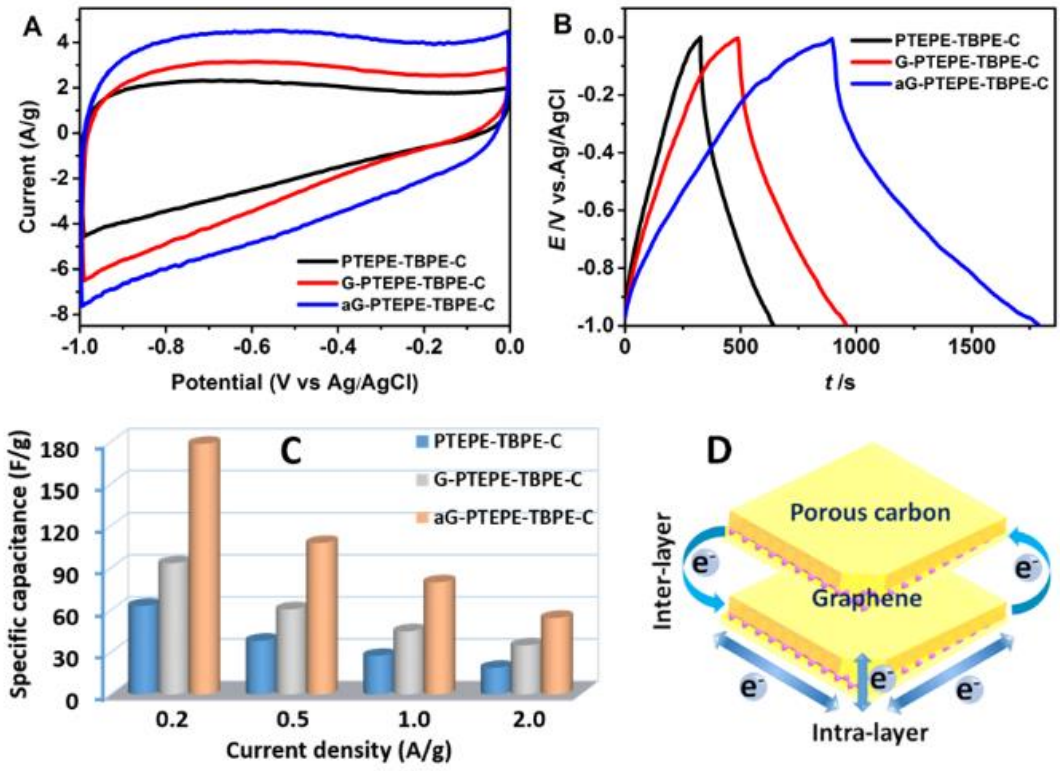

Figure 3.17 (A) Cyclic voltammograms at a scan rate of 100 mV/s in 6 M aqueous KOH solution, (B) galvanostatic charge/discharge curves at a current density of 0.2 A/g, and (C) specific capacitances at different current densities for the supercapacitors based on PTEPE-TBPE-C, G-PTEPE-TBPE-C and KOH-activated G-PTEPE-TBPE-C (aG-PTEPE-TBPE-C). (D) Scheme showing the inter/intra layer conductive paths in sandwich-like G-PTEPE-TBPE-C nanosheets during the charge/discharge processes.

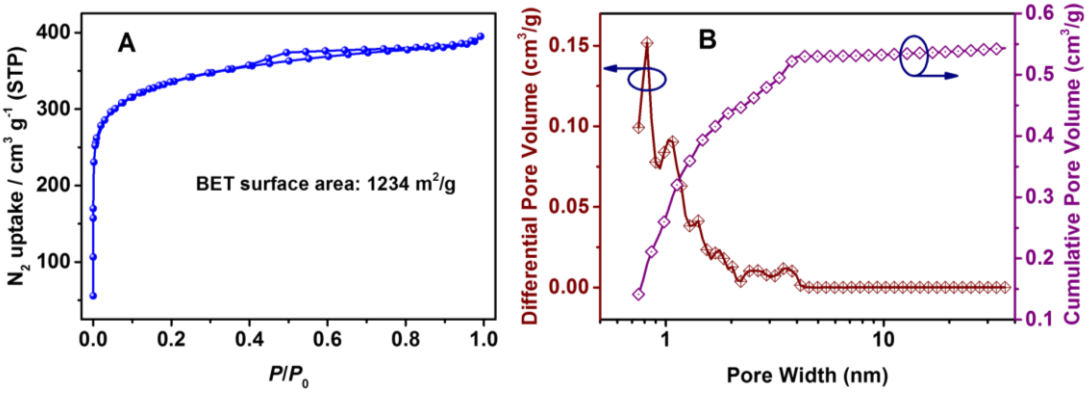

Figure 3.18 (A) Nitrogen adsorption/desorption isotherms and (B) pore size distribution profiles and corresponding cumulative pore volume of KOH-activated G-PTEPE-TBPE-C (aG-PTEPE-TBPE-C).

The electrochemical performance was further investigated in galvanostatic charge/discharge (GCD) cycles. The GCD curves and the calculated, corresponding specific capacitances of PTEPE-TBPE-C, G-PTEPE-TBPE-C and aG-PTEPE-TBPE-C at different current densities are shown in Figure 3.19 and Figure 3.17C, respectively. The calculated specific capacitance of G-PTEPE-TBPE-C of 94 F/g at a current density of 0.2 A/g is ca. 50% increased in relation to PTEPE-TBPE-C (63 F/g) and comparable to literature values of other carbon materials as metal located activated carbons and N-, P-, or Si-doped carbons (Table 3.1). In addition, the KOH-activated sample aG-PTEPE-TBPE-C gave a once more increased specific capacitance of 179 F/g at 0.2 A/g. The twofold higher value (if compared to G-PTEPE-TBPE-C) may be due to the improved porosity and the corresponding increased electrode-electrolyte interface. The improved performance of G-PTEPE-TBPE-C if compared to PTEPE-TBPE-C may base on the following reasons: The graphene scaffold renders G-PTEPE-TBPE-C with a high electrical conductivity, thus reducing the internal resistance. Lowering the equivalent series resistance is a critical issue in improving the performance of the supercapacitors. So, the graphene sheets of sandwich-type G-PTEPE-TBPE-C may both act as small-current collectors and long-distance charge transporting units during charging/discharging, by taking advantage of the high electrical conductivity of graphene. The hierarchical pore structure of the sandwiches with large aspect ratio should favor a rapid ion transport from or to the surface of the micropores, thus improving ion injection or extraction. Finally, an improved inter/intra layer electron transport (Figure 3.17D) in G-PTEPE-TBPE-C should shorten the average charge transport distance, thus contributing to the superior capacitance and energy storage capacity in comparison to the dot-to-dot charge transport pathways of the non-templated PTEPE-TBPE-C counterpart.[26,30,44,56]

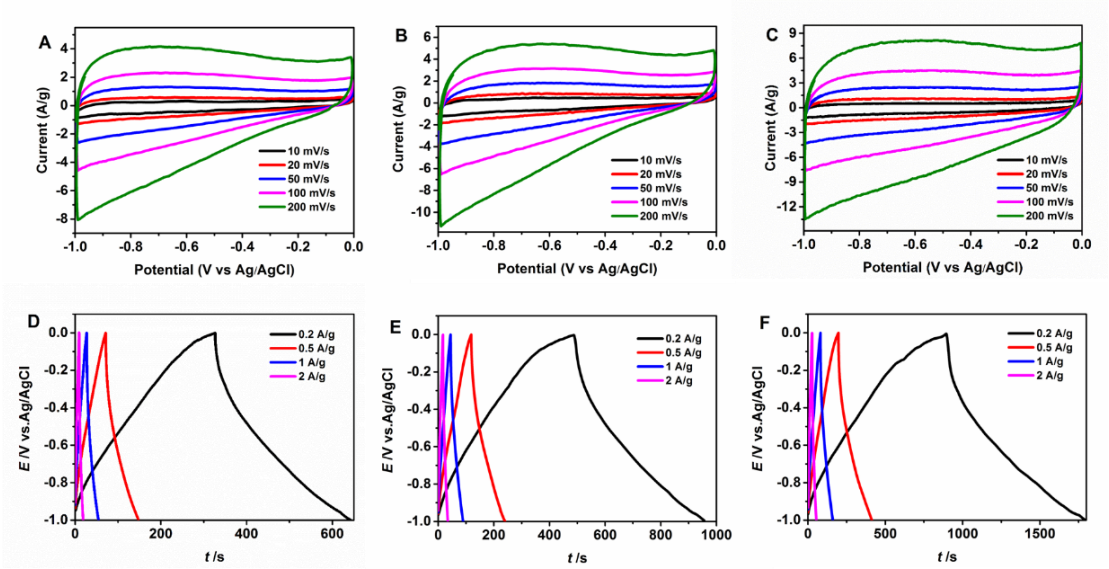

Figure 3.19 Cyclic voltammograms of (A) PTEPE-TBPE-C, (B) G-PTEPE-TBPE-C and (C) KOH-activated G-PTEPE-TBPE-C (aG-PTEPE-TBPE-C) at scan rates of 10, 20, 50, 100 and 200 mV/s in 6 M aqueous KOH solution. Galvanostatic charge/discharge curves of supercapacitor devices based on (D) PTEPE-TBPE-C, (E) G-PTEPE-TBPE-C and (F) aG-PTEPE-TBPE-C at different current densities.

Table 3.1 Comparison of literature data: gravimetric capacitances of carbon-based electrodes.

Materials	Gravimetric capacitance (F/g)	Electrolyte	References
Copper nanocrystal modified activated carbon	79	TEATFB	58
Cellulose-derived carbon	39	6 M KOH	59
Regenerated cellulose derived carbon	80	6 M KOH	59
Microporous activated carbon	60	PYR14TFS	60
Buckypaper carbon	63	$EMIBF_4$	61
RGO	41.5	6 M KOH	62
Mesoporous carbon spheres	39.4	6 M KOH	
N, P, and Si doped carbon	24	6 M KOH	63
	66	1M H_2SO_4	
Commercial glucose derived carbon	16	6 M KOH	64
cxPh-POSS-900-5 derived carbon	85	1 M $(C_2H_5)_4NBF_4$/PC	65
Sucrose derived carbon (C900)	62	1M H_2SO_4	66
G-PTEPE-TBPE-C	**94**	**6 M KOH**	**This work**

3.3 Conclusions

In summary, fluorescent, nanofibrous films of high porosity are simply fabricated by electrospinning CMP/PLA mixtures. High flexibility, porosity and surface-area-to-volume ratio of the nanofibrous films favor them as fast and sensitive fluorescent sensors for the detection of nitroaromatic and benzoquinone vapors as well as of oxidizing metal ions. Moreover, 4-iodophenyl-substituted graphene was employed as structure-directing template for the fabrication of sandwich-like graphene-based CMP nanosheets that are characterized by high surface areas and large aspect ratios. Starting from these graphene/CMP hybrids, hierarchically porous carbon nanosheets are produced by pyrolysis of the carbon-rich G-CMPs at 800 ^{o}C. The obtained carbon materials show a very promising supercapacitor behavior, 48% higher relative to the corresponding porous carbons without the graphene template. The incorporated graphene scaffolds favor an effective inter/intra layer electron transport, resulting in an improved ion injection/extraction from or to the electrodes and an improved energy storage capacity.

3.4 Experimental

All reagents, unless otherwise stated, were obtained from commercial sources (Sigma Aldrich, Alfa Aesar and Acros) and were used without further purification.

3.4.1 Synthesis of 1,1,2,2-Tetrakis(4-bromophenyl)ethene (TBPE).

TBPE was synthesized from 4,4'-dibromobenzophenone using a literature procedure.[67] To a solution of 4,4'-dibromobenzophenone (1.7 g, 5 mmol) and zinc dust (0.78 g, 12 mmol) in 60 mL of anhydrous tetrahydrofuran (THF) $TiCl_4$ (1.15 g, 6 mmol) was added dropwise under nitrogen at -78 ^{o}C. After stirring for 30 min, the reaction mixture was warmed up to room temperature and finally refluxed overnight. The reaction mixture was cooled to room temperature and poured into water. The aqueous layer was extracted with chloroform and the combined organic phases were washed with saturated brine solution and water and dried over anhydrous magnesium sulfate. After filtration and solvent evaporation, the residue was purified by silica-gel

column chromatography using hexane/dichloromethane as eluent. White, solid TBPE was obtained (1.33 g, 82.1%). ^{1}H NMR (600 MHz, $CDCl_3$) δ (TMS, ppm): 7.29 (d, 8H), 6.88 (d, 8H). ^{13}C NMR (150 MHz, $CDCl_3$) δ(ppm): 141.48, 139.64, 132.73, 131.31, 121.30.

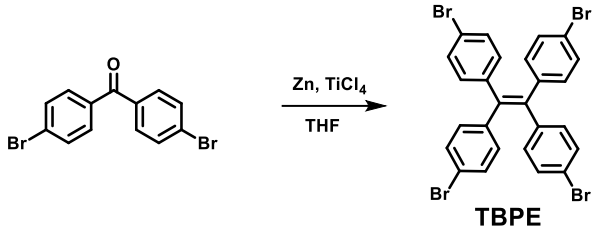

TBPE

3.4.2 Synthesis of 1,1,2,2-Tetrakis(4-ethynylphenyl)ethene (TEPE)

Synthesis of 4,4′-bis(trimethylsilylethynyl)benzophenone.[68] Into a 250 mL round-bottom flask $PdCl_2(PPh_3)_2$ (140.4 mg, 0.2 mmol), CuI (76.2 mg, 0.4 mmol), PPh_3 (157.4 mg, 0.6 mmol), 4,4'-dibromobenzophenone (1.7 g, 5 mmol), and finally a mixture of THF and triethylamine (TEA) (1:1 v/v) (50 mL) were added under nitrogen. After homogenization of the mixture, trimethylsilylacetylene (1.77 mL, 12.5 mmol) was injected. The solution was hold at 50 °C for 24 h, after which the formed solid was removed by filtration and washed with diethyl ether. The filtrate was concentrated by a rotary evaporator, and the crude product was purified by silica gel column chromatography using hexane/ethyl acetate mixture (v/v 100:1) as eluent. A white solid was obtained (1.81 g, 96.8%). ^{1}H NMR (400 MHz, $CDCl_3$) δ (TMS, ppm): 7.68 (d, 4H), 7.57 (d, 4H), 0.30 (s, 18H). ^{13}C NMR (100 MHz, $CDCl_3$) δ (ppm): 195.10, 136.76, 131.84, 129.79, 127.51, 103.99, 98.02, -0.17. MS (EI): m/z calcd 374.15; found 374.20.

Synthesis of 1,1,2,2-tetrakis[4-(trimethylsilylethynyl)phenyl]ethene. Into a 250 mL two-necked, round-bottom flask equipped with a reflux condenser 4,4'-bis(trimethylsilyl)benzophenone (1.78 g, 4.75 mmol) and zinc dust (0.932 g, 14.25 mmol) were placed. The flask was evacuated and flushed with dry nitrogen three times. After addition of THF (60 mL) $TiCl_4$ (1.37 g, 0.792 mL, 7.2 mmol) was dropped into the mixture under nitrogen at -78 °C. Next, the mixture was warmed up slowly to room temperature and refluxed overnight. After this the reaction mixture

was cooled to room temperature and poured into water. The aqueous layer was extracted with dichloromethane and the combined organic layers were washed with saturated brine solution and water and dried over anhydrous magnesium sulfate. After filtration and solvent evaporation, the crude product was purified by silica gel column chromatography using hexane as eluent. A white solid was obtained (1.56 g, 91.8%). ^{1}H NMR (600 MHz, $CDCl_3$) δ (TMS, ppm): 7.23 (d, 8H), 6.92 (d, 8H), 0.26 (s, 36H). ^{13}C NMR (150 MHz, $CDCl_3$) δ (ppm): 143.12, 140.85, 131.56, 131.18, 121.64, 104.96, 94.92, -0.07.

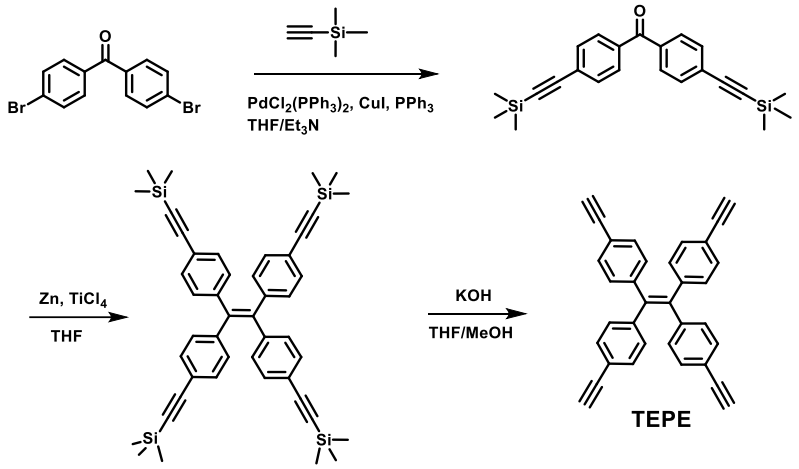

Synthesis of 1,1,2,2-tetrakis(4-ethynylphenyl)ethene (TEPE).[68] Into a 250 mL round-bottom flask 1,1,2,2-tetrakis[4-(trimethylsilylethynyl)phenyl]ethene (1.5 g, 2.1 mmol) and THF (40 mL) were placed. Then, KOH (1.8 g, 32 mmol) dissolved in 40 mL of methanol was added. The mixture was stirred at room temperature overnight. After most of the solvent was evaporated, 100 mL of 1 M aqueous HCl solution was added and the mixture extracted with dichlormethane (DCM) three times. The organic phases were combined and washed with water and brine and then dried over $MgSO_4$. After filtration and solvent evaporation, the crude product was purified by a silica gel column chromatography using hexane/DCM (100:1 by volume) mixture as eluent. TEPE was obtained as a pale yellow solid (0.84 g, 93.7%). ^{1}H NMR (600 MHz, $CDCl_3$) δ (TMS, ppm): 7.28 (d, 8H), 6.97 (d, 8H), 3.09 (s, 4H). ^{13}C NMR (150 MHz, $CDCl_3$) δ(ppm): 143.27, 140.86, 131.78, 131.20, 120.75, 83.46, 77.78. MS (EI): m/z calcd 428.15; found 428.20.

3.4.3 Synthesis of PTBPE and G-PTBPE

Synthesis of PTBPE. PTBPE was prepared in a Yamamoto-type coupling reaction according to a reported method.[15,69] 1,5-Cyclooctadiene (cod, 0.2 mL, 1.604 mmol) was added to bis(1,5-cyclooctadiene)nickel(0) ($Ni(cod)_2$, 442 mg, 1.604 mmol) and 2,2′-bipyridyl (252 mg, 1.604 mmol) in dehydrated DMF (10 mL), and the mixture was stirred for 1h at room temperature. To the resulting purple solution TBPE (200 mg, 0.308 mmol) dissolved in 10 mL of THF was added, and the mixture was stirred at room temperature for 72h to afford a deep purple suspension. Then, concentrated, aqueous HCl (8 mL) was added to the mixture. After filtration, the residue was washed with H_2O (3×50 mL), acetone (3×50 mL), $CHCl_3$ (3×50 mL), and THF (3×50 mL), extracted by Soxhlet-extration with H_2O, acetone, and THF for each 1 day, respectively. Finally, the product was dried under vacuum at room temperature for 24 h, to afford PTBPE as a yellow powder (yield: 98 mg).

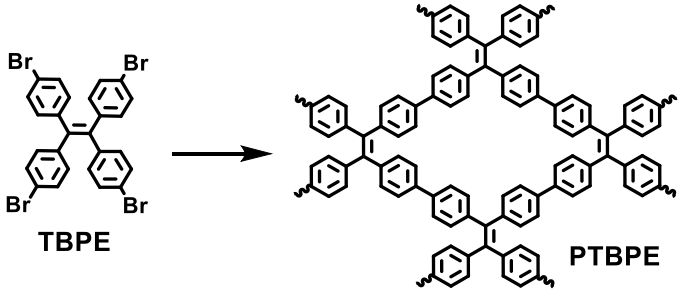

Synthesis of G-PTBPE. 1,5-Cyclooctadiene (cod, 0.2 mL, 1.604 mmol) was added to bis(1,5-cyclooctadiene)nickel(0) ([$Ni(cod)_2$], 442 mg, 1.604 mmol) and 2,2’-bipyridyl (252 mg, 1.604 mmol) in dehydrated DMF (6 mL). The mixture was stirred at room temperature for 1 h. A degassed solution of RGO-IBz (20 mg) in DMF (30 mL) was added to the reaction flask. To the resulting purple solution TBPE (200 mg, 0.308 mmol) in 18 mL of THF was added and the mixture was stirred at room temperature for 72h to afford a deep purple suspension. Then, concentrated, aqueous HCl (8 mL) was added to the mixture. After filtration, the residue was washed with H_2O (3×50 mL), acetone (3×50 mL) $CHCl_3$ (3×50 mL), and THF (3×50 mL), extracted by Soxhlet-extration with H_2O, acetone, and THF for each 1 day, respectively. Finally, the product was dried at room temperature under vacuum for 24

h, to afford G-PTBPE (yield: 114 mg).

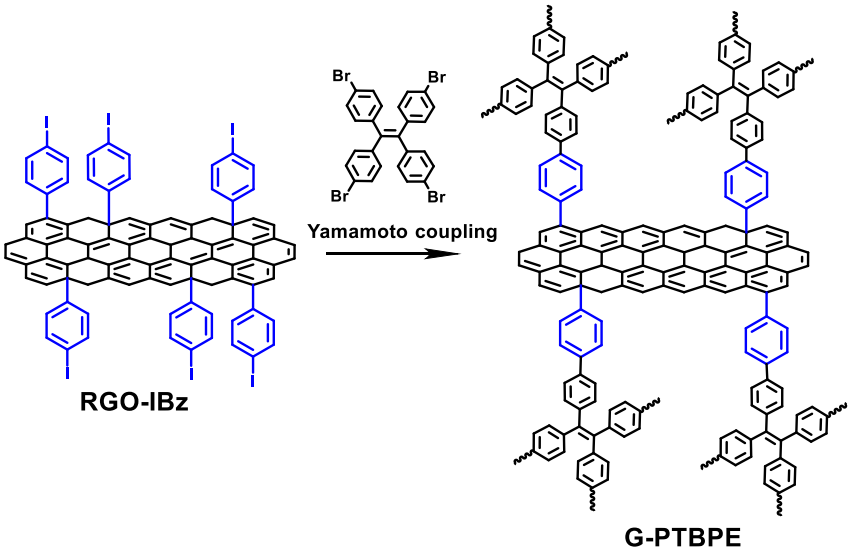

3.4.4 Synthesis of PTEPE-TBPE and G- PTEPE-TBPE

Synthesis of PTEPE-TBPE. 1,1,2,2-Tetrakis(4-ethynylphenyl)ethene (128 mg, 0.3 mmol), tetrakis(4-bromophenyl)ethene (194 mg, 0.3 mmol), tetrakis(triphenylphosphine) palladium (11 mg, 0.009 mmol), copper iodide (4.2 mg, 0.018 mmol) and Et_3N (5 mL) were added into a 250 mL flask. The reaction mixture was heated up to 140 °C, and stirred for 72 h under an N_2 atmosphere. The resulting insoluble product was filtered off and washed four times with chloroform, water, and acetone to remove unreacted monomers and catalyst residues. Further purification of the polymer networks was carried out by Soxhlet extraction with THF for 48 h. The product was dried at room temperature under vacuum for 24 h, to afford PTEPE-TBPE (yield: 223 mg).

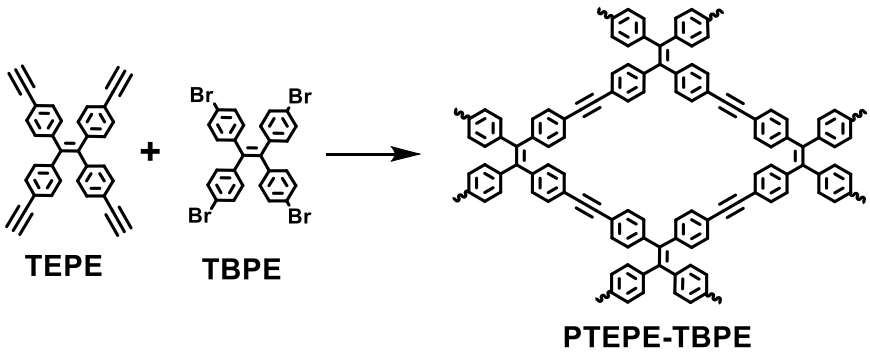

Synthesis of G-PTEPE-TBPE. First, RGO-IBz (60 mg) was sonicated in dry DMF (90 mL) until complete dispersion occured. Then, 1,1,2,2-tetrakis(4-ethynylphenyl)ethene (257 mg, 0.6 mmol), tetrakis(4-bromophenyl)ethene (322 mg, 0.5 mmol), tetrakis(triphenylphosphine) palladium (21 mg, 0.018 mmol), copper iodide (8.4 mg, 0.036 mmol) and Et_3N (5 mL) were added to the RGO-IBz dispersion. The reaction mixture was heated up to 140 °C, and stirred for 72 h under N_2 atmosphere. Next, the insoluble product was filtered off and washed four times with chloroform, water, and acetone to remove unreacted monomers and catalyst residues. Further purification of the polymer networks was carried out by Soxhlet extraction with THF for 48 h. The product was dried in vacuum for 24 h at room temperature, to afford G-TEPE-TBPE (yield: 416 mg).

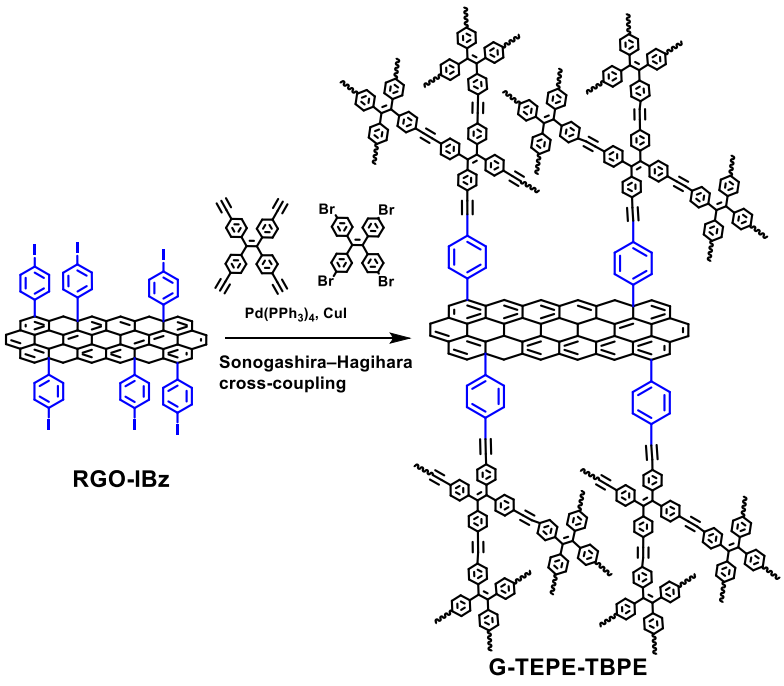

3.4.5 Characterization

NMR spectra were recorded on Bruker AVANCE 400 or AVANCE III 600 machines. ^{1}H and ^{13}C NMR spectra were measured with tetramethylsilane (TMS) as internal standard. Fourier transform infrared (FTIR) spectroscopy conducted on a JASCO FT/IR-4200 Fourier-transform-spectrometer. UV-Vis absorption spectra were recorded on a Shimadzu UV-2401 PC spectrophotometer at room temperature.

Fluorescence measurements were carried out on a Fluoromax-4 equipped with Quanta-Phi integration sphere (Horiba) at room temperature. The scanning electron microscopy (SEM) images were conducted by FEI on a Quanta-200F. The morphology of CMPs, G-CMPs and corresponding carbon materials were characterized by transmission electron microscopy (TEM, JEOL, JEM-2100F). The TEM samples were prepared by transferring CMPs, G-CMPs and corresponding carbon materials onto copper grids. Thermogravimetric analysis was performed on a Mettler Toledo TGA Stare System under argon flow. Raman spectra were recorded on a LabRAM HR Raman Microscope with an excitation wavelength of 514 nm. X-ray photoelectron spectroscopy (XPS) was carried out on a Kratos AXIS Ultra, performing at 15 kV and 15 mA with a monochromatic Al Kα source (hν = 1486.71 eV).

Nitrogen sorption measurements. The nitrogen adsorption-desorption measurements were performed on a BELSORB Max (BEL Japan Inc.). The surface areas were calculated using the BET model in the pressure range p/p_0 from 0.05-0.3. The total pore volume was determined at a relative pressure of 0.99. The pore size distribution was analyzed from the nitrogen adsorption data using the NLDFT method based on a slit pore model.

3.4.6 Chemosensing Experiments

First, vials with the solid analytes were placed in sealed glass flasks for 5 days to ensure that the equilibrium vapor pressure of the analytes is reached. Next, the electrospun nanofibrous PTBPE/PLA films were brought into the glass flasks for a specific time period for exposure to the vapors. The emission spectra were recorded without any delay by mounting the films on the sample holder for solids of the fluorescence spectrophotometer. The reference emission spectra of the nanofibrous PTBPE/PLA films were recorded before. For metal ions, the nanofibrous PTBPE/PLA films were placed in a quartz cuvette containing aqueous solution of the metal ions. The reference emission spectra were collected with deionized water.

For the recyclability test, the nanofibrous PTBPE/PLA films were exposed to the

analyte vapors, the emission spectra recorded, reduced pressure applied at 25 °C for 4 h to remove the absorbed analytes, the samples re-equilibrated in air for 30 min in the dark, and then utilized for the next around of detection.

3.4.7 Electrochemical Measurements and Caculations

The electrochemical experiments were carried out using a conventional, aqueous three-electrode system employing 6 M aqueous KOH as electrolyte at room temperature. The three-electrode cell incorporated an Ag/AgCl as reference electrode, Pt wire as the counter electrode and the active, porous carbon or carbon nanosheet materials as working electrode. The working electrode was prepared by loading active materials onto a glassy carbon electrode. Thereby, the porous carbon or carbon nanosheet material was dispersed in water by sonication under formation of a homogeneous dispersion (1 mg/mL). Next, 6 μL of the dispersion were loaded onto a glassy carbon electrode with a diameter of 5 mm. The modified electrode was slowly dried in air until a uniform layer was formed at the electrode surface. The following cyclic voltammetry (CV) and galvanostatic charge/discharge (GCD) measurements were performed using a PAR VersaSTAT 4 electrochemical workstation within the voltage range from -1 to 0 V.

The specific capacitance was calculated by the following equation:

$$C = I \Delta t / m \Delta V$$

where C (F/g) is the specific capacitance, I (mA) the discharge current, and Δt (s), m (mg), and ΔV (V) the total discharge time, the mass of active material, and the potential drop (by excluding the voltage (IR) drop) during discharge, respectively.

3.5 References

(1) Yuan, K.; Guo-Wang, P.; Hu, T.; Shi, L.; Zeng, R.; Forster, M.; Pichler, T.; Chen, Y.; Scherf, U. *Chem. Mater.* **2015**, *27*, 7403-7411.

(2) Cooper, A. I. *Adv. Mater.* **2009**, *21*, 1291-1295.

(3) Xu, Y.; Jin, S.; Xu, H.; Nagai, A.; Jiang, D. *Chem. Soc. Rev.* **2013**, *42*,

8012-8031.

(4) Jiang, J.-X.; Su, F.; Trewin, A.; Wood, C. D.; Campbell, N. L.; Niu, H.; Dickinson, C.; Ganin, A. Y.; Rosseinsky, M. J.; Khimyak, Y. Z.; Cooper, A. I. *Angew. Chem., Int. Ed.* **2007**, *46*, 8574-8578.

(5) Wu, D.; Xu, F.; Sun, B.; Fu, R.; He, H.; Matyjaszewski, K. *Chem. Rev.* **2012**, *112*, 3959-4015.

(6) Dawson, R.; Cooper, A. I.; Adams, D. J. *Prog. Polym. Sci.* **2012**, *37*, 530-563.

(7) Schmidt, J.; Werner, M.; Thomas, A. *Macromolecules.* **2009**, *42*, 4426-4429.

(8) Chen, Q.; Luo, M.; Hammershøj, P.; Zhou, D.; Han, Y.; Laursen, B. W.; Yan, C.-G.; Han, B.-H. *J. Am. Chem. Soc.* **2012**, *134*, 6084-6087.

(9) Dawson, R.; Stockel, E.; Holst, J. R.; Adams, D. J.; Cooper, A. I. *Energy Environ. Sci.* **2011**, *4*, 4239-4245.

(10) Chen, Q.; Liu, D.-P.; Luo, M.; Feng, L.-J.; Zhao, Y.-C.; Han, B.-H. *Small* **2014**, *10*, 308-315.

(11) Du, R.; Zhang, N.; Xu, H.; Mao, N.; Duan, W.; Wang, J.; Zhao, Q.; Liu, Z.; Zhang, J. *Adv. Mater.* **2014**, *26*, 8053-8058.

(12) Liu, X.; Xu, Y.; Jiang, D. *J. Am. Chem. Soc.* **2012**, *134*, 8738-8741.

(13) Gu, C.; Huang, N.; Gao, J.; Xu, F.; Xu, Y.; Jiang, D. *Angew. Chem., Int. Ed.* **2014**, *53*, 4850-4855.

(14) Chen, L.; Honsho, Y.; Seki, S.; Jiang, D. *J. Am. Chem. Soc.* **2010**, *132*, 6742-6748.

(15) Xu, Y.; Chen, L.; Guo, Z.; Nagai, A.; Jiang, D. *J. Am. Chem. Soc.* **2011**, *133*, 17622-17625.

(16) Xu, Y.; Nagai, A.; Jiang, D. *Chem. Commun.* **2013**, *49*, 1591-1593.

(17) Xie, Y.; Wang, T. T.; Liu, X. H.; Zou, K.; Deng, W. Q. *Nat. Commun.* **2013**, *4*, 1960.

(18) Zhuang, X.; Zhang, F.; Wu, D.; Forler, N.; Liang, H.; Wagner, M.; Gehrig, D.; Hansen, M. R.; Laquai, F.; Feng, X. *Angew. Chem., Int. Ed.* **2013**, *52*, 9668-9672.

(19) Zhang, Y.; Riduan, S. N. *Chem. Soc. Rev.* **2012**, *41*, 2083-2094.

(20) Xu, F.; Chen, X.; Tang, Z.; Wu, D.; Fu, R.; Jiang, D. *Chem. Commun.* **2014**, *50*, 4788-4790.

(21) Kou, Y.; Xu, Y.; Guo, Z.; Jiang, D. *Angew. Chem., Int. Ed.* **2011**, *50*, 8753-8757.

(22) Ma, B. C.; Ghasimi, S.; Landfester, K.; Vilela, F.; Zhang, K. A. I. *J. Mater. Chem. A* **2015**, *3*, 16064-16071.

(23) Xiang, Z.; Sun, H.; Zhu, Z.; Liang, W.; Yang, B.; Li, A. *RSC Adv.* **2015**, *5*, 24893-24898.

(24) Feng, X.; Liang, Y.; Zhi, L.; Thomas, A.; Wu, D.; Lieberwirth, I.; Kolb, U.; Müllen, K. *Adv. Funct. Mater.* **2009**, *19*, 2125-2129.

(25) Kang, N.; Park, J. H.; Choi, J.; Jin, J.; Chun, J.; Jung, I. G.; Jeong, J.; Park, J.-G.; Lee, S. M.; Kim, H. J.; Son, S. U. *Angew. Chem., Int. Ed.* **2012**, *51*, 6626-6630.

(26) Zhuang, X.; Gehrig, D.; Forler, N.; Liang, H.; Wagner, M.; Hansen, M. R.; Laquai, F.; Zhang, F.; Feng, X. *Adv. Mater.* **2015**, *27*, 3789-3796.

(27) Gu, C.; Chen, Y.; Zhang, Z.; Xue, S.; Sun, S.; Zhang, K.; Zhong, C.; Zhang, H.; Pan, Y.; Lv, Y.; Yang, Y.; Li, F.; Zhang, S.; Huang, F.; Ma, Y. *Adv. Mater.* **2013**, *25*, 3443-3448.

(28) Gu, C.; Huang, N.; Wu, Y.; Xu, H.; Jiang, D. *Angew. Chem., Int. Ed.* **2015**, *54*, 11540-11544.

(29) Palma-Cando, A.; Scherf, U. *ACS Appl. Mater. Interfaces* **2015**, *7*, 11127-11133.

(30) Zhuang, X.; Zhang, F.; Wu, D.; Feng, X. *Adv. Mater.* **2014**, *26*, 3081-3086.

(31) Wang, X.; Drew, C.; Lee, S.-H.; Senecal, K. J.; Kumar, J.; Samuelson, L. A. *Nano Lett.* **2002**, *2*, 1273-1275.

(32) Wang, Y.; La, A.; Ding, Y.; Liu, Y.; Lei, Y. *Adv. Funct. Mater.* **2012**, *22*, 3547-3555.

(33) Hong, Y.; Lam, J. W. Y.; Tang, B. Z. *Chem. Soc. Rev.* **2011**, *40*, 5361-5388.

(34) Zhao, Z.; Chen, S.; Shen, X.; Mahtab, F.; Yu, Y.; Lu, P.; Lam, J. W. Y.; Kwok, H. S.; Tang, B. Z. *Chem. Commun.* **2010**, *46*, 686-688.

(35) Wang, M.; Zhang, G.; Zhang, D.; Zhu, D.; Tang, B. Z. *J. Mater. Chem.* **2010**, *20*, 1858-1867.

(36) Yuan, W. Z.; Zhao, H.; Shen, X. Y.; Mahtab, F.; Lam, J. W. Y.; Sun, J. Z.; Tang,

B. Z. *Macromolecules.* **2009**, *42*, 9400-9411.

(37) Tong, H.; Hong, Y.; Dong, Y.; Hau; Lam, J. W. Y.; Li, Z.; Guo, Z.; Guo, Z.; Tang, B. Z. *Chem. Commun.* **2006**, 3705-3707.

(38) Yuan, K.; Xu, Y.; Uihlein, J.; Brunklaus, G.; Shi, L.; Heiderhoff, R.; Que, M.; Forster, M.; Chasse, T.; Pichler, T.; Riedl, T.; Chen, Y.; Scherf, U. *Adv. Mater.* **2015**, *27*, 6714-6721.

(39) Chan, C. Y. K.; Lam, J. W. Y.; Deng, C.; Chen, X.; Wong, K. S.; Tang, B. Z. *Macromolecules.* **2015**, *48*, 1038-1047.

(40) Zhou, H.; Li, J.; Chua, M. H.; Yan, H.; Tang, B. Z.; Xu, J. *Polymer Chemistry* **2014**, *5*, 5628-5637.

(41) Preis, E.; Dong, W.; Brunklaus, G.; Scherf, U. *J. Mater. Chem. C* **2015**, *3*, 1582-1587.

(42) Su, Y.; Liu, Y.; Liu, P.; Wu, D.; Zhuang, X.; Zhang, F.; Feng, X. *Angew. Chem., Int. Ed.* **2015**, *54*, 1812-1816.

(43) Sun, Y.; Li, C.; Shi, G. *J. Mater. Chem.* **2012**, *22*, 12810-12816.

(44) Li, X. J.; Xing, W.; Zhou, J.; Wang, G. Q.; Zhuo, S. P.; Yan, Z. F.; Xue, Q. Z.; Qiao, S. Z. *Chem. Eur. J.* **2014**, *20*, 13314-13320.

(45) Yang, X.; Zhuang, X.; Huang, Y.; Jiang, J.; Tian, H.; Wu, D.; Zhang, F.; Mai, Y.; Feng, X. *Polym. Chem.* **2015**, *6*, 1088-1095.

(46) Yuan, W.; Liu, A.; Huang, L.; Li, C.; Shi, G. *Adv. Mater.* **2013**, *25*, 766-771.

(47) Ferrari, A. C.; Basko, D. M. *Nat. Nanotechnol.* **2013**, *8*, 235-246.

(48) Ferrari, A. C.; Meyer, J. C.; Scardaci, V.; Casiraghi, C.; Lazzeri, M.; Mauri, F.; Piscanec, S.; Jiang, D.; Novoselov, K. S.; Roth, S.; Geim, A. K. *Phys. Rev. Lett.* **2006**, *97*, 187401.

(49)Zhang, L.; Zhang, F.; Yang, X.; Long, G.; Wu, Y.; Zhang, T.; Leng, K.; Huang, Y.; Ma, Y.; Yu, A.; Chen, Y. *Sci. Rep.* **2013**, *3*, 1408.

(50) Aboutalebi, S. H.; Chidembo, A. T.; Salari, M.; Konstantinov, K.; Wexler, D.; Liu, H. K.; Dou, S. X. *Energy Environ. Sci.* **2011**, *4*, 1855-1865.

(51) Zhang, J.; Jiang, J.; Li, H.; Zhao, X. S. *Energy Environ. Sci.* **2011**, *4*, 4009-4015.

(52) Gong, J.; Michalkiewicz, B.; Chen, X.; Mijowska, E.; Liu, J.; Jiang, Z.; Wen, X.;

Tang, T. *ACS Sustainable Chem. Eng.* **2014**, *2*, 2837-2844.

(53) Li, P.; Xing, C.; Qu, S.; Li, B.; Shen, W. *ACS Sustainable Chem. Eng.* **2015**, *3*, 1434-1442.

(54) Mai, L. Q.; Minhas-Khan, A.; Tian, X.; Hercule, K. M.; Zhao, Y. L.; Lin, X.; Xu, X. *Nat. Commun.* **2013**, *4*, 2923.

(55) Zhu, Y.; Murali, S.; Stoller, M. D.; Ganesh, K. J.; Cai, W.; Ferreira, P. J.; Pirkle, A.; Wallace, R. M.; Cychosz, K. A.; Thommes, M.; Su, D.; Stach, E. A.; Ruoff, R. S. *Science* **2011**, *332*, 1537-1541.

(56) Fan, X. M.; Yu, C.; Yang, J.; Ling, Z.; Hu, C.; Zhang, M. D.; Qiu, J. S. *Adv. Energy Mater.* **2015**, *5*, 1401761.

(57) Yun, Y. S.; Cho, S. Y.; Shim, J.; Kim, B. H.; Chang, S.-J.; Baek, S. J.; Huh, Y. S.; Tak, Y.; Park, Y. W.; Park, S.; Jin, H.-J. *Adv. Mater.* **2013**, *25*, 1993-1998.

(58) Zhang, L.; Candelaria, S. L.; Tian, J.; Li, Y.; Huang, Y.-x.; Cao, G. *J. Power Sources* **2013**, *236*, 215-223.

(59) Zhao, Z.; Hao, S.; Hao, P.; Sang, Y.; Manivannan, A.; Wu, N.; Liu, H. *J. Mater. Chem. A* **2015**, *3*, 15049-15056.

(60) Balducci, A.; Dugas, R.; Taberna, P. L.; Simon, P.; Plée, D.; Mastragostino, M.; Passerini, S. *J. Power Sources* **2007**, *165*, 922-927.

(61) Kong, C.; Qian, W.; Zheng, C.; Yu, Y.; Cui, C.; Wei, F. *Chem. Commun.* **2013**, *49*, 10727-10729.

(62) Lei, Z.; Christov, N.; Zhao, X. S. *Energy Environ. Sci.* **2011**, *4*, 1866-1873.

(63) Ramasahayam, S. K.; Hicks, Z.; Viswanathan, T. *ACS Sustainable Chem. Eng.* **2015**, *3*, 2194-2202.

(64) Gao, F.; Shao, G.; Qu, J.; Lv, S.; Li, Y.; Wu, M. *Electrochim. Acta* **2015**, *155*, 201-208.

(65) Li, Z.; Wu, D.; Liang, Y.; Fu, R.; Matyjaszewski, K. *J. Am. Chem. Soc.* **2014**, *136*, 4805-4808.

(66) Subramanian, N.; Viswanathan, B. *RSC Adv.* **2015**, *5*, 63000-63011.

(67) Chang, Z.; Jiang, Y.; He, B.; Chen, J.; Yang, Z.; Lu, P.; Kwok, H. S.; Zhao, Z.; Qiu, H.; Tang, B. Z. *Chem. Commun.* **2013**, *49*, 594-596.

(68) Wang, J.; Mei, J.; Zhao, E.; Song, Z.; Qin, A.; Sun, J. Z.; Tang, B. Z. *Macromolecules.* **2012**, *45*, 7692-7703.

(69) Yuan, D.; Lu, W.; Zhao, D.; Zhou, H.-C. *Adv. Mater.* **2011**, *23*, 3723-3725.

Chapter 4

Engineering the Morphology of Carbon Materials: 2D Porous Carbon Nanosheets for High Performance Supercapacitors[1]

4.1 Introduction

Driven by environmental and energy problems, the development of powerful and safe energy storage devices is of outstanding importance. Supercapacitors, have gained considerable attention and are considered as promising candidates for advanced electrical energy storage devices. This is attributed to features as high power density, rapid charging/discharging rate (charging times of seconds to minutes), high reliability, and exceptional cycling stability.[2-6] However, most supercapacitors show an only moderate energy density. Improvements of the energy density without losses in power density while maintaining a high cycling stability are considered as major challenge in the field. Two approaches to improve the energy density are often discussed, i.e., increasing the capacitance or/and the operational voltage (primarily limited by the electrolyte). The capacitance is mainly controlled by the electrode materials and is strongly related to the accessible specific surface area at the electrode/electrolyte interface and the transport kinetics of ions and electrons.[7] Generally, an ideal supercapacitor electrode material should characterized by a clever combination of unique physical and chemical properties: (i) occurrence of a hierarchical porous structure with high specific surface and well-balanced pore size distribution for an optimum ion-accessible surface and efficient charge storage, (ii) high electrical conductivity and minimum charge transfer resistance for high power density and rate capability, and (iii) superior compatibility with the electrolyte and good corrosion resistance for maximizing the ion-accessible surface area and ion diffusion as well as for improving the device stability.[5,7-9]

Graphene, a planar monolayer composed of sp^2-hybridized carbon atoms arranged in a honey comb network with highly delocalized π-electrons is characterized by a very high electrical conductivity. Combined with its high specific surface area and superior mechanical and chemical properties, graphene-based supercapacitor electrodes allow rapid charging/discharging and facilitate propagation of electrolyte ions.[10,11] Therefore, graphene materials are regarded as a very promising electrode materials for supercapacitors. However, the planar graphene sheets tend to restack driven by strong π-π interactions and van der Waals-forces between adjacent sheets under conversion into graphite-like structure.[12,13] This aggregation strongly reduces the specific surface area and leads to a significant decrease in the ion-accessible surface area, thus resulting in an inevitable deteriorated supercapacitor performance.[7] Hence, various strategies have been explored to prohibit the restacking of graphene layers, such as designing 3D graphene materials, introducing a second component between the neighboring graphene layers or preparing graphene based hybrid composites (graphene/polymer and graphene/transition metal oxides).[6,10,14,15] However, the complex procedures for the generation these materials, and poor rate and/or cycling performances are still critical problems that limit their application.

On the other hand, conjugated microporous polymers (CMPs) as a subclass of porous polymer materials got much attention due to their attractive set of properties such as high porosity with large specific surface area and controllable pore size by tuning the building blocks (tectons).[16-18] Heteroatoms (B, N, S and P) can be introduced into the CMP networks in a controlled fashion by using heteroatom-containing tectons. The CMPs can serve as potential precursor for the generation of hierarchical porous carbon materials by pyrolysis, as demonstrated in the pioneering work by Feng and co-workers.[19-21] Compared with traditional porous carbons, two-dimensional (2D), graphene-based porous carbon sheets with a continuous pore structure are very promising candidates for supercapacitor electrode materials. Thereby, a high aspect ratio, i.e. introduced by graphene templates,

facilitates a dense packing and supports the charge transport, the high specific surface area and hierarchical pore structure improves the ion transport, and the increased ion-accessible surface area reduces the average ion-transport length.[22] However, the fabrication of porous carbon materials with 2D sheet structure starting from CMPs remains challenging since the CMPs are formed under kinetic control, coupled to problems in the control of the resulting nanostructures.[19,21-23]

In this chapter, a graphene-inspired synthetic strategy was employed to prepare well-defined sandwich-like graphene-based conjugated microporous polymers (G-CMPs). In the G-CMPs, chemically modified graphene templates (RGO-I) are decorated with porous CMP shells. Our strategy effectively solves the aggregation problem of non-substituted graphene sheets. Moreover, our G-CMPs can be pyrolytically converted into porous carbon materials with maintained 2D morphology. Carbon nanosheet-based supercapacitors showed high specific capacitance as well as good rate capability and excellent cycling stability.

4.2 Results and Discussion

4.2.1 Synthesis of Graphene-Templated Conjugated Microporous Polymer Sandwiches (G-CMPs)

The strategy for the synthesis of the graphene-based conjugated microporous polymer sandwiches (G-CMPs) is illustrated in Figure 4.1. First, GO synthesized through a modified Hummers method was reduced with hydrazine hydrate (RGO) in the presence of sodium dodecylbenzene sulfonate and then functionalized with 4-iodophenyl diazonium salt under aqueous conditions.[19,24-27] The obtained 4-iodophenyl-functionalized RGO (RGO-I) can be well dispersed in various organic solvents including DMF, chlorobenzene and toluene. Next, arylacetylene building blocks (1,4-diethynylbenzene (DEB), 2,7-diethynyl-fluorene (DEF), or tris(4-ethynylphenyl)amine (TEPA)) were mixed with aryl halides (3,6-dibromocarbazole (C) or tris(4-bromophenyl)amine (TPA)) and RGO-I in anhydrous DMF in the presence of $Pd(PPh_3)_4$, CuI and Et_3N. Next, the reaction

mixture was reacted under Sonogashira-Hagihara reaction conditions. After filtration, black solids were collected and purified by Soxhlet extraction with THF for two days. Finally, sandwich-like G-CMPs were obtained after vacuum drying, denoted as G-DEB-TPA, G-DEB-C, G-DEF-TPA, G-DEF-C, G-TEPA-TPA and G-TEPA-C. For comparison, the corresponding conjugated microporous polymers without RGO-I were also synthesized using the same procedure, the obtained products are denoted as DEB-TPA, DEB-C, DEF-TPA, DEF-C, TEPA-TPA and TEPA-C.

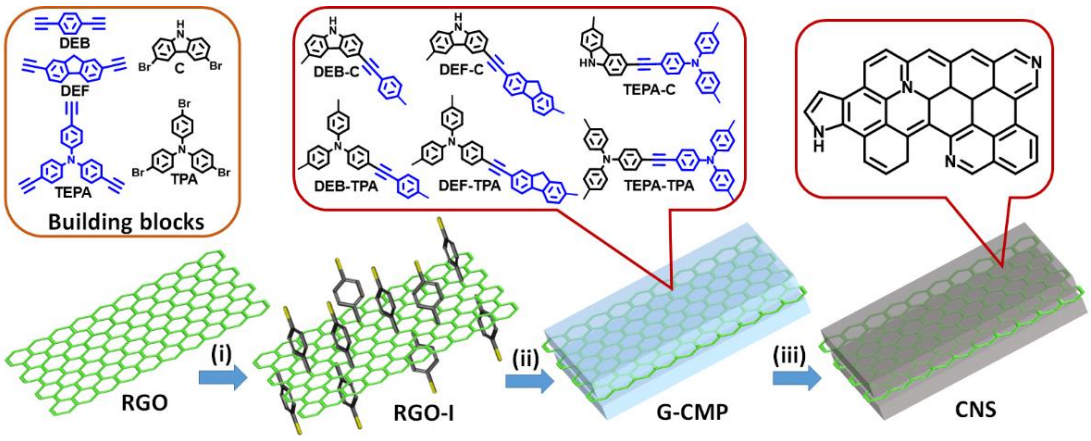

Figure 4.1 Schematic illustration of the synthesis of graphene-based porous conjugated micro-polymers (G-CMP), and corresponding porous carbon nanosheets (CNS) by pyrolysis. (i) 4-iodophenyl diazonium salt, 0 ^{o}C (2 h) to RT (4 h); (ii) building blocks: 1,4-diethynylbenzene (DEB), 2,7-diethynyl-fluorene (DEF), or tris(4-ethynylphenyl)amine (TEPA) and 3,6-dibromocarbazole (C), or tris(4-bromophenyl)amine (TPA), argon, $Pd(PPh_3)_4$, CuI, Et_3N, DMF, 140 ^{o}C, 3 days; (iii) argon, 10 ^{o}C min^{-1} , 800 ^{o}C, 2 h.

4.2.2 Structural Characterization of G-CMPs

The molecular structure of the G-CMPs was investigated by solid-state ^{13}C cross-polarization/magic angle spinning nuclear magnetic resonance (CP/MAS NMR) spectroscopy (Figures 4.2) and Fourier transform infrared (FTIR) spectroscopy (Figure 4.3). G-DEB-TPA is now discussed as a typical example (Figure 4.4A). The disappearance of the -C≡CH (at ca. 3270 cm^{-1}) and the C-Br stretching modes (ca. 1070 cm^{-1}) in the FTIR spectra of the G-CMPs indicate the occurrence of an efficient arylacetylene-aryl coupling. Moreover, diaryl alkyne peaks at 88-90 ppm are observed in the CP/MAS NMR spectrum of G-DEB-TPA, thus supporting the expected chemical structure. The G-CMPs were further investigated by X-ray

photoelectron spectroscopy (XPS, Figure 4.3D). All G-CMPs showed almost similar components (C, N and O, no Br). These results together suggest a high degree of conversion of functional groups in the RGO-I-templated synthesis of G-CMPs.

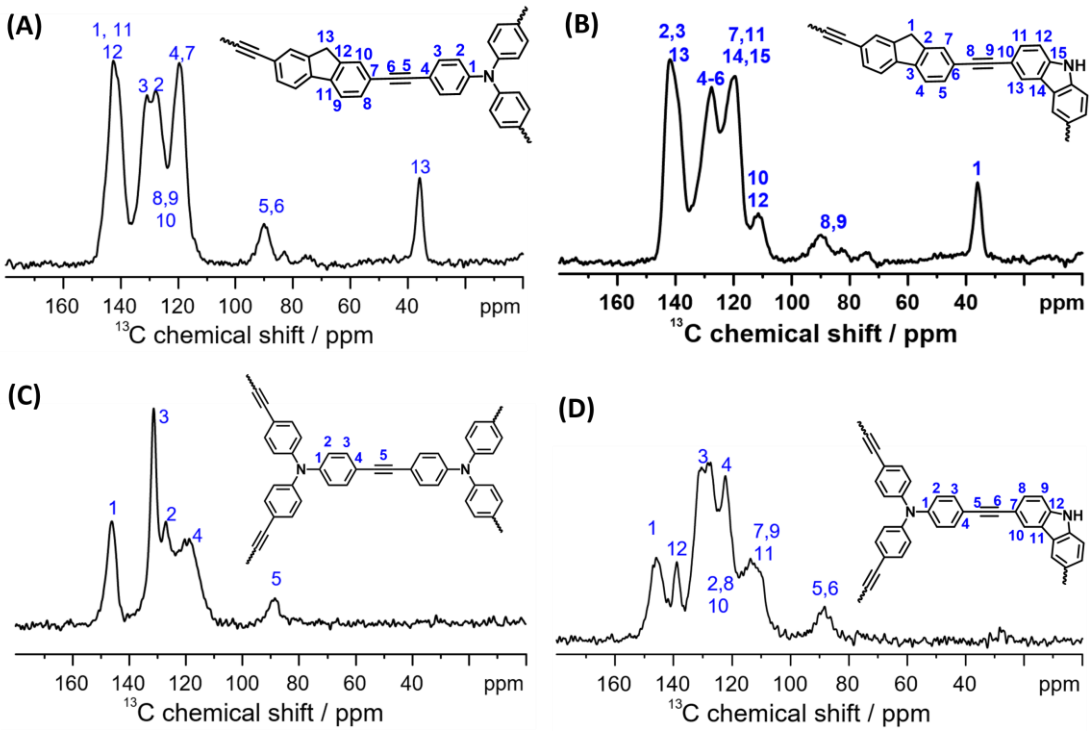

Figure 4.2 Solid-state ^{13}C CP/MAS NMR spectra of (A) G-DEF-TPA, (B) G-DEF-C, (C) G-TEPA-TPA and (D) G-TEPA-C.

4.2.3 Morphological Characterization of G-CMPs

Morphology and microstructure of the G-CMPs were investigated by SEM, TEM and HRTEM. As indicated by the SEM (Figure 4.5) and TEM (Figure 4.6) images, all G-CMPs show a similar sheet morphology, G-TEPA-TPA is discussed here as a typical example. The TEM images of G-TEPA-TPA (Figure 4.4B) sheets displays wrinkled features with a graphene-like morphology. No free porous polymer particles or "naked" graphene sheets were observed in the TEM images. This suggests that, as expected, most of the monomers have been grafted onto the surface of graphene. The microporous structure of the G-CMPs can be directly visualized by HRTEM showing that the micropores are very homogenously distributed (Figure 4.4C).

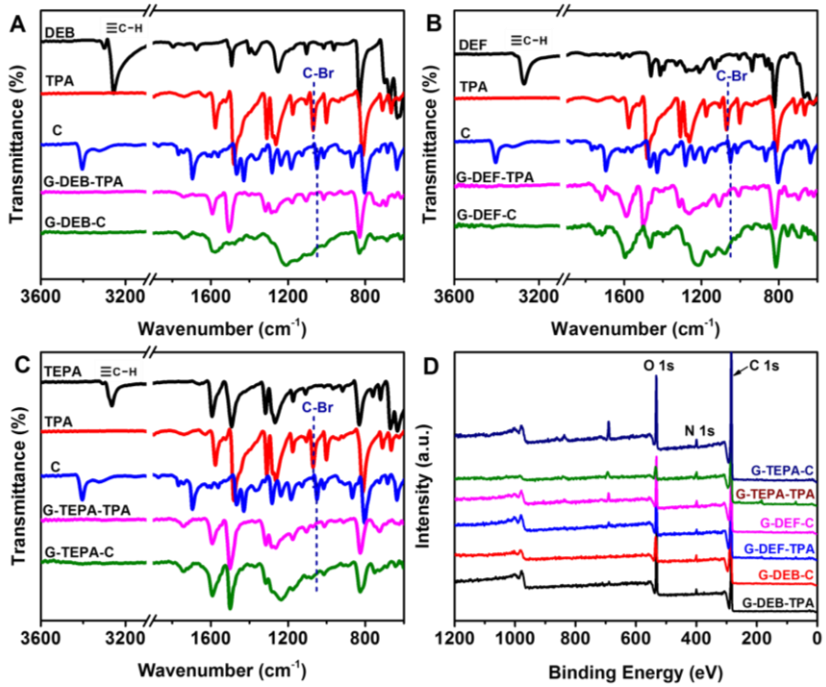

Figure 4.3 (A-C) FTIR spectra of the monomeric building blocks and the resulting G-CMPs. G-DEB-TPA, G-DEB-C, G-DEF-TPA, G-DEF-C, G-TEPA-TPA and G-TEPA-C. (D) Overview XPS spectra of G-DEB-TPA, G-DEB-C, G-DEF-TPA, G-DEF-C, G-TEPA-TPA and G-TEPA-C.

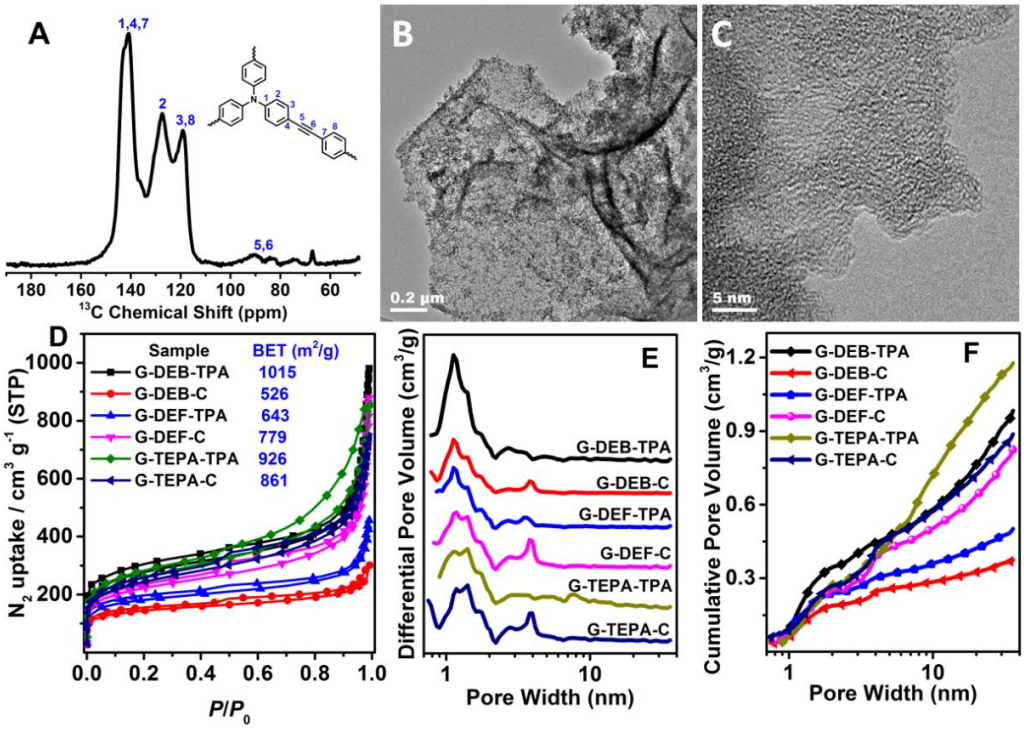

Figure 4.4 (A) Solid-state ^{13}C CP/MAS spectrum of G-DEB-TPA. (B) TEM and (C) HRTEM images of G-TEPA-TPA. (D) Nitrogen adsorption/desorption isotherms and corresponding BET surface areas, (E) NLDFT-based pore size distribution profiles, and (F) cumulative pore volumes of G-DEB-TPA, G-DEB-C, G-DEF-TPA, G-DEF-C, G-TEPA-TPA, and G-TEPA-C.

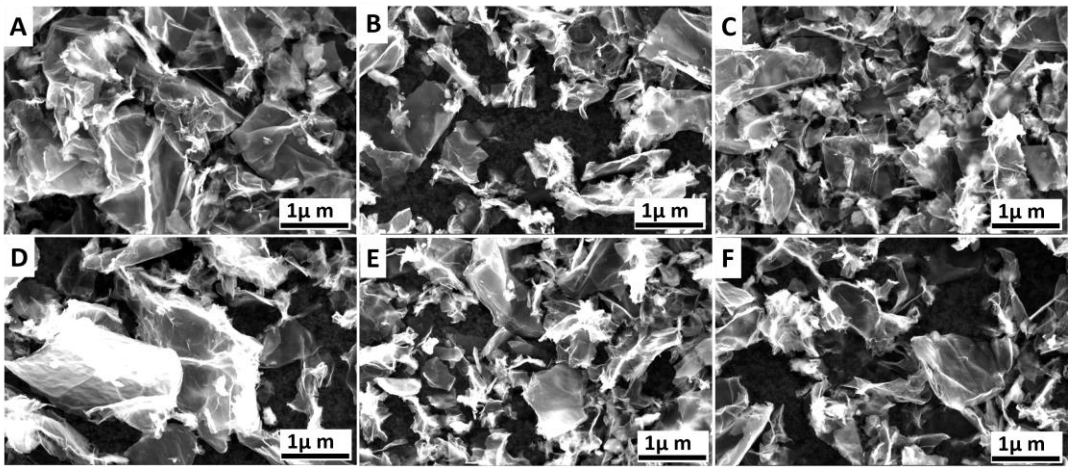

Figure 4.5 SEM images of (A) G-DEB-TPA, (B) G-DEB-C, (C) G-DEF-TPA, (D) G-DEF-C, (E) G-TEPA-TPA and (F) G-TEPA-C.

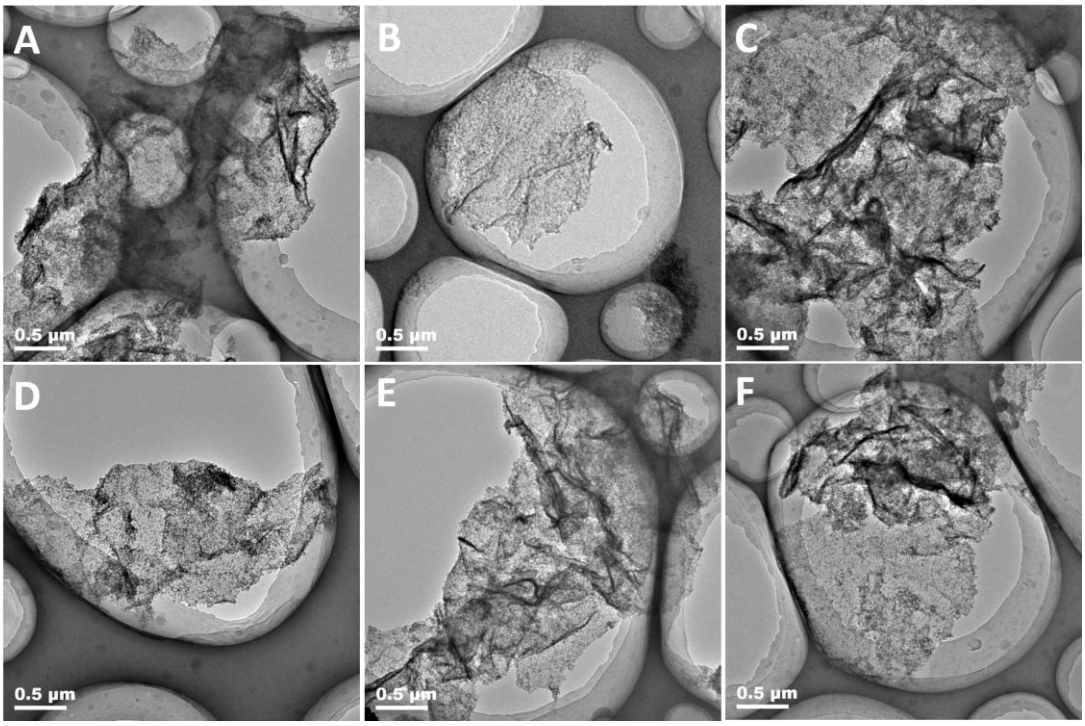

Figure 4.6 TEM images of (A) G-DEB-TPA, (B) G-DEB-C, (C) G-DEF-TPA, (D) G-DEF-C, (E) G-TEPA-TPA and (F) G-TEPA-C.

4.2.4 Porosity of CMPs and G-CMPs

The porosity of the G-CMPs and conjugated microporous polymers synthesized without RGO-I were examined by nitrogen adsorption/desorption measurements performed at 77 K (Figure 4.4D and Figure 4.7). The isotherms and the extracted Brunauer-Emmett-Teller (BET) surface areas of the G-CMPs are given in Figure 4.4D. All G-CMPs showed reversible isotherms that are characteristic of microporous materials, with BET surface areas of 1015, 526, 643, 779, 926 and 861 m^2/g for G-DEB-TPA, G-DEB-C, G-DEF-TPA, G-DEF-C, G-TEPA-TPA and G-TEPA-C, respectively. In the isotherms, the steep gas adsorption below p/p_0 = 0.1 and the hysteresis loops for high p/p_0 values indicate that both micro- and mesopores are present in the G-CMPs. This hierarchical pore structure can be unambiguously verified in a pore size distribution analysis (Figure 4.4E) as well as single-point pore volume calculations for different relative pressures (Figure 4.4F), by using a nonlocal density functional theory (NLDFT) approach.

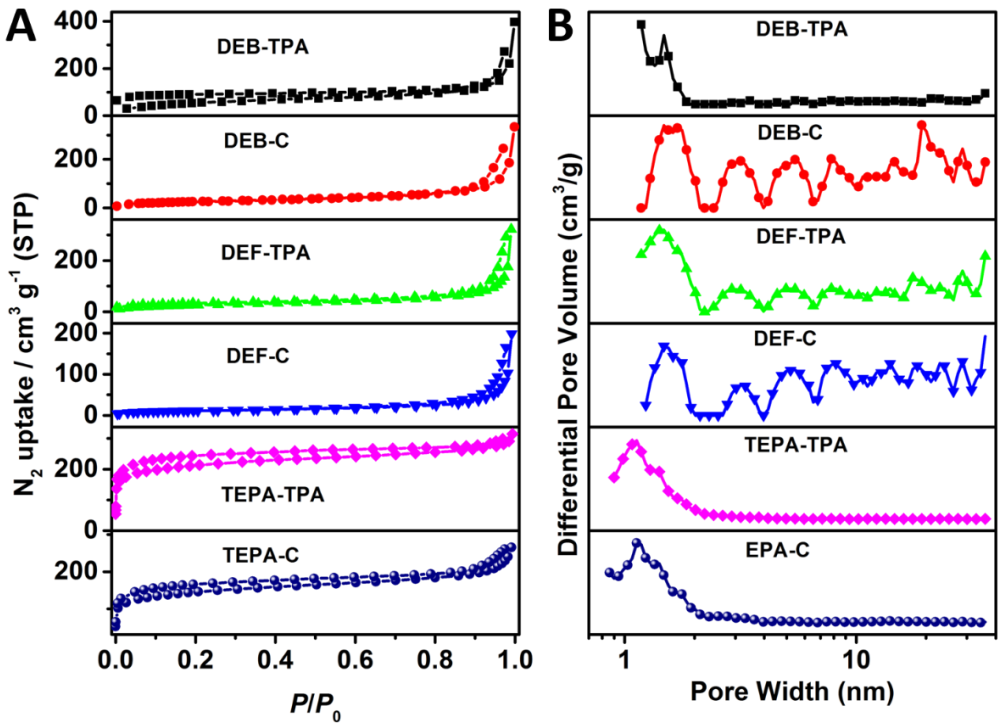

Figure 4.7. (A) Nitrogen adsorption/desorption isotherms and (B) NLDFT-based pore size distribution profiles for DEB-TPA, DEB-C, DEF-TPA, DEF-C, TEPA-TPA and TEPA-C.

4.2.5 Pyrolytic Generation and Characterization of CMPs- and G-CMPs-Derived Carbon Materials

The carbon-rich G-CMPs with their hierarchically pore structure can be used as precursors for a thermal conversion into carbon nanosheets. Such hierarchically porous carbon materials are discussed as potential candidates for various applications, such as gas storage/separation,[28] metal-free catalysts,[19,29] lithium ion batteries[30] and supercapacitors[19,20,31,32] as well as other energy conversion and storage.[33,34] Thermogravimetric analysis (TGA) confirmed that our G-CMPs can be pyrolyzed into porous carbon materials with high yields (77-87%, Figure 4.8), probably supported by the incorporation of the inherently thermostable graphene templates. The pyrolysis of G-CMPs (G-DEB-TPA, G-DEB-C, G-DEF-TPA, G-DEF-C, G-TEPA-TPA and G-TEPA-C) was carried out at 800 °C under argon atmosphere for 2 h. The resulting carbon materials are denoted as G-DEB-TPA-C, G-DEB-C-C, G-DEF-TPA-C, G-DEF-C-C, G-TEPA-TPA-C and G-TEPA-C-C, respectively.

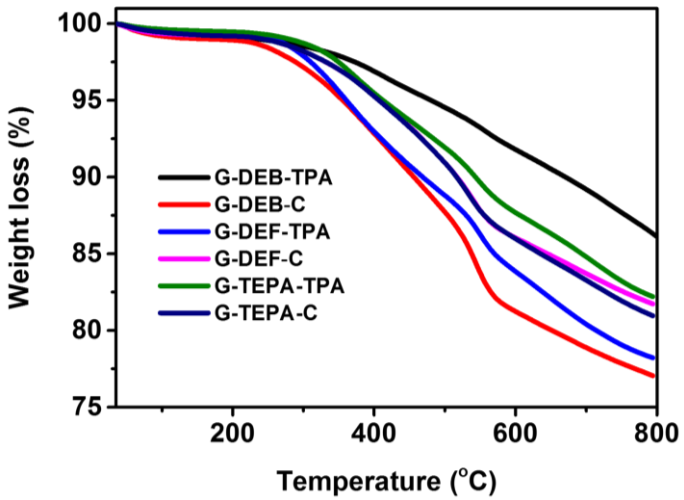

Figure 4.8 TGA profiles of G-DEB-TPA, G-DEB-C, G-DEF-TPA, G-DEF-C, G-TEPA-TPA and G-TEPA-C.

As example, the SEM and TEM images of G-TEPA-TPA-C (Figures 4.9A and Figure 4.10) indicate that the carbon material maintains the 2D nanostructure of the G-CMP precursor with its high large aspect ratio. The individual nanosheets are, thereby, ridged and wrinkled, as visualized in the HRTEM image of Figure 4.9B. Nitrogen adsorption/desorption isotherms (Figure 4.9C) again point for a

hierarchically porous structure of the carbon materials with BET surface areas of 719, 239, 552, 467, 764, and 493 m^2/g, respectively. The reduced BET surface area for the porous carbon nanosheets compared to the corresponding G-CMP precursors is attributed to the restructuring during pyrolysis of the polymeric precursors with a recombination of fragments during carbonization. The NLDFT-based pore size distributions (Figure 4.9D) and cumulative pore volumes (Figure 4.9E) indicate that both micro- and mesopores are present in our carbon materials. For comparison, porous carbons were also prepared by the same procedure from conjugated microporous polymer without RGO-I template, and are named as DEB-TPA-C, DEB-C-C, DEF-TPA-C, DEF-C-C, TEPA-TPA-C and TEPA-C-C, respectively. The nitrogen adsorption/desorption isotherms and NLDFT-based pore size distributions of these porous carbons are presented in Figure 4.11.

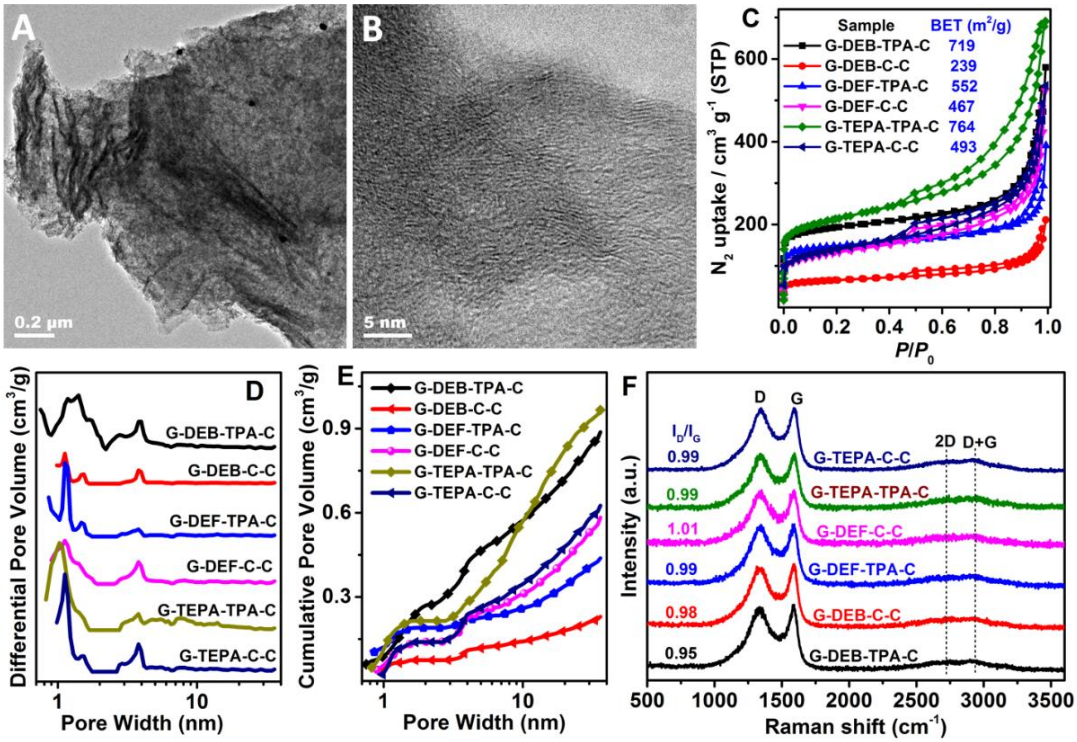

Figure 4.9 Characterization of graphene-based porous carbon nanosheets (CNSs). (A) TEM and (B) HRTEM images of G-TEPA-TPA-C. (C) Nitrogen adsorption/desorption isotherms and corresponding BET surface areas, (D) NLDFT-based pore size distribution profiles, (E) cumulative pore volumes, and (F) Raman spectra of G-DEB-TPA-C, G-DEB-C-C, G-DEF-TPA-C, G-DEF-C-C, G-TEPA-TPA-C, and G-TEPA-C-C.

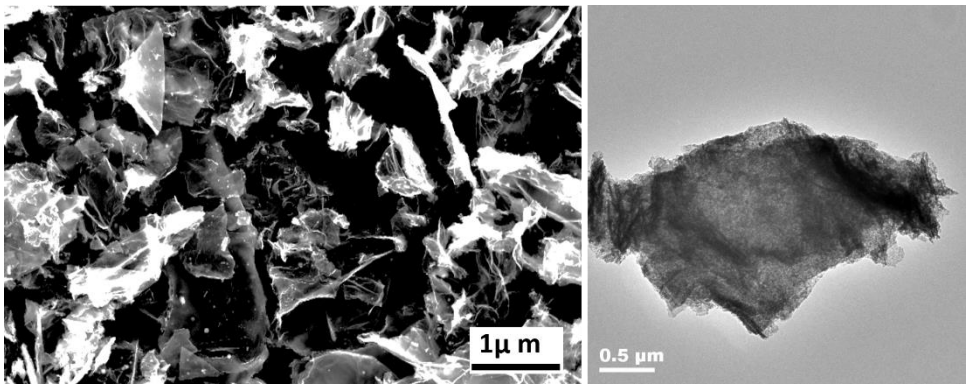

Figure 4.10 SEM (left) and TEM (right) images of G-TEPA-TPA-C.

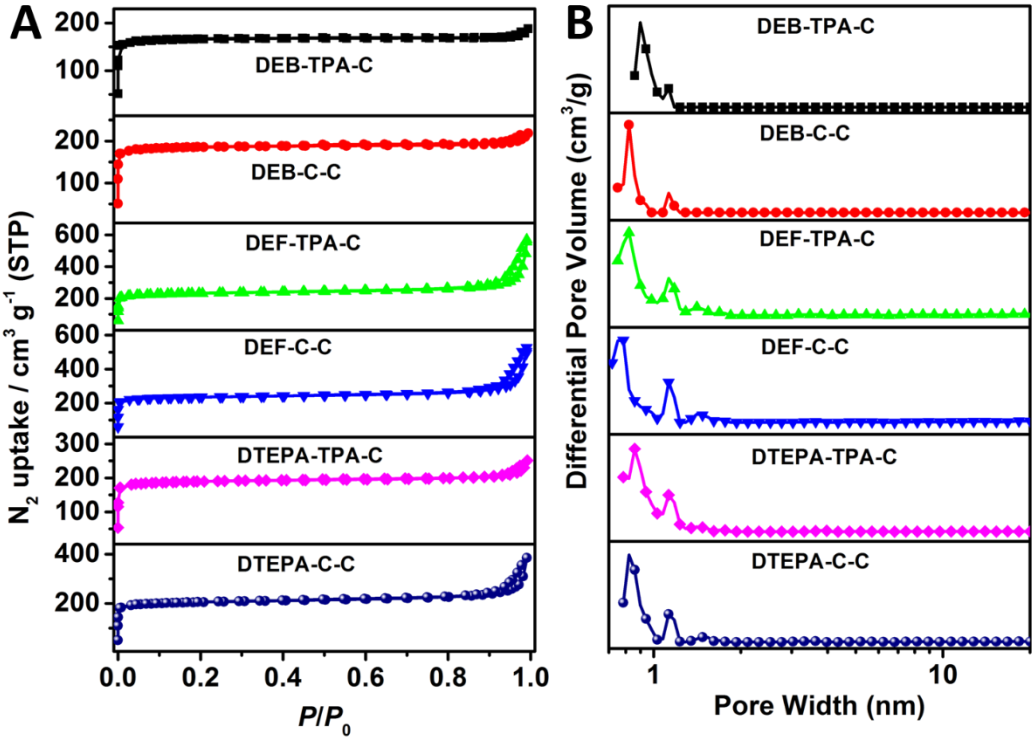

Figure 4.11 (A) Nitrogen adsorption/desorption isotherms and (B) NLDFT-based pore size distribution profiles for DEB-TPA-C, DEB-C-C, DEF-TPA-C, DEF-C-C, TEPA-TPA-C and TEPA-C-C.

Raman spectroscopy plays an important role in the structural characterization of carbon and graphene-based materials as fast, high resolution and non-destructive characterization tool.[35,36] Our porous carbon nanosheet materials all show two broad peaks (Figure 4.9F), i.e. a D-band (for disordered carbons) at ca. 1345 cm^{-1} and a

G-band (for sp^2-hybridized graphitic carbons) at ca. 1590 cm^{-1}. To investigate valence states and chemical nature of near the surface in our carbon nanosheets, XPS analysis was also carried out. The overview XPS spectra of our carbon nanosheets are presented in Figure 4.12A, C 1s, O 1s and N 1s signals can be seen. The most oxygen atoms should be introduced during carbonization or from absorbed oxygen or water molecules.[37] In the high resolution C 1s spectra (Figure 4.12B), the overwhelming strong peak at 284.6 eV (assigned to graphitic/graphenic carbons) demonstrats that most of the carbon atoms are sp^2-carbons.[38] The individual peaks at 285.7 eV, 286.2 eV and 288.5 eV were assigned to C-N, -C-OH and -C=O/-COOH species, respectively.[37,39,40] The N 1s spectra of our carbon nanosheet samples could be deconvoluted into two sub-peaks (Figure 4.12C), assigned to pyridinic (398.2 eV) and graphitic (401.2 eV) nitrogens,[41] thus confirming the effective doping of nitrogen atoms into the carbon lattice. Doping with nitrogen atoms can strongly affect the electron distribution of carbon materials, enhance wettability and electro-active surface area of corresponding electrode materials. Morover, nitrogens can also introduce pseudocapacitances (in aqueous supercapacitors), beneficial for enhancing the supercapacitor performance.[7,40,42]

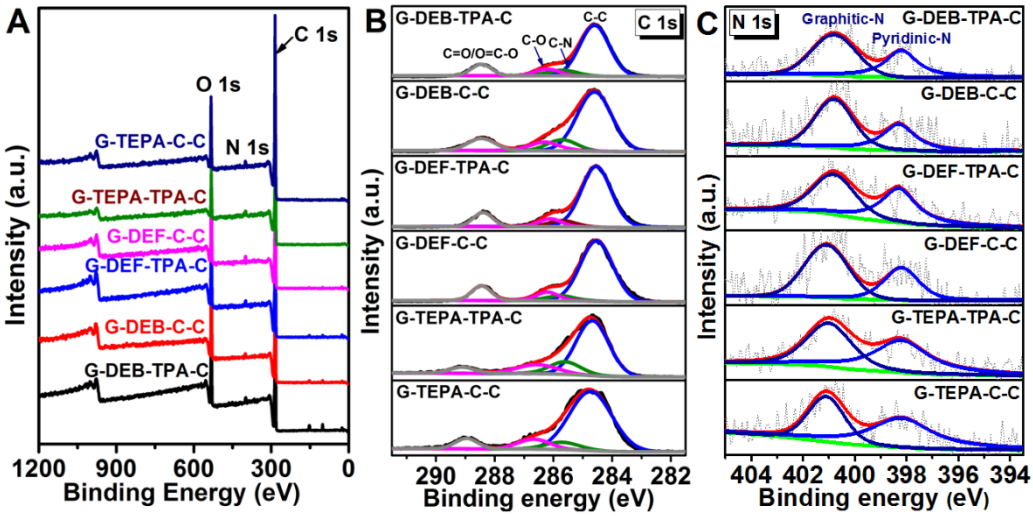

Figure 4.12 Overview (A) and high resolution XPS spectra, in the (B) C 1s, and (C) N 1s region of G-DEB-TPA-C, G-DEB-C-C, G-DEF-TPA-C, G-DEF-C-C, G-TEPA-TPA-C and G-TEPA-C-C.

4.2.6 Electrochemical Properties of Carbon Materials

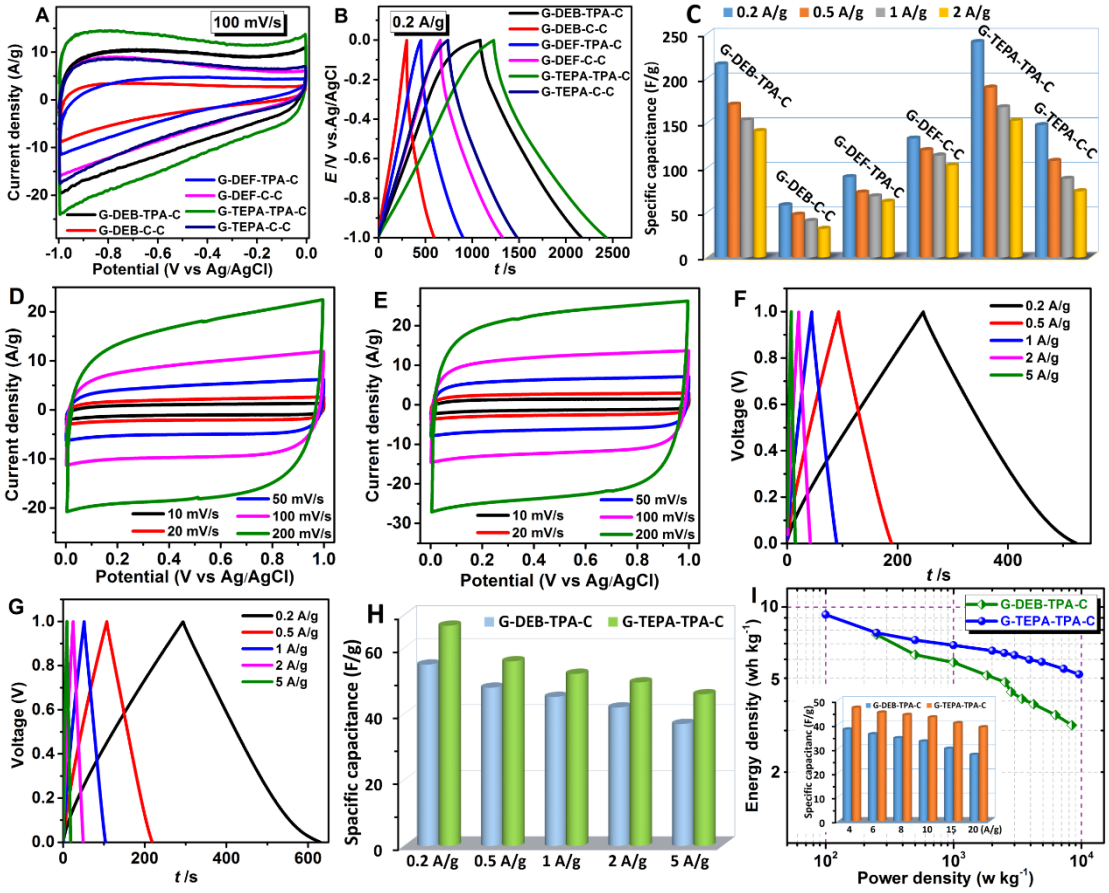

Figure 4.13 Electrochemical characterization of graphene-based CNSs (A-C, three-electrode system, D-I, two-electrode system) in 6 M aqueous KOH solution as electrolyte. (A) CV curves at a scan rate of 100 mv/s. (B) Galvanostatic charge/discharge (GCD) curves at a current density of 0.2 A/g. (C) Gravimetric capacitances at different charge/discharge current densities. CV curves of (D) G-DEB-TPA-C- and (E) G-TEPA-TPA-C-based supercapacitors at different scan rates. GCD curves of (F) G-DEB-TPA-C- and (G) G-TEPA-TPA-C-based supercapacitors at different current densities. (H) Gravimetric capacitances at different charge/discharge current densities. (I) Ragone plots of gravimetric energy density versus power density for G-DEB-TPA-C- and G-TEPA-TPA-C-based supercapacitors, the inset shows the corresponding specific capacitance values.

The unique porous structure of our carbon nanosheet materials seems promising for an application as electrode materials of supercapacitors. The electrochemical properties of our carbon nanosheets were first examined by cyclic voltammetry (CV) and galvanostatic charge-discharge (GCD) measurements in 6 M aqueous KOH solution in a three electrode cell. Figure 4.13A shows the CV curves of

supercapacitors at a scanning rate of 100 mV/s between -1 and 0 V. Electrodes made from our carbon nanosheet materials exhibit almost rectangular CV curves. Current density and enclosed CV area are best for G-TEPA-TPA-C as electrode materials thus indicating its good electrochemical performance and energy storage capability. When increasing the scan rate to 200 mV/s, the electrodes made from G-DEB-TPA-C and G-TEPA-TPA-C retain their rectangular CV profiles (Figure 4.14).

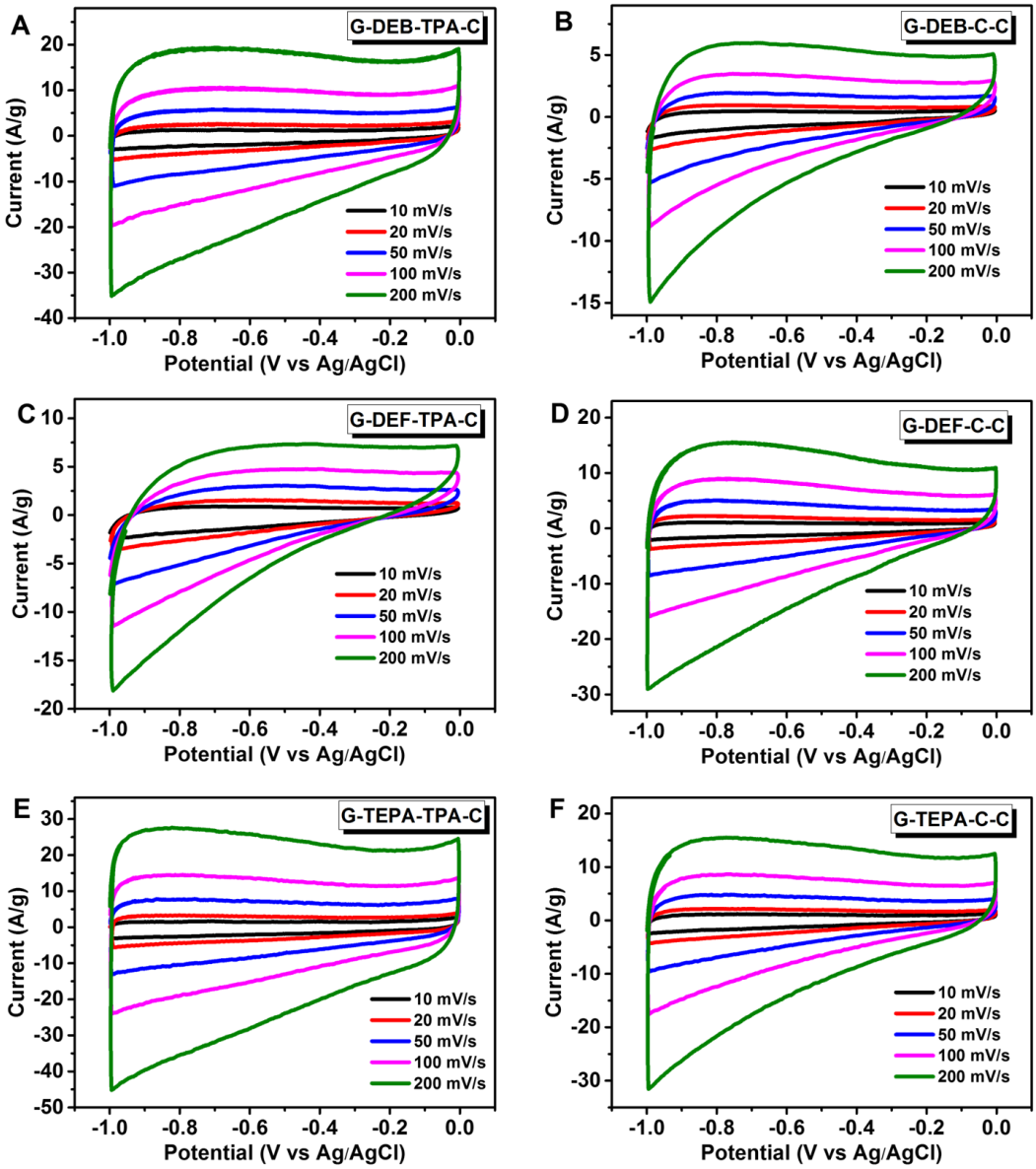

Figure 4.14 CV curves of graphene-based porous carbon nanosheets at different scan rates in a three-electrode system using 6 M aqueous KOH solution as electrolyte.

Figure 4.13B shows the GCD curves for a current density of 0.2 A/g, Figure 4.15 presents GCD curves at different current densities. The specific capacitances are summarized in Figure 4.13C. The calculated, specific capacitance values are 216, 58, 90, 133, 241 and 148 F/g for a current density of 0.2 A/g for G-DEB-TPA-C, G-DEB-C-C, G-DEF-TPA-C, G-DEF-C-C, G-TEPA-TPA-C and G-TEPA-C-C, respectively. Notably, G-DEB-TPA-C and G-TEPA-TPA-C show the highest specific capacitance values, most probably originating from their maximum BET surface areas (Figure 4.9C). The specific capacitance values of the carbon nanosheets are higher than those of corresponding porous carbons synthesized without graphene (Figure 4.16-4.18). During the electrochemical processes, the graphene layer in the sandwich-like carbon nanosheets is expected to act as a long distance in-plane charge transporter, by taking advantage of its 2D electron transport feature and superior electrical conductivity.

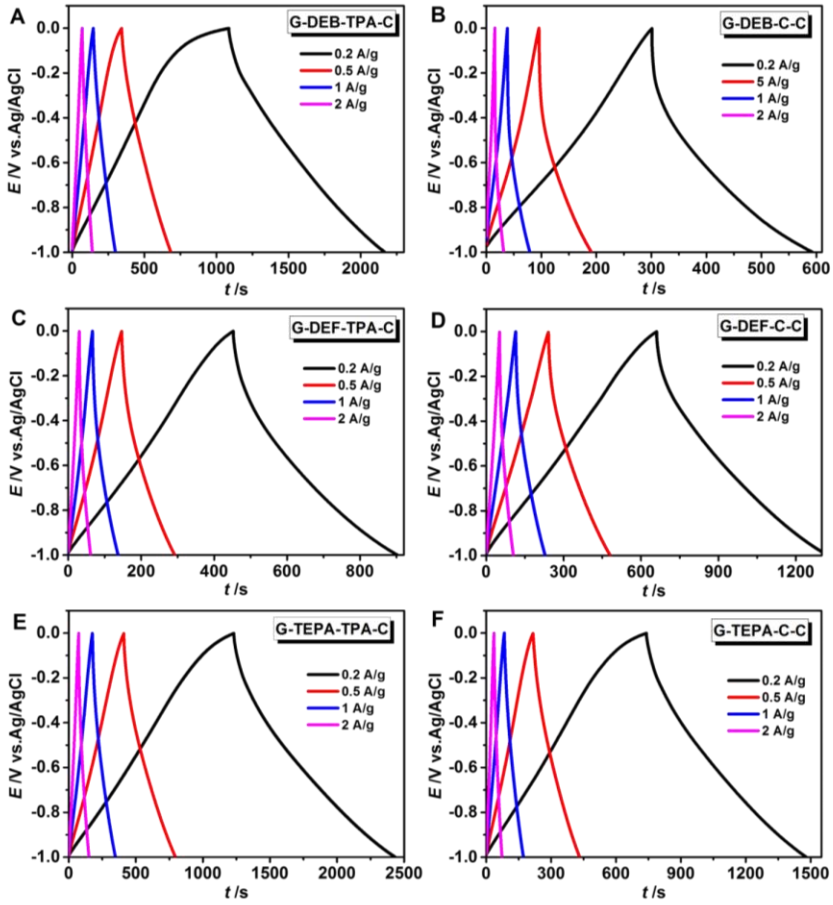

Figure 4.15 GCD curves of graphene-based porous carbon nanosheets at different charge/discharge current densities in a three-electrode system using 6 M aqueous KOH solution as electrolyte.

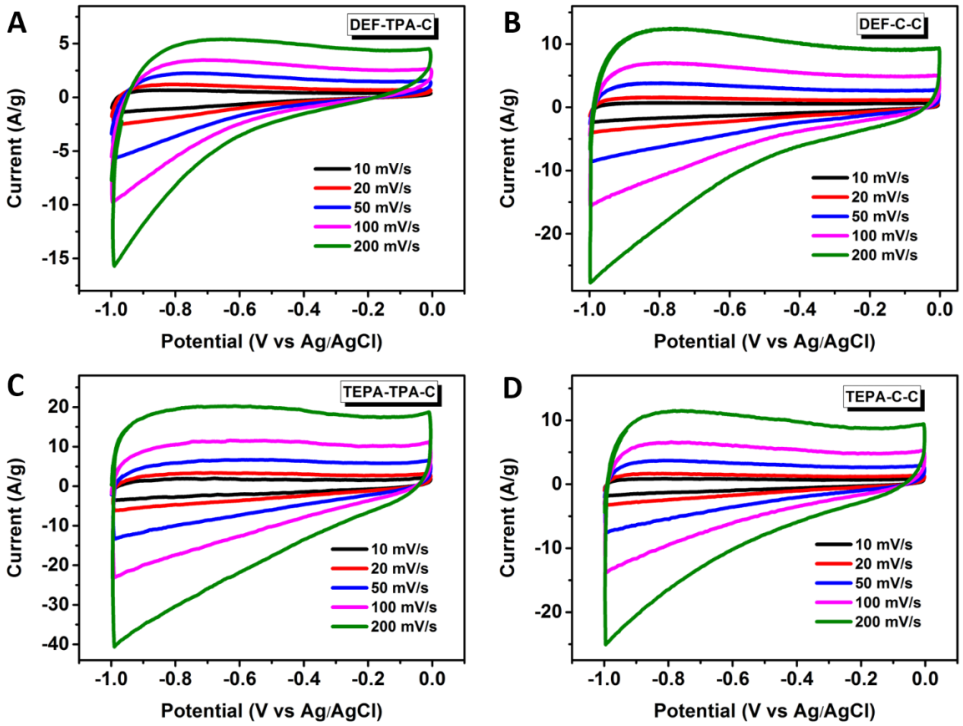

Figure 4.16 CV curves for (A) DEF-TPA-C, (B) DEF-C-C, (C) TEPA-TPA-C, and (D) TEPA-C-C at different scan rates.

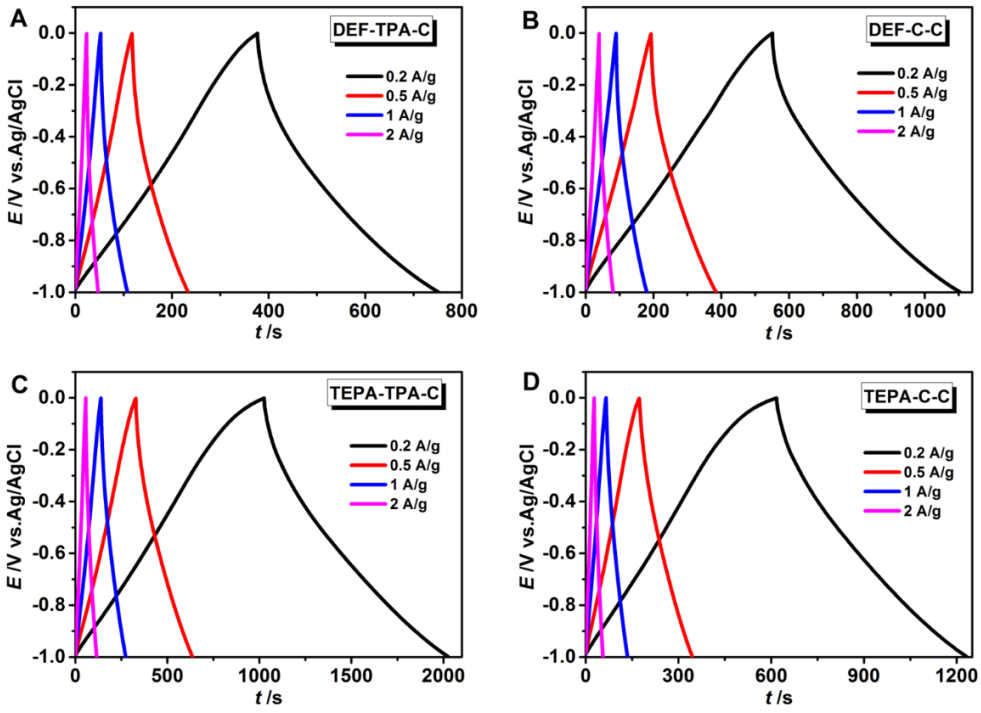

Figure 4.17 Galvanostatic charge/discharge (GCD) curves for (A) DEF-TPA-C, (B) DEF-C-C, (C) TEPA-TPA-C, and (D) TEPA-C-C at different charge/discharge current densities.

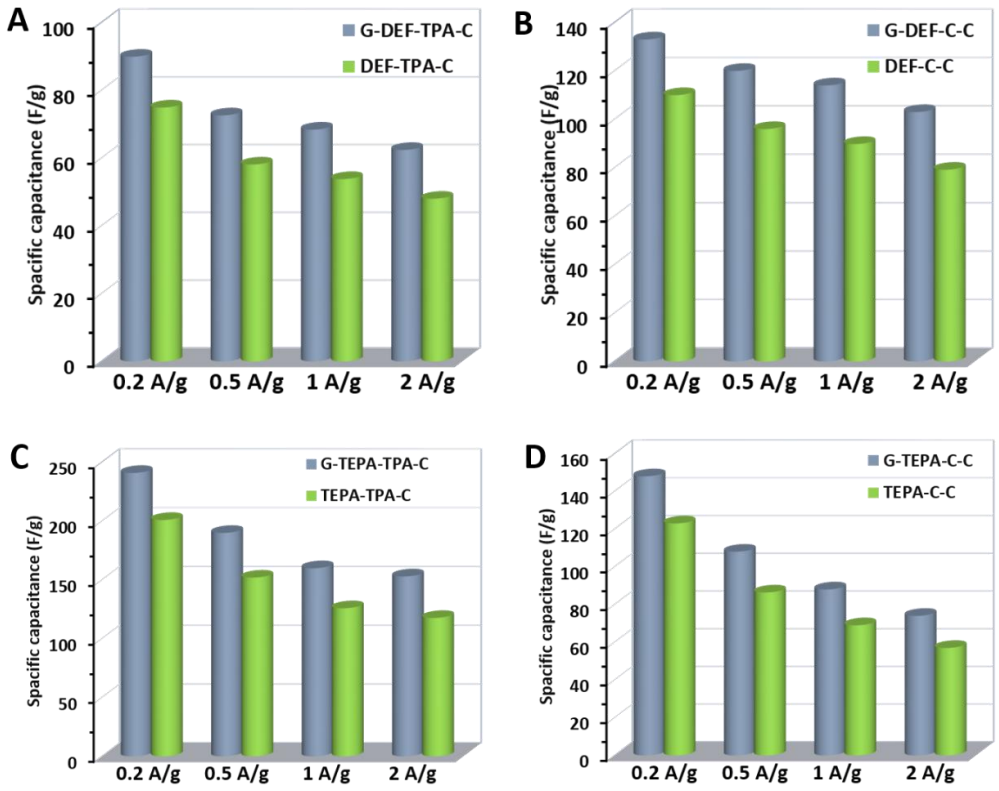

Figure 4.18 Gravimetric capacitances for (A) G-DEF-TPA-C and DEF-TPA-C, (B) G-DEF-C-C and DEF-C-C, (C) G-TEPA-TPA-C and TEPA-TPA-C, and (D) G-TEPA-C-C and TEPA-C-C at different charge/discharge current densities.

4.2.7 Supercapacitors Based on G-DEB-TPA-C and G-TEPA-TPA-C

In order to further evaluate the potential of our carbon nanosheet materials for electrochemical energy storage, symmetrical two-electrode supercapacitors were assembled with G-DEB-TPA-C and G-TEPA-TPA-C as active electrode materials using 6 M aqueous KOH solution as electrolyte. Figure 4.13D, E exhibit the CV profiles of G-DEB-TPA-C- and G-TEPA-TPA-C-based symmetric supercapacitors, respectively. The CV curves maintain quasi-rectangular shapes at all applied scanning rates from 10 to 200 mV/s, corresponding to the pronounced capacitive character of the charging/discharging process. The CV curves of G-DEB-TPA-C-based supercapacitors displayed a more fusiform shape for high scan rate (200 mV/s) if compared to that of G-TEPA-TPA-C based supercapacitors thus suggesting superior supercapacitive behavior and rate capability, as well as the smaller equivalent series resistance for G-TEPA-C-based electrodes.[7]

Next, GCD measurements have been carried out for different current densities between 0.2 and 20 A/g. The GCD curves of the G-DEB-TPA-C- and G-TEPA-TPA-C-based devices show highly symmetry and nearly triangular shapes with a rather limited voltage (*IR*) drop (Figure 4.13F, G and Figure 4.19). The relationship between specific capacitances (extracted from the discharge slopes) and current density for G-DEB-TPA-C and G-TEPA-TPA-C based devices are presented in Figure 4.13H and the inset of Figure 4.13I. G-DEB-TPA-C- and G-TEPA-TPA-C-based devices provide gravimetric capacitances of 55 F/g and 67 F/g at 0.2 A/g, respectively, corresponding to 220 and 268 F/g for the single electrode capacitance, respectively.[39] These capacitance values well compare to those of 3D porous carbons, N-doped graphene and other previously reported carbon materials (Table 4.1), with G-TEPA-TPA-C as the most promising material.

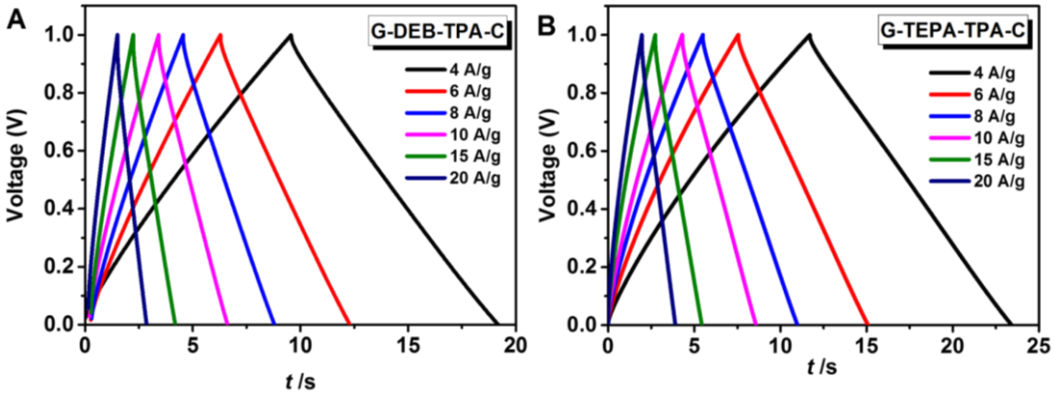

Figure 4.19 GCD curves of (A) G-DEB-TPA-C- and (B) G-TEPA-TPA-C-based supercapacitors at different charge/discharge current densities.

The unique structure of our 2D hybrid materials should ensure a high ion accessible surface area and good ion and charge transport behavior, resulting in promising specific capacitances and rate capability (Table 4.2), combined with excellent cycling stability (ca. 95% after 5000 cycle at 5 A/g, Figure 4.20 and Table 4.3). Ragone plots connect power and energy density as a very useful indicator for the performance of supercapacitor devices. For our G-DEB-TPA-C- and G-TEPA-TPA-C-based devices, the maximum energy and power densities are 7.6 and 9.3 Wh/kg or 8426 and 9581 W/kg, respectively. As concrete illustration of the energy

storage performance of our supercapacior devices, a red-emitting light-emitting diode (LED) that is powered by three G-TEPA-TPA-C-based supercapacior devices connected in series is depicted in Figure 4.21.

Table 4.1 Comparison of the gravimetric capacitances of carbon-based supercapacitor electrodes from the literature.

Materials	Gravimetric capacitance (F/g)	Electrolyte	References
High density porous graphene macroform	238 (0.1 A/g)	6 M KOH	43
S-porous carbon/graphene	109 (0.05 A/g)	6 M KOH	44
Reduced graphite oxide with high density	182 (1 A/g)	6 M KOH	45
Porous graphene nanosheets	241 (2 mV/s)	6 M KOH	46
Activated microwave exfoliated graphite oxide	137 (1 A/g)	BMIM BF_4/AN	47
	154 (1 A/g)	EMIM TFSI/AN	
KOH activated graphene	166 (0.7 A/g)	BMIM BF_4/AN	48
Compressed KOH activated graphene	147 (1.24 A/g)	BMIM BF_4/AN	49
Hydrazine reduced graphene oxide	123 (10 mV/s)	6 M KOH	50
Activated graphene-derived carbon	174	Ionic liquid	51
Holey graphene framework	298 (1 A/g)	BMIM BF_4/AN	52
Nitrogen-enriched nonporous carbon	115 (0.05 A/g)	1 M H_2SO_4	53
Seaweeds derived carbon	198 (2 mV/s)	1 M H_2SO_4	54
Activated carbon aerogel	220 (0.125 A/g)	1 M H_2SO_4	55
Copper nanocrystal modified activated carbon	79 (0.2 A/g)	TEATFB	56
N-doped reduced graphene oxide	255 (0.5 A/g)	6 M KOH	57
3D nitrogen and boron co-doped graphene	239 (1 A/g)	1 M H_2SO_4	58
Crumpled N-doped graphene nanosheets	245.9 (1 A/g)	BMIM BF_4/AN	59
3D Nitrogen-doped graphene-CNT	180 (0.5 A/g)	6 M KOH	60
Boron-doped graphene nanoplatelets	160 (1 A/g)	6 M KOH	61
Graphene sponge	204.66 (5 mV/s)	1 M NaCl	62
3D porous carbon	176 (10 mV/s)	1 M H_2SO_4	63
Reduced graphene oxide	41.5 (0.1 A/g)	6 M KOH	64
G-TEPA-TPA-C	**241 (0.2 A/g)**	**6 M KOH**	**This work**

Table 4.2 Comparison of the rate capabilities of carbon-based supercapacitor electrodes in two-electrode symmetric cell configuration, from the literature.

Materials	Current density	Retention ratio (%)	references
Porous N-doped hollow carbon spheres	0.5-10 A/g	55.6	65
N-doped ordered nanoporous carbon	0.1-10 A/g	50	66
3D N-doped graphene-CNT	0.5-5 A/g	52.8	60
Microporous carbon nanosphere	0.02-2 A/g	57.9	67
Active nitrogen-rich carbon	0.2-2 A/g	68	68
Boron-doped graphene	0.2-10 A/g	51	69
PAF-Carbon	0.2-10 A/g	41	70
N-PAF-Carbon	0.2-10 A/g	43	70
$CoMoO_4$-3D graphene	1.43-9.28 A/g	68	71
CNT supported graphene-based aerogel	0.1-10 A/g	36.9	72
N-doped graphene	0.2-3 A/g	66	73
Mesoporous graphene	0.5-8 A/g	59	74
3D N-containing porous frameworks	0.2-10 A/g	62	40
Porous active carbon	0.25-10 A/g	49	75
3D Porous graphene/carbon composites	0.1-0.5 A/g	59	31
Layered polyaniline/graphene film	0.5-10 A/g	50	76
Graphene-based fiber	0.49-6.13 A/g	59	77
G-TEPA-TPA-C	**0.2-10 A/g**	**64.4**	**This work**
	0.5-10 A/g	**76.8**	
	0.5-5 A/g	**82.1**	

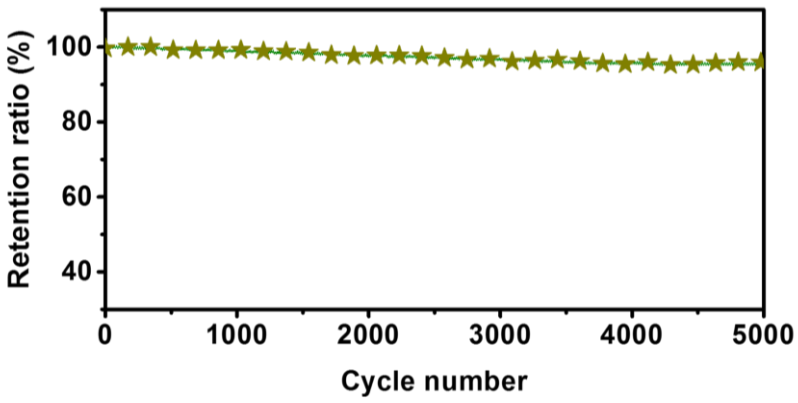

Figure 4.20 Cycling stability of a G-TEPA-TPA-C-based supercapacitor for 5000 cycles at a current density of 5 A/g.

Table 4.3 Comparison of the cycling stability of carbon-based supercapacitor electrodes, from the literature.

Materials	Electrolyte	Current density, or scan rate	Retention ratio	References
Polyoxometalate/RGO	0.5 M H_2SO_4	10 A/g	77% (2000 cycles)	78
Graphene/polyaniline nanofiber	1 M H_2SO_4	3 A/g	79% (800 cycles)	79
Microporous carbon nanofibers	6 M KOH	1 A/g	92% (1000 cycles)	80
P/N doped porous carbon	6 M KOH	5 mV/s	86% (5000 cycles)	81
rGO-MoS_2 hybrid fiber	PVA-H_2SO_4	-	~80% (1000 cycles)	82
Mesoporous carbon/RGO	6 M KOH	0.5 A/g	~94% (1000 cycles)	64
RGO-RuO_2	2 M H_2SO_4	-	70% (2500 cycles)	39
Porous carbon nanosheets	6 M KOH	10 A/g	95% (5000 cycles)	83
Graphite flakes/Polypyrrole	1 M H_2SO_4	-	91% (5000 cycles)	84
Fe_3O_4@graphene	Saturated KCl	5 mA/g	91.5% (1000 cycles)	85
Carbon decorated graphene	6 M KOH	0.5 A/g	95.4% (1000 cycles)	86
Porous active carbon	6 M KOH	4 A/g	89.4% (2000 cycles)	75
Hydrazine reduced GO paper	30 wt% KOH	0.5 A/g	~90% (1200 cycles)	87
N-doped graphene	0.5 M H_2SO_4	1 A/g	90.3% (5000 cycles)	73
Graphene paper	1 M H_2SO_4	2 A/g	86.9% (1000 cycles)	58
Thermal-reduced GO	6 M KOH	200 mV/s	<90% (2000 cycles)	88
Aniline tetramer-GO	1 M H_2SO_4	100 mV/s	89.1% (1000 cycles)	89
G-TEPA-TPA-C	**6 M KOH**	**5 A/g**	**95% (5000 cycles)**	**This work**

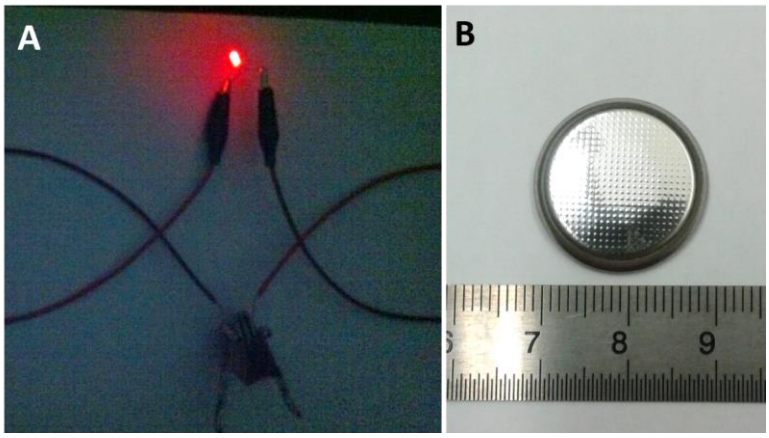

Figure 4.21 Photographs of (A) a red light-emitting-diode (LED) powered by three supercapacitor devices connected in series, and (B) an individual coin-sized G-TEPA-TPA-C-based supercapacitor device.

4.3 Conclusions

In summary, 2D graphene-based conjugated microporous polymer sandwiches (G-CMPs) were synthesized starting from 4-iodophenyl-substituted graphene (RGO-I) templates via Sonogashira-Hagihara coupling. RGO-I represents an efficient 2D template for the growth of porous CMPs onto the graphene surface. Moreover, our G-CMPs could be easily converted into porous carbon materials with maintained 2D morphology by thermal carbonization. The carbonized hybrid materials were tested as electrode materials of supercapacitors, leading to maximum energy and power densities of 9.3 Wh/kg and 9581 W/kg, respectively. Considering the simple and convenient preparation of the hybrid materials, our strategy seems promising towards low cost, high performance supercapacitors.

4.4 Experimental

All reagents, unless otherwise stated, were obtained from commercial sources (Sigma Aldrich, Alfa Aesar and Acros) and were used without further purification.

4.4.1 Synthesis of 2,7-Bis[(trimethylsilyl)ethynyl]-fluorene

2,7-bis[(trimethylsilyl)ethynyl]-fluorene was prepared according to a literature procedure.[90,91] Reaction of 3.242 g (10 mmol) 2,7-dibromo-fluorene, 2.48 g (4.2 mL, 30 mmol) trimethylsilylacetylene, 0.395 g (0.5 mmol) $Pd(PPh_3)_2Cl_2$, 76 mg (0.5 mmol) PPh_3 and 95 mg (0.5 mmol) CuI in 40 mL of 7:3 mixture of anhydrous toluene and diisopropylamine in 100 mL flask under nitrogen gave a crude product which was purified by column chromatography on silica gel (eluent: $CHCl_2$/hexane, 1:9). The product was obtained as a pale yellow solid (3.36 g, 93.6%). ^{1}H NMR (400 MHz, $CDCl_3$) δ (TMS, ppm): 7.69-7.48 (m, 6H), 3.87 (s, 2H), 0.29 (m, 18H). GCMS (EI): m/z calcd 358.16; found 358.20.

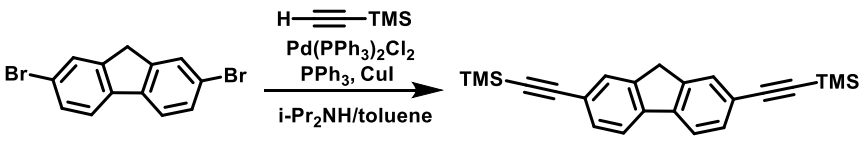

4.4.2 Synthesis of 2,7-Diethynyl-fluorene

2,7-diethynyl-fluorene was prepared following a literature procedure.[90,91] Reaction of 3.00 g (8.4 mmol) 2,7-bis[(trimethylsilyl)ethynyl]-fluorene in 60 mL of THF and 2.79 g (50.4 mmol) of KOH in 45 mL of methanol afforded a crude product which was purified by flash column chromatography on silica gel (eluent: $CHCl_2$/hexane, 2:3). The product was isolated as a pale yellow solid (1.68 g, 93.8%). ^{1}H NMR (400 MHz, $CDCl_3$) δ (TMS, ppm): 7.73 (s, 2H), 7.70 (d, 2H), 7.54 (d, 2H), 3.16 (s, 2H). ^{13}C NMR (100 MHz, $CDCl_3$) δ (TMS, ppm): 143.43, 141.49, 131.14, 128.71, 120.67, 120.07, 84.16, 77.35, 36.46. GCMS (EI): m/z calcd 214.08; found 214.10.

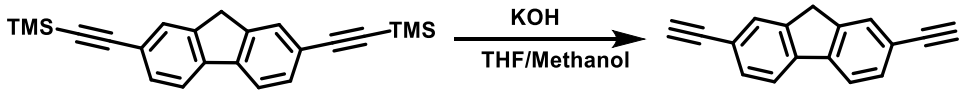

4.4.3 Synthesis of Tris(4-ethynylphenyl)amine

Synthesis of (4-HOMe$_2$CC≡CC$_6$H$_4$)$_3$N.[92] 2-Methylbut-3-yn-2-ol (9.7 mL, 100.0 mmol) was added to a mixture of tris(p-bromophenyl)amine (4.82 g, 10.0 mmol), $PdCl_2(PPh_3)_2$ (0.28 g, 0.4 mmol), and CuI (152 mg, 0.8 mmol) in triethylamine (100 mL). The reaction mixture was heated at 80 °C for 48 h, cooled to room temperature, and the solvents were removed by rotary evaporation. The residue was extracted with ethyl acetate and filtered. The filtrate was washed with water and saturated brine solution. The aqueous layer was extracted with ethyl acetate and the extracts were again washed with saturated brine solution. The organic layers were combined and dried over anhydrous magnesium sulfate, and the solvents removed by rotary evaporation under reduced pressure to give the crude product as a dark oil. The crude product was purified by a silica gel column chromatography using hexane/ethyl acetate (1:1) as eluent. After recrystallization from ethyl acetate/hexane the product was obtained as yellow crystals (4.21 g, 85.6%). ^{1}H NMR (600 MHz, $CDCl_3$) δ (TMS, ppm): 7.35-7.30 (m, 6H), 6.99 (d, 6H), 2.05 (s, 3H), 1.63 (d, 18H). ^{13}C NMR (150 MHz, $CDCl_3$) δ (TMS, ppm): 146.71, 132.81, 123.88, 117.43, 93.64, 81.85, 65.66,

31.54. MS (APLI): calcd. 491.25; found 491.237.

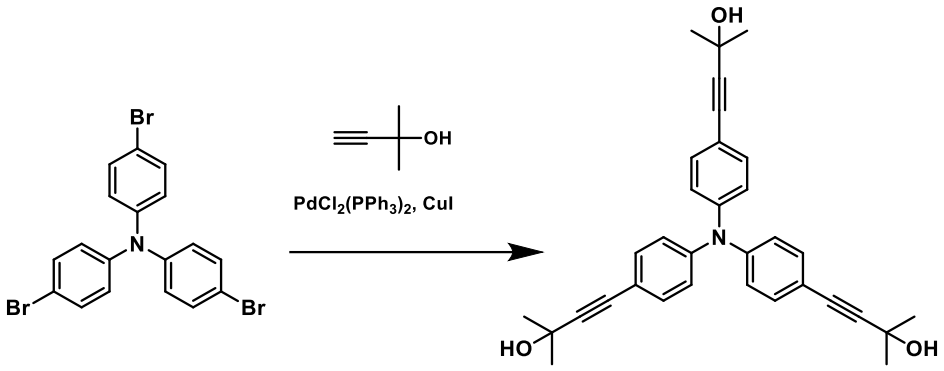

Synthesis of tris(4-ethynylphenyl)amine.[92] (4-$HOMe_2CC{\equiv}CC_6H_4)_3N$ (3.932 g, 8.0 mmol) and powdered KOH (6.732 g, 120.0 mmol) were suspended in toluene (300 mL) and heated to 80 °C overnight. The reaction mixture was cooled to room temperature and filtered through a short pad of celite. The celite pad was washed with toluene three times and the combined organic phases were evaporated under reduced pressure. The resulting oil was adsorbed onto silica and subjected to column chromatography. Elution with hexane/CH_2Cl_2 (4:1) gave tris(4-ethynylphenyl) amine as a yellow solid, after evaporation of the solvent (2.17 g, 85.5%). ^{1}H NMR (400 MHz, $CDCl_3$) δ (TMS, ppm):7.44 (d, 6H), 7.07 (d, 6H), 3.08 (s, 3H). ^{13}C NMR (100 MHz, $CDCl_3$) δ (TMS, ppm): 147.04, 133.37, 123.93, 116.89, 83.40, 77.32 (s). GCMS (EI): calcd. 317.12; found 317.10.

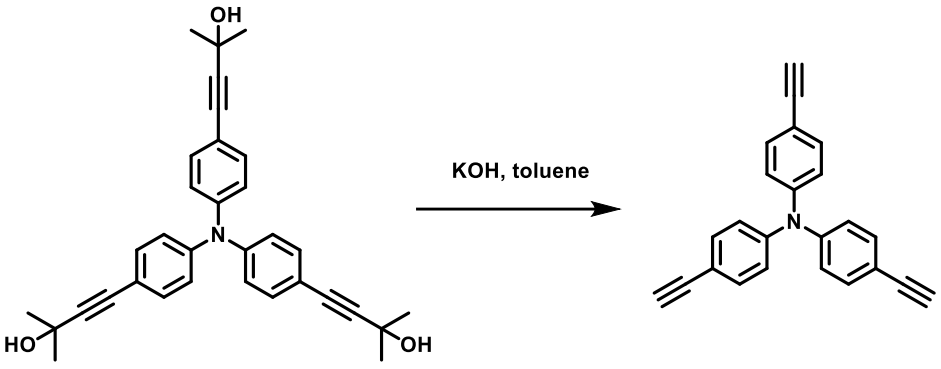

4.4.4 Synthesis of 4-Iodophenyl-Substituted Graphene (RGO-I)

Graphene oxide (GO) was prepared from graphite flakes by a modified Hummers method, as show in Scheme 4.2.[24] 400 mg GO were reduced with hydrazine hydrate in the presence of sodium dodecylbenzene sulfonate (SDBS) under reflux.[93] The functionalization of reduced graphene oxide (RGO) was carried out according to a published procedure.[19,23,26,27,94] The 4-iodophenyl diazonium salt that is used for the functionalization of graphene was prepared *in situ* starting from 4-iodoaniline: 1.535 g (7 mmol) 4-iodoaniline were dissolved in 80 mL of deionized water by adding a minimum amount of conc. aqueous HCl dropwise. The 4-iodoaniline solution was then transferred into a round bottom flask that is kept at 0 ^{o}C in an ice bath. To this solution, 526 mg $NaNO_2$ (7.6 mmol) and 6 mL of 20% aqueous HCl (6.4 M) were added and stirred for 45 min. The color of the solution changed from colorless to yellow due to the formation of the diazonium salt.

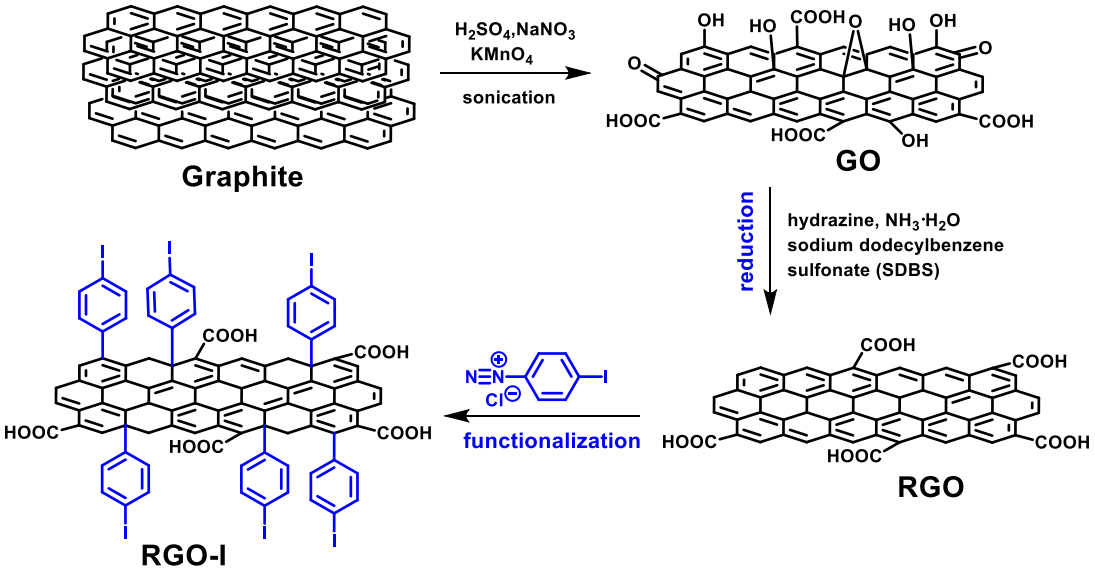

Scheme 4.2 Idealized formula scheme depicting the reduction of GO and functionalization of the resulting RGO with 4-iodophenyl side groups under formation of RGO-I.

The solution of the diazonium salt was next added dropwise under rapid stirring to the RGO dispersion. The reaction mixture was maintained at 0 ^{o}C for additional 2 hours. After stirring at room temperature for additional 6 hours, the mixture was poured into acetone. Purification of the RGO-I reaction product was done by filtration

and washing with deionized water, acetone, and DMF. The solid product was dried in vacuum at room temperature (yield: 376 mg RGO-I).

4.4.5 Synthesis of G-CMPs

The G-CMPs (graphene-based conjugated microporous polymers) were prepared in palladium-catalyzed Sonogashira-Hagihara cross-coupling reactions of RGO-I[19,21] with an arylacetylene (1,4-diethynylbenzene (DEB), 2,7-diethynyl-9H-fluorene (DEF), tris(4-ethynylphenyl)amine (TEPA)), and an aryl halide component (3,6-dibromocarbazole (C), tris(4-bromophenyl)amine (TPA)). A representative experimental procedure (for G-DEB-TPA) synthesis is given below.

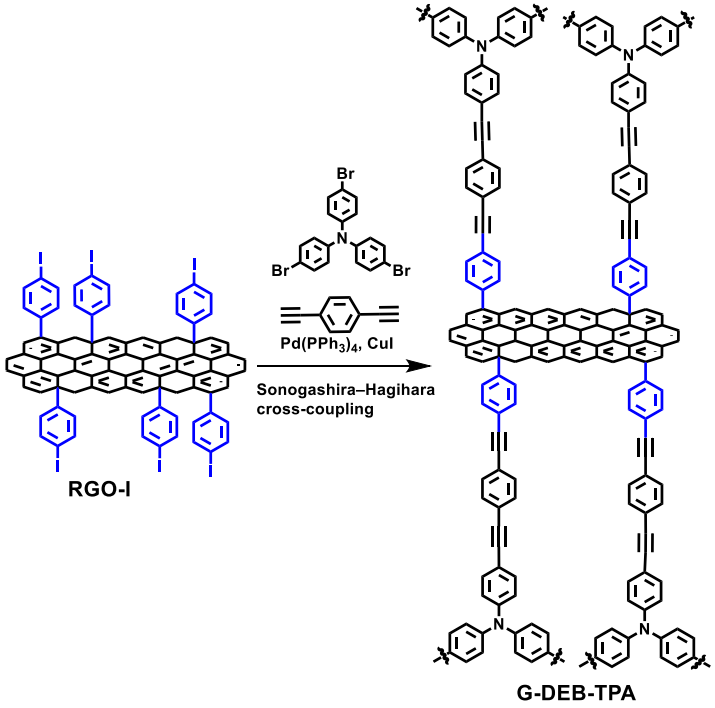

Synthesis of G-DEB-TPA. RGO-I (100 mg) was sonicated in dry DMF (150 mL) until complete dispersion occurs. Then, tris(4-bromophenyl)amine (482 mg, 1 mmol), 1,4-diethynylbenzene, (504mg, 4.0 mmol), tetrakis-(triphenylphosphine) palladium (70 mg, 0.06 mmol), copper iodide (28 mg, 0.12 mmol), and Et_3N (6 mL) were added to the RGO-I dispersion. The reaction mixture was heated to 140 °C and stirred for 3 days at this temperature under argon atmosphere. Next, the insoluble, precipitated product was filtered off and washed four times with chloroform, water,

and acetone to remove unreacted monomers or catalyst residues. Further purification of the polymer networks was carried out by Soxhlet extraction with THF for 48 h. The product was dried in vacuum for 24 h at room temperature, to afford G-DEB-TPA (yield: 826 mg).

4.4.6 Characterization

Solution NMR spectra were recorded on Bruker AVANCE 400 or AVANCE III 600 machines. ^{1}H and ^{13}C NMR spectra were measured with tetramethylsilane (TMS) as internal standard. Fourier transform infrared (FTIR) spectroscopy was carried out on a JASCO FT/IR-4200 Fourier-Transform-spectrometer. UV-Vis absorption spectra were recorded on a Shimadzu UV-2401 PC spectrophotometer at room temperature. The morphology of G-CMPs and corresponding carbon nanosheets were characterized by transmission electron microscopy (TEM, JEOL, JEM-2100F). The TEM samples were prepared by transferring G-CMPs and corresponding carbon nanosheets onto copper grids. Thermogravimetric analysis was performed on a Mettler Toledo TGA Stare System under argon flow. Raman spectra were recorded on a LabRAM HR Raman Microscope with an excitation wavelength of 514 nm. X-ray photoelectron spectroscopy was carried out on a Kratos AXIS Ultra, performing at 15 kV and 15 mA with a monochromatic Al Kα source (hν = 1486.71 eV).

Nitrogen adsorption-desorption measurements. The nitrogen adsorption-desorption measurements were performed on a BELSORB Max (BEL Japan Inc.). The surface areas were calculated using the BET model in the pressure range p/p_0 from 0.05-0.3. The total pore volume was determined at a relative pressure of 0.99. The pore size distribution was analyzed from the nitrogen adsorption data using by NLDFT analysis with a slit pore model.

Solid-state NMR measurements. Solid-state ^{13}C MAS NMR spectra were recorded at 75.48 MHz using a Bruker Avance III 300 spectrometer with a contact time of 2.5 ms coadding 4096 up to 16392 transients, depending on the required relaxation delay of 2 s up to 60 s. All experiments were carried out at room

temperature using a standard Bruker 4 mm double resonance MAS probe spinning at 12 kHz, typical π/2-pulse lengths of 4 μs and SPINAL64 proton decoupling. The spectra were referenced with respect to tetramethyl silane (TMS) using solid adamantane as secondary standard (29.46 ppm for ^{13}C).

4.4.7 Supercapacitor Fabrication

Coin-cell-type symmetric supercapacitors were fabricated to evaluate the supercapacitive performance. Briefly, 80 wt% porous carbon nanosheets, 10 wt% active carbon, and 10 wt% polyvinylidene fluoride (PVDF, as binder) were homogeneously mixed into a paste. Then, the mixture was rolled onto a nickel foil as current collector. After drying at 120 ^{o}C overnight, the electrodes/collectors were assembled into CR2032 stainless steel coin cells with 6 M aqueous KOH solution and a porous cellulose membrane as electrolyte and separator, respectively.

4.4.8 Electrochemical Measurements and Caculations.

The electrochemical experiments were carried out using a conventional, aqueous three-electrode system employing 6 M aqueous KOH as electrolyte at room temperature. The three-electrode cells consist of Ag/AgCl as reference electrode, Pt as counter electrode, and the porous carbon nanosheets as working electrode. The working electrode was prepared by loading our porous carbon nanosheets onto a glassy carbon electrode. Thereby, the porous carbon nanosheets were first dispersed in water by sonication under formation of a homogeneous dispersion (1 mg/mL). Next, 6 μL of the dispersion were loaded onto a glassy carbon electrode with a diameter of 5 mm. The modified electrode was slowly dried in air until a uniform porous carbon nanosheets layer was formed at the electrode surface. The following cyclic voltammetry (CV) and galvanostatic charge/discharge (GCD) measurements in both three-electrode and two-electrode arrangements were performed using a PAR VersaSTAT 4 electrochemical workstation within the voltage range from -1 to 0 V.

The specific capacitance was calculated by the following equation:

$$C = I \Delta t / m \Delta V$$

where C (F/g) is the specific capacitance, I (mA) the discharge current, and Δt (s), m (mg), and ΔV (V) the total discharge time, the mass of active material, and the potential drop (by excluding the voltage (IR) drop) during discharge, respectively.

The energy density (E) was calculated from the discharge profiles of the two-electrode system by using the following equation:

$$E = 0.5C\Delta V^2/3.6$$

where E (Wh kg^{-1}) is the energy density, C (F g^{-1}) the specific capacitance of the active material and ΔV (V) the discharge voltage range. With a factor 3.6, the energy density is converted from J g^{-1} to Wh kg^{-1}.

4.5 References

(1) Yuan, K.; Hu, T.; Xu, Y.; Graf, R.; Brunklaus, G.; Forster, M.; Chen, Y.; Scherf, U. *ChemElectroChem* **2016**, *3*, 822-828.

(2) Simon, P.; Gogotsi, Y.; Dunn, B. *Science* **2014**, *343*, 1210-1211.

(3) Miller, J. R.; Simon, P. *Science* **2008**, *321*, 651-652.

(4) Ghidiu, M.; Lukatskaya, M. R.; Zhao, M.-Q.; Gogotsi, Y.; Barsoum, M. W. *Nature* **2014**, *516*, 78-81.

(5) Yan, J.; Wang, Q.; Wei, T.; Fan, Z. J. *Adv. Energy Mater.* **2014**, *4*, 1300816.

(6) Xu, Y.; Shi, G.; Duan, X. *Acc. Chem. Res.* **2015**, *48*, 1666-1675.

(7) Zhao, J.; Lai, H.; Lyu, Z.; Jiang, Y.; Xie, K.; Wang, X.; Wu, Q.; Yang, L.; Jin, Z.; Ma, Y.; Liu, J.; Hu, Z. *Adv. Mater.* **2015**, *27*, 3541-3545.

(8) Pandolfo, A. G.; Hollenkamp, A. F. *J. Power Sources* **2006**, *157*, 11-27.

(9) Simon, P.; Gogotsi, Y. *Nat. Mater.* **2008**, *7*, 845-854.

(10) Shao, Y.; El-Kady, M. F.; Wang, L. J.; Zhang, Q.; Li, Y.; Wang, H.; Mousavi, M. F.; Kaner, R. B. *Chem. Soc. Rev.* **2015**, *44*, 3639-3665.

(11) Bonaccorso, F.; Colombo, L.; Yu, G.; Stoller, M.; Tozzini, V.; Ferrari, A. C.; Ruoff, R. S.; Pellegrini, V. *Science* **2015**, *347*, 1246501.

(12) Fang, Y.; Luo, B.; Jia, Y.; Li, X.; Wang, B.; Song, Q.; Kang, F.; Zhi, L. *Adv. Mater.* **2012**, *24*, 6348-6355.

(13) Yang, X.; Zhu, J.; Qiu, L.; Li, D. *Adv. Mater.* **2011**, *23*, 2833-2838.

(14) Meng, Y.; Wang, K.; Zhang, Y.; Wei, Z. *Adv. Mater.* **2013**, *25*, 6985-6990.

(15) Song, Y.; Liu, T.-Y.; Xu, X.-X.; Feng, D.-Y.; Li, Y.; Liu, X.-X. *Adv. Funct. Mater.* **2015**, *25*, 4626-4632.

(16) Cooper, A. I. *Adv. Mater.* **2009**, *21*, 1291-1295.

(17) Xu, Y.; Jin, S.; Xu, H.; Nagai, A.; Jiang, D. *Chem. Soc. Rev.* **2013**, *42*, 8012-8031.

(18) Jiang, J.-X.; Su, F.; Trewin, A.; Wood, C. D.; Campbell, N. L.; Niu, H.; Dickinson, C.; Ganin, A. Y.; Rosseinsky, M. J.; Khimyak, Y. Z.; Cooper, A. I. *Angew. Chem., Int. Ed.* **2007**, *46*, 8574-8578.

(19) Zhuang, X.; Zhang, F.; Wu, D.; Forler, N.; Liang, H.; Wagner, M.; Gehrig, D.; Hansen, M. R.; Laquai, F.; Feng, X. *Angew. Chem., Int. Ed.* **2013**, *52*, 9668-9672.

(20) Zhuang, X.; Zhang, F.; Wu, D.; Feng, X. *Adv. Mater.* **2014**, *26*, 3081-3086.

(21) Zhuang, X.; Gehrig, D.; Forler, N.; Liang, H.; Wagner, M.; Hansen, M. R.; Laquai, F.; Zhang, F.; Feng, X. *Adv. Mater.* **2015**, *27*, 3789-3796.

(22) Zheng, X.; Luo, J.; Lv, W.; Wang, D. W.; Yang, Q. H. *Adv. Mater.* **2015**, *27*, 5388-5395.

(23) Yuan, K.; Guo-Wang, P.; Hu, T.; Shi, L.; Zeng, R.; Forster, M.; Pichler, T.; Chen, Y.; Scherf, U. *Chem. Mater.* **2015**, *27*, 7403-7411.

(24) Hummers, W. S.; Offeman, R. E. *J. Am. Chem. Soc.* **1958**, *80*, 1339-1339.

(25) Li, D.; Muller, M. B.; Gilje, S.; Kaner, R. B.; Wallace, G. G. *Nat. Nanotechnol.* **2008**, *3*, 101-105.

(26) Kumar, R.; Suresh, V. M.; Maji, T. K.; Rao, C. N. R. *Chem. Commun.* **2014**, *50*, 2015-2017.

(27) Yuan, K.; Xu, Y.; Uihlein, J.; Brunklaus, G.; Shi, L.; Heiderhoff, R.; Que, M.; Forster, M.; Chasse, T.; Pichler, T.; Riedl, T.; Chen, Y.; Scherf, U. *Adv. Mater.* **2015**, *27*, 6714-6721.

(28) Yuan, W.; Liu, A.; Huang, L.; Li, C.; Shi, G. *Adv. Mater.* **2013**, *25*, 766-771.

(29) Sun, Y.; Li, C.; Shi, G. *J. Mater. Chem.* **2012**, *22*, 12810-12816.

(30) Su, Y.; Liu, Y.; Liu, P.; Wu, D.; Zhuang, X.; Zhang, F.; Feng, X. *Angew. Chem., Int. Ed.* **2015**, *54*, 1812-1816.

(31) Li, X. J.; Xing, W.; Zhou, J.; Wang, G. Q.; Zhuo, S. P.; Yan, Z. F.; Xue, Q. Z.; Qiao, S. Z. *Chem. Eur. J.* **2014**, *20*, 13314-13320.

(32) Yang, X.; Zhuang, X.; Huang, Y.; Jiang, J.; Tian, H.; Wu, D.; Zhang, F.; Mai, Y.; Feng, X. *Polym. Chem.* **2015**, *6*, 1088-1095.

(33) Yang, Z.; Ren, J.; Zhang, Z.; Chen, X.; Guan, G.; Qiu, L.; Zhang, Y.; Peng, H. *Chem. Rev.* **2015**, *115*, 5159-5223.

(34) Zhang, J.; Xia, Z.; Dai, L. *Sci. Adv.* **2015**, *1*, e1500564.

(35) Ferrari, A. C.; Meyer, J. C.; Scardaci, V.; Casiraghi, C.; Lazzeri, M.; Mauri, F.; Piscanec, S.; Jiang, D.; Novoselov, K. S.; Roth, S.; Geim, A. K. *Phys. Rev. Lett.* **2006**, *97*, 187401.

(36) Ferrari, A. C.; Basko, D. M. *Nat. Nanotechnol.* **2013**, *8*, 235-246.

(37) Xiang, Z.; Cao, D.; Huang, L.; Shui, J.; Wang, M.; Dai, L. *Adv. Mater.* **2014**, *26*, 3315-3320.

(38)Zhang, L.; Zhang, F.; Yang, X.; Long, G.; Wu, Y.; Zhang, T.; Leng, K.; Huang, Y.; Ma, Y.; Yu, A.; Chen, Y. *Sci. Rep.* **2013**, *3*, 1408.

(39) Zhang, J.; Jiang, J.; Li, H.; Zhao, X. S. *Energy Environ. Sci.* **2011**, *4*, 4009-4015.

(40) Hao, L.; Ning, J.; Luo, B.; Wang, B.; Zhang, Y.; Tang, Z.; Yang, J.; Thomas, A.; Zhi, L. *J. Am. Chem. Soc.* **2014**, *137*, 219-225.

(41)Wu, Z.-S.; Chen, L.; Liu, J.; Parvez, K.; Liang, H.; Shu, J.; Sachdev, H.; Graf, R.; Feng, X.; Müllen, K. *Adv. Mater.* **2014**, *26*, 1450-1455.

(42) Zhao, L.; Fan, L.-Z.; Zhou, M.-Q.; Guan, H.; Qiao, S.; Antonietti, M.; Titirici, M.-M. *Adv. Mater.* **2010**, *22*, 5202-5206.

(43) Tao, Y.; Xie, X.; Lv, W.; Tang, D. M.; Kong, D.; Huang, Z.; Nishihara, H.; Ishii, T.; Li, B.; Golberg, D.; Kang, F.; Kyotani, T.; Yang, Q. H. *Sci. Rep.* **2013**, *3*, 2975.

(44) Seredych, M.; Bandosz, T. J. *J. Mater. Chem. A* **2013**, *1*, 11717-11727.

(45) Li, Y.; Zhao, D. *Chem. Commun.* **2015**, *51*, 5598-5601.

(46) Fan, Z.; Zhao, Q.; Li, T.; Yan, J.; Ren, Y.; Feng, J.; Wei, T. *Carbon* **2012**, *50*,

1699-1703.

(47) Ghaffari, M.; Zhou, Y.; Xu, H.; Lin, M.; Kim, T. Y.; Ruoff, R. S.; Zhang, Q. M. *Adv. Mater.* **2013**, *25*, 4879-4885.

(48) Zhu, Y.; Murali, S.; Stoller, M. D.; Ganesh, K. J.; Cai, W.; Ferreira, P. J.; Pirkle, A.; Wallace, R. M.; Cychosz, K. A.; Thommes, M.; Su, D.; Stach, E. A.; Ruoff, R. S. *Science* **2011**, *332*, 1537-1541.

(49) Murali, S.; Quarles, N.; Zhang, L. L.; Potts, J. R.; Tan, Z.; Lu, Y.; Zhu, Y.; Ruoff, R. S. *Nano Energy* **2013**, *2*, 764-768.

(50) Yan, J.; Wei, T.; Shao, B.; Ma, F.; Fan, Z.; Zhang, M.; Zheng, C.; Shang, Y.; Qian, W.; Wei, F. *Carbon* **2010**, *48*, 1731-1737.

(51) Kim, T.; Jung, G.; Yoo, S.; Suh, K. S.; Ruoff, R. S. *ACS Nano* **2013**, *7*, 6899-6905.

(52) Xu, Y.; Lin, Z.; Zhong, X.; Huang, X.; Weiss, N. O.; Huang, Y.; Duan, X. *Nat. Commun.* **2014**, *5*, 4554.

(53) Hulicova-Jurcakova, D.; Kodama, M.; Shiraishi, S.; Hatori, H.; Zhu, Z. H.; Lu, G. Q. *Adv. Funct. Mater.* **2009**, *19*, 1800-1809.

(54) Raymundo-Piñero, E.; Leroux, F.; Béguin, F. *Adv. Mater.* **2006**, *18*, 1877-1882.

(55) Zapata-Benabithe, Z.; Carrasco-Marín, F.; Moreno-Castilla, C. *J. Power Sources* **2012**, *219*, 80-88.

(56) Zhang, L.; Candelaria, S. L.; Tian, J.; Li, Y.; Huang, Y.-x.; Cao, G. *J. Power Sources* **2013**, *236*, 215-223.

(57) Lei, Z.; Lu, L.; Zhao, X. S. *Energy Environ. Sci.* **2012**, *5*, 6391-6399.

(58) Wu, Z.-S.; Winter, A.; Chen, L.; Sun, Y.; Turchanin, A.; Feng, X.; Müllen, K. *Adv. Mater.* **2012**, *24*, 5130-5135.

(59) Wen, Z.; Wang, X.; Mao, S.; Bo, Z.; Kim, H.; Cui, S.; Lu, G.; Feng, X.; Chen, J. *Adv. Mater.* **2012**, *24*, 5610-5616.

(60) You, B.; Wang, L.; Yao, L.; Yang, J. *Chem. Commun.* **2013**, *49*, 5016-5018.

(61) Han, J.; Zhang, L. L.; Lee, S.; Oh, J.; Lee, K.-S.; Potts, J. R.; Ji, J.; Zhao, X.; Ruoff, R. S.; Park, S. *ACS Nano* **2013**, *7*, 19-26.

(62) Xu, X.; Sun, Z.; Chua, D. H.; Pan, L. *Sci. Rep.* **2015**, *5*, 11225.

(63) Wu, Z.-S.; Sun, Y.; Tan, Y.-Z.; Yang, S.; Feng, X.; Müllen, K. *J. Am. Chem. Soc.* **2012**, *134*, 19532-19535.

(64) Lei, Z.; Christov, N.; Zhao, X. S. *Energy Environ. Sci.* **2011**, *4*, 1866-1873.

(65) Han, J.; Xu, G.; Ding, B.; Pan, J.; Dou, H.; MacFarlane, D. R. *J. Mater. Chem. A* **2014**, *2*, 5352-5357.

(66) Liang, Y.; Liu, H.; Li, Z.; Fu, R.; Wu, D. *J. Mater. Chem. A* **2013**, *1*, 15207-15211.

(67) Li, Z.; Wu, D.; Liang, Y.; Fu, R.; Matyjaszewski, K. *J. Am. Chem. Soc.* **2014**, *136*, 4805-4808.

(68) Gao, F.; Shao, G.; Qu, J.; Lv, S.; Li, Y.; Wu, M. *Electrochim. Acta* **2015**, *155*, 201-208.

(69) Peng, Z.; Ye, R.; Mann, J. A.; Zakhidov, D.; Li, Y.; Smalley, P. R.; Lin, J.; Tour, J. M. *ACS Nano* **2015**, *9*, 5868-5875.

(70) Xiang, Z.; Wang, D.; Xue, Y.; Dai, L.; Chen, J. F.; Cao, D. *Sci. Rep.* **2015**, *5*, 8307.

(71) Yu, X.; Lu, B.; Xu, Z. *Adv. Mater.* **2014**, *26*, 1044-1051.

(72) Ma, Z.; Zhao, X.; Gong, C.; Zhang, J.; Zhang, J.; Gu, X.; Tong, L.; Zhou, J.; Zhang, Z. *J. Mater. Chem. A* **2015**, *3*, 13445-13452.

(73) Haque, E.; Islam, M. M.; Pourazadi, E.; Hassan, M.; Faisal, S. N.; Roy, A. K.; Konstantinov, K.; Harris, A. T.; Minett, A. I.; Gomes, V. G. *RSC Adv.* **2015**, *5*, 30679-30686.

(74) Liu, C.; Yu, Z.; Neff, D.; Zhamu, A.; Jang, B. Z. *Nano Lett.* **2010**, *10*, 4863-4868.

(75) Zhao, Z.; Hao, S.; Hao, P.; Sang, Y.; Manivannan, A.; Wu, N.; Liu, H. *J. Mater. Chem. A* **2015**, *3*, 15049-15056.

(76) Tong, Z.; Yang, Y.; Wang, J.; Zhao, J.; Su, B.-L.; Li, Y. *J. Mater. Chem. A* **2014**, *2*, 4642-4651.

(77) Zhao, X.; Zheng, B.; Huang, T.; Gao, C. *Nanoscale* **2015**, *7*, 9399-9404.

(78) Yang, M.; Choi, B. G.; Jung, S. C.; Han, Y.-K.; Huh, Y. S.; Lee, S. B. *Adv. Funct. Mater.* **2014**, *24*, 7301-7309.

(79) Wu, Q.; Xu, Y.; Yao, Z.; Liu, A.; Shi, G. *ACS Nano* **2010**, *4*, 1963-1970.

(80) Le, T.; Yang, Y.; Huang, Z.; Kang, F. *J. Power Sources* **2015**, *278*, 683-692.

(81) Nasini, U. B.; Bairi, V. G.; Ramasahayam, S. K.; Bourdo, S. E.; Viswanathan, T.; Shaikh, A. U. *J. Power Sources* **2014**, *250*, 257-265.

(82) Sun, G.; Liu, J.; Zhang, X.; Wang, X.; Li, H.; Yu, Y.; Huang, W.; Zhang, H.; Chen, P. *Angew. Chem., Int. Ed.* **2014**, *53*, 12576-12580.

(83) Fan, X. M.; Yu, C.; Yang, J.; Ling, Z.; Hu, C.; Zhang, M. D.; Qiu, J. S. *Adv. Energy Mater.* **2015**, *5*, 1401761.

(84) Raj, C. J.; Kim, B. C.; Cho, W.-J.; Lee, W.-g.; Jung, S.-D.; Kim, Y. H.; Park, S. Y.; Yu, K. H. *ACS Appl. Mater. Interfaces* **2015**, *7*, 13405-13414.

(85) Li, B.; Cao, H.; Shao, J.; Qu, M.; Warner, J. H. *J. Mater. Chem.* **2011**, *21*, 5069-5075.

(86) Li, M.; Ding, J.; Xue, J. *J. Mater. Chem. A* **2013**, *1*, 7469-7476.

(87) Wang, Y.; Shi, Z.; Huang, Y.; Ma, Y.; Wang, C.; Chen, M.; Chen, Y. *J. Phys. Chem. C* **2009**, *113*, 13103-13107.

(88) Jiang, L. L.; Sheng, L. Z.; Long, C. L.; Wei, T.; Fan, Z. J. *Adv. Energy Mater.* **2015**, *5*, 1500771.

(89) Yan, J.; Yang, L. P.; Cui, M. Q.; Wang, X.; Chee, K. J. J. Z.; Nguyen, V. C.; Kumar, V.; Sumboja, A.; Wang, M.; Lee, P. S. *Adv. Energy Mater.* **2014**, *4*, 1400781.

(90) Lewis, J.; Raithby, P. R.; Wong, W.-Y. *J. Organomet. Chem.* **1998**, *556*, 219-228.

(91) Hwang, E.; Lusker, K. L.; Garno, J. C.; Losovyj, Y.; Nesterov, E. E. *Chem. Commun.* **2011**, *47*, 11990-11992.

(92)Grelaud, G.; Cifuentes, M. P.; Schwich, T.; Argouarch, G.; Petrie, S.; Stranger, R.; Paul, F.; Humphrey, M. G. *Eur. J. Inorg. Chem.* **2012**, *2012*, 65-75.

(93) Zhang, K.; Mao, L.; Zhang, L. L.; On Chan, H. S.; Zhao, X. S.; Wu, J. *J. Mater. Chem.* **2011**, *21*, 7302-7307.

(94) Jahan, M.; Bao, Q.; Yang, J.-X.; Loh, K. P. *J. Am. Chem. Soc.* **2010**, *132*, 14487-14495.

Chapter 5

Nitrogen-doped Porous Carbon/Graphene Nanosheets Derived from Two-Dimensional Conjugated Microporous Polymer Sandwiches with Promising Capacitive Performance[1]

5.1 Introduction

Supercapacitors are very appealing power sources for various energy storage applications owning to their key advantages, including low cost, rapid charge-discharge kinetics, high power density, superior lifespan and environmental friendliness.[2-4] The merits of porous carbon materials attribute to facts as high chemical stability, lightweight, high specific surface area, good electric conductivity and wide availability thus enabling them to be the primary candidates for electrode materials of electrical double-layer capacitors.[5-9] The ion transport time (τ) is calculated by $\tau = l^2/d$, where l and d are the ionic transport distance and coefficient, respectively.[10] However, the severe pore tortuosity in most available porous carbon material-based electrodes limits their performance, especially the energy density at high current density due to kinetic limitations in ionic diffusion and transport.[11,12] Thus the key to achieve high energy density for porous carbon-based electrodes is to shorten the ion transport time.

In order to address this problem, it is vital to shorten the effective diffusion paths and provide minimized diffusive resistance for maximized mass transport at the electrode/electrolyte interface. As an alternative, nanostructured, two-dimensional (2D) porous carbon materials with their intrinsic large aspect ratios and thinness could significantly shorten the ion transport distance in the nanoscale dimension.[10,11,13-17] In principle, graphene, with its high theoretical specific surface area (2675 $m^2\ g^{-1}$) and capacitance (550 $F\ g^{-1}$), would be a perfect candidate for

elevating the energy density of supercapacitors.[18,19] Therefore, highly conductive graphene-based 2D materials with large aspect ratio and without pore tortuosity have emerged as promising electrodes of high performance supercapacitors.[20-22] Unfortunately, the spontaneously occuring graphene layer overlap and aggregation (self-restacking) during electrode processing and electrical cycling, as a result of strong sheet-to-sheet van der Waals interactions, significantly reduces the "real" surface area that is available for charge storage. The stacking process results in a substantial loss of the overall electrochemical performance.[11,18,19]

On the other hand, chemical modification of graphene enables for a fine-tuning of its physical and chemical properties, for example, improving the solution processability in common solvents.[23-25] Moreover, the covalent functionalization of graphene creates functional groups that can serve as anchor sites for further modification.[26-28] Thus, ultrathin, functionalized graphene nanosheets with large specific surface area are very promising building blocks for constructing hierarchically organized hybrid architectures. Both sides of the functionalized graphene nanosheets can be utilized for the growth of functional coatings (such as microporous polymer networks) to form unique sandwich-type structures.[29,30] Such 2D sandwich-type hybrids are potentially attractive materials for application in catalysis, or electrochemical energy conversation and storage.[30,31]

Conjugated microporous polymers (CMPs) are useful precursors for the pyrolytic formation of porous carbons. They show great potential for various applications, e.g., as catalyst carriers or in gas storage and separation devices, supercapacitors and lithium ion batteries.[29,30,32-35] CMPs are constructed by polymerization of rigid building blocks, called tectons. Heteroatoms (such as B, N, P and S) can be controllably introduced into the CMP networks. The pore size can be defined through the selection of the tectons.[36-38] Consequently, heteroatom-doped porous carbon materials can be obtained by pyrolysis of the CMPs. However, since most of the CMPs are formed under kinetic control, they are mostly obtained as

amorphous powders without long-range order. Carbon materials derived from CMPs usually conserve the morphology of the CMP precursors. Therefore, the direct pyrolysis of CMPs into 2D microporous carbon nanosheets with large aspect ratio and high specific surface area remains a challenge.

In this chapter, we report the functionalization of reduced graphene oxide sheets with 4-iodophenyl functions on both sides of the basal plane. This functionalized graphene then acts both as building block and structure-directing template for the construction of nitrogen-rich graphene-CMP (GMP) sandwiches in a solution-based approach. The resulting GMP hybrids possess large aspect ratio and specific BET surface areas of up to 852 m^2/g. The microporous polymer shells spontaneously grow onto both sides of the graphene templates, thus guaranteeing a full separation of the individual graphene sheets. So, the sandwich-like architecture effectively prevents the agglomeration of graphene planes during high-temperature conversion into nitrogen-doped porous carbon/graphene nanosheets. The obtained hybrid nanosheets have been used as electrode materials for supercapacitor devices with promising capacitive performance, superior to porous carbon materials originating from the corresponding graphene-free CMPs.

5.2 Results and Discussion

5.2.1 Synthesis of Nitrogen-Rich Graphene-CMP Sandwiches (GMPs)

Our synthetic approach to graphene-based conjugated microporous polymer (GMP) sandwiches is illustrated in Scheme 5.1. Reduced graphene oxide (RGO) from the treatment of graphene oxide (GO) with hydrazine hydrate[39] was modified with 4-iodophenyl diazonium salt under aqueous conditions. The iodo functions of the 4-iodophenyl substituents represent good leaving groups (-I)[25] in the aryl-aryl-couplings, thus favouring polymer growth on the surface of the 4-iodophenyl-substituted graphene (RGO-I) sheets. Subsequently, covalently crosslinked microporous polymer networks were grown on both sides of the RGO-I nanosheets, resulting in GMP sandwiches. Tris(4-ethynylphenyl)amine in

combination with aryl halide monomers (2,5-dibromopyridine, 2,5-dibromopyrazine, or 2,4,6-trichloro-1,3,5-triazine) were selected as the representative functional tectons for fabricating the envisaged GMP sandwiches in Sonogashira-Hagihara-type couplings. The precipitated solid materials were collected by filtration and purified by Soxhlet extraction. Finally, the GMP sandwiches were vacuum dried, and denoted as GMP1N, GMP2N and GMP3N for the pyridine-, pyrazine-, and triazine-containing materials, respectively. For comparison, corresponding CMPs without RGO-I templates were also prepared by following similar procedures: the obtained products are named as MP1N, MP2N and MP3N for the pyridine-, pyrazine-, and triazine-containing polymer networks, respectively.

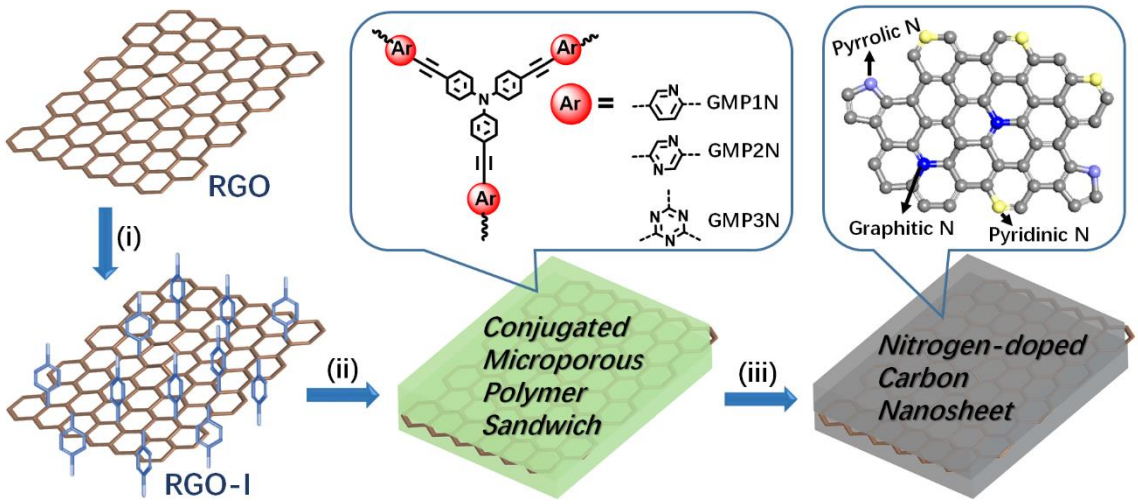

Scheme 5.1 Preparation of graphene-based conjugated microporous polymer sandwiches and related nitrogen-doped microporous carbon nanosheets. (i) Sodium dodecylbenzenesulfonate, 4-iodophenyl diazonium salt, 0 ^{o}C (2 h) to RT (4 h); (ii) building blocks: tris(4-ethynylphenyl)amine and 2,5-dibromopyridine, or 2,5-dibromopyrazine, or 2,4,6-trichloro-1,3,5-triazine, argon, $Pd(PPh_3)_4$, CuI, Et_3N, DMF, 120 ^{o}C, 3 days; (iii) argon, RT to 800 ^{o}C, 10 ^{o}C min^{-1}, 2 h.

5.2.2 Structural Characterization of GMPs

The chemical composition and molecular structure of the GMP sandwiches were studied by Fourier transform infrared (FTIR) spectroscopy (Figure 5.1) and solid-state ^{13}C cross-polarization/magic angle spinning nuclear magnetic resonance (CP/MAS NMR) spectroscopy (Figure 5.2). The FTIR spectra clearly indicate the disappearance of the alkynyl C≡C-H stretching modes near 3300 cm^{-1} of the

tris(4-ethynylphenyl)amine building blocks as well as of the C-Br (ca. 1070 cm^{-1}) or C-Cl (ca. 850 cm^{-1}) modes of the aryl halides (Figure 5.1). In addition, all GMPs exhibited a typical new C≡C stretching mode of diarylacetylenes at about 2200 cm^{-1}, thus suggesting the success of the arylacetylene-aryl coupling. Moreover, the ^{13}C NMR spectrum of GMP1N shows typical diaryl-C≡C peaks signals in the range of 88-90 ppm (Figure 5.3a). The chemical shift at 152 ppm in the ^{13}C NMR spectrum of GMP1N can be assigned to the pyridinic carbons next to the nitrogen atoms (Figure 5.3a). The ^{13}C NMR spectra of GMP2N and GMP3N (Figures 5.2) can be similarly interpreted indicating the successful formation of the CMP networks on the graphene surfaces. X-ray photoelectron spectroscopy (XPS) investigations (Figures 5.1) indicate almost identical components (C, N and O) for all GMPs, as a proof for the structural identity of the GMPs.

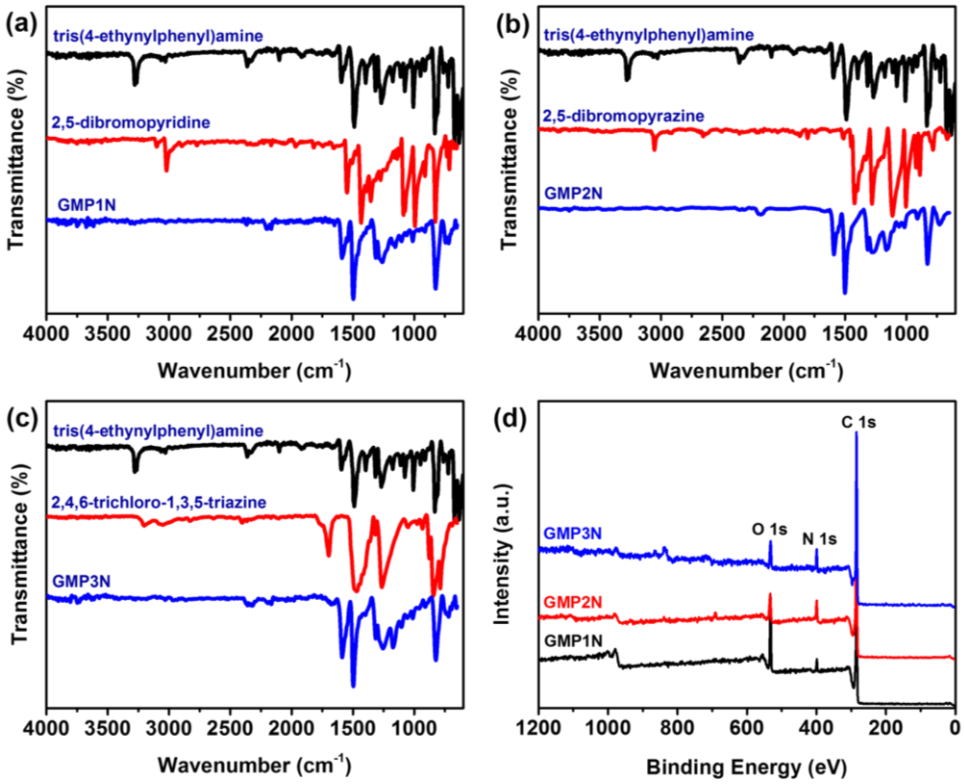

Figure 5.1 (a-c) FTIR spectra of tris(4-ethynylphenyl)amine, the aryl halides (2,5-dibromopyridine, 2,5-dibromopyrazine, and 2,4,6-trichloro-1,3,5-triazine) and the corresponding graphene-based conjugated microporous polymers (GMP1N, GMP2N and GMP3N). (d) XPS spectra of graphene-based, conjugated microporous polymers.

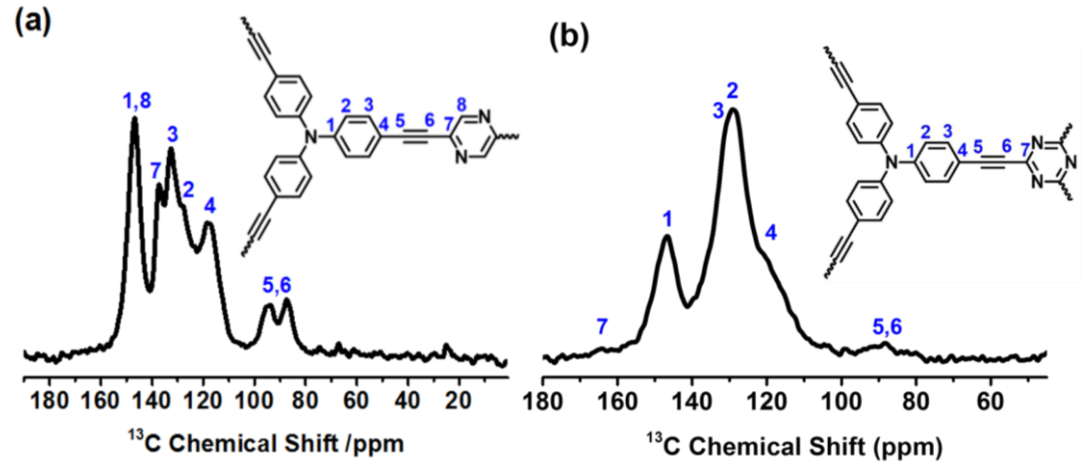

Figure 5.2 ^{13}C CP/MAS NMR spectra of (a) GMP2N and (b) GMP3N.

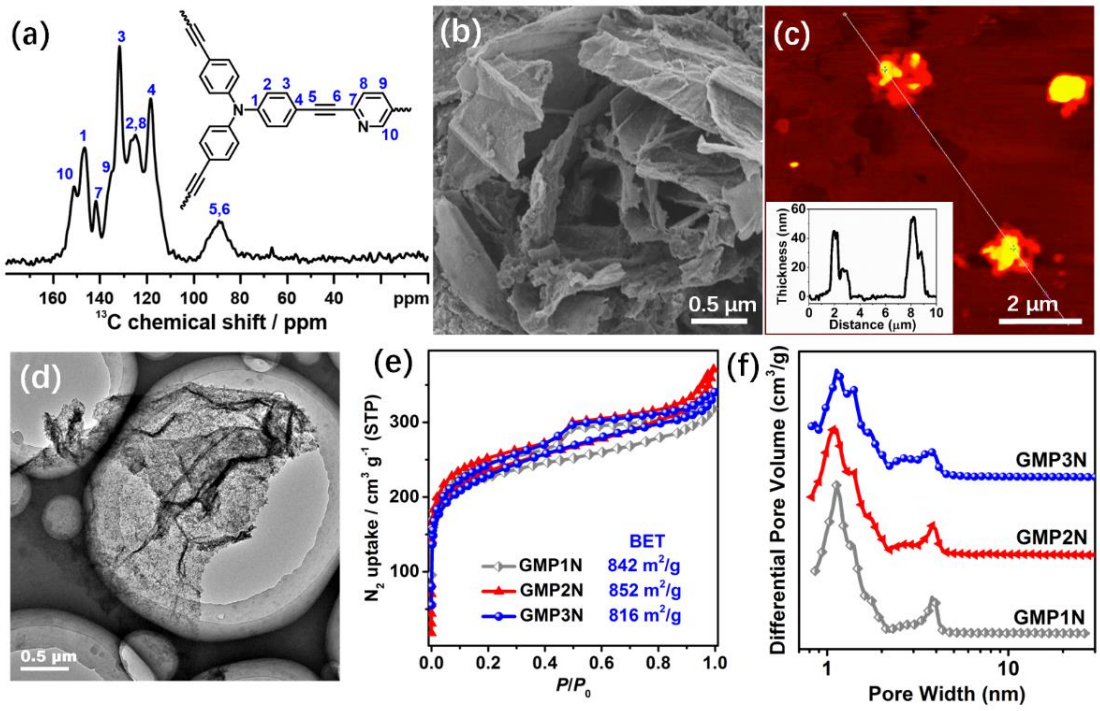

Figure 5.3 Structure and morphological characterization of graphene-based conjugated microporous polymers (GMPs). (a) ^{13}C CP/MAS NMR spectrum of GMP1N. (b) SEM, (c) AFM and (d) TEM images of GMP2N. (e) Nitrogen adsorption/desorption isotherms and (f) pore size distribution profiles of GMPs.

5.2.3 Morphology and Microstructure of GMPs

Morphology and microstructure of our GMPs were examined by scanning electron microscopy (SEM), transmission electron microscopy (TEM), high resolution TEM (HRTEM) and atomic force microscopy (AFM). All GMPs show

similar uniform sheet-like shapes (Figure 5.3b-d and Figure 5.4), reflecting the morphology of the 2D RGO-I templates. No “naked” graphene sheets or “free” polymer particles were observed in either SEM or TEM images. These results imply the preference for formation of hybrids between CMPs and graphene, most of the monomers are deposited on both sides of the graphene sheets under generation of sandwich-like objects. The sandwich-like structure effectively impedes the reagglomeration of graphene sheets, also during the following high-temperature treatment. The sizes of these 2D sandwiches range from hundreds of nanometers to several micrometers. AFM images also illustrate the 2D morphology of the GMPs with a uniform thickness of around 50 nm (Figure 5.3c). As revealed by the TEM images, the wrinkled surface of the nanosheets with numerous dark and light areas (Figure 5.3d) indicates the presence of a porous structure with pores of different sizes. Moreover, the micropores that are homogenously distributed over the GMP nanosheets can be directly visualized by HRTEM (Figure 5.4). In contrast, CMPs synthesized without RGO-I templates are formed as nanoparticles (Figure 5.5). These results confirm that the RGO-I-based template strategy allows for the growth of uniform CMP shells on both sides of the graphene sheets.

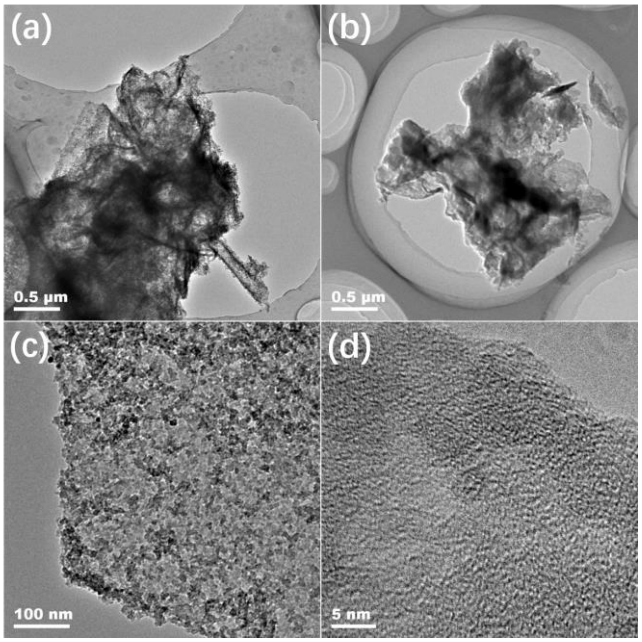

Figure 5.4 TEM images of (a) GMP1N and (b) GMP3N. (c) TEM and (d) HRTEM images of GMP2N.

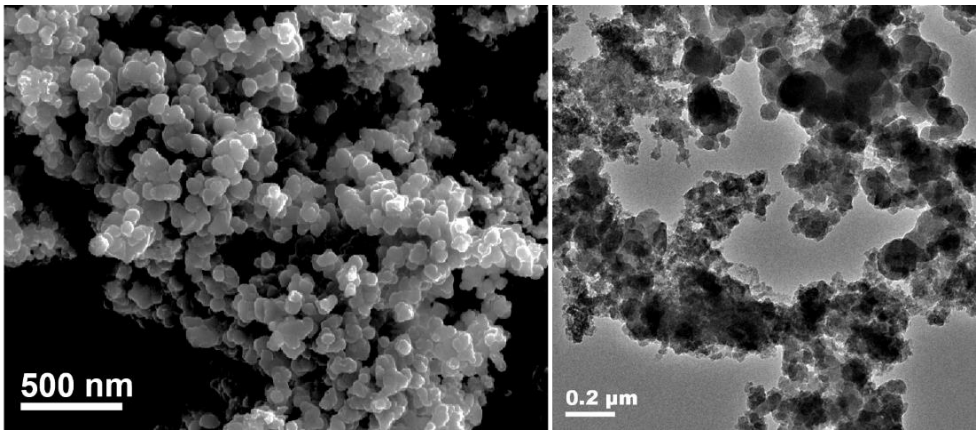

Figure 5.5 SEM (left) and TEM (right) images of MP2N.

5.2.4 Porosity of GMPs

The porosity of the GMPs was investigated by N_2 adsorption/desorption measurements performed at 77K. As indicated in Figure 5.3e, all GMPs feature type-IV isotherms, characteristic for a hierarchical pore structure. The steep adsorption increase in the low p/p_0 region (below 0.1) and the hysteretic loops in the high p/p_0 region reflect the presence of micro- and mesopores, respectively.[40] This hierarchical distribution of pore sizes is also documented in the plots of the cumulative pore volume vs. different relative pressure (Figure 5.6) as well as in the non-localized density functional theory (NLDFT)-derived pore size distribution diagrams (Figure 5.3f). The pore size distribution is of a bimodal shape with maxima at around 1.1 nm and 3.8 nm for the three porous GMPs with Brunauer-Emmet-Teller (BET)-related surface areas of 842, 852 and 816 m^2/g (Table 5.1) for GMP1N, GMP2N and GMP3N, respectively. For comparison, Figure 5.7 presents the sorption isotherms, pore size distributions, and cumulative pore volumes of the graphene-free CMPs. As expected, the graphene-free CMPs exhibit a narrow and unimodal pore size distribution with one maximum centered at around 1.1 nm with the the pore volume and surface area contributions dominatingly from micropores (<2 nm). In accordance with these findings, the graphene-free CMPs show lower BET surface areas of 739, 632 and 699 m^2/g for MP1N, MP2N and MP3N, respectively.

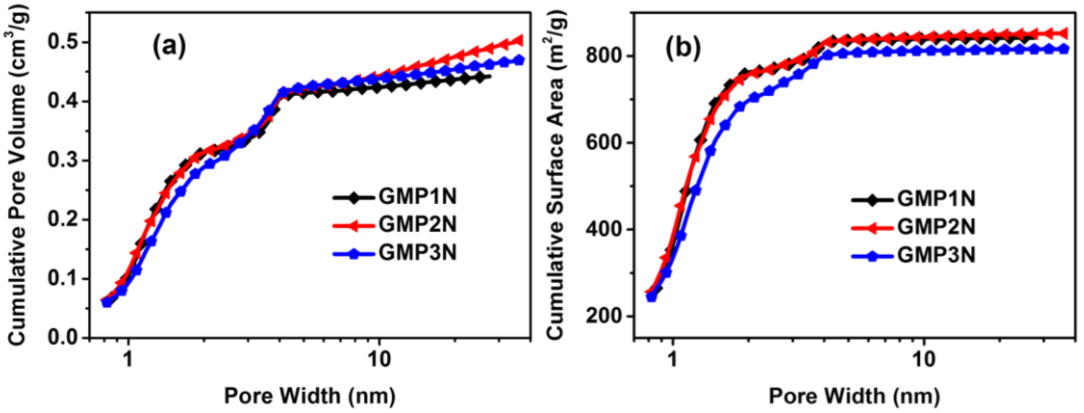

Figure 5.6 (a) Cumulated pore volume and (b) surface area as a function of pore width for graphene-based, conjugated microporous polymers.

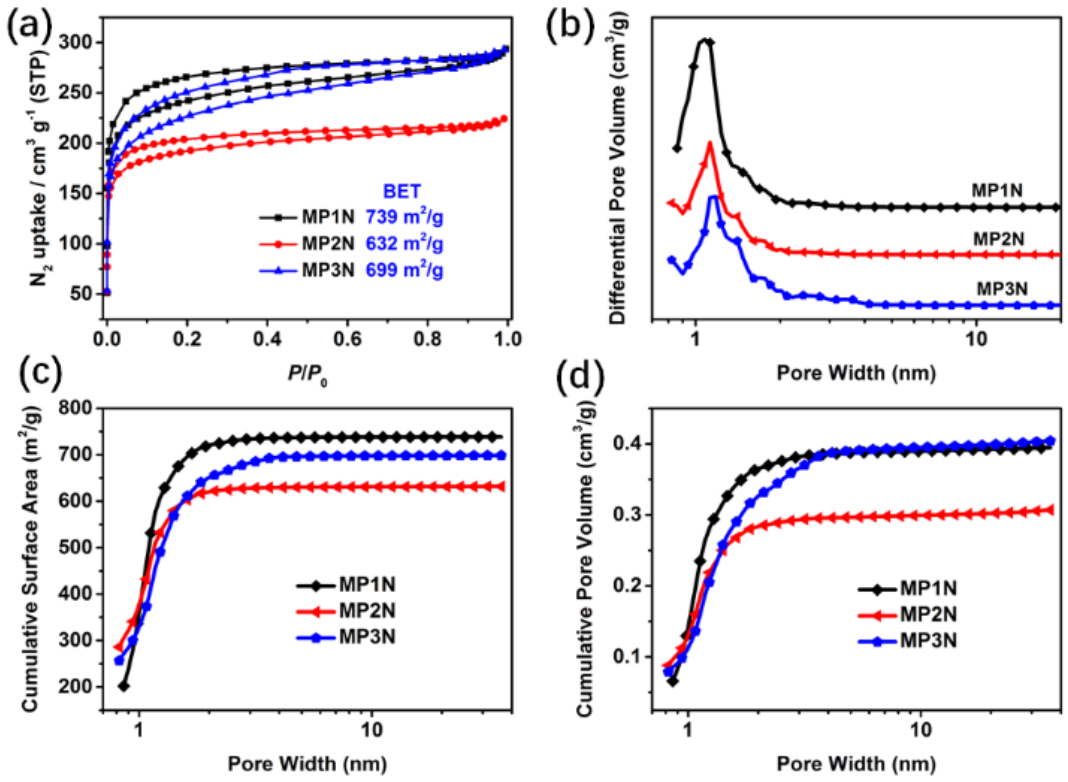

Figure 5.7 (a) Nitrogen adsorption/desorption isotherms, (b) pore size distribution, (c) cumulated surface areas, and (d) pore volumes as function of the pore width for the graphene-free conjugated microporous polymers.

Table 5.1 Summary of the N_2 sorption data for the conjugated porous polymers and graphene-templated, conjugated porous polymers.

sample	S_{BET} (m^2/g)	S_{micro} (m^2/g)	S_{meso} (m^2/g)	V_{total} (cm^3/g)	V_{micro} (cm^3/g)	V_{meso} (cm^3/g)
MP1N	739	722	17	0.39	0.36	0.03
MP2N	632	621	11	0.31	0.28	0.03
MP3N	699	653	46	0.4	0.33	0.07
GMP1N	842	764	78	0.44	0.31	0.13
GMP2N	852	758	94	0.50	0.31	0.19
GMP3N	816	699	117	0.47	0.29	0.18

5.2.5 Pyrolytic Generation and Characterization GMPs-Derived Carbon Nanosheets

Microporous, conjugated polymer networks are attractive precursors for the pyrolytic generation of porous, carbonaceous materials.[29,30,32,41] Thermogravimetric analyses (TGA) suggest that all GMPs are converted into carbon materials with a high yield (ca. 80-90%) at 800 ^oC (Figure 5.8). Therefore, we carried out the further carbonizations at 800 ^oC for achieving a conversion of the N-rich GMPs into N-doped carbon materials. The resulting N-doped carbon nanosheets derived from GMP1N, GMP2N and GMP3N are denoted as GMP1NC, GMP2NC and GMP3NC, respectively. For comparison, porous carbons were also prepared under similar conditions from the graphene-free CMPs, and are named as MP1NC, MP2NC and MP3NC, respectively. SEM and TEM images of GMP2NC (Figure 5.9a,b) reveal that the obtained carbon material still exhibites a well-pronounced nanosheet morphology. The corresponding HRTEM image (Figure 5.9c) shows multilayered, wrinkled graphene-cores that are surrounded by deposits originating from the CMP coatings. The specific surface area of the obtained hybrid carbon nanosheets were measured by the nitrogen sorption technique at 77K (Figure 5.9d): the calculated BET surface areas of GMP1NC, GMP2NC and GMP3NC are 523, 642 and 693 m^2/g (Table 5.2), respectively. The reduction of the BET surface areas for the porous carbon nanosheets if compared to the corresponding GMPs is attributed to some restructuring of the initial polymeric networks with a partial shrinkage of the pores during

pyrolysis.[29,41,42] The type-IV isotherms, the cumulated pore volume-plots for different relative pressures (Figure 5.10) and the NLDFT-based pore size distribution profiles with maxima centered around 1.1 and 3.8 nm (Figure 5.9e-f) suggest the occurrence of a hierarchical porosity with presence of both micro- and mesopores. In contrast, the isotherms of the graphene-free carbons show a dominating gas adsorption at low p/p_0 (below 0.1, Figure 5.11), which is characteristic of a microporous material.[43]

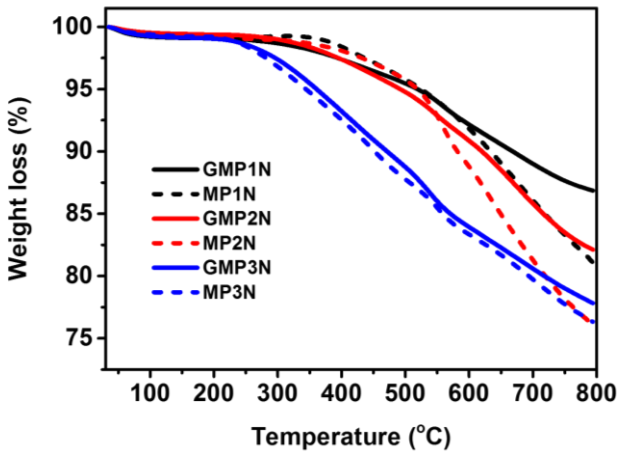

Figure 5.8 TGA profiles of graphene-based, conjugated microporous polymers and corresponding graphene-free, conjugated microporous polymers.

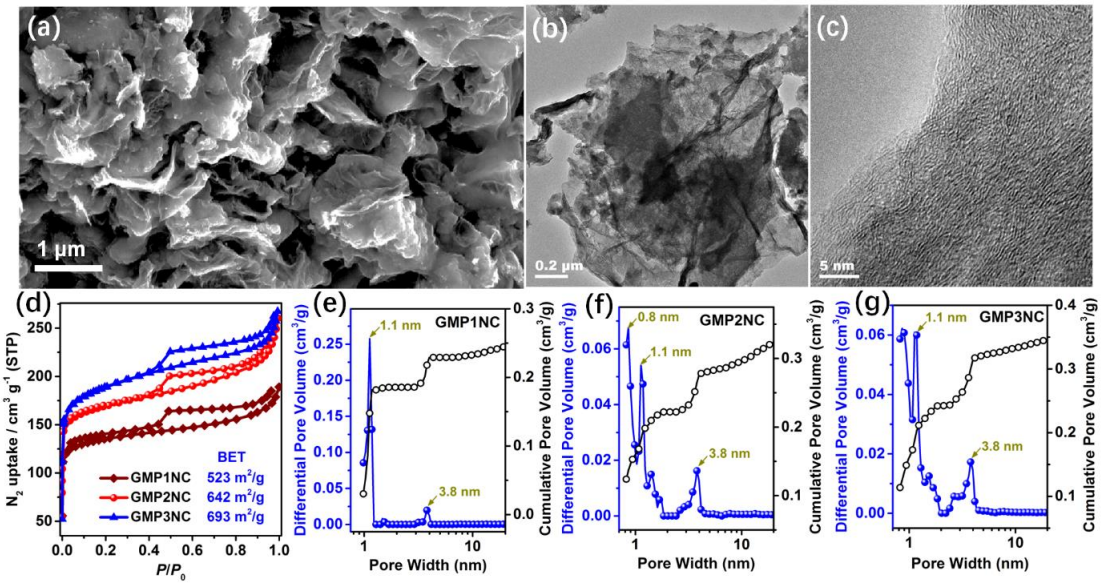

Figure 5.9 (a) SEM, (b) TEM and (c) HRTEM images of GMP2NC. (d) Nitrogen adsorption/desorption isotherms and (e-f) NLDFT-based pore size distribution and cumulated pore volume of GMP-derived carbon nanosheets.

Table 5.2 Summary of the N_2 sorption data for the porous carbon materials without or with graphene templates.

sample	S_{BET} (m^2/g)	S_{micro} (m^2/g)	S_{meso} (m^2/g)	V_{total} (cm^3/g)	V_{micro} (cm^3/g)	V_{meso} (cm^3/g)
MP1NC	746	738	8	0.35	0.28	0.07
MP2NC	883	881	2	0.35	0.33	0.01
MP3NC	909	893	16	0.45	0.34	0.11
GMP1NC	523	483	40	0.26	0.18	0.12
GMP2NC	642	597	45	0.35	0.22	0.13
GMP3NC	693	639	54	0.36	0.24	0.12

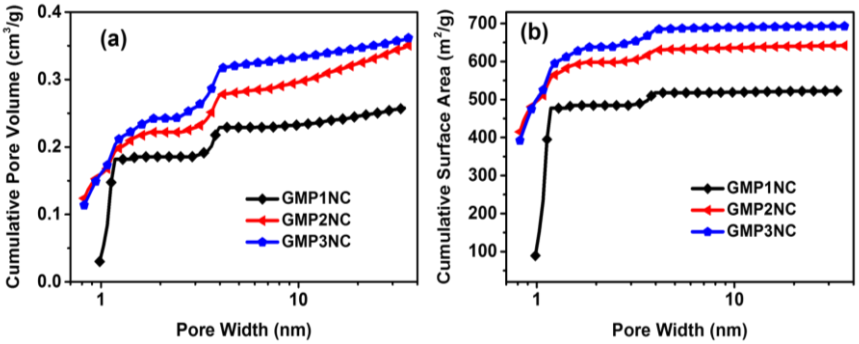

Figure 5.10 (a) Cumulated pore volumes, and (b) surface areas as a function of pore width for GMP-derived carbon nanosheets.

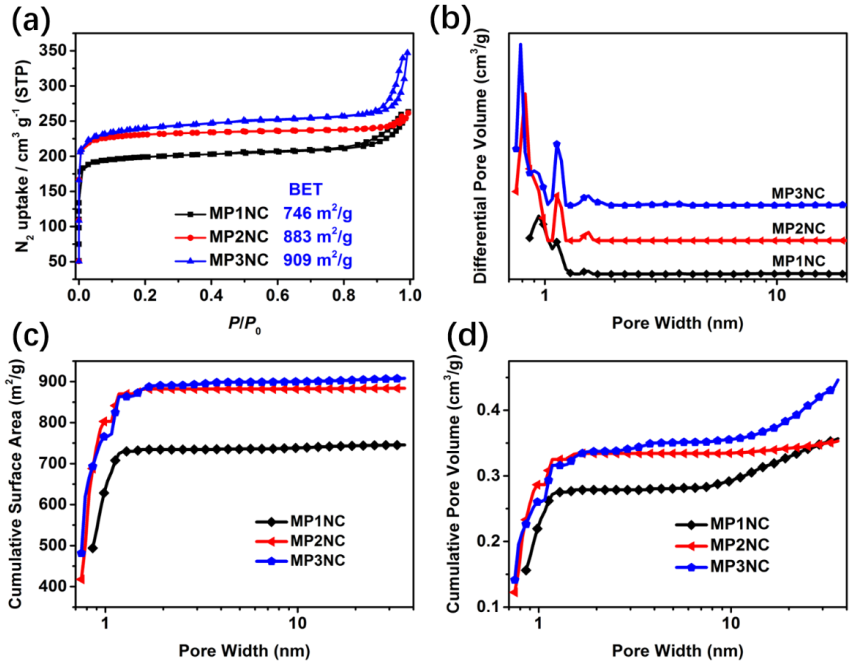

Figure 5.11 (a) Nitrogen adsorption/desorption isotherms, (b) pore size distributions, (c) cumulated surface areas, and (d) pore volumes as function of the pore width for the carbons derived from graphene-free conjugated microporous polymers.

XPS measurements were carried out for a further investigation of bonding states and compositions of the carbon materials. From our XPS results (Figure 5.12a,b and Figure 5.13) the atomic percentages of N in GMP1NC, GMP2NC and GMP3NC is calculated to be about 2.13, 3.05 and 2.61 wt%, respectively. High resolution XPS N 1s spectra of GMP1NC, GMP2NC and GMP3NC (Figure 5.12a) could be deconvoluted into two sub-peaks that have been assigned to pyridinic nitrogens at 398.3 eV and graphitic nitrogens at 400.8 eV, respectively.[44,45] The main sharp peak at ca. 284.6 eV in the high resolution XPS C 1s spectra for the carbonized samples (Figure 5.13) indicates that the majority of carbon atoms is incorporated into graphitic domains.[32] Raman spectra are a versatile characterization tool for carbon materials.[46] As presented in Figure 5.12c, the Raman spectra of GMP1NC, GMP2NC and GMP3NC show relatively strong D bands in relation to the corresponding G bands (I_D/I_G around 1.2). Thereby, the D bands of the carbon materials are attributed to long range disorder and defects. The introduction of N-dopant heteroatoms as defects also contributes to the intensity of the D band.[32]

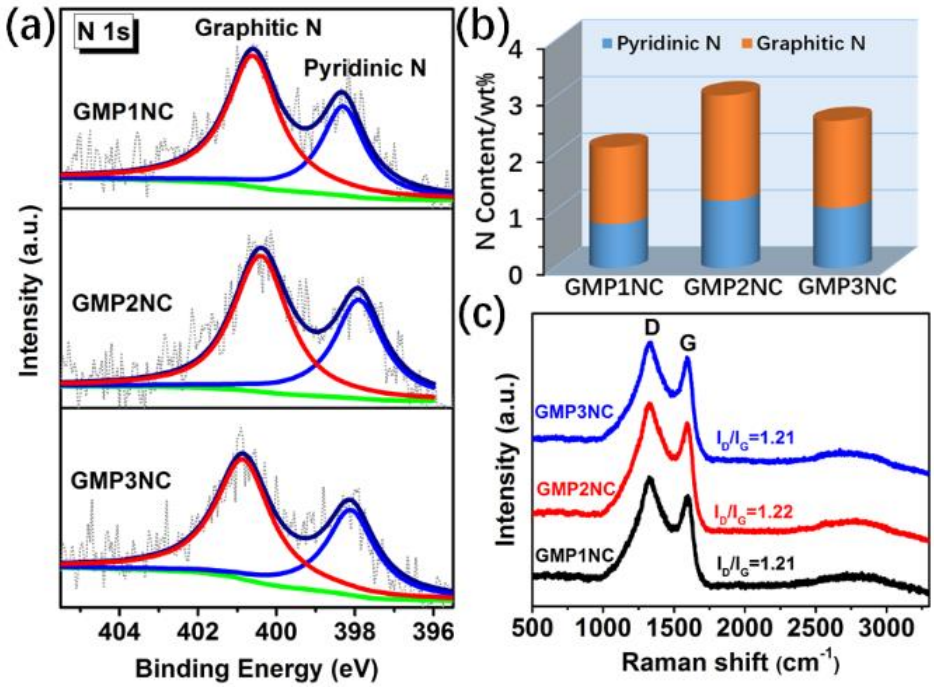

Figure 5.12 (a) High resolution N 1s XPS spectra and (b) the content of different nitrogen species in the GMP-derived carbon nanosheets. (c) Raman spectra of GMP-derived carbon nanosheets.

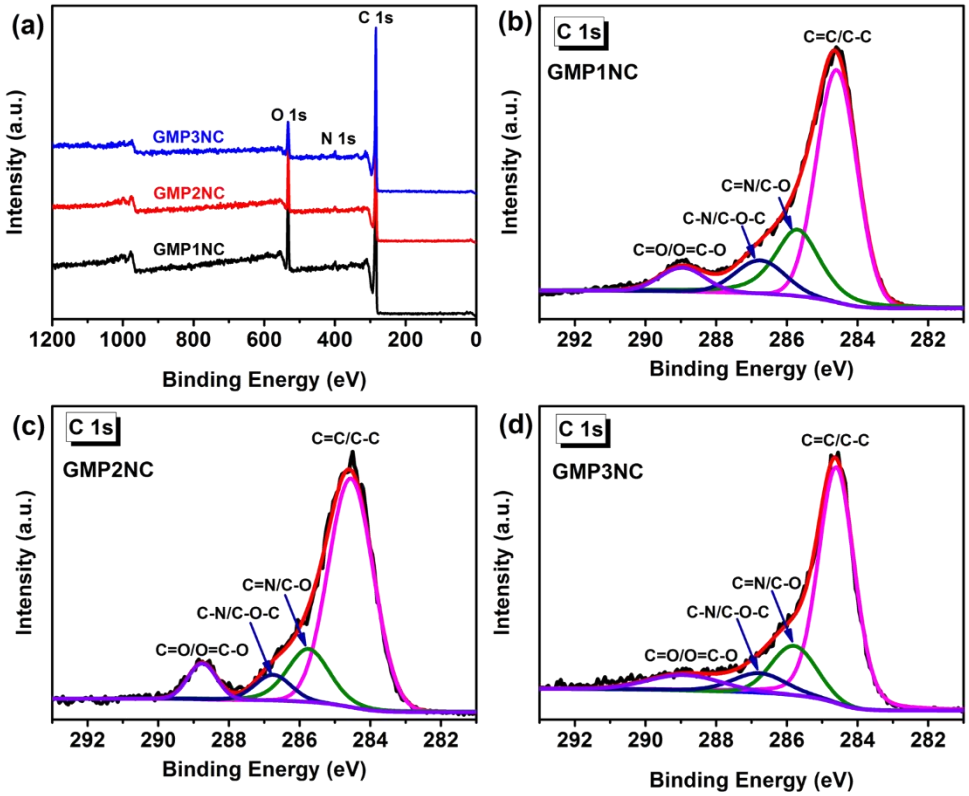

Figure 5.13 (a) XPS spectra of GMP-derived carbon nanosheets. High resolution XPS C 1s spectra of (b) GMP1NC, (c) GMP2NC and (d) GMP3NC.

4.2.6 Electrochemical Properties of GMPs-Derived Carbon Nanosheets

Based on the above discussed hierarchically porous structure with well-defined micro- and mesopores, the N-doping and the well-pronounced 2D morphology, the carbon hybrid nanosheets should be promising candidates for application as electrodes of supercapacitors. In this line, we first investigated the electrochemical properties of the porous carbon nanosheets by cyclic voltammetry (CV) and galvanostatic charge-discharge (GCD) techniques using a three-electrode configuration in 6 M aqueous KOH as electrolyte. Figure 5.14a shows the CV curves of the porous carbon nanosheets and the corresponding carbons derived from the graphene-free CMPs at a scan rate of 100 mV/s in the potential window of -1 to 0 V. The CV curves of the porous carbon materials exhibit a rectangular shape, indicating that the charge storage is mainly governed by a typical, capacitive double-layer behavior. Observed current density and enclosed CV area of the porous carbon

nanosheets are higher than those of the corresponding carbons derived from the graphene-free CMPs, thus showing their higher supercapacitive performance.

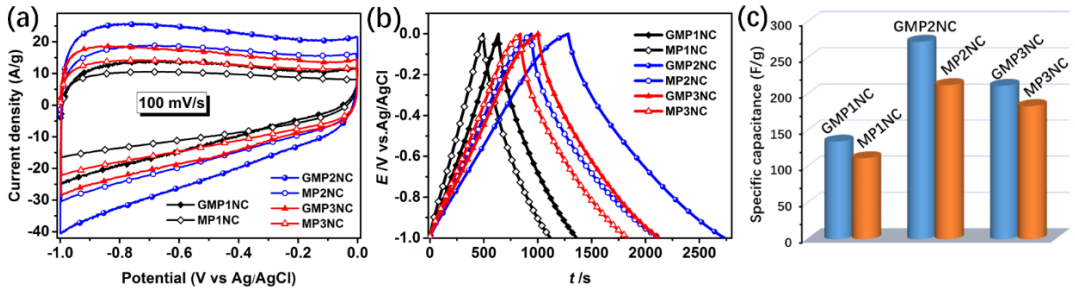

Figure 5.14 (a) Electrochemical characterization of the carbon materials derived from GMPs and graphene-free MPs in three-electrode systems using 6 M aqueous KOH solution as electrolyte. (a) CV curves at a scan rate of 100 mv/s. (b) GCD curves and (c) corresponding gravimetric capacitances at a current density of 0.2 A/g.

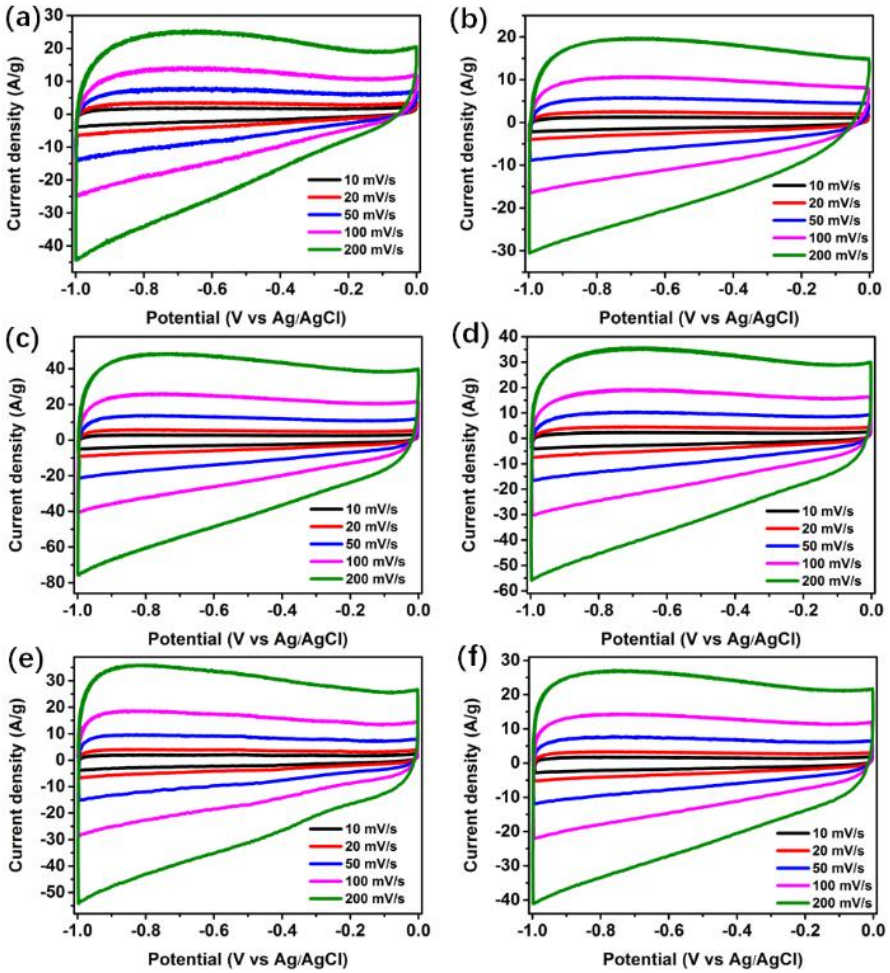

Figure 5.15 CV curves of (a) GMP1NC, (b) MP1NC, (c) GMP2NC, (d) MP2NC, (e) GMP3NC, and (f) MP3NC at different scan rates in a three-electrode system using 6 M aqueous KOH solution as electrolyte.

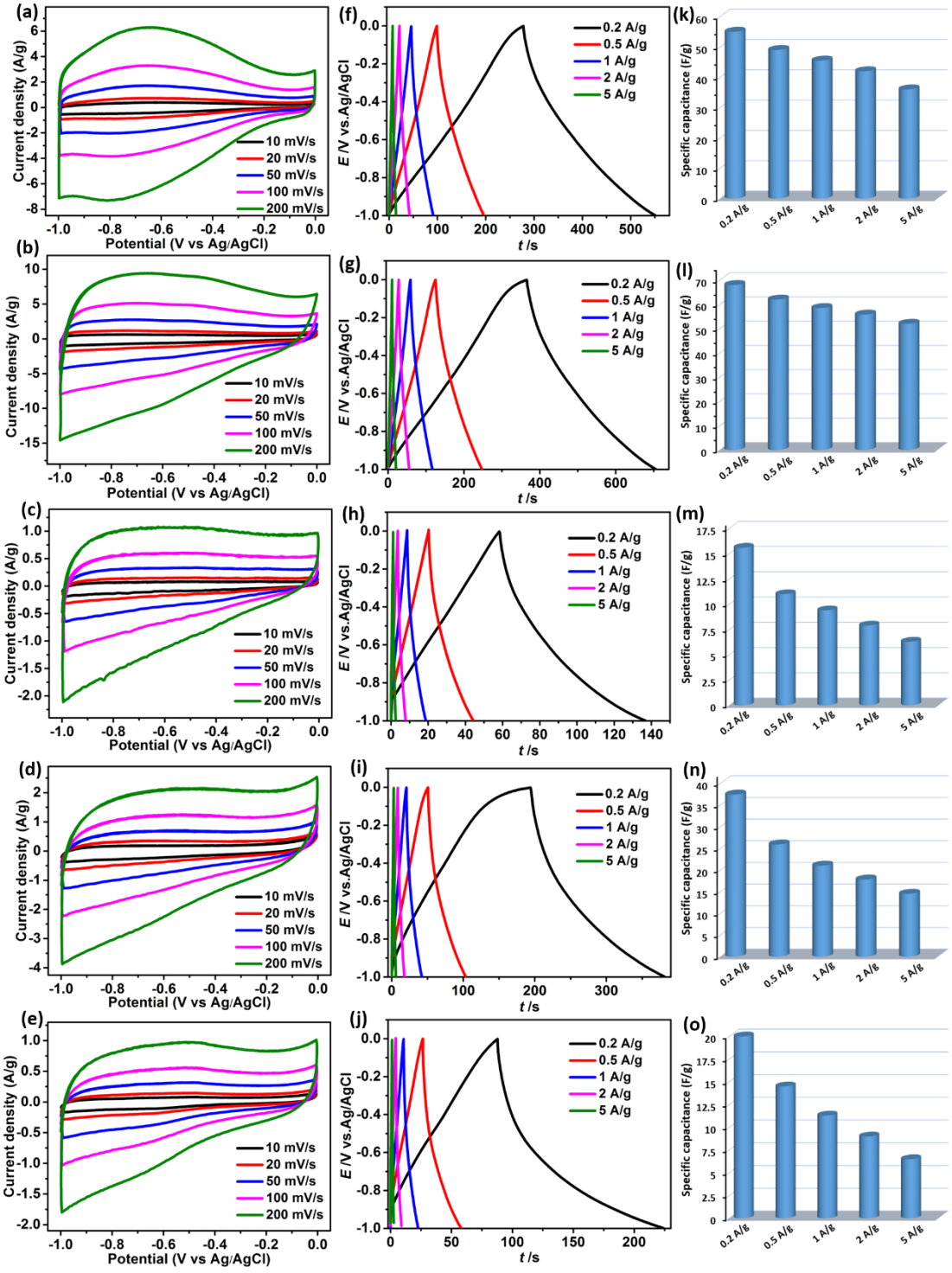

Figure 5.16 (a-e) CV curves for RGO, RGO-I, GMP1N, GMP2N and GMP3N, respectively, at different scan rates in a three-electrode system using 6 M aqueous KOH solution as electrolyte. (f-j) GCD curves and (k-o) gravimetric capacitances for RGO, RGO-I, GMP1N, GMP2N and GMP3N, respectively, at different charge/discharge current densities.

The CV curves of the porous carbon nanosheets at different scan rates from 10 to 200 mV/s are shown in Figure 5.15, the current density linearly increases with the scan rate, implying a good electrochemical reversibility. For comparison, the electrochemical properties of RGO, RGO-I and GMPs were also investigated by CV and GCD (Figure 5.16). Due to their lower electrical conductivity and hydrophobicity, the GMPs show inferior electrochemical properties if compared to the porous carbon nanosheets.

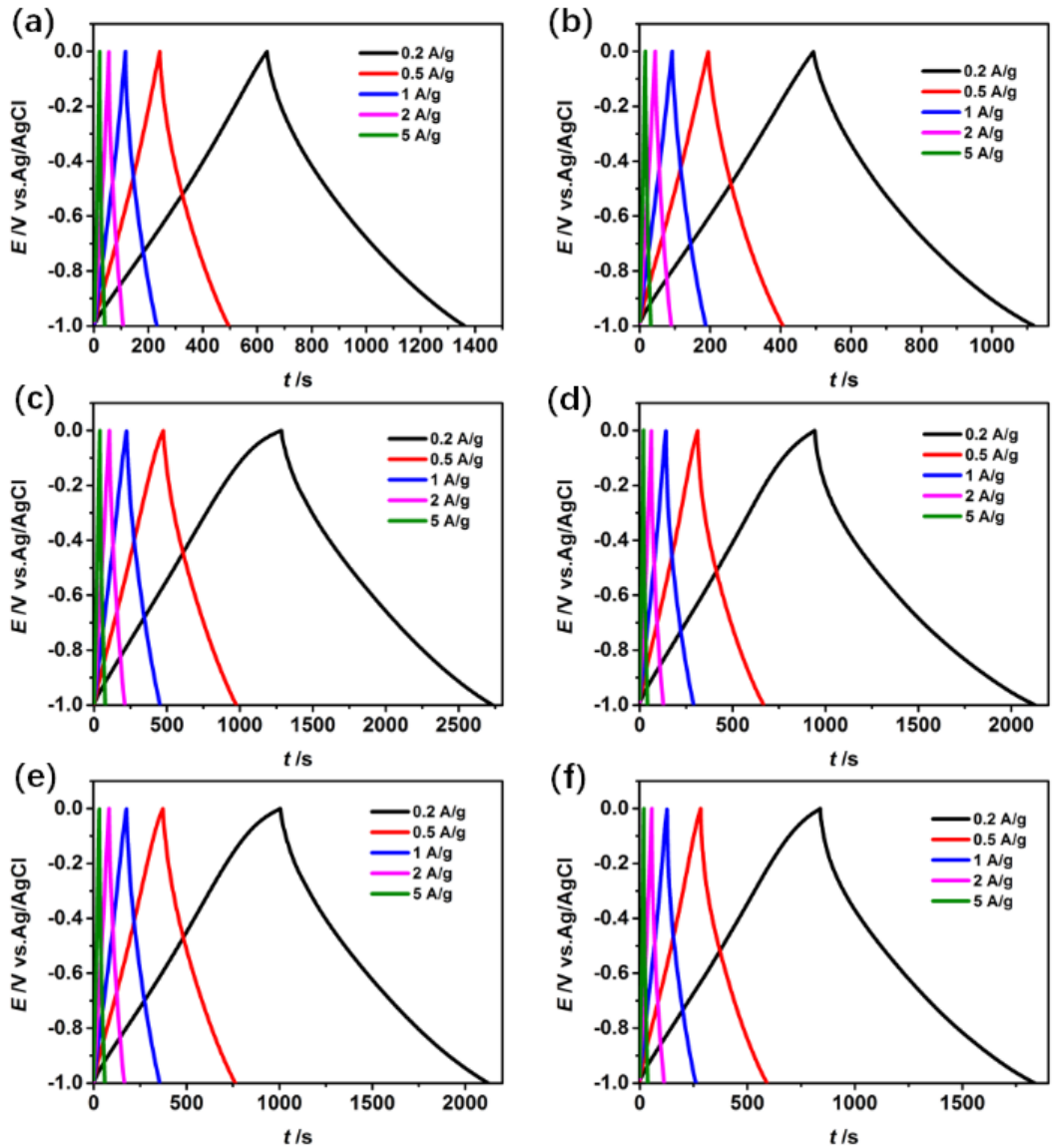

Figure 5.17 GCD curves of (a) GMP1NC, (b) MP1NC, (c) GMP2NC, (d) MP2NC, (e) GMP3NC, and (f) MP3NC at different charge/discharge current densities in a three-electrode system using 6 M aqueous KOH solution as electrolyte.

Figure 5.14b,c present the GCD curves at a current density of 0.2 A/g and the calculated corresponding specific capacitances. The specific capacitances of GMP1NC, GMP2NC and GMP3NC are 135, 273, and 212 F/g at a current density of 0.2 A/g (Figure 5.14c), respectively, again higher than those of the carbons derived from the graphene-free CMPs (112, 213, and 184 F/g for MP1NC, MP2NC and MP3NC, respectively). The GCD profiles and corresponding specific capacitances of the porous carbon materials at different current densities are shown in Figure 5.17-5.18. It should be noted that the capacitance retention of the porous carbon nanosheets is significantly higher than those corresponding carbons derived from the graphene-free CMPs. For example, the calculated specific capacitances of the GMP2NC hybrid are 273 F/g at 0.2 A/g, and 193 F/g at 5 A/g, corresponding to a capacitance retention of 70.7% with the current density increases from 0.2 to 5 A/g. The obtained capacitance values for the graphene-free MP2NC are 213 F/g at 0.2 A/g, and 105 F/g at 5 A/g, corresponding to a capacitance retention of 49.3% with the current density increases from 0.2 to 5 A/g. Moreover, in a peer comparison, our capacitance values for the GMP2NC nanosheets well compare to those of reduced graphene oxides, N-doped graphene, N-doped carbon and other previously reported carbon materials from the literature (Table 5.3).

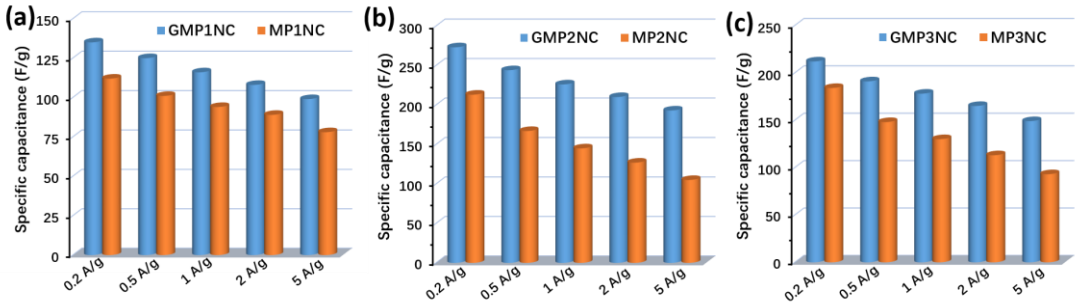

Figure 5.18 Gravimetric capacitances for (a) GMP1NC and MP1NC, (b) GMP2NC and MP2NC, and (c) GMP3NC and MP3NC at different charge/discharge current densities in a three-electrode system using 6 M aqueous KOH solution as electrolyte.

The increased specific capacitance and capacitance retention values of the porous carbon nanosheets should originate from the "implanted" graphene core of the sandwich-like carbon nanosheets. The charge/discharge process takes advantage of

the 2D charge transport ability and superior electrical conductivity of the graphene cores that act as long distance, in-plane charge transporters and collectors.[29,30] In synergy with the nitrogen-doping, large specific surface area and the multiscaled porous structure fast ion and electron transport as well as sufficient space for charge storage are ensured.

Table 5.3 Comparison of the gravimetric capacitances of carbon-based supercapacitor electrode materials from the literature.

Materials	Gravimetric capacitance (F/g)	Electrolyte	References
Reduced graphene oxide	41.5 (0.1 A/g)	6 M KOH	47
Reduced graphite oxide with high density	182 (1 A/g)	6 M KOH	48
High density porous graphene macroform	238 (0.1 A/g)	6 M KOH	49
Porous graphene nanosheets	241 (2 mV s^{-1})	6 M KOH	50
Hydrazine reduced graphene oxide	123 (10 mV s^{-1})	6 M KOH	51
Graphene sponge	204.66 (5 mV s^{-1})	1 M NaCl	52
Activated microwave exfoliated graphite oxide	137 (1 A/g)	BMIM BF_4/AN	53
	154 (1 A/g)	EMIM TFSI/AN	
KOH activated graphene	166 (0.7 A/g)	BMIM BF_4/AN	54
Compressed KOH activated graphene	147 (1.24 A/g)	BMIM BF_4/AN	55
S-porous carbon/graphene	109 (0.05 A/g)	6 M KOH	56
Activated graphene-derived carbon	174	Ionic liquid	57
Nitrogen-enriched nonporous carbon	115 (0.05 A/g)	1 M H_2SO_4	58
Seaweeds derived carbon	198 (2 mV s^{-1})	1 M H_2SO_4	59
Activated carbon aerogel	220 (0.125 A/g)	1 M H_2SO_4	60
Copper nanocrystal modified AC	79 (0.2 A/g)	TEATFB	61
N-doped reduced graphene oxide	255 (0.5 A/g)	6 M KOH	62
3D N,B-co-doped graphene	239 (1 A/g)	1 M H_2SO_4	63
Crumpled N-doped graphene nanosheets	245.9 (1 A/g)	BMIM BF_4/AN	64
3D Nitrogen-doped graphene-CNT	180 (0.5 A/g)	6 M KOH	65
Boron-doped graphene nanoplatelets	160 (1 A/g)	6 M KOH	66
3D porous carbon	176 (10 mV s^{-1})	1 M H_2SO_4	67
GMP2NC	**273 (0.2 A g^{-1})**	**6 M KOH**	**This work**

4.2.7 Electrochemical Properties of GMP2NC- and MP2NC-Based Supercapacitors

To further evaluate the supercapacitive performance of the carbon nanosheets, two-electrode coin-type supercapacitor cells were fabricated using GMP2NC as active materials with 6 M aqueous KOH solution as electrolyte. For comparison, supercapacitors based on graphene-free MP2NC were also fabricated in as similar procedure. The electrochemical performances for the GMP2NC- and MP2NC-based supercapacitors are shown in Figure 5.19. Both CV curves exhibit nearly symmetrical rectangular shapes at the scan rate of 10 mV/s. Increasing the scan rate to 200 mV/s, the GMP2NC-based supercapacitor still maintains a well-pronounced rectangular shape of the CV curve. The enclosed CV area is distinctly higher than that of the MP2NC-based supercapacitor (Figure 5.19a). This difference clearly demonstrates a better supercapacitive behavior for the GMP2NC-based supercapacitor (Figure 5.20).[44,68]

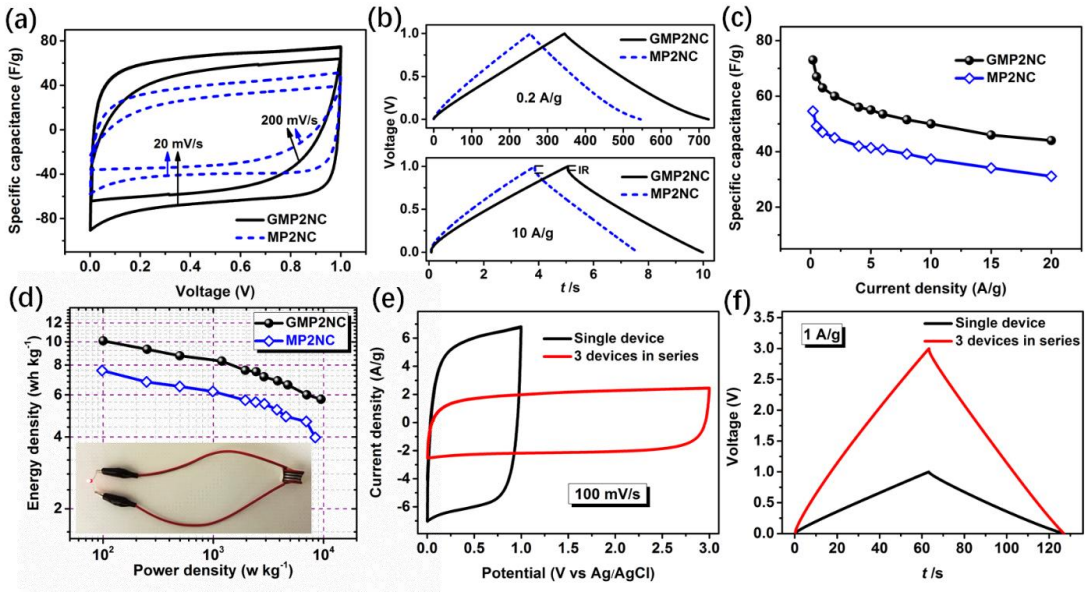

Figure 5.19 Electrochemical characterizations of GMP2NC- and MP2NC-based supercapacitor devices using 6 M aqueous KOH solution as electrolyte. (a) CV curves at the scan rates of 20 and 200 mV/s. (b) GCD curves at the current densities of 0.2 and 10 A/g. (c) Gravimetric capacitances at different charge-discharge current densities. (d) Ragone plots of gravimetric energy versus power density for GMP2NC- and MP2NC-based supercapacitors, the inset shows the photograph of a red light-emitting-diode (LED) powered by three GMP2NC-based supercapacitor devices connected in series. (e) CV and (f) GCD curves of three GMP2NC-based supercapacitor devices connected in series.

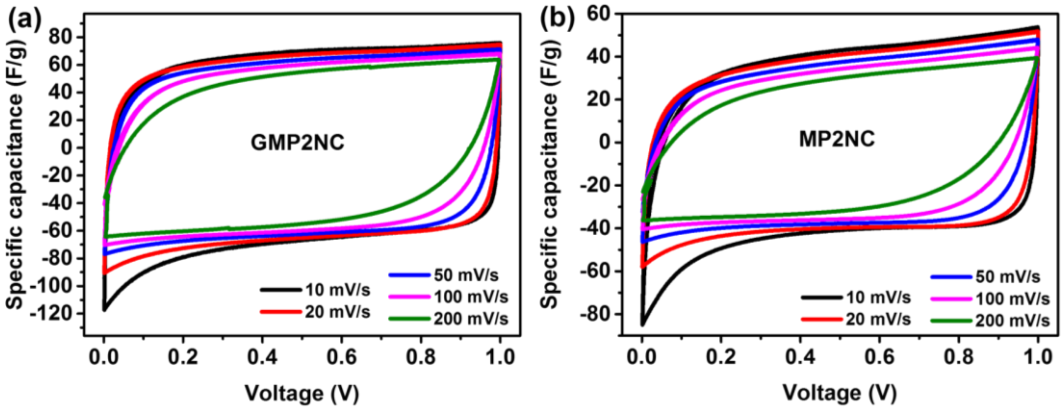

Figure 5.20 CV curves of (a) GMP2NC- and (b) MP2NC-based supercapacitors at the scan rates from 10 to 200 mV/s using 6 M aqueous KOH solution as electrolyte.

Next, GCD measurements were performed for different current densities from 0.2 to 20 A/g to further characterize the supercapacitor performance. The GCD curves of the GMP2NC-based supercapacitor exhibit high symmetry and linear slopes with a limited voltage (*IR*) drop even when the current density is increased to 10 A/g, as depicted in Figure 5.19b. The GMP2NC-based supercapacitor delivers a gravimetric capacitance value of 73 F/g (corresponds to 292 F/g single electrode capacitance) while the MP2NC-based supercapacitor shows a lower gravimetric capacitance of 54.6 F/g (corresponds to 218.4 F/g single electrode capacitance) at 0.2 A/g (Figure 5.19c).[69] For all current densities (0.2-20 A/g), the GMP2NC-based supercapacitor displays smaller *IR* drops and slower slopes if compared to the MP2NC-based supercapacitor (Figure 5.19b and Figure 5.21). These results indicate a higher internal resistance of the MP2NC-based supercapacitor, fully consistent with the aforementioned CV results. Based on this, the area-normalized capacitance values of the GMP2NC-based supercapacitor (e.g. 11.4 μF/cm^2 at 0.2 A/g) are much higher than that of the MP2NC-based supercapacitor (6.2 μF/cm^2 at 0.2 A/g), as presented in Figure 5.22. The Ragone plots (energy vs. power density) of the GMP2NC- and MP2NC-based supercapacitors are shown in Figure 5.19d. The energy density of the GMP2NC-based supercapacitor reaches 10.1 Wh/kg at a current density of 0.2 A/g and with the power density of 9.5 Kw/kg at a current density of 20 A/g. Notably, the energy density is 33% higher than that of MP2N-based supercapacitor (7.58 Wh/kg)

at a current density of 0.2 A/g. In addition, the GMP2NC-based supercapacitor showed excellent cycling stability since ca. 94.7% of the initial capacitance is maintained after a long-term charge/discharge cycling test (5000 cycles) at a current density of 5 A/g, see Figure 5.22.

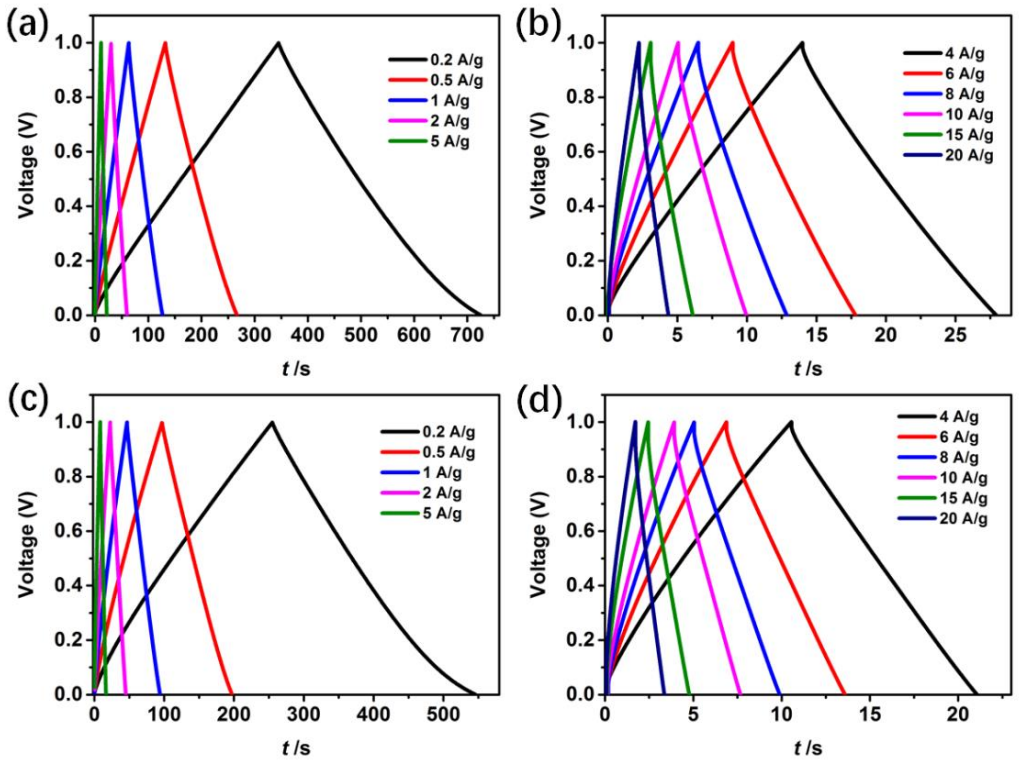

Figure 5.21. GCD curves of (a, b) GMP2NC- and (c, d) MP2NC-based supercapacitors at different charge/discharge current densities using 6 M aqueous KOH solution as electrolyte.

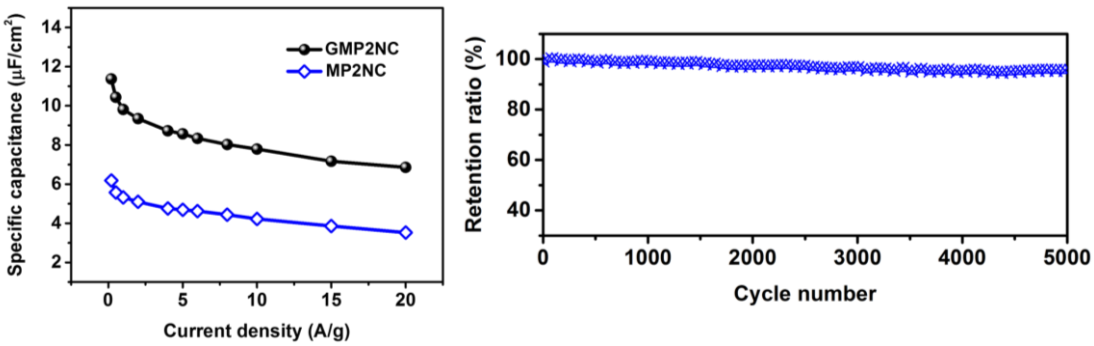

Figure 5.22 (Left) Area-normalized capacitances at different charge-discharge current densities of GMP2NC- and MP2NC-based supercapacitors. (Right) Cycling performance in terms of capacitance retention at 5 A/g for a GMP2NC-based supercapacitor (the capacitance from the first cycle is set to 100%).

Having demonstrated the excellent performance of a GMP2NC-based supercapacitor, we have finally assembled three individual GMP2NC-based supercapacitors in series to meet specific energy needs for various practical applications. The operating voltage of GMP2NC-based supercapacitors connected in series were measured by CV with a scan rate of 100 mV/s (Figure 5.19e). The rectangular CV curves now display an increased voltage window (from 1 V for a single cell to 3 V for three GMP2NC-based supercapacitors in series). As expected, the GCD working voltage of the three connected GMP2NC-based supercapacitors is increased by three times with an almost unchanged charge/discharge time if compared to the single cell supercapacitor at the same current density (Figure 5.19f). The supercapacitors array can be used as a power source when charged with a voltage of 3 V, as exemplified for the lighting of a commercial red light-emitting diode (LED, inset of Figure 5.19d). These results confirm the scalability and high potential of GMP2NC-based supercapacitors for energy supply applications.

5.3 Conclusions

In summary, nitrogen-rich CMP-graphene (GMP) sandwiches have been synthesized in a solution-based approach using 4-iodophenyl-modified graphene (RGO-I) both as building block and structure-directing template. The controllable growth of uniform CMP shells onto both sides of the graphene sheets effectively prevents re-aggregation and restacking of the graphene-based hybrids even during the following high-temperature treatment. Thereby, by direct pyrolysis of the GMP sandwiches well-defined nitrogen-doped porous carbon-graphene nanosheets with large aspect ratio were obtained. The hierarchically porous nitrogen-doped porous carbon-graphene nanosheets were utilized as electrode materials for supercapacitor devices with promising capacitive performance, superior to the performance of the corresponding porous carbons made from graphene-free CMPs. The good conductivity and the 2D electron transport ability of the graphene cores of the carbon nanosheets allow for a fast charge transfer during charging/discharging. Moreover, the intimate contact between porous carbon and graphene layers guarantees an

optimum interfacial interaction. Together, optimized electrode/electrolyte interface and high electrochemically active surface enable for a rapid charge transfer and minimized ion diffusion lengths during the charge/discharge processes, thus effectively elevating the capacitive performance of the supercapacitors.

5.4 Experimental

All reagents, unless otherwise stated, were obtained from commercial sources (Sigma Aldrich, Alfa Aesar and Acros) and were used without further purification.

5.4.1 Synthesis of Graphene-Based Conjugated Microporous Polymers (GMPs)

The GMPs were synthesized by palladium-catalyzed Sonogashira-Hagihara cross-coupling reactions of RGO-I[29,30] with tris(4-ethynylphenyl)amine and the specific aryl halide building block (2,5-dibromopyridine, or 2,5-dibromopyrazine, or 2,4,6-trichloro-1,3,5-triazine, Scheme 5.2). The synthesis of GMP1N as a representative experimental procedure is given below.

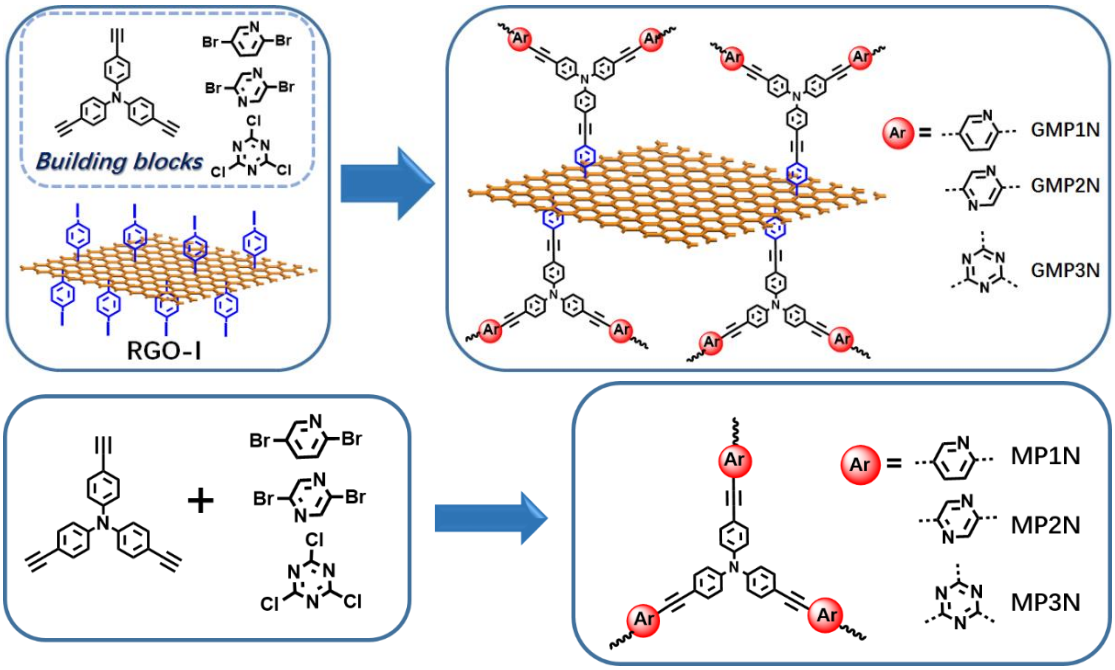

Scheme 5.2 Preparation of graphene-based conjugated microporous polymer sandwiches and corresponding graphene-free conjugated microporous polymers by palladium-catalyzed Sonogashira-Hagihara cross-coupling reaction.

Synthesis of GMP1N. RGO-I (100 mg) was sonicated in dry DMF (150 mL) until complete dispersion occurs. Then, tris(4-ethynylphenyl)amine (317 mg, 1 mmol), 2,5-dibromopyridine, (235mg, 1 mmol), tetrakis-(triphenylphosphine) palladium (35 mg, 0.03 mmol), copper iodide (14 mg, 0.06 mmol), and Et_3N (20 mL) were added to the RGO-I dispersion. The reaction mixture was heated to 120 °C and stirred for 3 days under argon atmosphere. Next, the insoluble, precipitated product was filtered off and washed four times with chloroform, water, and acetone to remove unreacted monomers or catalyst residues. Further purification of the product was carried out by Soxhlet extraction with THF for 48 h. The product was dried under vacuum for 24 h at room temperature to afford GMP1N (yield: 447 mg).

5.4.2 Characterization

Solution NMR spectra were recorded on Bruker AVANCE 400 or AVANCE III 600 machines. ^{1}H and ^{13}C NMR spectra were measured with tetramethylsilane (TMS) as internal standard. Fourier transform infrared (FTIR) spectroscopy was carried out on a JASCO FT/IR-4200 Fourier-Transform-spectrometer. UV-Vis absorption spectra were recorded on a Shimadzu UV-2401 PC spectrophotometer at room temperature. The morphology of G-CMPs and corresponding carbon nanosheets were characterized by transmission electron microscopy (TEM, JEOL, JEM-2100F). The TEM samples were prepared by transferring G-CMPs and corresponding carbon nanosheets onto copper grids. Thermogravimetric analysis were performed on a Mettler Toledo TGA Stare System under argon flow. Raman spectra were recorded on a LabRAM HR Raman Microscope with an excitation wavelength of 514 nm. X-ray photoelectron spectroscopy (XPS) was carried out on a Kratos AXIS Ultra, performing at 15 kV and 15 mA with a monochromatic Al Kα source (hν = 1486.71 eV).

Nitrogen adsorption-desorption measurements. The nitrogen adsorption-desorption measurements were performed on a BELSORB Max (BEL Japan Inc.). The surface areas were calculated using the BET model in the pressure range p/p_0 from 0.05-0.3. The total pore volume was determined at a relative pressure

of 0.99. The pore size distribution was analyzed from the nitrogen adsorption data using by NLDFT analysis with a slit pore model.

Solid-state NMR measurements. The measurements have been performed on a Bruker Avance III console operating at 700 MHz 1H Larmor frequency, using a commercial 2.5 mm double resonance MAS NMR probe, spinning at 25 kHz MAS spinning frequency. The CP contact time was 2ms in order to sufficiently polarize even non-protonated 13C sites.

5.4.3 Supercapacitor Fabrication

Coin-cell-type symmetric supercapacitors were fabricated to evaluate the supercapacitive performance. Briefly, 80 wt% porous carbon materials (GMP2NC or MP2NC), 10 wt% active carbon, and 10 wt% polyvinylidene fluoride (PVDF, as binder) were homogeneously mixed into a paste. Then, the mixture was rolled onto a nickel foil as current collector. After drying at 120 ^{o}C overnight, the electrodes/collectors were assembled into CR2032 stainless steel coin cells with 6 M aqueous KOH solution and a porous cellulose membrane as electrolyte and separator, respectively. The following cyclic voltammetry (CV) and galvanostatic charge/discharge (GCD) measurements were performed using a PAR VersaSTAT 4 electrochemical workstation.

5.5 References

(1) Yuan, K.; Hu, T.; Xu, Y.; Graf, R.; Shi, L.; Forster, M.; Pichler, T.; Riedl, T.; Chen, Y.; Scherf, U. *Mater. Chem. Front.* **2017,** DOI: 10.1039/C6QM00012F.

(2) Gogotsi, Y.; Simon, P. *Science* **2011**, *334*, 917-918.

(3) Simon, P.; Gogotsi, Y.; Dunn, B. *Science* **2014**, *343*, 1210-1211.

(4) Yan, J.; Wang, Q.; Wei, T.; Fan, Z. J. *Adv. Energy Mater.* **2014**, *4*, 1300816.

(5) Wang, Q.; Yan, J.; Fan, Z. *Energy Environ. Sci.* **2016**, *9*, 729-762.

(6) Zhang, L. L.; Zhao, X. S. *Chem. Soc. Rev.* **2009**, *38*, 2520-2531.

(7) Simon, P.; Gogotsi, Y. *Nat. Mater.* **2008**, *7*, 845-854.

(8) Zhai, Y.; Dou, Y.; Zhao, D.; Fulvio, P. F.; Mayes, R. T.; Dai, S. *Adv. Mater.* **2011**, *23*, 4828-4850.

(9) Lin, T.; Chen, I.-W.; Liu, F.; Yang, C.; Bi, H.; Xu, F.; Huang, F. *Science* **2015**, *350*, 1508-1513.

(10) Wang, H.; Xu, Z.; Kohandehghan, A.; Li, Z.; Cui, K.; Tan, X.; Stephenson, T. J.; King'ondu, C. K.; Holt, C. M. B.; Olsen, B. C.; Tak, J. K.; Harfield, D.; Anyia, A. O.; Mitlin, D. *ACS Nano* **2013**, *7*, 5131-5141.

(11) Zheng, X.; Luo, J.; Lv, W.; Wang, D. W.; Yang, Q. H. *Adv. Mater.* **2015**, *27*, 5388-5395.

(12) Fan, X. M.; Yu, C.; Yang, J.; Ling, Z.; Hu, C.; Zhang, M. D.; Qiu, J. S. *Adv. Energy Mater.* **2015**, *5*, 1401761.

(13) Hou, J.; Cao, C.; Idrees, F.; Ma, X. *ACS Nano* **2015**, *9*, 2556-2564.

(14) Krishnan, D.; Raidongia, K.; Shao, J.; Huang, J. *ACS Nano* **2014**, *8*, 449-457.

(15) Sevilla, M.; Fuertes, A. B. *ACS Nano* **2014**, *8*, 5069-5078.

(16) Ling, Z.; Wang, Z.; Zhang, M.; Yu, C.; Wang, G.; Dong, Y.; Liu, S.; Wang, Y.; Qiu, J. *Adv. Funct. Mater.* **2016**, *26*, 111-119.

(17) Fan, Z.; Liu, Y.; Yan, J.; Ning, G.; Wang, Q.; Wei, T.; Zhi, L.; Wei, F. *Adv. Energy Mater.* **2012**, *2*, 419-424.

(18) Raccichini, R.; Varzi, A.; Passerini, S.; Scrosati, B. *Nat. Mater.* **2015**, *14*, 271-279.

(19) El-Kady, M. F.; Strong, V.; Dubin, S.; Kaner, R. B. *Science* **2012**, *335*, 1326-1330.

(20) Bonaccorso, F.; Colombo, L.; Yu, G.; Stoller, M.; Tozzini, V.; Ferrari, A. C.; Ruoff, R. S.; Pellegrini, V. *Science* **2015**, *347*, 1246501.

(21) Shao, Y.; El-Kady, M. F.; Wang, L. J.; Zhang, Q.; Li, Y.; Wang, H.; Mousavi, M. F.; Kaner, R. B. *Chem. Soc. Rev.* **2015**, *44*, 3639-3665.

(22) Xu, C.; Xu, B.; Gu, Y.; Xiong, Z.; Sun, J.; Zhao, X. S. *Energy Environ. Sci.* **2013**, *6*, 1388-1414.

(23) Lomeda, J. R.; Doyle, C. D.; Kosynkin, D. V.; Hwang, W.-F.; Tour, J. M. *J. Am. Chem. Soc.* **2008**, *130*, 16201-16206.

(24) Zhu, Y.; Higginbotham, A. L.; Tour, J. M. *Chem. Mater.* **2009**, *21*, 5284-5291.

(25) Yuan, K.; Xu, Y.; Uihlein, J.; Brunklaus, G.; Shi, L.; Heiderhoff, R.; Que, M.; Forster, M.; Chasse, T.; Pichler, T.; Riedl, T.; Chen, Y.; Scherf, U. *Adv. Mater.* **2015**, *27*, 6714-6721.

(26) Dubey, G.; Urcuyo, R.; Abb, S.; Rinke, G.; Burghard, M.; Rauschenbach, S.; Kern, K. *J. Am. Chem. Soc.* **2014**, *136*, 13482-13485.

(27) Criado, A.; Melchionna, M.; Marchesan, S.; Prato, M. *Angew. Chem., Int. Ed.* **2015**, *54*, 10734-10750.

(28) Jahan, M.; Bao, Q.; Loh, K. P. *J. Am. Chem. Soc.* **2012**, *134*, 6707-6713.

(29) Zhuang, X.; Zhang, F.; Wu, D.; Forler, N.; Liang, H.; Wagner, M.; Gehrig, D.; Hansen, M. R.; Laquai, F.; Feng, X. *Angew. Chem., Int. Ed.* **2013**, *52*, 9668-9672.

(30) Zhuang, X.; Gehrig, D.; Forler, N.; Liang, H.; Wagner, M.; Hansen, M. R.; Laquai, F.; Zhang, F.; Feng, X. *Adv. Mater.* **2015**, *27*, 3789-3796.

(31) Liu, S.; Gordiichuk, P.; Wu, Z. S.; Liu, Z.; Wei, W.; Wagner, M.; Mohamed-Noriega, N.; Wu, D.; Mai, Y.; Herrmann, A.; Mullen, K.; Feng, X. *Nat. Commun.* **2015**, *6*, 8817.

(32) Xiang, Z.; Cao, D.; Huang, L.; Shui, J.; Wang, M.; Dai, L. *Adv. Mater.* **2014**, *26*, 3315-3320.

(33) Lin, Q.; Bu, X.; Kong, A.; Mao, C.; Bu, F.; Feng, P. *Adv. Mater.* **2015**, *27*, 3431-3436.

(34) Liao, Y. Z.; Weber, J.; Faul, C. F. J. *Macromolecules.* **2015**, *48*, 2064-2073.

(35) Talapaneni, S. N.; Hwang, T. H.; Je, S. H.; Buyukcakir, O.; Choi, J. W.; Coskun, A. *Angew. Chem., Int. Ed.* **2016**, *55*, 3106-3111.

(36) Xu, Y.; Jin, S.; Xu, H.; Nagai, A.; Jiang, D. *Chem. Soc. Rev.* **2013**, *42*, 8012-8031.

(37) Cooper, A. I. *Adv. Mater.* **2009**, *21*, 1291-1295.

(38) Sakaushi, K.; Antonietti, M. *Acc. Chem. Res.* **2015**, *48*, 1591-1600.

(39) Li, D.; Muller, M. B.; Gilje, S.; Kaner, R. B.; Wallace, G. G. *Nat. Nanotechnol.* **2008**, *3*, 101-105.

(40) Du, R.; Zhang, N.; Xu, H.; Mao, N.; Duan, W.; Wang, J.; Zhao, Q.; Liu, Z.; Zhang, J. *Adv. Mater.* **2014**, *26*, 8053-8058.

(41) Yuan, K.; Guo-Wang, P.; Hu, T.; Shi, L.; Zeng, R.; Forster, M.; Pichler, T.; Chen, Y.; Scherf, U. *Chem. Mater.* **2015**, *27*, 7403-7411.

(42) Zhuang, X.; Zhang, F.; Wu, D.; Feng, X. *Adv. Mater.* **2014**, *26*, 3081-3086.

(43) Assresahegn, B. D.; Belanger, D. *Adv. Funct. Mater.* **2015**, *25*, 6775-6785.

(44) Zhao, J.; Lai, H.; Lyu, Z.; Jiang, Y.; Xie, K.; Wang, X.; Wu, Q.; Yang, L.; Jin, Z.; Ma, Y.; Liu, J.; Hu, Z. *Adv. Mater.* **2015**, *27*, 3541-3545.

(45) Chen, S.; Bi, J.; Zhao, Y.; Yang, L.; Zhang, C.; Ma, Y.; Wu, Q.; Wang, X.; Hu, Z. *Adv. Mater.* **2012**, *24*, 5593-5597.

(46) Ferrari, A. C.; Basko, D. M. *Nat. Nanotechnol.* **2013**, *8*, 235-246.

(47) Lei, Z.; Christov, N.; Zhao, X. S. *Energy Environ. Sci.* **2011**, *4*, 1866-1873.

(48) Li, Y.; Zhao, D. *Chem. Commun.* **2015**, *51*, 5598-5601.

(49) Tao, Y.; Xie, X.; Lv, W.; Tang, D. M.; Kong, D.; Huang, Z.; Nishihara, H.; Ishii, T.; Li, B.; Golberg, D.; Kang, F.; Kyotani, T.; Yang, Q. H. *Sci. Rep.* **2013**, *3*, 2975.

(50) Fan, Z.; Zhao, Q.; Li, T.; Yan, J.; Ren, Y.; Feng, J.; Wei, T. *Carbon* **2012**, *50*, 1699-1703.

(51) Yan, J.; Wei, T.; Shao, B.; Ma, F.; Fan, Z.; Zhang, M.; Zheng, C.; Shang, Y.; Qian, W.; Wei, F. *Carbon* **2010**, *48*, 1731-1737.

(52) Xu, X.; Sun, Z.; Chua, D. H.; Pan, L. *Sci. Rep.* **2015**, *5*, 11225.

(53) Ghaffari, M.; Zhou, Y.; Xu, H.; Lin, M.; Kim, T. Y.; Ruoff, R. S.; Zhang, Q. M. *Adv. Mater.* **2013**, *25*, 4879-4885.

(54) Zhu, Y.; Murali, S.; Stoller, M. D.; Ganesh, K. J.; Cai, W.; Ferreira, P. J.; Pirkle, A.; Wallace, R. M.; Cychosz, K. A.; Thommes, M.; Su, D.; Stach, E. A.; Ruoff, R. S. *Science* **2011**, *332*, 1537-1541.

(55) Murali, S.; Quarles, N.; Zhang, L. L.; Potts, J. R.; Tan, Z.; Lu, Y.; Zhu, Y.; Ruoff, R. S. *Nano Energy* **2013**, *2*, 764-768.

(56) Seredych, M.; Bandosz, T. J. *J. Mater. Chem. A* **2013**, *1*, 11717-11727.

(57) Kim, T.; Jung, G.; Yoo, S.; Suh, K. S.; Ruoff, R. S. *ACS Nano* **2013**, *7*,

6899-6905.

(58) Hulicova-Jurcakova, D.; Kodama, M.; Shiraishi, S.; Hatori, H.; Zhu, Z. H.; Lu, G. Q. *Adv. Funct. Mater.* **2009**, *19*, 1800-1809.

(59) Raymundo-Piñero, E.; Leroux, F.; Béguin, F. *Adv. Mater.* **2006**, *18*, 1877-1882.

(60) Zapata-Benabithe, Z.; Carrasco-Marín, F.; Moreno-Castilla, C. *J. Power Sources* **2012**, *219*, 80-88.

(61) Zhang, L.; Candelaria, S. L.; Tian, J.; Li, Y.; Huang, Y.-x.; Cao, G. *J. Power Sources* **2013**, *236*, 215-223.

(62) Lei, Z.; Lu, L.; Zhao, X. S. *Energy Environ. Sci.* **2012**, *5*, 6391-6399.

(63) Wu, Z.-S.; Winter, A.; Chen, L.; Sun, Y.; Turchanin, A.; Feng, X.; Müllen, K. *Adv. Mater.* **2012**, *24*, 5130-5135.

(64) Wen, Z.; Wang, X.; Mao, S.; Bo, Z.; Kim, H.; Cui, S.; Lu, G.; Feng, X.; Chen, J. *Adv. Mater.* **2012**, *24*, 5610-5616.

(65) You, B.; Wang, L.; Yao, L.; Yang, J. *Chem. Commun.* **2013**, *49*, 5016-5018.

(66) Han, J.; Zhang, L. L.; Lee, S.; Oh, J.; Lee, K.-S.; Potts, J. R.; Ji, J.; Zhao, X.; Ruoff, R. S.; Park, S. *ACS Nano* **2013**, *7*, 19-26.

(67) Wu, Z.-S.; Sun, Y.; Tan, Y.-Z.; Yang, S.; Feng, X.; Müllen, K. *J. Am. Chem. Soc.* **2012**, *134*, 19532-19535.

(68) Hao, L.; Ning, J.; Luo, B.; Wang, B.; Zhang, Y.; Tang, Z.; Yang, J.; Thomas, A.; Zhi, L. *J. Am. Chem. Soc.* **2014**, *137*, 219-225.

(69) Zhang, J.; Jiang, J.; Li, H.; Zhao, X. S. *Energy Environ. Sci.* **2011**, *4*, 4009-4015.

Chapter 6

Two-dimensional Core-Shelled Porous Hybrids as Highly Efficient Catalysts for Oxygen Reduction Reaction[1]

6.1 Introduction

Graphene as the best-known two-dimensional (2D) nanomaterial has been intensively studied due to its exceptional physical and chemical properties since 2004.[2] Covalent functionalization of graphene has been demonstrated as a viable approach for tailoring the electronic and chemical properties of graphene based materials, enabling the introduction of reactive groups for subsequent functionalization.[3-7] Functionalized graphenes are promising templates for the construction of 2D hybrid materials, such as 2D metal oxides, metal sulfides, carbon nanosheets, and microporous polymer hybrids.[8-12] Beyond graphene, more and more other 2D nanomaterials attracted tremendous attentions in recent years.[13-16] Among these 2D materials, semiconducting transition-metal dichalcogenides (TMDs) such as MoS_2, WS_2, $MoSe_2$ and WSe_2 are one of the primary focuses of research.[17] Because of their unique electronic, mechanical, optical and chemical properties, TMDs showed high application potential in electronic devices and for catalysis and energy storage.[13] The covalent functionalization of TMDs can further enhance the versatility of 2D TMDs.[18] For example, improving the solubility in common solvents facilitates their integration into polymer matrices.[19] Furthermore, entirely new materials can be designed by attaching functional ligands.[20] In contrast to graphene, reports on the covalent functionalization of TMDs remain scarce.[18,19,21] Up to now, only a few covalently connected polymer-MoS_2 hybrids have been reported.[18,20,22]

Ultrathin MoS_2 nanosheets are excellent candidates for constructing hybrids with high specific surface areas and high flexibility.[9,23,24] Both sides of the MoS_2 nanosheets can be used as templates for the growth of functional composites with

sandwich-like structure.[9,24] Heteroatom-doped carbons as promising materials for catalysis or energy conversion and storage have attracted growing attention due to their unique structural and electronic properties.[25-29] Conjugated microporous polymers (CMPs) with high specific surface area and hierarchical pore distribution are favored for a controllable construction of carbon-based materials.[11,30-32] Heteroatoms can be controllably introduced into CMPs network via heteroatom-containing tectons (building blocks).[33-35] In this regard, the combination of MoS_2 nanosheets and CMPs may generate 2D hybrid sandwiches for applications in catalysis and electrochemical energy-related devices. However, using MoS_2 as templates for the generation of 2D sandwich-like materials with remarkable properties still remains great challenge due to their poor solvent processability.

In this chapter, we demonstrate the fabrication of MoS_2-templated conjugated microporous polymers (M-CMPs) nanosheets by growing nitrogen-rich CMPs on 4-iodophenyl-functionalized MoS_2 templates. Unique polymer-MoS_2 sandwiches with high specific surface areas and hierarchically porous structure were achieved. As-prepared 2D porous polymer-MoS_2 sandwiches can be converted into the corresponding 2D porous carbon hybrids by direct pyrolysis the M-CMPs nanosheets. As proof-of-concept, oxygen reduction reaction (ORR) and supercapacitor performances were studied. The strong interaction between nitrogen-doped porous carbon and MoS_2 within the sandwich structure boost the performance for ORR and electrochemical energy storage. As a result, the 2D porous carbon hybrids display a more positive half-wave potential (-0.14 V vs. -0.13 V for Pt/C) and a higher diffusion-limited current (ca. 5.4 mA cm^{-2}) in ORR in comparison with MoS_2-free porous carbons derived from CMPs. Moreover, the 2D hybrids deliver high capacitance up to 344 F/g at 0.2 A/g, 45% higher than that of corresponding MoS_2-free porous carbons (237 F/g).

6.2 Results and Discussion

6.2.1 Fabrication of MoS_2-Templated Conjugated Microporous Polymers (M-CMPs) Nanosheets

The synthesis strategy for M-CMPs is illustrated in Scheme 6.1. First, chemically exfoliated MoS_2 (CE-MoS_2) was generated by reacting bulk MoS_2 with *n*-butyllithium (*n*-BuLi). Then, CE-MoS_2 was functionalized with 4-iodophenyl diazonium salt under aqueous conditions (detailed experimental procedures are given in the Supporting Information).[19,21] The obtained 4-iodophenyl-functionalized MoS_2 (MoS_2-I) can be well-dispersed in various organic solvents, such as DMF (Figure 6.1a) and toluene. The successful functionalization of MoS_2 was evidenced by several analytical techniques as depicted in Figure 6.1-6.4.

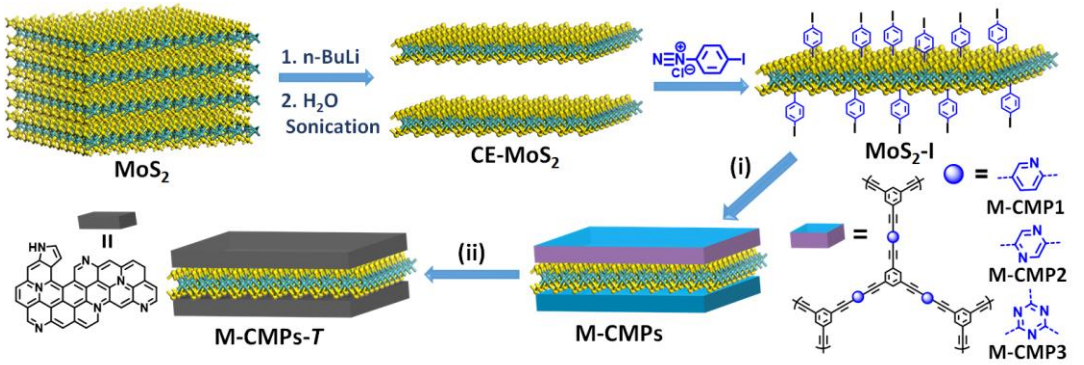

Scheme 6.1 Idealized formula scheme depicting the chemical exfoliation of bulk MoS_2 and subsequent functionalization with 4-iodophenyl substituents under formation of MoS_2-I as well as the preparation of MoS_2-templated conjugated microporous polymers (M-CMPs) and the corresponding MoS_2/nitrogen-doped porous carbon (M-CMPs-*T*) hybrids. (i) monomers: 1,3,5-triethynylbenzene and 2,5-dibromopyridine, 2,5-dibromopyrazine, or 2,4,6-trichloro-1,3,5-triazine, argon, $Pd(PPh_3)_4$, CuI, Et_3N, DMF, 100 °C, 3 days; (ii) argon, heating rate: 10 °C min^{-1}, pyrolysis temperature: 700, 800, or 900 °C, 2 h.

As shown in Figure 6.1a, most of the excitonic transitions are suppressed in the 4-iodophenyl-functionalized MoS_2 (MoS_2-I) in comparison with chemically exfoliated MoS_2 (CE-MoS_2).[19] In the Fourier transform infrared (FTIR) spectra (Figure 6.1b), a band at ca. 700 cm^{-1} is detected that can be assigned to the S-C stretching vibration.[19,21] In the Raman spectra (Figure 6.1c) of CE-MoS_2 and MoS_2-I, the second-order longitudinal acoustic phonon (2LA(M) at 450 cm^{-1}) appears with decreased intensity for the MoS_2-I sample. As indicated by the thermogravimetric

analyses (TGA, Figure 6.1d), the different weight loss of CE-MoS_2 and MoS_2-I, respectively, reflects the degradation of the 4-iodophenyl functional groups.[19,21]) In the TEM energy-dispersive X-ray spectra (EDS) of MoS_2-I (Figure 6.2-6.3) iodine was detected thus confirming the successful attachment of the 4-iodophenyl functions. The I 3d, I 3p and I 4d signals in the X-ray photoelectron spectroscopy (XPS) spectra (Figure 6.4) further confirm the presence of 4-iodophenyl substituents in MoS_2-I.

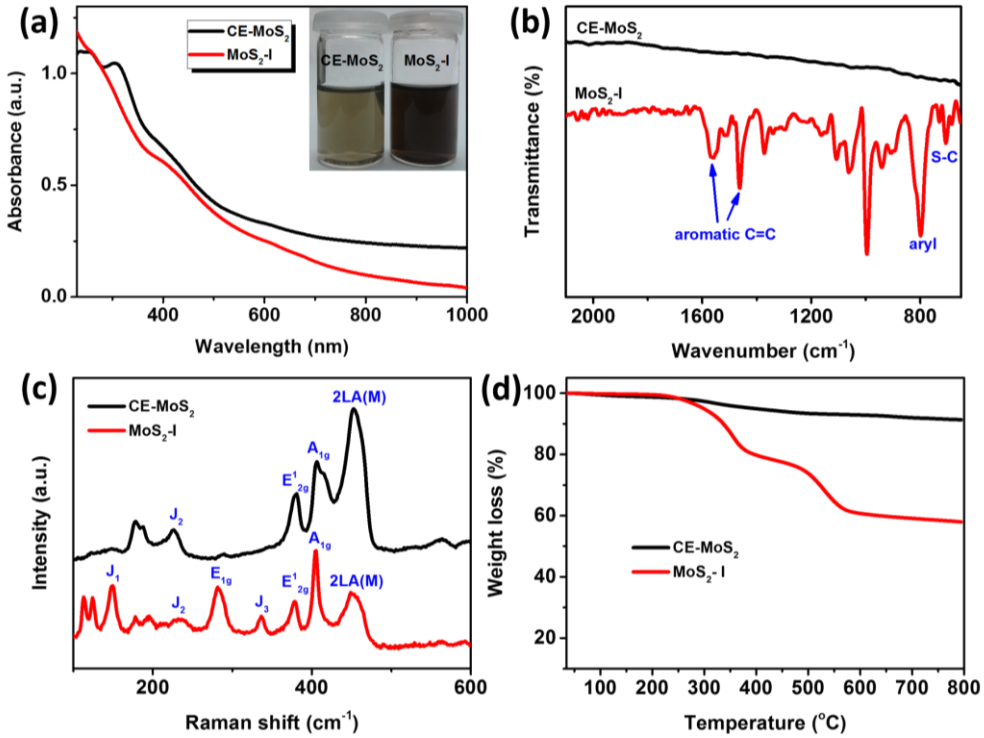

Figure 6.1 (a) Normalized UV-vis spectra of chemically exfoliated MoS_2 (CE-MoS_2) and 4-iodophenyl-functionalized MoS_2 (MoS_2-I). Inset: photography of CE-MoS_2 and MoS_2-I dispersions in DMF. (b) FTIR, (c) Raman spectra, and (d) TGA profiles of CE-MoS_2 and MoS_2-I.

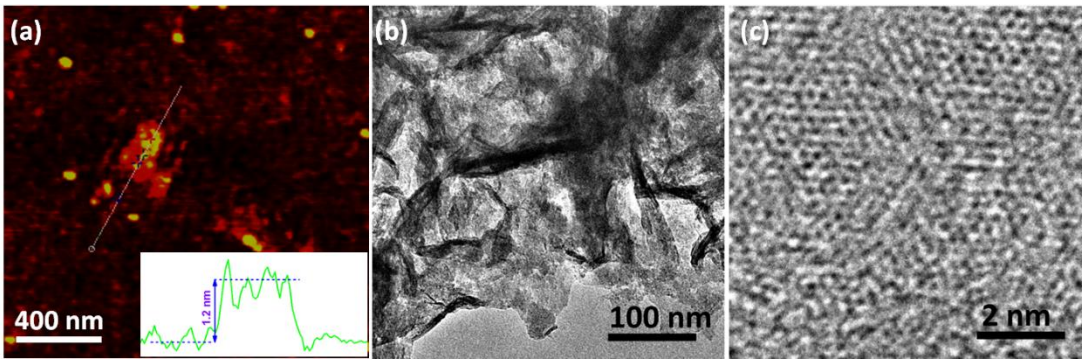

Figure 6.2 (a) AFM, (b) TEM, and (c) HRTEM images of chemically exfoliated MoS_2.

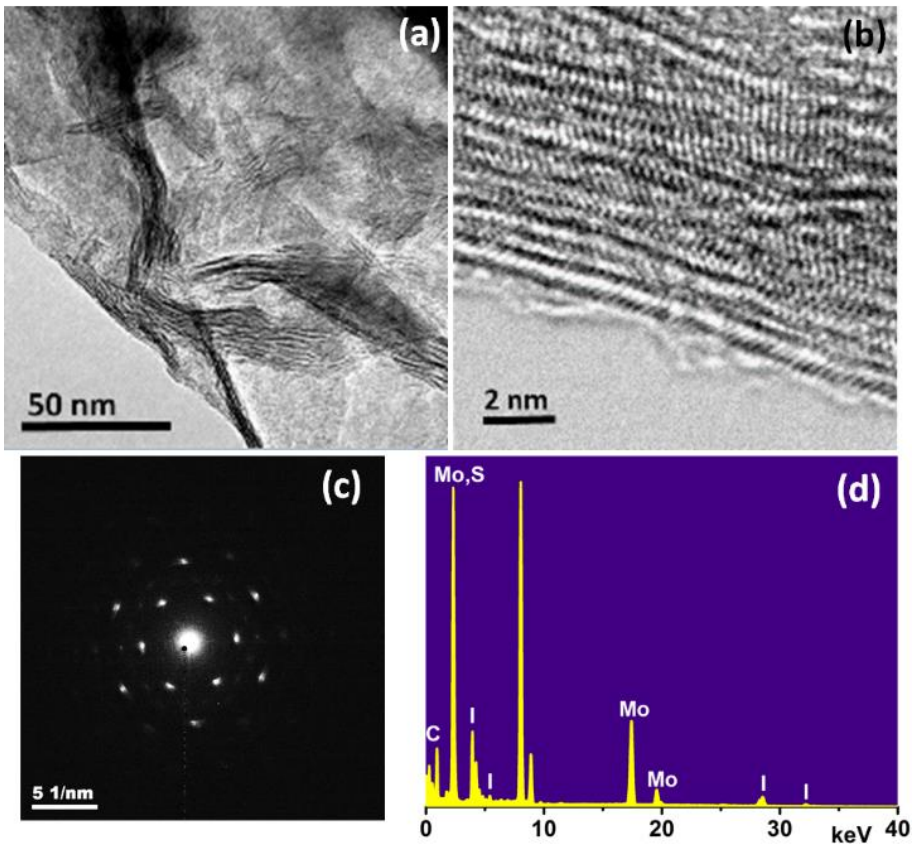

Figure 6.3 (a) TEM and (b) HRTEM images of MoS_2-I. (c) The corresponding selected-area electron diffraction (SAED) pattern of MoS_2-I. The SAED pattern indicates a hexagonal structure. (d) Energy-dispersive X-ray spectroscopy (EDS) profile of MoS_2-I. Iodine was found in the MoS_2-I sample confirming the successful attachment of the 4-iodophenyl functions.

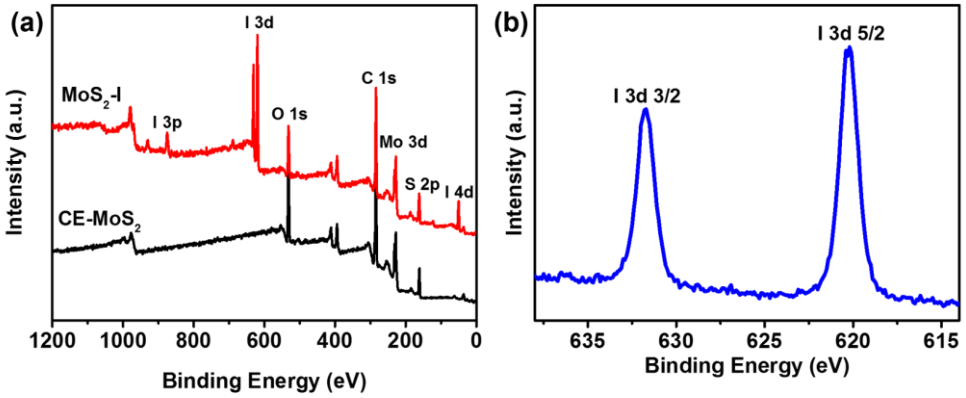

Figure 6.4 (a) The survey XPS spectra of chemically exfoliated MoS_2 (CE-MoS_2) and 4-iodophenyl-functionalized MoS_2 (MoS_2-I). (b) High resolution I 3d XPS spectra of MoS_2-I. The I 3d, I 3p and I 4d signals in the XPS spectra further confirm the presence of the 4-iodophenyl substituents in MoS_2-I.

Next, the arylacetylene building block 1,3,5-triethynylbenzene mixed with an aryl di- or trihalide (2,5-dibromopyridine, 2,5-dibromopyrazine, or 2,4,6-trichloro-1,3,5-triazine) was reacted with MoS_2-I in anhydrous DMF in the presence of $Pd(PPh_3)_4$, CuI and Et_3N under inert atmosphere. This Sonogashira-Hagihara reaction was carried out at 100 ^oC for 3 days under vigorous stirring and yielded an insoluble, crude product that was collected by filtration and purified by Soxhlet extraction with THF for two days. Finally, the sandwich-like M-CMPs, denoted as M-CMP1, M-CMP2 and M-CMP3 for the pyridine-, pyrazine- and triazine-containing polymers, respectively, were obtained after vacuum drying. The corresponding conjugated microporous polymers (CMPs), denoted as CMP1, CMP2 and CMP3 for the pyridine-, pyrazine- and triazine-containing polymers, respectively, without the MoS_2 template were also synthesized for comparison in a similar procedure.

6.2.2 Morphologies and Microstructures of M-CMPs

Morphologies and microstructures of the M-CMPs were investigated by scanning electron microscopy (SEM), transmission electron microscopy (TEM), high resolution TEM (HRTEM) and atomic force microscopy (AFM). All of the M-CMPs display similar sheet-like structures. Therefore, M-CMP2 will be discussed as a typical example. As shown in Figure 6.5a and Figure 6.5b, M-CMP2 possesses a wrinkled sheet morphology similar to that of MoS_2 layers. The surface of the M-CMP sandwiches shown a similar average roughness as the non-templated CMPs due to the coating of the porous CMPs on MoS_2 (Figure 6.6). No free CMP particles or "naked" MoS_2 sheets were observed, thus indicating that the majority of the monomers have been grafted onto the MoS_2 surface. In the HRTEM image of M-CMP2, the alternating bright and dark areas may be attributed to the microporous structure of the M-CMPs with homogenously distributed pores in M-CMPs (Figure 6.6). AFM and thickness analyses (Figure 6.5c) indicate the presence of M-CMP sandwiches with a uniform thickness of 35±6 nm. Oppositely, the non-templated CMPs display a granular structure (Figure 6.6c). These results confirm the role of MoS_2-I as template for the growth of the CMPs layers on both sides of MoS_2 sheet.

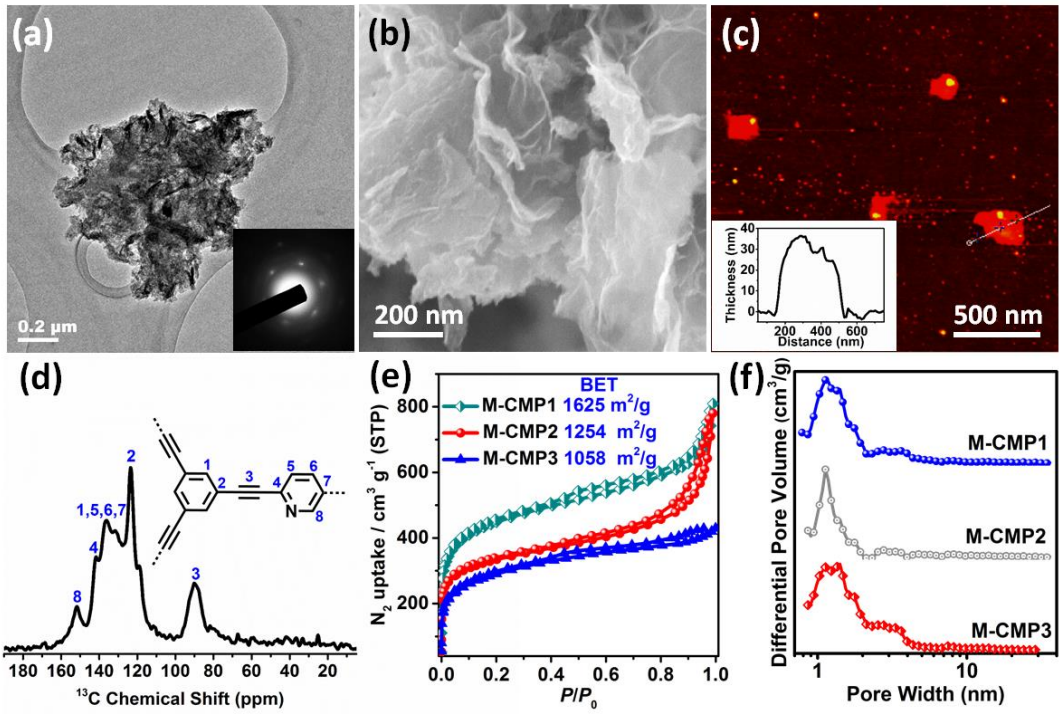

Figure 6.5 (a) TEM, (b) SEM, and (c) AFM images of M-CMP2. Inset of (a) is the selected-area electron diffraction (SAED) pattern of a M-CMP2 nanosheet. (d) Solid-state ^{13}C CP/MAS spectrum of M-CMP1 and its peak assignments. (e) Nitrogen adsorption/desorption isotherms, and (f) corresponding pore size distribution profiles of M-CMPs.

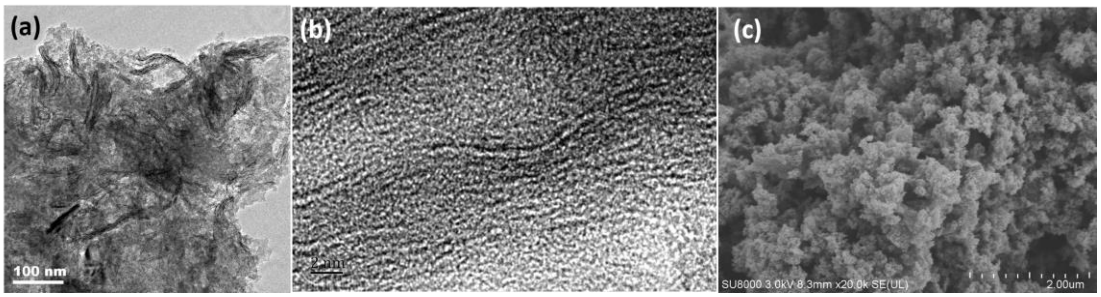

Figure 6.6 TEM (a) and HRTEM (b) images of M-CMP2, the homogenously distributed micropores can be directly visualized. (c) SEM image of CMP2. CMP2 displays the granular structure.

6.2.3 Chemical Structure of M-CMPs

The chemical structure of the M-CMPs was analyzed by FTIR and solid-state ^{13}C cross-polarization/magic angle spinning nuclear magnetic resonance (CP/MAS NMR) spectroscopy. The disappearance of the C-Br (at ca. 1080 cm^{-1}) and alkynyl C-H (at ca. 3275 cm^{-1}) stretch vibrations in the FTIR spectra of M-CMP1 imply the occurrence of an efficient arylacetylene-aryl coupling (Figure 6.7). In the ^{13}C NMR

spectrum of M-CMP1 the signal at 152 ppm can be assigned to the pyridine carbons in the proximity of the nitrogen atom (Figure 6.5d). Moreover, diaryl C≡C signals at 88-90 ppm are observed again indicating successful formation of the CMP skeleton on MoS_2 surface. The FTIR and NMR spectra of M-CMP2 and M-CMP3 (Figure 6.7 and Figure 6.8) can be interpreted in similar manner. M-CMPs were further characterized by XPS (Figure 6.7d). All M-CMPs are composed of similar components, C, N, S and Mo. All structure characterization data indicate the successful synthesis of the microporous MoS_2/polymer hybrid nanosheets by utilizing MoS_2-I as template.

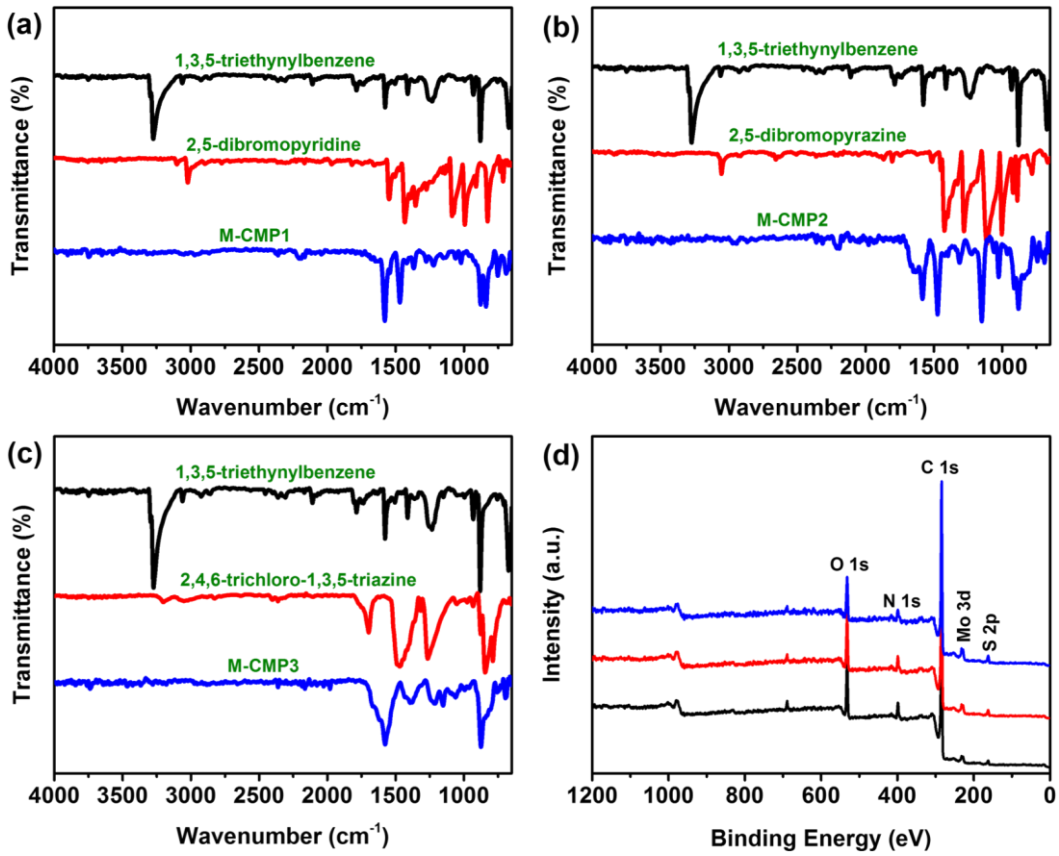

Figure 6.7 (a-c) FTIR spectra of 1,3,5-triethynylbenzene, aryl halides (2,5-dibromopyridine, 2,5-dibromopyrazine, and 2,4,6-trichloro-1,3,5-triazine) and the corresponding MoS_2-templated conjugated microporous polymers (M-CMP1, M-CMP2 and M-CMP3). (d) Survey XPS spectra of M-CMP1, M-CMP2 and M-CMP3.

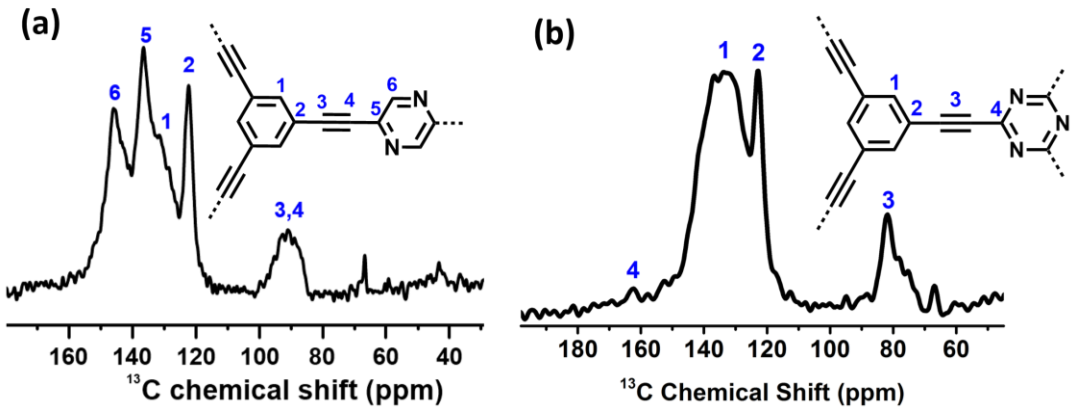

Figure 6.8 Solid-state ^{13}C CP/MAS spectra of M-CMP2 (top) and M-CMP3 (bottom), and the corresponding peak assignments.

6.2.4 Porosity of M-CMPs

Consequently, nitrogen adsorption/desorption measurements were carried out for investigation of the porous nature of our M-CMPs. The nitrogen sorption isotherms and the corresponding pore size distributions of the M-CMPs are presented in Figure 6.5e,f. All M-CMPs showed reversible type-IV isotherms with BET surface areas of 1625, 1254, and 1058 m^2/g for M-CMP1, M-CMP2 and M-CMP3, respectively. The pore size distributions based on non-local density functional theory (NLDFT) method (Figure 6.5f) indicate the presence of both meso- and micropores in the M-CMPs. Notably, M-CMPs show much higher BET surface areas than those for CMPs without MoS_2 (1086, 886 and 392 m^2/g), respectively (Figure 6.9-6.10). This effect may originate from a synergetic effect of the MoS_2 template on the CMP porosity.

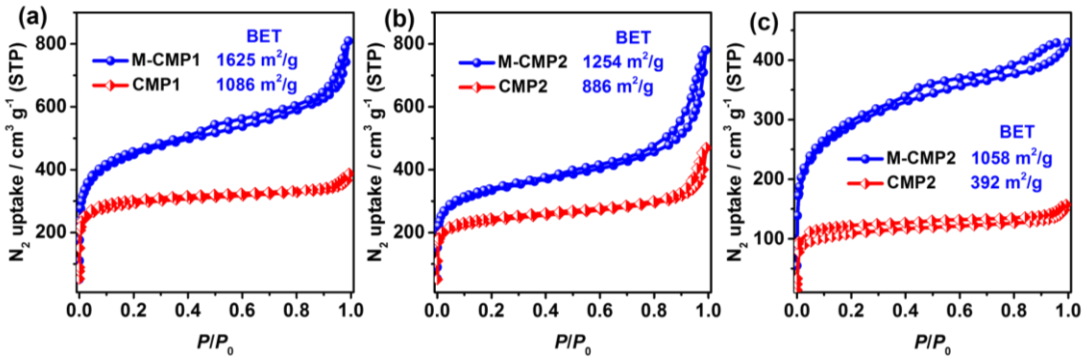

Figure 6.9 Nitrogen adsorption/desorption isotherms and corresponding BET surface areas of (a) M-CMP1 and CMP1, (b) M-CMP2 and CMP2, (c) M-CMP3 and CMP3 measured at 77 K.

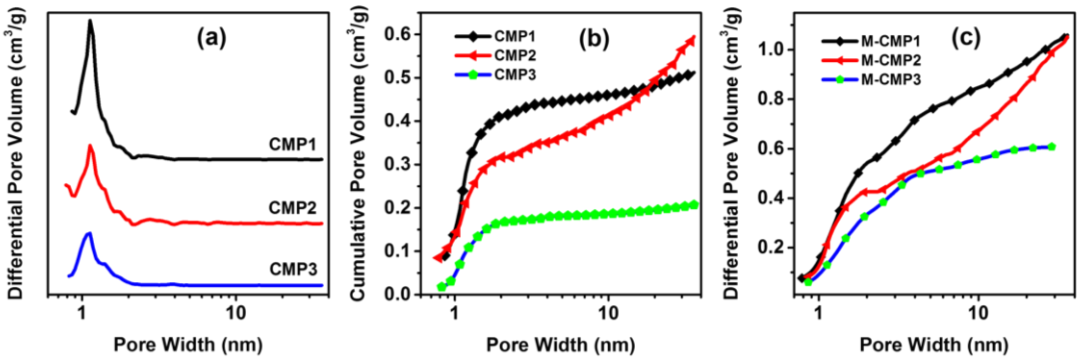

Figure 6.10 (a) Pore size distributions, and (b) cumulative pore volumes of CMP1, CMP2 and CMP3. (c) Cumulative pore volumes of M-CMP1, M-CMP2 and M-CMP3.

6.2.5 Pyrolytic Generation and Characterization MoS_2/Carbon Hybrid Nanosheets

CMPs-derived porous carbons with integrated heteroatoms, metal clusters or metal nanoparticles, or metal oxides are promising materials for various applications such as gas storage and separation, energy conversion and storage, or electrochemical catalysis.[11,30,31,36] Thermogravimetric analysis (TGA) of M-CMPs revealed that they can be easily transformed into MoS_2/carbon hybrid materials (ca. 80% residual at 800 ^oC, Figure 6.11). Therefore, M-CMP1, M-CMP2 and M-CMP3 were pyrolyzed at 700, 800, or 900 ^oC for 2 h under an argon atmosphere (Scheme 6.1). The resulting MoS_2/nitrogen-doped porous carbon (M-CMPs-*T*) hybrids are denoted as M-CMP1-*T*, M-CMP2-*T* and M-CMP3-*T*, respectively, in which *T* represents the pyrolysis temperature. For comparison, porous carbons without MoS_2 were also prepared by pyrolysis of the CMPs at *T* ^oC, denoted as the corresponding CMP*n*-*T* (*n*=1, 2, 3, *T*=800), respectively.

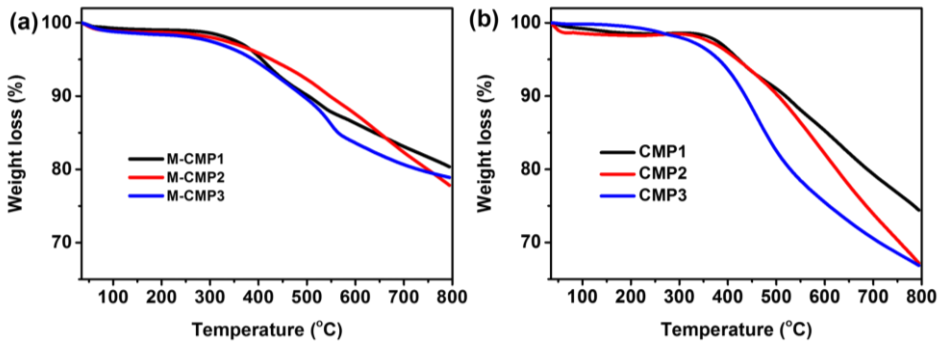

Figure 6.11 TGA profiles of (a) M-CMPs and (b) CMPs.

The SEM and TEM images of the M-CMPs-*T* hybrids still display the preserved nanosheet morphology (Figure 6.12a,b and Figure 6.13). On the contrary, the CMPs-derived carbons exhibit a particular morphology (Figure 6.13). HRTEM image and corresponding SAED pattern of M-CMP2-800 indicate that the porous carbons in close connected with MoS_2 templates (Figure 6.12c). Scanning transmission electron microscopy (STEM) element mapping images (Figure 6.12d and Figure 6.14) clearly show homogeneous distribution of C, N, Mo and S in the M-CMP2-800 nanosheets.

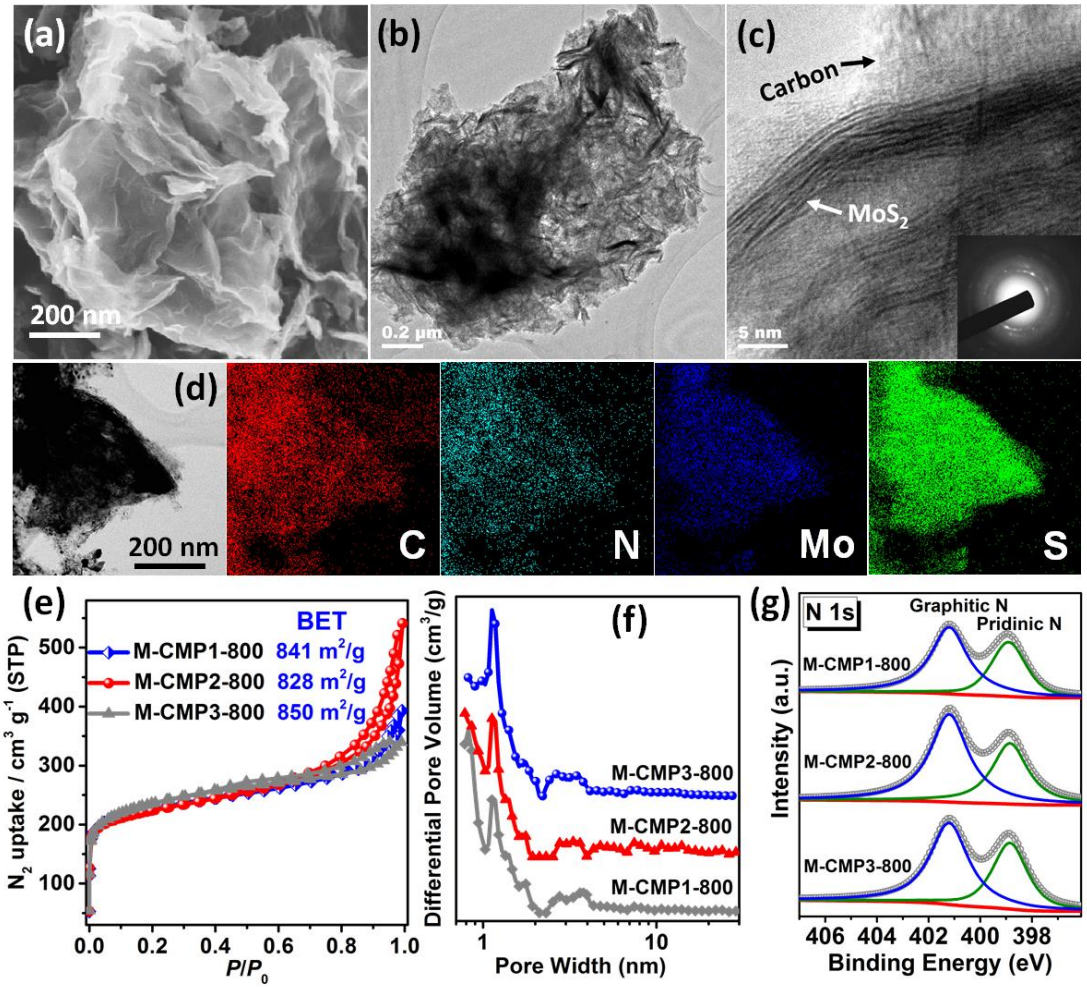

Figure 6.12 Characterization of MoS_2-based porous carbon nanosheets. (a) SEM, (b) TEM, and (c) HRTEM images of M-CMP2-800. Inset of (c) shows the corresponding SAED pattern. (d) STEM image of M-CMP2-800 and corresponding EDS elemental mapping images for C, N, Mo and S. (e) Nitrogen adsorption/desorption isotherms and corresponding BET surface areas. (f) Pore size distributions of M-CMP1-800, M-CMP2-800, and M-CMP3-800. (g) N 1s core level XPS spectra of M-CMP1-800, M-CMP2-800, and M-CMP3-800.

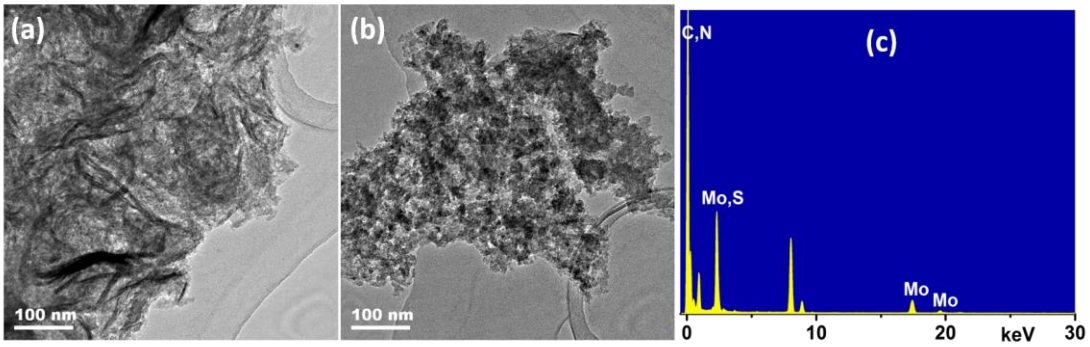

Figure 6.13 TEM image of (a) M-CMP2-800 and (b) CMP2-800. (c) EDS profile of M-CMP2-800.

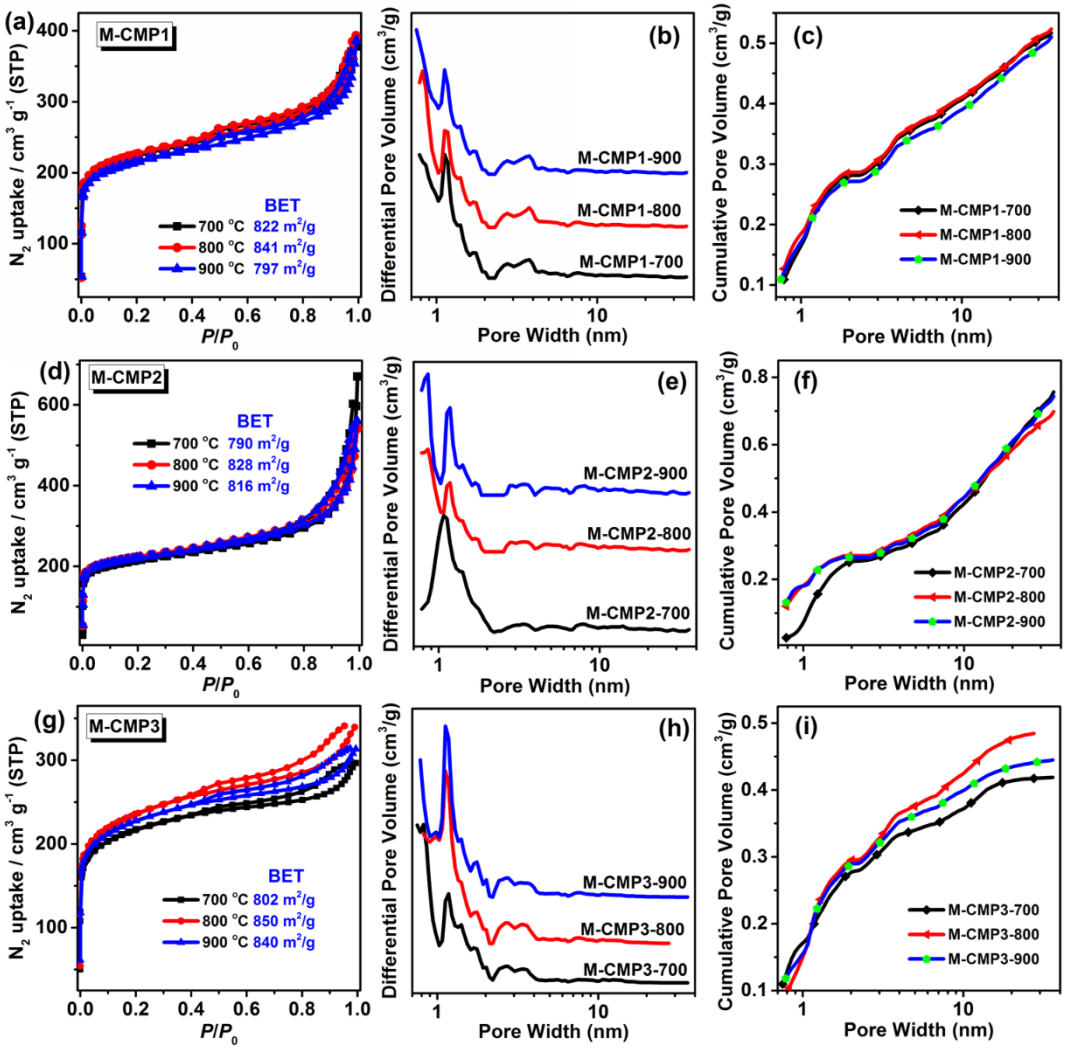

Figure 6.14 (a,d,g) Nitrogen adsorption/desorption isotherms and corresponding BET surface areas of M-CMPs after pyrolysis at different temperatures (700, 800, and 900 °C). (b,e,h) Pore size distributions, and (c,f,i) cumulative pore volumes of M-CMPs after pyrolysis at different temperatures (700, 800 and 900 °C).

After pyrolysis, the obtained MoS_2/porous carbon hybrids still show high BET surface area (790-850 m^2/g) indicating that the pore structure is mainly preserved after pyrolysis (Figure 6.12e and Figure 6.14). Thereby, the surface areas of the MoS_2-templated hybrids are higher than those of the corresponding porous carbons (681-828 m^2/g) derived from the MoS_2-free CMPs thus demonstrating the advantages of MoS_2 templating strategy (Figure 6.15-6.16 and Table 6.1). The large gas uptake at low relative pressure (below p/p_0 = 0.1) and the hysteretic loops in the high p/p_0 region of the isotherms indicate the coexistence of micro- and mesopores in the M-CMPs-*T* hybrids.[37] The peaks for diameters around 1.1 and 3.5 nm in the pore size distribution profiles (Figure 6.12f and Figure 6.14) further confirm the hierarchical porous structure. Such large specific surface areas together with the hierarchical porous structure are crucial for accelerating electron- and mass-transport for energy device related applications, such as electrochemically catalyzied oxygen reduction reaction (ORR) and supercapacitor.

Table 6.1 Summary of the N_2 sorption data for the porous carbons without MoS_2 or with MoS_2 templates prepared at different conditions.

sample	S_{BET} (m^2/g)	S_{micro} (m^2/g)	S_{meso} (m^2/g)	V_{total} (cm^3/g)	V_{micro} (cm^3/g)	V_{meso} (cm^3/g)
CMP1-800	681	674	7	0.29	0.24	0.05
CMP2-800	746	707	39	0.48	0.26	0.22
CMP3-800	828	815	13	0.37	0.31	0.06
M-CMP1-700	822	743	79	0.51	0.28	0.23
M-CMP1-800	841	766	75	0.52	0.29	0.23
M-CMP1-900	797	722	75	0.50	0.27	0.23
M-CMP2-700	790	649	41	0.76	0.25	0.51
M-CMP2-800	828	727	101	0.70	0.27	0.43
M-CMP2-900	816	713	103	0.74	0.27	0.47
M-CMP3-700	802	740	62	0.42	0.28	0.14
M-CMP3-800	850	766	84	0.48	0.30	0.18
M-CMP3-900	840	770	70	0.44	0.29	0.15

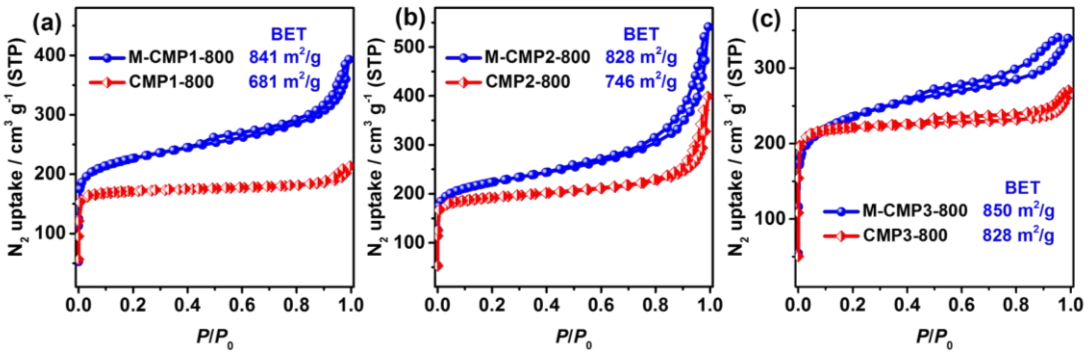

Figure 6.15 Nitrogen adsorption and desorption isotherms and corresponding BET surface areas of M-CMP1-800, CMP1-800, M-CMP2-800, CMP2-800, M-CMP3-800, and CMP3-800 measured at 77 K.

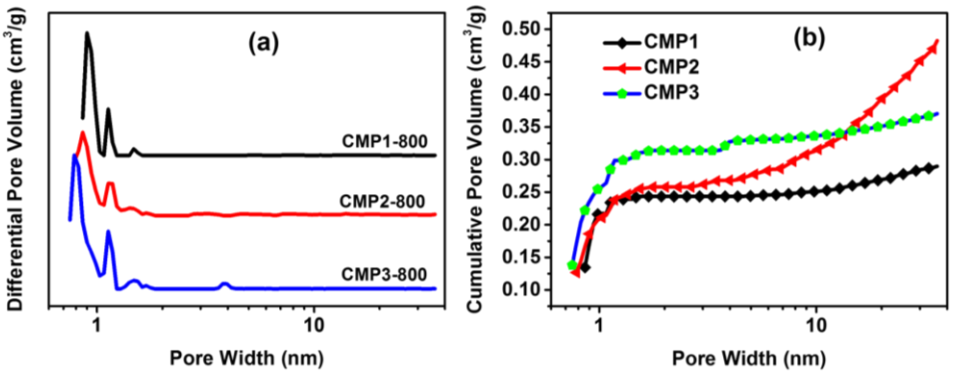

Figure 6.16 (a) Pore size distribution profiles, and (b) cumulative pore volumes of CMP1-800, CMP2-800, and CMP3-800.

In the Raman spectra of M-CMPs-*T* (Figure 6.17), the MoS_2-related part (300-500 cm^{-1}) and two peaks around 1330 and 1590 cm^{-1} assigned to disordered (D-band) and ordered graphitic carbons (G-band), respectively, are clearly observed for all hybrids.[38] The observed relatively high intensity of the D band (I_D/I_G ratio: ca. 1.2) for all M-CMPs-*T* hybrids can be attributed to disorder associated with edge defects.[30,39] The introduction of nitrogen centers into the porous carbons also contributes to the D band-intensity.[30] XPS measurements were carried out for identifying the elemental components of M-CMPs-*T* hybrids. Based on the XPS analysis (Figure 6.12g and Figure 6.17c), pyridinic and graphitic N were found at a nominal nitrogen level of 2.8, 3.6 and 3.1 wt% for M-CMP1-800, M-CMP2-800 and M-CMP3-800, respectively (Table 6.2). The pyridinic and graphitic nitrogen doping

leads to a redistribution of charge and spin density of the adjacent carbons, which is favorable for carbon-based energy storage/conversion, e.g. ORR or supercapacitors.[30,40]

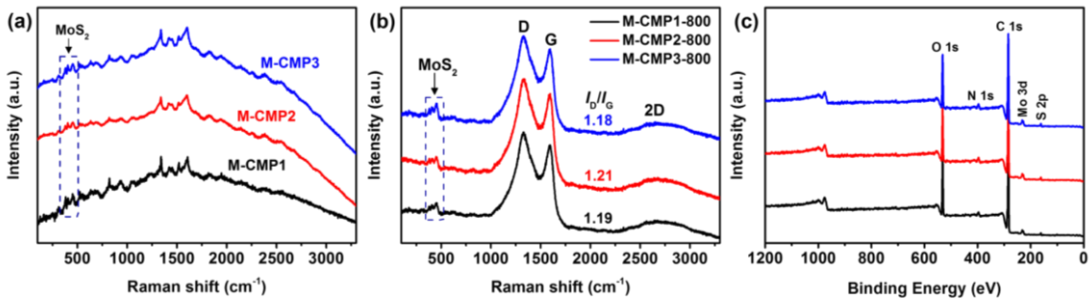

Figure 6.17 Raman spectra of (a) M-CMP1, M-CMP2, and M-CMP3, (b) M-CMP1-800, M-CMP2-800, and M-CMP3-800. (c) X-ray photoelectron (XPS) spectra of M-CMP1-800, M-CMP2-800, and M-CMP3-800. As expected, the characteristic peaks for Mo, S, graphitic C (centered at 284.6 eV) and N (around 398.6 eV), were observed. The O 1s peaks result from physically adsorbed oxygen or water molecules.

Table 6.2 Elemental content of C, N, Mo and S based on XPS analysis for M-CMP1-800, M-CMP2-800, and M-CMP3-800.

	C	N	Mo	S
	Weight content (%)			
M-CMP1-800	85.9	2.8	6.7	4.6
M-CMP2-800	83.6	3.6	7.4	5.4
M-CMP3-800	84.8	3.1	7.2	4.9

6.2.6 Oxygen Reduction Reaction Performance

Based on the above discussed hierarchical porous structure, their heteroatom-doping feature and 2D morphology, M-CMPs-*T* are promising candidates for electrochemical catalyzed ORR. The ORR activity of M-CMPs-*T* was studied under alkaline condition (0.1 M KOH). A scheme depicting of the ORR process at the M-CMPs-*T* hybrids is shown in Figure 6.18a, with the active sites homogeneously distributed throughout the M-CMPs-*T* nanosheets. O_2 molecules can be directly reduced into OH^- at the active sites. Cyclic voltammetry (CV) revealed a well-defined cathodic ORR peak for all the M-CMPs-*T* hybrids in O_2-saturated solutions in

contrast to N_2-saturated solutions indicating a pronounced catalytic activity of the hybrids. Thereby, M-CMP2-800 exhibited the highest peak current density at most positive potential (-0.21 V versus Ag/AgCl) in comparison with other 2D hybrids (Figure 6.18b and Figure 6.19) and CMP2-800 (Figure 6.20).

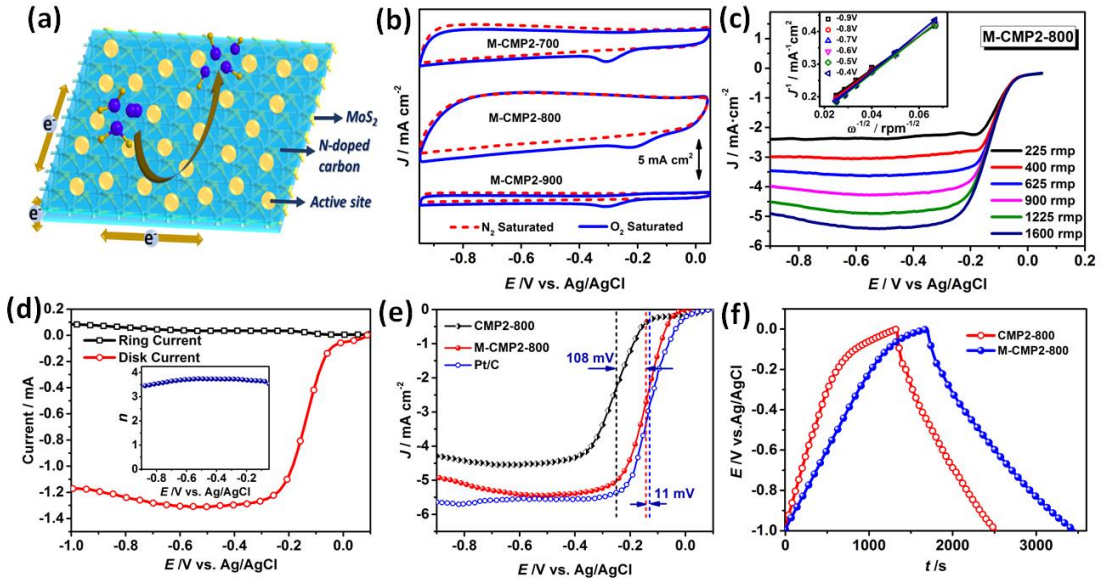

Figure 6.18 (a) Schematic illustration of the ORR process taking place at the surface of the M-CMPs-*T* hybrids in alkaline conditions. (b) CV curves in N_2- and O_2-saturated 0.1M KOH; (c) LSV curves for M-CMP2-800 at different rotation rates in O_2-saturated 0.1 M KOH at 5 mV s^{-1}. The inset shows the Koutecky-Levich (K-L) plots. (d) RRDE curve for M-CMP2-800 for a rotation speed of 1600 rpm (the inset shows the calculated electron transfer number (*n*) against the electrode potential); (e) LSV curves for CMP2-800, M-CMP2-800, and Pt/C in O_2-saturated 0.1 M KOH solution at 1600 rpm and a scan rate of 5 mV s^{-1}; (f) Galvanostatic charge/discharge curves of CMP2-800 and M-CMP2-800 at a current density of 0.2 A g^{-1}.

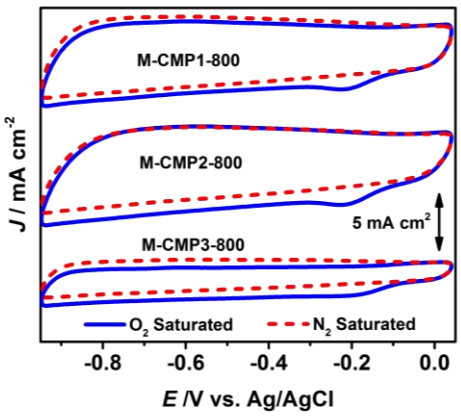

Figure 6.19 CV curves for M-CMP1-800, M-CMP2-800, and M-CMP3-800 in N_2- and O_2-saturated 0.1M KOH. M-CMP2-800 exhibits the most positive potential at the highest current density, thus indicating that M-CMP2-800 possesses the highest catalytic activity in the ORR.

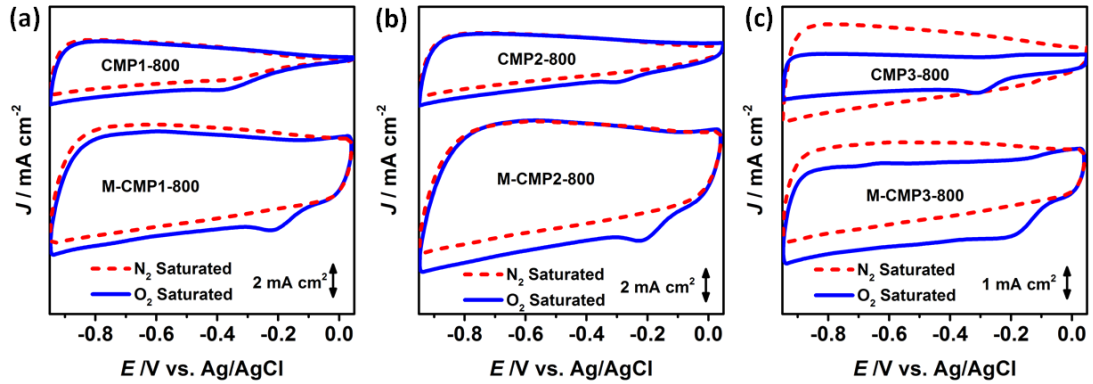

Figure 6.20 Comparison of CV curves of carbon materials prepared at 800 °C with and without MoS_2. CV curves for (a) CMP1-800 and M-CMP1-800, (b) CMP2-800 and M-CMP2-800, (c) CMP3-800 and M-CMP3-800 in N_2- and O_2-saturated 0.1M KOH.

To gain further insight into the ORR process, linear sweep voltammetry (LSV) measurements were recorded on the rotating disk electrode (RDE). Based on the LSV curves under a rotation of 1600 rpm (Figure 6.21), the diffusion-limited currents at -0.60 V were 5.5, 4.7, 5.4, and 3.4 mA cm^{-2} for commercial Pt/C, M-CMP1-800, M-CMP2-800 and M-CMP3-800, respectively. MCMP2-800 again showed the highest diffusion-limited current and the most positive onset potential among M-CMPs-*T* hybrids, possibly as a result of the high specific surface area and high N content (3.6 wt%, Table 6.2).

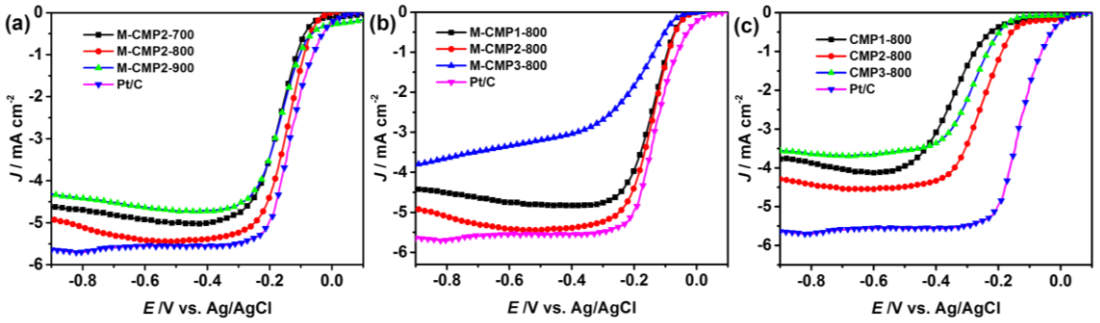

Figure 6.21 LSV curves of (a) M-CMP2-700, M-CMP2-800, M-CMP2-900, and Pt/C, (b) M-CMP1-800, M-CMP2-800, M-CMP3-800, and Pt/C, (c) CMP1-800, CMP2-800, CMP3-800, and Pt/C in O_2-saturated 0.1M aqueous KOH solution at 1600 rpm and a scan rate of 5 mV s^{-1}.

The electron transfer number per oxygen molecule (*n*) for ORR was calculated based on the LSV curves at different rotation rates (400-1600 rpm) and potentials (-0.4--0.9 V) by using the Koutechy-Levich (K-L) equation[41] (Supporting Information). The K-L plots show a good linearity for all potentials (Figure 6.18c and Figure 6.22-6.23). The electron transfer number *n* is calculated as ca. 4.0 between -0.4 and -0.9 V for M-CMP2-800. Based on the rotating ring-disk electrode (RRDE) curves (Figure 6.18d) a similar value for *n* is calculated (ca. 3.8, inset of Figure 6.18d), which is higher than the value for M-CMP1-800 (3.6) and M-CMP3-800 (3.3). Additionally, M-CMP2-800 shown the lowest peroxide yield (Figure 6.24), suggesting that the ORR catalyzed by M-CMP2-800 is mainly dominated by a four-electron transfer pathway. From the intercept of the K-L plots, the kinetic current density J_k corrected for mass transport is calculated as 26.3 mA cm^{-2} for M-CMP2-800, which is also higher than the values for the other samples (19.2 mA cm^{-2} for M-CMP1-800 and 9.1 mA cm^{-2} for M-CMP3-800). The half-wave potential (HWP) of M-CMP2-800 occurred at -0.14 V, 108 mV lower than that for MoS_2-free CMP2-800 (Figure 6.18e), and only 11 mV higher than the value of commercial Pt/C, impressively demonstrating its high catalytic activity. M-CMP1-800 and M-CMP3-800 display a similar decrease of the HWP values (Figure 6.25) in comparison with those of the MoS_2-free CMP1-800 (by 194 mV) and CMP3-800 (by 106 mV), respectively. These results indicate a lower energy consumption and operation voltage for M-CMPs-*T* hybrids in comparison with corresponding MoS_2-free counterparts.

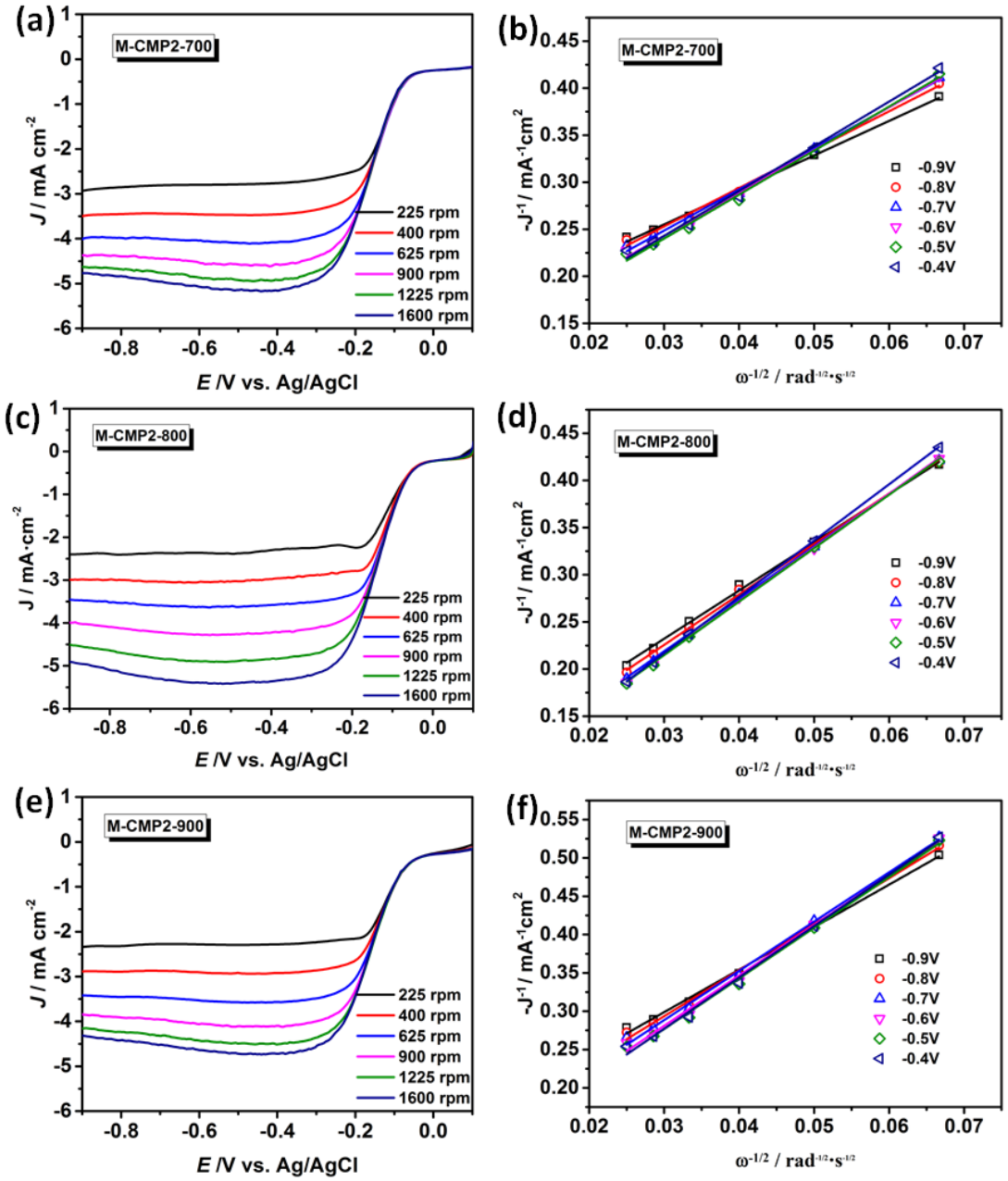

Figure 6.22 LSV curves for (a) M-CMP2-700, (c) M-CMP2-800, and (e) M-CMP2-900 for different rotation speeds in O_2-saturated 0.1 M aqueous KOH solution at 5 mV s^{-1}. Corresponding Koutecky-Levich (K-L) plots for (b) M-CMP2-700, (d) M-CMP2-800, and (f) M-CMP2-900 for different potentials.

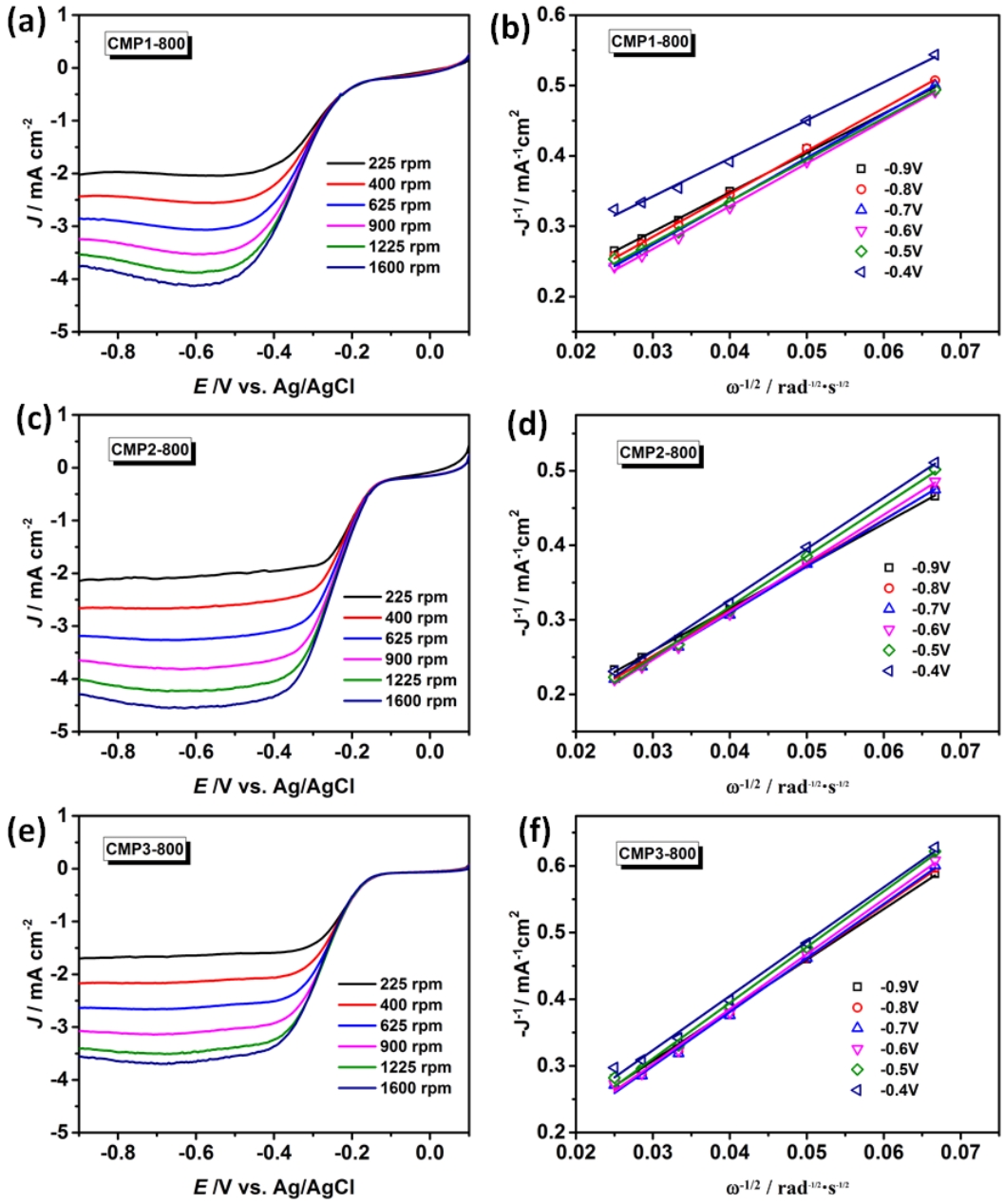

Figure 6.23 LSV curves for (a) CMP1-800, (c) CMP2-800 and (e) CMP3-800 for different rotation speeds in O_2 -saturated 0.1 M aqueous KOH solution at 5 mV s^{-1}. Corresponding Koutecky-Levich (K-L) plots for (b) CMP1-800, (d) CMP2-800, and (f) CMP3-800 for different potentials.

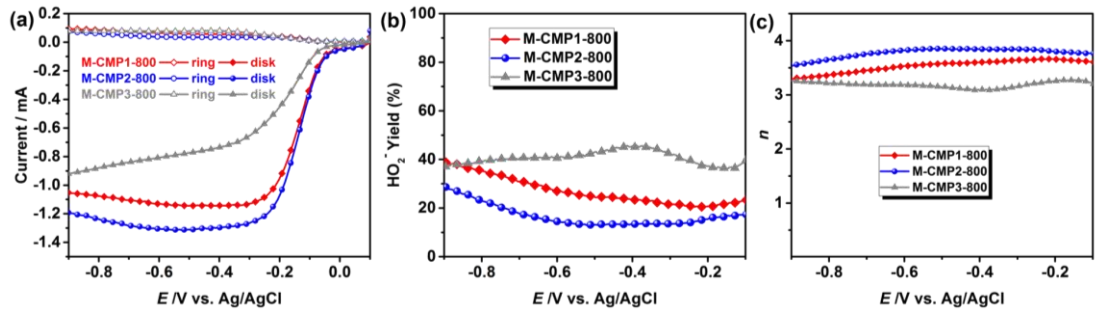

Figure 6.24 (a) Rotating ring-disk electrode voltammograms recorded for M-CMP1-800, M-CMP2-800, and M-CMP3-800 in O_2-saturated 0.1 M aqueous KOH at 1,600 rpm. (b) Peroxide yields and (c) electron transfer numbers (*n*) obtained for the rotating ring-disk electrode measurements. M-CMP2-800 exhibits the lowest peroxide yield. Also the corresponding electron transfer number of M-CMP2-800 is higher if compared to M-CMP1-800 or M-CMP2-800.

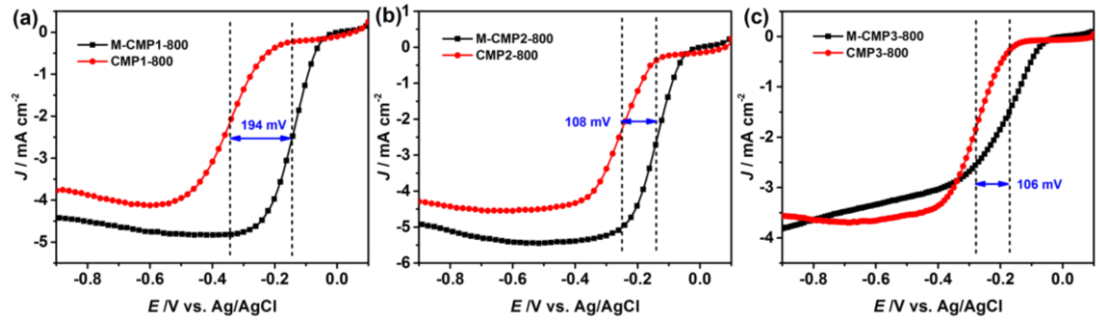

Figure 6.25 LSV curves for (a) M-CMP1-800 and CMP1-800, (b) M-CMP2-800 and CMP2-800 and (c) M-CMP3-800 and CMP3-800 at 1600 rpm in O_2-saturated 0.1 M aqueous KOH solution at 5 mV s^{-1}.

6.2.7 Electrochemical Energy Storage Performance

MoS_2-based materials can efficiently store charges by formation of intersheet and intrasheet double-layers or pseudocapacitances (faradaic charge-transfer process on the Mo center).[42,43] Regarding this point, M-CMPs-*T* hybrids have also been examined as electrode materials of supercapacitors for electrochemical energy storage (Figure 6.18f). The capacitive performance was investigated by CV and galvanostatic charge/discharge (GCD) measurements (Figure 6.18f and Figure 6.26-6.27). Near-rectangular shape CV curves were observed for both M-CMP2-800 and CMP2-800, indicating ideal capacitive behavior. A markedly higher current density was observed for M-CMP2-800 if compared to CMP2-800, which suggests that the

MoS_2 layer significantly contributes to the increase in the capacitance. Notably, reversible peaks are also found in the CV profiles of M-CMP2-800 that indicate a pseudocapacitive process. The two peaks are attributed to the oxidation/reduction processes of edge Mo centers of MoS_2 layers (Mo(IV) ⇔ Mo(V) ⇔ Mo(VI)) and make a significant contribution to the total capacitance of the hybrid materials.[42] The CV data showing reversible redox process suggest an excellent electrochemical stability of the hybrid materials. On the basis of the GCD curves, the specific gravimetric capacitance of M-CMP2-800 was calculated to be 344 F/g at 0.2 A/g, which is 45% higher than that of CMP2-800 (237 F/g). The superior supercapacitor performance of M-CMP2-800 should be associated with the maximized interaction between MoS_2 and porous carbon layers as well as with high surface area and hierarchical pore structure of the hybrid nanosheets.

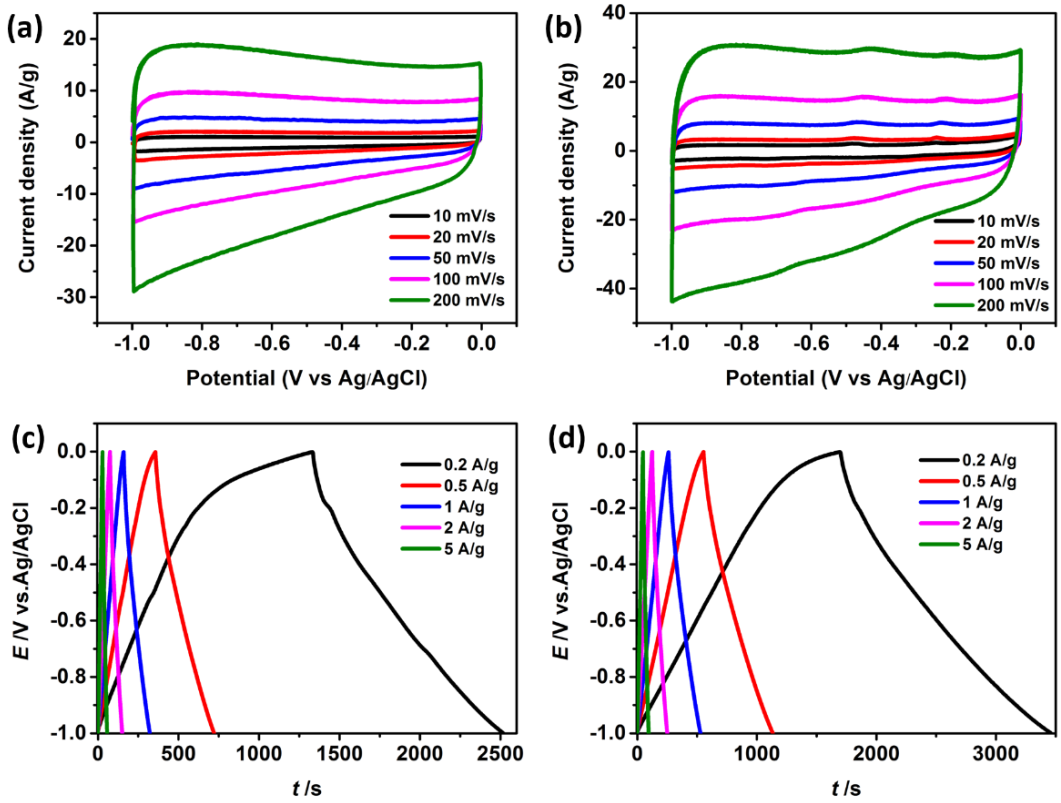

Figure 6.26 Cyclic voltammograms (CV) of (a) CMP2-800 and (b) M-CMP2-800 at different scan rates, and galvanostatic charge/discharge (GCD) curves of (c) CMP2-800 and (d) M-CMP2-800 at different current densities in 6 M aqueous KOH solution in three-electrode cell configuration using Ag/AgCl as the reference electrode.

The specific capacitance of M-CMP2-800 outperforms the values for other MoS_2-based electrodes, such as metallic 1T phase MoS_2,[44] hollow MoS_2 nanospheres[45] and MoS_2/graphene,[42,46] and is comparable to the performance of heteroatom-doped graphene and porous carbon-based electrodes,[11,30] (Table 6.3). The superior ORR and supercapacitor performances of M-CMPs-*T* hybrids should be significantly associated with a maximized synergistic interaction between MoS_2 and porous carbon layers combined with the presence of a hierarchical porous structure, providing channels for effective mass-transport, and thus facilitating electrolyte penetration and ion diffusion.

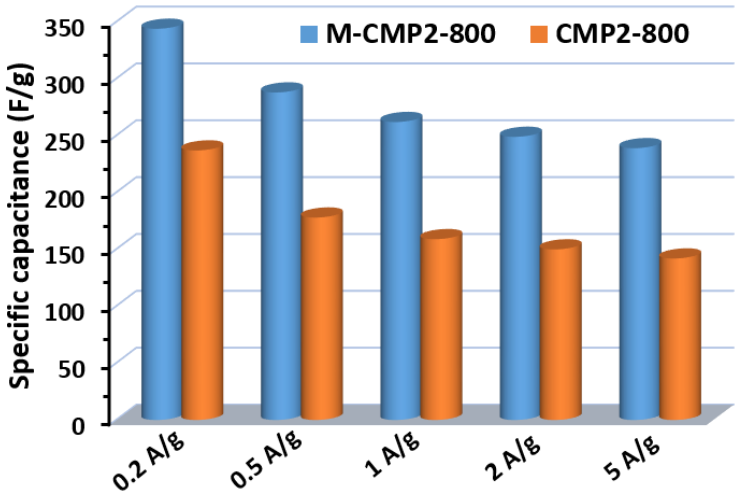

Figure 6.27 Specific capacitances of M-CMP2-800 and CMP2-800 at different current densities in 6 M aqueous KOH solution using Ag/AgCl as the reference electrode.

6.3 Conclusions

In conclusion, a series of sandwich-like MoS_2-templated conjugated microporous polymer nanosheets with high specific surface area was successfully developed by utilizing 4-iodophenyl-functionalized MoS_2 as template. By direct pyrolysis, 2D MoS_2/nitrogen-doped porous carbon (M-CMPs-*T*) hybrids were obtained with large specific surface areas and aspect ratios as well as hierarchical porous structure. In these hybrids, both sides of the single-layer MoS_2 nanosheets were uniformly decorated with the nitrogen-doped porous carbon layers for good interfacial contact. The M-CMPs-*T* hybrids have been used for electrochemical

catalyzed ORR with high activity and selectivity as well as excellent supercapacitor performance. We expect that our novel strategy can be extended for the generation of various other layered hybrid materials for energy conversion and storage.

Table 6.3 Comparison of the gravimetric capacitances of MoS_2- and carbon-based electrodes.

Materials	Gravimetric capacitance (F/g)	Electrolyte	References
$MCMoS_2$/RGO	265 (10 mV s^{-1})	1 M $HClO_4$	42
Metallic 1T phase MoS_2 nanosheets	110 (0.5 A/g)	0.5 M K_2SO_4	44
Defect-rich MoS_2 ultrathin nanosheets	154.9 (1 A/g)	3 M KCl	47
Layered MoS_2-graphene composites	243 (1 A/g)	1 M Na_2SO_4	48
MoS_2@MPC	189 (1 A/g)	1 M H_2SO_4	49
Porous tubular carbon/MoS_2	210 (1 A/g)	3.0 M KOH	50
Nitrogen-doped carbon/MoS_2	158 (0.5 A/g)	0.5 M H_2SO_4	51
2D RGO/MoS_2	235 (5 mV s^{-1})	1 M H_2SO_4	52
KOH activated porous carbon nanosheets	300 (0.5 A/g)	6 M KOH	53
Reduced graphene oxide	41.5 (0.1 A/g)	6 M KOH	54
2D porous carbon nanosheets	244-304 (0.1 A/g)	6 M KOH	11
S-porous carbon/graphene	109 (0.05 A/g)	6 M KOH	55
KOH activated graphene	166 (0.7 A/g)	BMIM BF_4/AN	56
Nitrogen-enriched nonporous carbon	115 (0.05 A/g)	1 M H_2SO_4	57
N-doped reduced graphene oxide	255 (0.5 A/g)	6 M KOH	58
3D nitrogen and boron co-doped graphene	239 (1 A/g)	1 M H_2SO_4	59
Boron-doped graphene nanoplatelets	160 (1 A/g)	6 M KOH	60
3D porous carbon	176 (10 mV s^{-1})	1 M H_2SO_4	61
Multifunctional carbon	142 (2 mV s^{-1})	0.65 M K_2SO_4	62
Nitrogen-doped holey graphitic carbon	206 (0.1 A/g)	6 M KOH	30
M-CMP2-800	**344 (0.2 A/g)**	**6 M KOH**	**This work**
	288 (0.5 A/g)	**6 M KOH**	
	262 (1 A/g)	**6 M KOH**	

6.4 Experimental

All reagents, unless otherwise stated, were obtained from commercial sources (Sigma Aldrich, Alfa Aesar and Acros) and were used without further purification.

6.4.1 Synthesis of Chemically Exfoliated MoS_2 (CE-MoS_2)

Chemically exfoliated MoS_2 (CE-MoS_2) was synthesized by lithium

intercalation into bulk MoS_2 powder according to a previously reported procedure.[19] Briefly, 1.5 mL of a 2.0 M *n*-butyllithium solution in hexane were added to 1.5 g bulk MoS_2 powder under argon atmosphere. After addition of 10 mL of dry hexane, the dispersion was heated up to 65 °C for 2 days. The mixture was then filtered and washed with hexane to remove the excess of *n*-butyllithium. The intercalated powder was then exfoliated in water at a concentration of 1 mg/mL, sonicated for 1 h, and centrifuged to remove lithium cations as well as the non-exfoliated materials.

6.4.2 Synthesis of 4-Iodophenyl Functionalized MoS_2 (MoS_2-I)

The aqueous solution of the as prepared 4-iodophenyl diazonium salt was added to 400 mL of the CE-MoS_2 dispersion in water dropwise under exposure to light. After addition of only a few drops of the reagent, a black precipitate formed. The reaction mixture was stirred overnight and filtered through a reinforced cellulose membrane filter (0.2 μm). Washing with isopropyl alcohol to remove organic side products and with distilled water yielded the 4-iodophenyl functionalized MoS_2 product after drying under vacuum (yield: 352 mg MoS_2-I).

6.4.3 Synthesis of 1,3,5-Triethynylbenzene

Synthesis of 1,3,5-triethynylbenzene.[63] To a solution of 1,3,5-tribromobenzene (3.0 g, 9.6 mmol) in dry triethylamine (200 mL) $Pd(PPh_3)_2Cl_2$ (195 mg, 0.3 mmol) and CuI (57 mg, 0.3 mmol) were added and the mixture was stirred for 20 minutes under argon atmosphere. Trimethylsilylacetylene (9.6 mL, 68.1 mmol) was added and the reaction was heated to 65 °C and stirred for 24 hours. After cooling down to room temperature, the reaction mixture was filtered. After evaporation of the solvent, the residue was purified by column chromatography on silica gel with hexane as eluent to give 1,3,5-tris(trimethylsilylethynyl)benzene (3.26 g, 93.3%) as pale yellow solid. This product was dissolved in THF (30 mL) and a solution of anhydrous potassium hydroxide (4.48 g, 80 mmol) dissolved in 30 mL of methanol was added and the mixture was stirred at room temperature overnight. After most of the solvent was evaporated, 100 mL of 1 M aqueous HCl solution were added and the mixture

extracted with dichlormethane (DCM) three times. The organic phases were combined and then dried over $MgSO_4$. After filtration and solvent evaporation, the crude product was purified by a silica gel column chromatography using hexane as eluent. 1,3,5-triethynylbenzene was obtained as a white solid (1.27 g, 95.5%). ^{1}H NMR (400 MHz, $CDCl_3$) δ 7.59 (s, 3H), 3.13 (s, 3H). ^{13}C NMR (100 MHz, $CDCl_3$) δ 135.64, 122.95, 81.61, 78.66. MS (EI): m/z calcd 150.05; found 150.10.

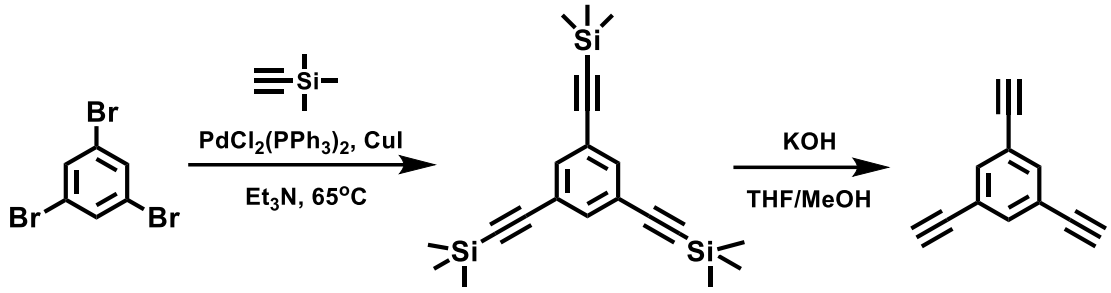

6.4.4 Preparation of MoS_2-Templated CMPs (M-CMPs) and MoS_2-Free CMPs

The MoS_2-templated conjugated microporous polymers (M-CMPs) were constructed in palladium-catalyzed Sonogashira-Hagihara cross-coupling reactions of MoS_2-I, 1,3,5-triethynylbenzene, and aryl halide (2,5-dibromopyridine, 2,5-dibromopyrazine, and 2,4,6-trichloro-1,3,5-triazine), as show in Scheme 6.2. The control samples (CMPs) were prepared using the same procedure without MoS_2-I. The following procedure for M-CMP1 synthesis is given as a representative example.

First, MoS_2-I (100 mg) was sonicated in dry DMF (150 mL) until complete dispersion occurred. Then, 1,3,5-triethynylbenzene (255 mg, 1.7 mmol), 2,5-dibromopyridine (474 mg, 2.0 mmol), tetrakis(triphenylphosphine) palladium (35 mg, 0.03 mmol), copper iodide (7 mg, 0.03 mmol), and Et_3N (20 mL) were added to the MoS_2-I dispersion. The reaction mixture was heated up to 100 °C, and stirred for 72 h under N_2 atmosphere. Next, the insoluble product was filtered off and washed four times with chloroform, water, and acetone to remove unreacted monomers and catalyst residues. Further purification of the polymer networks was carried out by Soxhlet extraction with THF for 48 h. The product was dried in vacuum for 24 h at

room temperature, to afford M-CMP1 (yield: 496 mg).

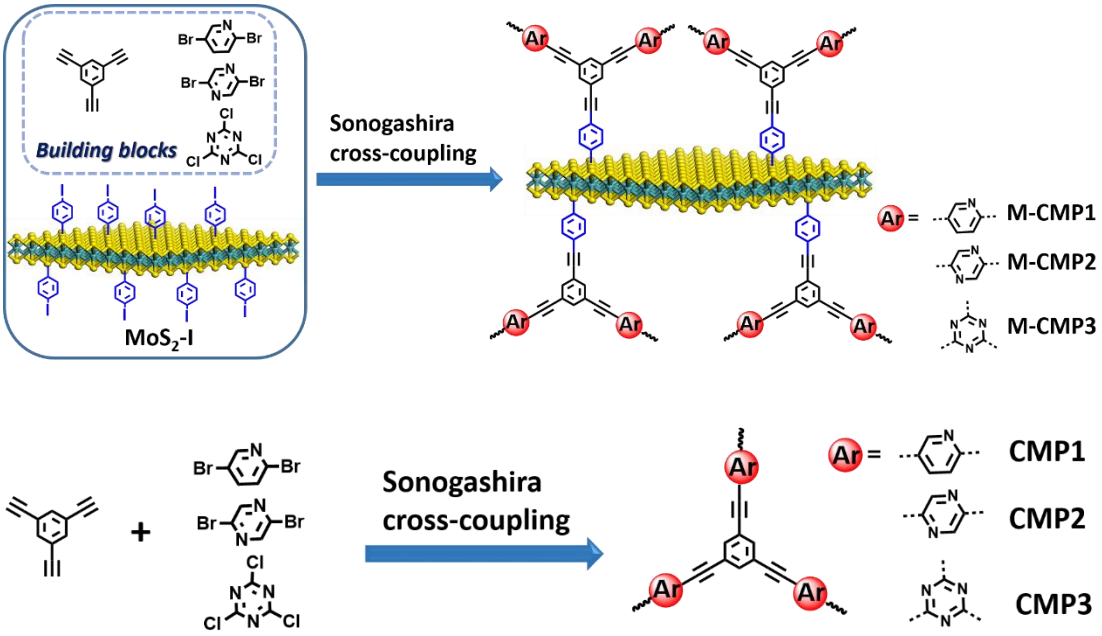

Scheme 6.2 Idealized formula scheme depicting the preparation of MoS_2-templated conjugated microporous polymers (M-CMPs) and conjugated microporous polymers (CMPs) without MoS_2.

6.4.5 Characterizations

Fourier transform infrared (FTIR) spectroscopy studies were conducted on a JASCO FT/IR-4200 Fourier-transform IR-spectrometer. Raman spectra were recorded on a LabRAM HR Raman Microscope with an excitation length of 633 nm. UV-Vis absorption spectra were recorded on a Shimadzu UV-2401 PC spectrophotometer at room temperature. The nanomorphology of MoS_2-I, M-CMPs and MoS_2-templated carbon materials were characterized by transmission electron microscopy (TEM, JEOL, JEM-2100F). The AFM images were obtained with an atomic force microscope Bruker diInnova operated in the tapping mode. The SEM studies were carried out at a Philips XL30S FEG microscope with a field emission cathode. Thermogravimetric analyses were performed on a Mettler Toledo TGA Stare System under argon flow. X-ray photoelectron spectroscopy (XPS) was carried out on a Kratos AXIS Ultra, performing at 15 kV and 15 mA with a monochromatic Al Kα

source (hν = 1486.71 eV).

Nitrogen adsorption-desorption measurements. The nitrogen adsorption-desorption measurements were performed on a BELSORB Max (BEL Japan Inc.). The surface areas were calculated using the BET model in the pressure range p/p_0 from 0.05-0.3. The total pore volume was determined at a relative pressure of 0.99. The pore size distribution was analyzed from the nitrogen adsorption data using a NLDFT method with a slit pore model.

Solid-State NMR measurements. ^{13}C cross-polarization/magic-angle spinning (CP/MAS) NMR spectra were recorded at 50.33 MHz using a Bruker AVANCE III 200 NMR spectrometer with a contact time of 2.5 ms, by averaging 16384 transients at a relaxation delay of 2 s. All experiments were carried out at room temperature using a standard Bruker 2.5 mm double resonance-MAS probe with spinning at 20 kHz, typical π/2-pulse lengths of 2.5 μs, and SPINAL64 proton decoupling (200.15 MHz; 10π/12 pulse set to 4.2 μs) at rather modest power levels of 46.5 Watt (^{13}C) and 19 Watt (^{1}H), respectively. The ^{13}C spectra were referenced with respect to tetramethylsilane (TMS) using solid adamantane as secondary standard (29.46 ppm for ^{13}C).

6.4.6 Oxygen Reduction Reaction (ORR) Measurement

Cyclic voltammetry (CV) and Rotating Disk Electrode (RDE) Measurements:

First, 10 mg of the sample were blended with 500 μL of a 1 wt % Nafion ethanol solution, and then sonicated until a homogeneous dispersion is formed. Next, a certain volume of the catalyst dispersion was pipetted onto a glassy carbon electrode with a diameter of 5 mm (0.6 mg/cm^2). For comparison, the Pt/C catalyst dispersion was prepared by dispersing 4 mg of Pt/C (20 wt% Pt) in 1 mL of ethanol with 35 μL of 5 wt% Nafion solution (40 wt% of Nafion to catalyst ratio). Next, 5 μL of the Pt/C dispersion was loaded onto a glassy carbon electrode. The catalyst dispersion was

dried slowly in air until a uniform catalyst distribution across the electrode surface was obtained.

Electrochemical measurements (cyclic voltammetry (CV), rotating disk electrode (RDE) and rotating ring-disk electrode (RRDE) measurements) were performed with a bipotentiostat (Pine Research Instrumentation, USA) in a three-electrode cell system. A rotating glassy carbon disk and platinum ring electrode (Pine Research Instrumentation, USA) after loading with the electrocatalyst were used as working electrode, an Ag/AgCl (KCl, 3 M) electrode as reference electrode, and a Pt wire as counter electrode. The electrochemical experiments were conducted in a 0.1 M KOH aqueous electrolyte (saturated with oxygen by bubbling O_2) for the oxygen reduction reaction. The potential range was cycled between -0.9 and 0.1 V at a scan rate of 100 mV/s at room temperature after purging O_2 gas for 30 min through the cell. A flow of O_2 was maintained through the electrolyte during recording of CVs. In control experiments, CV measurements were performed in a N_2-saturated electrolyte. RDE measurements were scanned cathodically at a rate of 5 mV s^{-1} for different rotating speeds from 225 to 1600 rpm.

The Koutecky-Levich (*K-L*) plots (J^{-1} vs $\omega^{-1/2}$) were analyzed at various electrode potentials. The slopes of the linear lines were used to calculate the number of electrons transferred (*n*) per oxygen molecule in the ORR process at the electrodes according to the *K-L* equation, and J_K can be calculated from the inverse of intercept.

$$\frac{1}{J} = \frac{1}{J_L} + \frac{1}{J_K} = \frac{1}{B\omega^{1/2}} + \frac{1}{J_K}$$

$$B = 0.62nF\,C_0\,(D_0)^{2/3}\,v^{-1/6}$$

$$J_K = nFkC_0$$

where J is the measured current density, J_K and J_L are the kinetic- and diffusion-limited current densities, ω is the angular velocity of the rotating electrode ($\omega = 2\pi N$, N is the linear rotation speed), F is the Faraday constant (F = 96485 C mol^{-1}), C_0 is the concentration of O_2 in 0.1 M KOH (1.2×10^{-3} M), D_0 is the diffusion

coefficient of O_2 in 0.1 M KOH (1.9×10^{-5} cm^2 s^{-1}), v is the kinematic viscosity of the electrolyte (0.01cm^2 s^{-1}), and k is the electron transfer rate constant.

Rotating Ring-Disk Electrode (RRDE) Measurement:

Catalyst inks and electrodes were prepared by the same method as above. The disk electrode was scanned cathodically at a rate of 5 mV s^{-1}, and the ring potential was constant at 0.5 V *vs*. Ag/AgCl.

Based on the RRDE results, the HO_2^- (%) and the electron transfer number (n) were determined by the following equations:

$$n = \frac{4I_{Disk}}{I_{Disk} + \frac{I_{Ring}}{N}}$$

$$\%(HO_2^-) = \frac{200 \times \frac{I_{Ring}}{N}}{I_{Disk} + \frac{I_{Ring}}{N}}$$

where I_{disk} is disk current, I_{ring} is ring current, and N is current collection efficiency of the Pt ring, which was provided as 0.37 by the manufacturer.

6.4.6 Electrochemical Energy Storage (*Supercapacitor*) Performance

Electrochemical measurements for M-CMP2-800 and CMP2-800 as electrode materials: The electrochemical experiments were carried out using a conventional, aqueous three-electrode system employing 6 M aqueous KOH as electrolyte at room temperature. The three-electrode cell incorporates Ag/AgCl as reference electrode, Pt as counter electrode, and the M-CMP2-800 or CMP2-800 samples as working electrodes. The working electrode was prepared by loading CMP2-800 or CMP2-800 onto a glassy carbon electrode. Thereby, 1 mg of CMP2-800 or CMP2-800 and 50 μL of Nafion (5 wt%) were first mixed in 950 μL solvent (1:1 v/v water/isopropanol) by sonication under formation of a homogeneous dispersion (1 mg/mL). Next, 5 μL of the dispersion were loaded onto a glassy carbon electrode with a diameter of 5 mm. The modified electrode was slowly dried in air until a uniform active layer was formed at the electrode surface. The following cyclic voltammetry (CV) and

galvanostatic charge/discharge (GCD) measurements were performed using a PAR VersaSTAT 4 electrochemical workstation within the voltage range from -1 to 0 V.

6.5 References

(1) Yuan, K.; Zhuang, X.; Fu, H.; Brunklaus, G.; Forster, M.; Chen, Y.; Feng, X.; Scherf, U. *Angew. Chem., Int. Ed.* **2016**, *55*, 6858-6863.

(2) Novoselov, K. S.; Geim, A. K.; Morozov, S. V.; Jiang, D.; Zhang, Y.; Dubonos, S. V.; Grigorieva, I. V.; Firsov, A. A. *Science* **2004**, *306*, 666-669.

(3) Lomeda, J. R.; Doyle, C. D.; Kosynkin, D. V.; Hwang, W.-F.; Tour, J. M. *J. Am. Chem. Soc.* **2008**, *130*, 16201-16206.

(4) Bekyarova, E.; Itkis, M. E.; Ramesh, P.; Berger, C.; Sprinkle, M.; de Heer, W. A.; Haddon, R. C. *J. Am. Chem. Soc.* **2009**, *131*, 1336-1337.

(5) Zhu, Y.; Higginbotham, A. L.; Tour, J. M. *Chem. Mater.* **2009**, *21*, 5284-5291.

(6) Greenwood, J.; Phan, T. H.; Fujita, Y.; Li, Z.; Ivasenko, O.; Vanderlinden, W.; Van Gorp, H.; Frederickx, W.; Lu, G.; Tahara, K.; Tobe, Y.; Uji, I. H.; Mertens, S. F.; De Feyter, S. *ACS Nano* **2015**, *9*, 5520-5535.

(7) Criado, A.; Melchionna, M.; Marchesan, S.; Prato, M. *Angew. Chem., Int. Ed.* **2015**, *54*, 10734-10750.

(8) Colson, J. W.; Woll, A. R.; Mukherjee, A.; Levendorf, M. P.; Spitler, E. L.; Shields, V. B.; Spencer, M. G.; Park, J.; Dichtel, W. R. *Science* **2011**, *332*, 228-231.

(9) Liu, S.; Gordiichuk, P.; Wu, Z. S.; Liu, Z.; Wei, W.; Wagner, M.; Mohamed-Noriega, N.; Wu, D.; Mai, Y.; Herrmann, A.; Mullen, K.; Feng, X. *Nat. Commun.* **2015**, *6*, 8817.

(10) Jahan, M.; Bao, Q.; Yang, J.-X.; Loh, K. P. *J. Am. Chem. Soc.* **2010**, *132*, 14487-14495.

(11) Zhuang, X.; Zhang, F.; Wu, D.; Forler, N.; Liang, H.; Wagner, M.; Gehrig, D.; Hansen, M. R.; Laquai, F.; Feng, X. *Angew. Chem., Int. Ed.* **2013**, *52*, 9668-9672.

(12) Zhuang, X.; Zhang, F.; Wu, D.; Feng, X. *Adv. Mater.* **2014**, *26*, 3081-3086.

(13) Chia, X.; Eng, A. Y.; Ambrosi, A.; Tan, S. M.; Pumera, M. *Chem. Rev.* **2015**, *115*, 11941-11966.

(14) Bhimanapati, G. R.; Lin, Z.; Meunier, V.; Jung, Y.; Cha, J.; Das, S.; Xiao, D.; Son, Y.; Strano, M. S.; Cooper, V. R.; Liang, L.; Louie, S. G.; Ringe, E.; Zhou, W.; Kim, S. S.; Naik, R. R.; Sumpter, B. G.; Terrones, H.; Xia, F.; Wang, Y.; Zhu, J.; Akinwande, D.; Alem, N.; Schuller, J. A.; Schaak, R. E.; Terrones, M.; Robinson, J. A. *ACS Nano* **2015**, *9*, 11509-11539.

(15) Zhang, H. *ACS Nano* **2015**, *9*, 9451-9469.

(16) Gupta, A.; Sakthivel, T.; Seal, S. *Prog. Mater. Sci.* **2015**, *73*, 44-126.

(17) Lv, R.; Terrones, H.; Elías, A. L.; Perea-López, N.; Gutiérrez, H. R.; Cruz-Silva, E.; Rajukumar, L. P.; Dresselhaus, M. S.; Terrones, M. *Nano Today* **2015**, *10*, 559-592.

(18) Presolski, S.; Pumera, M. *Mater Today* **2016**, *19*, 140-145.

(19) Knirsch, K. C.; Berner, N. C.; Nerl, H. C.; Cucinotta, C. S.; Gholamvand, Z.; McEvoy, N.; Wang, Z.; Abramovic, I.; Vecera, P.; Halik, M.; Sanvito, S.; Duesberg, G. S.; Nicolosi, V.; Hauke, F.; Hirsch, A.; Coleman, J. N.; Backes, C. *ACS Nano* **2015**, *9*, 6018-6030.

(20) Liu, T.; Wang, C.; Gu, X.; Gong, H.; Cheng, L.; Shi, X.; Feng, L.; Sun, B.; Liu, Z. *Adv. Mater.* **2014**, *26*, 3433-3440.

(21) Voiry, D.; Goswami, A.; Kappera, R.; SilvaCecilia de Carvalho Castro, e.; Kaplan, D.; Fujita, T.; Chen, M.; Asefa, T.; Chhowalla, M. *Nat. Chem.* **2015**, *7*, 45-49.

(22) Nguyen, E. P.; Carey, B. J.; Ou, J. Z.; van Embden, J.; Gaspera, E. D.; Chrimes, A. F.; Spencer, M. J. S.; Zhuiykov, S.; Kalantar-zadeh, K.; Daeneke, T. *Adv. Mater.* **2015**, *27*, 6225-6229.

(23) Tang, H.; Wang, J.; Yin, H.; Zhao, H.; Wang, D.; Tang, Z. *Adv. Mater.* **2015**, *27*, 1117-1123.

(24) Jiang, H.; Ren, D.; Wang, H.; Hu, Y.; Guo, S.; Yuan, H.; Hu, P.; Zhang, L.; Li, C. *Adv. Mater.* **2015**, *27*, 3687-3695.

(25) Silva, R.; Voiry, D.; Chhowalla, M.; Asefa, T. *J. Am. Chem. Soc.* **2013**, *135*,

7823-7826.

(26) Meng, Y.; Voiry, D.; Goswami, A.; Zou, X.; Huang, X.; Chhowalla, M.; Liu, Z.; Asefa, T. *J. Am. Chem. Soc.* **2014**, *136*, 13554-13557.

(27) Chen, S.; Bi, J.; Zhao, Y.; Yang, L.; Zhang, C.; Ma, Y.; Wu, Q.; Wang, X.; Hu, Z. *Adv. Mater.* **2012**, *24*, 5593-5597.

(28) Wei, J.; Hu, Y. X.; Liang, Y.; Kong, B. A.; Zhang, J.; Song, J. C.; Bao, Q. L.; Simon, G. P.; Jiang, S. P.; Wang, H. T. *Adv. Funct. Mater.* **2015**, *25*, 5768-5777.

(29) Yang, S.; Zhi, L.; Tang, K.; Feng, X.; Maier, J.; Müllen, K. *Adv. Funct. Mater.* **2012**, *22*, 3634-3640.

(30) Xiang, Z.; Cao, D.; Huang, L.; Shui, J.; Wang, M.; Dai, L. *Adv. Mater.* **2014**, *26*, 3315-3320.

(31)Wu, Z.-S.; Chen, L.; Liu, J.; Parvez, K.; Liang, H.; Shu, J.; Sachdev, H.; Graf, R.; Feng, X.; Müllen, K. *Adv. Mater.* **2014**, *26*, 1450-1455.

(32) Hao, L.; Zhang, S.; Liu, R.; Ning, J.; Zhang, G.; Zhi, L. *Adv. Mater.* **2015**, *27*, 3190-3195.

(33) Xu, Y.; Jin, S.; Xu, H.; Nagai, A.; Jiang, D. *Chem. Soc. Rev.* **2013**, *42*, 8012-8031.

(34) Hao, L.; Ning, J.; Luo, B.; Wang, B.; Zhang, Y.; Tang, Z.; Yang, J.; Thomas, A.; Zhi, L. *J. Am. Chem. Soc.* **2014**, *137*, 219-225.

(35) Xiang, Z.; Xue, Y.; Cao, D.; Huang, L.; Chen, J.-F.; Dai, L. *Angew. Chem., Int. Ed.* **2014**, *53*, 2433-2437.

(36) Zhuang, X.; Gehrig, D.; Forler, N.; Liang, H.; Wagner, M.; Hansen, M. R.; Laquai, F.; Zhang, F.; Feng, X. *Adv. Mater.* **2015**, *27*, 3789-3796.

(37) Du, R.; Zhang, N.; Xu, H.; Mao, N.; Duan, W.; Wang, J.; Zhao, Q.; Liu, Z.; Zhang, J. *Adv. Mater.* **2014**, *26*, 8053-8058.

(38) Ferrari, A. C.; Meyer, J. C.; Scardaci, V.; Casiraghi, C.; Lazzeri, M.; Mauri, F.; Piscanec, S.; Jiang, D.; Novoselov, K. S.; Roth, S.; Geim, A. K. *Phys. Rev. Lett.* **2006**, *97*, 187401.

(39) Ferrari, A. C.; Basko, D. M. *Nat. Nanotechnol.* **2013**, *8*, 235-246.

(40) Liang, H. W.; Zhuang, X.; Bruller, S.; Feng, X.; Mullen, K. *Nat. Commun.* **2014**,

5, 4973.

(41) Liang, Y.; Li, Y.; Wang, H.; Zhou, J.; Wang, J.; Regier, T.; Dai, H. *Nat. Mater.* **2011**, *10*, 780-786.

(42) da Silveira Firmiano, E. G.; Rabelo, A. C.; Dalmaschio, C. J.; Pinheiro, A. N.; Pereira, E. C.; Schreiner, W. H.; Leite, E. R. *Adv. Energy Mater.* **2014**, *4*, 1301380.

(43) Sun, G.; Zhang, X.; Lin, R.; Yang, J.; Zhang, H.; Chen, P. *Angew. Chem., Int. Ed.* **2015**, *54*, 4651-4656.

(44) Acerce, M.; Voiry, D.; Chhowalla, M. *Nat. Nanotechnol.* **2015**, *10*, 313-318.

(45) Wang, L.; Ma, Y.; Yang, M.; Qi, Y. *Electrochim. Acta* **2015**, *186*, 391-396.

(46) Mahmood, Q.; Park, S. K.; Kwon, K. D.; Chang, S.-J.; Hong, J.-Y.; Shen, G.; Jung, Y. M.; Park, T. J.; Khang, S. W.; Kim, W. S.; Kong, J.; Park, H. S. *Adv. Energy Mater.* **2016**, *6*, 1501115.

(47) Wu, Z.; Li, B.; Xue, Y.; Li, J.; Zhang, Y.; Gao, F. *J. Mater. Chem. A* **2015**, *3*, 19445-19454.

(48) Huang, K.-J.; Wang, L.; Liu, Y.-J.; Liu, Y.-M.; Wang, H.-B.; Gan, T.; Wang, L.-L. *Int. J. Hydrogen. Energ.* **2013**, *38*, 14027-14034.

(49) Weng, Q.; Wang, X.; Wang, X.; Zhang, C.; Jiang, X.; Bando, Y.; Golberg, D. *J. Mater. Chem. A* **2015**, *3*, 3097-3102.

(50) Hu, B.; Qin, X.; Asiri, A. M.; Alamry, K. A.; Al-Youbi, A. O.; Sun, X. *Electrochim. Acta* **2013**, *100*, 24-28.

(51) Yang, M.; Hwang, S.-K.; Jeong, J.-M.; Huh, Y. S.; Choi, B. G. *Synthetic. Met.* **2015**, *209*, 528-533.

(52) Mahmood, Q.; Park, S. K.; Kwon, K. D.; Chang, S.-J.; Hong, J.-Y.; Shen, G.; Jung, Y. M.; Park, T. J.; Khang, S. W.; Kim, W. S.; Kong, J.; Park, H. S. *Adv. Energy Mater.* **2015**, 1501115.

(53) Fan, X. M.; Yu, C.; Yang, J.; Ling, Z.; Hu, C.; Zhang, M. D.; Qiu, J. S. *Adv. Energy Mater.* **2015**, *5*, 1401761.

(54) Lei, Z.; Christov, N.; Zhao, X. S. *Energy Environ. Sci.* **2011**, *4*, 1866-1873.

(55) Seredych, M.; Bandosz, T. J. *J. Mater. Chem. A* **2013**, *1*, 11717-11727.

(56) Zhu, Y.; Murali, S.; Stoller, M. D.; Ganesh, K. J.; Cai, W.; Ferreira, P. J.; Pirkle, A.; Wallace, R. M.; Cychosz, K. A.; Thommes, M.; Su, D.; Stach, E. A.; Ruoff, R. S. *Science* **2011**, *332*, 1537-1541.

(57) Hulicova-Jurcakova, D.; Kodama, M.; Shiraishi, S.; Hatori, H.; Zhu, Z. H.; Lu, G. Q. *Adv. Funct. Mater.* **2009**, *19*, 1800-1809.

(58) Lei, Z.; Lu, L.; Zhao, X. S. *Energy Environ. Sci.* **2012**, *5*, 6391-6399.

(59) Wu, Z.-S.; Winter, A.; Chen, L.; Sun, Y.; Turchanin, A.; Feng, X.; Müllen, K. *Adv. Mater.* **2012**, *24*, 5130-5135.

(60) Han, J.; Zhang, L. L.; Lee, S.; Oh, J.; Lee, K.-S.; Potts, J. R.; Ji, J.; Zhao, X.; Ruoff, R. S.; Park, S. *ACS Nano* **2013**, *7*, 19-26.

(61) Wu, Z.-S.; Sun, Y.; Tan, Y.-Z.; Yang, S.; Feng, X.; Müllen, K. *J. Am. Chem. Soc.* **2012**, *134*, 19532-19535.

(62) Assresahegn, B. D.; Belanger, D. *Adv. Funct. Mater.* **2015**, *25*, 6775-6785.

(63) Xie, Y.; Wang, T.-T.; Yang, R.-X.; Huang, N.-Y.; Zou, K.; Deng, W.-Q. *ChemSusChem* **2014**, *7*, 2110-2114.

Chapter 7

Summary and Outlook

7.1 Summary of Chapters 2-6

Graphene nanosheets show a high tendency for re-aggregation and stacking due to their high surface area as well as strong π-π interactions and van der Waals forces between adjacent graphene sheets, thus resulting in a deteriorated supercapacitor performance in the course of an utilization as electrode materials. In this dissertation, it is found that the formation of porous graphene frameworks (PGF) can effectively prevent the re-aggregation via introduction of layer-to-layer oligophenyl pillars. The inherent porous structure of PGF combined with the excellent electrical conductivity results in an efficient ion extraction or/and insertion and an efficient formation of electrochemical double layers on the graphene surface, coupled to increased specific capacitances, high cycling stability as well as high rate capability.

CMPs are usually insoluble and non-processable powders. We successfully fabricated CMP-based nanofibrous films by electrospinning CMP/PLA mixtures. CMP-based nanofibrous films can be used as efficient fluorescence sensors for detecting nitroaromatic and benzoquinone vapors as well as oxidizing metal ions with high sensitivity.

4-iodophenyl-substituted graphene (RGO-I) was both used as building block and structure directing template for the construction of graphene-CMP (GMP) sandwiches in a solution-based approach. The 2D structure of RGO-I with its large aspect ratio allows for the growth of uniform CMP shells onto both sides of the graphene sheets. Thereby, aggregation and restacking of the graphene sheets can be effectively suppressed even during high-temperature treatment. Thus, well-defined porous carbon/graphene nanosheets were readily obtained by direct pyrolysis of the GMP

sandwiches. The sandwich-like porous carbon/graphene nanosheets were used as electrode materials of supercapacitor devices with very promising capacitive performance. The good 2D electron transport ability of graphene together with the intimate interactions between porous carbon and graphene layers provide a very useful combination of high electrochemical active surface area for charge transfer and minimized ion diffusion paths during thecharge/discharge process. This unique set of physical properties effectively boosts the capacitive performance.

MoS_2-templated CMP nanosheets were fabricated by growing nitrogen-rich CMPs onto 4-iodophenyl-functionalized MoS_2 templates. Hierarchically 2D porous MoS_2/nitrogen-doped porous carbon hybrids are fabricated by pyrolysis of MoS_2-templated CMP sandwiches. The hybrids are characterized by high specific surface areas and aspect ratios and showed a promising performance in the oxygen reduction reaction as well as a promising supercapacitor performance due to the maximized interfacial interaction between nitrogen-doped porous carbon and MoS_2 layers.

7.2 Outlook

The electrode materials play an important role in the performance of supercapacitors. Carbonaceous materials with high specific surface area can act as active material and as current collector for an optimum access of the electrolyte ions. Although carbonaceous materials have demonstrated stable electrochemical properties, their energy densities are still limited and need to be further improved. In addition to an improvement of the capacitance, an increase of the operation voltage window, e.g. by using proper organic electrolytes or ionic liquids based electrolyte is regarded as another promising strategy to enhance the energy density. Therefore, hybrid materials are attractive alternatives to realize high performance supercapacitors, due to their high mechanical integrity and the improved electrochemical properties of pseudocapacitive hybrid materials. For an optimum performance of hybrid materials, their composition and structure, the interface interactions, and pore size disstributions

must be delicately controlled.

Apart from the electrode materials, device configuration is another major factor that determines the supercapacitor performance. Until now, various supercapacitor designs with different device configurations have been developed. For example, the use of asymmetric supercapacitors can lead to increased cell voltages for realizeing a high energy density. In-plane supercapacitors can improve the capacitance by increasing the load with active materials while maintaining high power capability. Finally, flexible supercapacitors show great potential for use in various flexible and wearable electronic devices. For more practical applications of flexible supercapacitors, much attention is needed for designing high performance flexible supercapacitors by integrating multiple functions, such as transparence, and self-powering, or by miniaturization. Such multifunctional, flexible supercapacitors may be widely applied in wearable electronics, bio-implantable systems, flexible and rollable displays, etc. in the future.

Publications

[1] **Kai Yuan**, Ting Hu, Yazhou Xu, Robert Graf, Lei Shi, Michael Forster, Thomas Pichler, Thomas Riedl, Yiwang Chen* and Ullrich Scherf*. Nitrogen-doped Porous Carbon/Graphene Nanosheets Derived from Two-Dimensional Conjugated Microporous Polymer Sandwiches with Promising Capacitive Performance. *Mater. Chem. Front.*, **2017**, DOI: 10.1039/C6QM00012F. (Chapter 5)

[2] **Kai Yuan**, Xiaodong Zhuang*, Ting Hu, Lei Shi, Stavroula Sfaelou, Ulrike Polnick, Michael Forster, Thomas Pichler, Thomas Riedl, Xinliang Feng, Yiwang Chen*, and Ullrich Scherf*. 2D-Heterostructures Derived from MoS_2-Templated, Cobalt-Containing Conjugated Microporous Polymer Sandwiches for Oxygen Reduction Reaction and Electrochemical Energy Storage. *ChemElectroChem*, **2017**, DOI: 10.1002/celc.201600850.

[3] **Kai Yuan**, Xiaodong Zhuang, Haiyan Fu, Gunther Brunklaus, Michael Forster, Yiwang Chen, Xinliang Feng* and Ullrich Scherf*. Two-dimensional Core-Shelled Porous Hybrids as Highly Efficient Catalysts for Oxygen Reduction Reaction. *Angew. Chem. Int. Ed.*, **2016**, 55, 6858-6863. (Chapter 6)

[4] **Kai Yuan**, Ting Hu, Yazhou Xu, Robert Graf, Gunther Brunklaus, Michael Forster, Yiwang Chen* and Ullrich Scherf*. Engineering the Morphology of Carbon Materials: 2D Porous Carbon Nanosheets for High Performance Supercapacitors. *ChemElectroChem*, **2016**, 3, 822-828. (Chapter 4)

[5] **Kai Yuan**, Yazhou Xu, Johannes Uihlein, Gunther Brunklaus, Lei Shi, Ralf Heiderhoff, Mingming Que, Michael Forster, Thomas Chassé, Thomas Pichler, Thomas Riedl, Yiwang Chen* and Ullrich Scherf*. Straightforward Generation of Pillared, Microporous Graphene Frameworks for Use in Supercapacitors. *Adv. Mater.*, **2015**, 27, 6714-6721. (Chapter 2)

[6] **Kai Yuan**, Peiyao Guo-Wang, Ting Hu, Lei Shi, Rong Zeng, Michael Forster, Thomas Pichler, Yiwang Chen* and Ullrich Scherf*. Nanofibrous and Graphene-Templated Conjugated Microporous Polymer Materials for Flexible Chemosensors and Supercapacitors. *Chem. Mater*., **2015**, 27, 7403-7411. (Chapter 3)

[7] **Kai Yuan**, Lie Chen, and Yiwang Chen*. In Situ Photocatalytically Heterostructured ZnO-Ag Nanoparticle Composites as Effective Cathode-Modifying Layers for Air-Processed Polymer Solar Cells. *Chem. Eur. J.*, **2015**, 21, 11899-11906.

[8] **Kai Yuan**, Lie Chen, and Yiwang Chen*. Direct Anisotropic Growth of CdS Nanocrystals in Thermotropic Liquid Crystal Templates for Heterojunction Optoelectronics. *Chem. Eur. J.*, **2014**, 20, 11488-11495.

[9] **Kai Yuan**, Lie Chen, Licheng Tan and Yiwang Chen*. Performance Enhancement of Bulk Heterojunction Solar Cells with Direct Growth of CdS-Cluster-Decorated Graphene Nanosheets. *Chem. Eur. J.*, **2014**, 20, 6010-6018.

[10] **Kai Yuan**, Lie Chen and Yiwang Chen*. Optical Engineering of Uniformly Decorated Graphene Oxide Nanoflakes via in Situ Growth of Silver Nanoparticles with Enhanced Plasmonic Resonance. *ACS Appl. Mater. Interfaces*, **2014**, 6, 21069-21077.

[11] **Kai Yuan**, Lie Chen, and Yiwang Chen*. Versatile Electron-Collecting Interfacial Layer by in situ Growth of Silver Nanoparticles in Nonconjugated Polyelectrolyte Aqueous Solution for Polymer Solar Cells. *J. Phys. Chem. B*, **2014**, 118, 11563-11572.

[12] **Kai Yuan**, Lie Chen, and Yiwang Chen*. Photovoltaic Performance Enhancement of P3HT/PCBM Solar Cells Driven by Incorporation of Conjugated Liquid Crystalline Rod-Coil Block Copolymers. *J. Mater. Chem. C*, **2014**, 2, 3835-3845.

[13] **Kai Yuan**, Lie Chen, Fan Li, and Yiwang Chen*. Nanostructured Hybrid ZnO@CdS Nanowalls Grown *in situ* for Inverted Polymer Solar Cells. *J. Mater. Chem. C*, **2014**, 2, 1018-1027.

[14] **Kai Yuan**, Lie Chen, and Yiwang Chen*. Nanostructuring Compatibilizers of Block Copolymers for Organic Photovoltaics. *Polym. Int*., **2014**, 63, 593-606.

[15] **Kai Yuan**, Fan Li, Lie Chen, Hongming Wang and Yiwang Chen*. Understanding the Mechanism of Poly(3-hexylthiophene)-*b*-Poly(4-vinylpyridine) as a Nanostructuring Compatibilizer for Improving the Performance of Poly(3-hexylthiophene)/ZnO-Based Hybrid Solar Cells. *J. Mater. Chem. A*, **2013**, 1, 10881-10888.

[16] **Kai Yuan**, Fan Li*, Lie Chen, Yongfang Li and Yiwang Chen*. Liquid Crystal Helps ZnO Nanoparticles Self-assemble for Performance Improvement of Hybrid Solar Cells. *J. Phys. Chem. C*, **2012**, 116, 6332-6339.

[17] **Kai Yuan**, Fan Li, Lie Chen, and Yiwang Chen*. Approach to a Block Polymer Precursor from P3HT Nitroxide-Mediated in situ Polymerization for Stabilization of P3HT/ZnO Hybrid Solar Cells. *Thin Solid Films*, 2012, 520, 6299-6306.

[18] **Kai Yuan**, Fan Li*, Yiwang Chen*, Xiaofeng Wang and Lie Chen*. In situ Growth Nanocomposites Composed of Rodlike ZnO Nanocrystals Arranged by Nanoparticles in a Self-assembling Diblock Copolymer for Heterojunction Optoelectronics. *J. Mater. Chem.*, 2011, 21, 11886-11894.

[19] Mingming Que, Yongfen Tong, Guochang Wei, **Kai Yuan**, Junchao Wei, Yaoquan Jiang, Hui Zhu* and Yiwang Chen*. Safe and flexible ion gel based composite electrolyte for lithium batteries. *J. Mater. Chem. A*, 2016, 4, 14132-14140.

[20] Ting Hu, Longbin Li, Shuqin Xiao, **Kai Yuan**, Hanjun Yang, Lie Chen, Yiwang Chen*. In situ implanting carbon nanotube-gold nanoparticles into ZnO as efficient nanohybrid cathode buffer layer for polymer solar cells. *Org. Electron*. 2016, 38, 350-356.

[21] Ting Hu, Ping Jiang, Lie Chen, **Kai Yuan**, Hanjun Yang, Yiwang Chen*. Amphiphilic fullerene derivative as effective interfacial layer for inverted polymer solar cells. *Org. Electron*. 2016, 37, 35-41.

[22] Ting Hu, Lie Chen, **Kai Yuan**, and Yiwang Chen*. Amphiphilic Fullerene/ZnO Hybrids as Cathode Buffer Layers to Improve Charge Selectivity of Inverted Polymer Solar Cells. *Nanoscale*, **2015**, 7, 9194-9203.

[23] Ting Hu, Lie Chen, **Kai Yuan**, and Yiwang Chen*. Poly(N-vinyl pyrrolidone) Decorated Reduced Graphene Oxide via in situ Growth of ZnO as Cathode Buffer Layer for Polymer Solar Cells. *Chem. Eur. J.*, **2014**, 20, 17178-17184.

Conference publication:

[1] **Kai Yuan**, Michael Forster, Yiwang Chen, and Ullrich Scherf*. Carbon-Based Materials for Use in Supercapacitors. *Leibniz Young Polymer Scientist Forum*, July 6-7, **2016**, Aachen, Germany.

Acknowledgements

How time flies! My PhD journey is coming to an end. Here I would like to express my sincere gratitude to my PhD advisor, Prof. Dr. Ullrich Scherf. Thanks for offering me the opportunity to work in Macromolecular Chemistry Research Group, for his visionary guidance, insightful advices, continuous supports and encouragements in my PhD program. I really appreciate his patience and tolerance, and I also enjoy this experience working with him.

Additionally, I would like to appreciate the funding support from China Scholarship Council offering me the chance to study at University of Wuppertal.

Many thanks to Kerstin Müller, Dr. Wenyue Dong, Dr. Michael Forster, Dr. Eduard Preis, Dr. Suman K. Samanta, and Alex Palma for their kindness help in my life and research work in Germany. I feel so blessed to meet all of them.

I would like to acknowledge my colleagues from Scherf's group, for their generous helps whenever and wherever I needed. It's my pleasure to work with a group of brilliant and warmhearted people.

Particular acknowledgement goes to Prof. Dr. Xinliang Feng, Dr. Xiaodong Zhuang, Prof. Dr. Yiwang Chen, Dr. Lei Shi, Dr. Brunklaus Gunther, Prof. Dr. Thomas Riedl and Dr. Robert Graf, just to name a few, all of whom have been always so supportive, helpful and collaborative to the research work demonstrated here.

Finally, I am deeply grateful to my parents and wife as well as all my family members and friends for their boundless love, continuous understanding and support of my oversea studies in Germany.